DISSERTATION

Titel der Dissertation

Experimental all-optical one-way quantum computing

angestrebter akademischer Grad

Doktor der Naturwissenschaften (Dr. rer.nat.)

Verfasserin / Verfasser:	Robert Prevedel
Matrikel-Nummer:	0006784
Dissertationsgebiet (lt. Studienblatt):	Experimentalphysik
Betreuerin / Betreuer:	o.Univ.-Prof. Dr. DDr. h. c. Anton Zeilinger

Wien, am 27. April 2009

"The most beautiful experience we can have is the mysterious."

Albert Einstein

Contents

Abstract

In recent years, the relatively new field of quantum information processing (QIP) has attracted the attention of many scientists around the world due to its promise of increased computational speed, absolute secure communication and the potential to simulate complex quantum mechanical systems. The very essence of this new quantum information technology are two concepts at the very heart of quantum mechanics, namely superposition and entanglement.

The present Thesis contains the results of four different experiments that were all aimed at the demonstration of an entirely new model for quantum computing with linear optics — the "one-way" quantum computer. For this purpose a multi-photon entangled state of four photons has been generated via the process of spontaneous parametric down-conversion and by using an interferometric setup. This entangled state acts as a resource that allowed for novel demonstrations of quantum algorithms and relevant experimental techniques.

By exploiting the advances developed in both theory and experiment, in this Thesis we report the implementation of fast, active feed-forward that allowed, for the first time, the realization of deterministic linear-optics quantum computing at an unprecedented speed. Further we were able to demonstrate the Deutsch algorithm on our one-way quantum computer, an important quantum algorithm that is capable of distinguishing whether a function is constant or balanced. Classically one needs to query the algorithm at least $2^{N-1} + 1$ times for an N-bit binary input string, however, in the quantum regime, this can be done with one evaluation of the algorithm, independent of the size of the input. In another experiment we succeeded in playing an instance of a quantum game — the so-called Prisoner's dilemma — on our one-way quantum computer. Playing such a game is essentially the execution of a quantum algorithm made up of a distinct set of one- and two-qubit gates. This allows the individual players to increase their strategy space, as they can also choose between superposition of classical input states while their choices get entangled. Evaluating the payoff function of this game for different strategy sets, we were able to experimentally show that the so-called "dilemma", that occurs in the classical version of this game, can be resolved in the quantum domain. Unfortunately, one of the main obstacles on the road towards the realization of large-scale quantum computers is decoherence, the ubiquitous loss of information encoded in a quantum system due to its uncontrollable interaction with an environment. One possible approach to overcome this challenge is to perform the computation in a so-called decoherence-free subspace (DFS). Building up on previous work on concepts of DFS we have been able to theoretically adapt these concepts to the model of one-way quantum computing. This allowed us to demonstrate for the first time the decoherence-free execution of a one-way quantum computing protocol while the photons were exposed to severe phase-damping noise. Remarkable protection of information was accomplished, delivering nearly ideal outcomes.

Although the experiments presented in this Thesis are proof-of-principle they are of great significance in the field of QIP and will hopefully pave the way for ever more exciting inventions and experimental demonstrations in the future.

Zusammenfassung

In den vergangenen Jahren hat das relative neue Feld der Quanteninformationsverarbeitung (QIP) das Interesse vieler Wissenschafter geweckt, da es schnellere Rechenleistung von Computern, absolute sichere Kommunikation sowie ein Potential zum Simulieren von komplexen quantenmechanischen Systemen verspricht. Die Essenz dieser neuen Quanteninformationstechnologie sind zwei Grundkonzepte der Quantenmechanik, nämlich die der Superposition und der Verschränkung. Diese Dissertation enthält die Resultate von vier verschiedenen Experimenten die alle die Demonstration eines neuen Quantencomputer-Models mit linearer Optik, des sogenannten "Einweg-Quantencomputers", zum Ziel hatten. Zu diesem Zweck wurde ein multiphotonen-verschränkter Zustand mit Hilfe des Prozesses der spontanen parametrischen Down-Konversion in einem interferometrischen Setup erzeugt. Dieser verschränkte Zustand agiert als eine Art Ressource, die für Demonstrationen von neuen Quantenalgorithmen und anderen relevanten experimentellen Techniken genutzt wurde. In dieser Dissertation wird über neue Fortschritte in der Theorie und im Experiment berichtet, unter anderem wurde zum ersten Mal eine schnelle, aktive Vorwärtskopplung implementiert, die eine Realisation eines deterministischen Quantencomputer mit einer noch nicht dagewesenen Geschwindigkeit erlaubt. Weiters wurde der sogenannte Deutsch-Algorithmus mit unserem Quantencomputer implementiert. Der Quantenalgorithmus erlaubt es mit nur einer Evaluation zu erkennen, ob eine mathematische Funktion konstant oder balanciert ist, während ein klassischer Algorithmus mindestens $2^{N-1} + 1$ Evaluationen benötigt. In einem anderen Experiment wurde ein Quantenspiel, das sogenannte Gefangenen-Dilemma, realisiert. Ein solches Spiel ist im Prinzip die Ausführung eines Quantenalgorithmus der aus einer bestimmten Folge aus Ein- und Zwei-qubit Quantengattern aufgebaut ist. Dieses Spiel erlaubt den individuellen Spielern ihren Strategieraum zu vergrößern, da sie auch Superpositionen von klassischen Strategien wählen und diese miteinander verschränken können. Die Erfolgsfunktion des Spieles wurde für verschiedene Strategiesets evaluiert und es konnte experimentell gezeigt werden, dass das sogenannte "Dilemma", welches in der klassischen Version des Spieles auftritt, in der Quantenwelt beseitigt werden kann. Unglücklicherweise ist Dekohärenz, der ungewollte Verlust von in Quantensystemen kodierter Information durch unkontrollierte Wechselwirkung mit der Umgebung, eines der Haupthindernisse für die Realisierung eines Quantencomputers im großen Rahmen. Ein möglicher Lösungsansatz ist die Rechnung in einem sogenannten dekohärenzfreien Unterraum (DFS) durchzuführen. Auf früheren Arbeiten aufbauend gelang es diese theoretischen Konzepte auf unser Einweg-Quantencomputermodel zu übertragen und zum ersten Mal die dekohärenzfreie Durchführung einer Rechnung zu zeigen, während die Photonen starkem Phasenrauschen ausgesetzt waren. Beachtenswerter Schutz der Information konnte erreich werden, der annähernd die idealen Ergebnisse lieferte. Obwohl die Experimente in dieser Dissertation nur einen "proof-of-principle" Charakter aufweisen haben sie trotzdem große Bedeutung für das Feld der QIP und werden hoffentlich den Weg für weitere und aufregende Erfindungen und experimentellen Demonstrationen in der Zukunft ebnen.

List of publications

The titles of publications that are directly relevant for this dissertation are written in bold face.

Articles in refereed journals

1. N.K. Langford, T.J. Weinhold, R. Prevedel, K.J. Resch, A. Gilchrist, J.L. O'Brien, G.J. Pryde and A.G. White,
   "Demonstration of a Simple Entangling Optical Gate and Its Use in Bell-State Analysis",
   Phys. Rev. Lett. **95**, 210504 (2005)

2. R. Prevedel, P. Walther, F. Tiefenbacher, P. Böhi, R. Kaltenbaek, T. Jennewein and A. Zeilinger,
   "High-speed linear optics quantum computing using active feed-forward",
   Nature **445**, 65-69 (2007)

3. R. Prevedel, C. Brukner, M. Aspelmeyer, T.D. Jennewein and A. Zeilinger,
   "Photonic entanglement as a resource in quantum computing and quantum communication", J. Opt. Soc. Am. B **24**, 241-248 (2007)

4. M.S. Tame, R. Prevedel, M. Paternostro, P. Böhi, M.S. Kim and A. Zeilinger,
   "Experimental Realization of Deutsch's Algorithm in a One-way Quantum Computer", Phys. Rev. Lett. **98**, 140501 (2007)

5. K.J. Resch, K.L. Pregnell, R. Prevedel, A. Gilchrist, G.J. Pryde, J.L. O'Brien and A.G. White, *"Time-Reversal and Super-Resolving Phase Measurements"*,
   Phys. Rev. Lett. **98**, 223601(2007)

6. R. Prevedel, A. Stefanov, P. Walther and A. Zeilinger,
   "Experimental realization of a quantum game on a one-way quantum computer", New J. Phys. **9**, 205 (2007)

7. P. Böhi, R. Prevedel, T. Jennewein, A. Stefanov, F. Tiefenbacher and A. Zeilinger,
   "Implementation and characterization of active feed-forward for deterministic linear optics quantum computing", Appl. Phys. B **89**, 499-505 (2007)

8. R. Prevedel, M.S Tame, A. Stefanov, M. Paternostro, M.S. Kim and A. Zeilinger,
   "Experimental demonstration of decoherence-free one-way information transfer", Phys. Rev. Lett. **99**, 250503 (2007)

9. A. Fedrizzi, R. Ursin, T. Herbst, M. Nespoli, R. Prevedel, T. Scheidl, F. Tiefenbacher, T. Jennewein and A. Zeilinger, *"High-fidelity transmission of entanglement over a high-loss freespace channel"*, arXiv:0902.2015, Nature Physics (2009), in press

10. R. Kaltenbeak, R. Prevedel, M. Aspelmeyer and A. Zeilinger, *"High-fidelity entanglement swapping with independent sources"*, arXiv:0809.3991,
Phys. Rev. A (Rapid Communication) (2009), in press

Submitted or in preparation

11. T. Paterek, R. Prevedel, J. Kofler, P. Klimek, M. Aspelmeyer, A. Zeilinger and C. Brukner, *"Mathemtical undecidability and quantum randomness"*, arXiv:0811.4542, submitted (2008)

12. T. Scheidl, R. Ursin, A. Fedrizzi, S. Ramelow, X.-S. Ma, T. Herbst, R. Prevedel, L. Ratschbacher, J. Kofler, T. Jennewein and A.Zeilinger,
"Testing the symmetry advantage of entanglement based QKD", submitted (2008)

13. R. Prevedel, G. Cronenberg, M.S Tame, M. Paternostro, P. Walther, M.S. Kim and A. Zeilinger, *"Experimental realization of Dicke states of up to six qubits for multiparty quantum networking"*, arXiv:0903.2212, submitted (2009)

14. T. Scheidl, R. Prevedel, F. Tiefenbacher and A.Zeilinger,
"An entangled, pulsed ppKTP source for multi-photon experiments",
in preparation (2009)

Theses

- R. Prevedel
  Experimental Realization of a Simple Entangling Optical Gate for Quantum Computation
  Diploma Thesis, Universität Wien, Austria (2005).

Preface

Today, quantum theory is generally accepted as one of the most precise theories of nature. The understanding of quantum physics has already influenced a large fraction of our world economy: Semiconductors, lasers, some advanced medical instruments etc. would all not exist without the underlying theory and the advances that have been achieved over the years in numerous research labs all around the world.

However at the very beginning, the weirdness of many effects in quantum mechanics, such as the superposition principle or the concept of entanglement, have long been regarded as a drawback of the theory rather than an important, quintessential feature that will lead to new insights and technologies. Fortunately, this has changed in recent years and this change in perception was accompanied by significant experimental progress in many laboratories around the world that strive to obtain increasing control over individual quantum systems of increasing size and complexity.

Already in 1982, R.P. Feynman [1] pronounced the idea that certain computations could be performed much more efficiently with quantum mechanical systems than with classical computers[1]. While conventional computers perform calculations on fundamental pieces of information called bits, which can take the values 0 or 1, quantum computers rely on quantum bits, or qubits, which can also exist in a superposition of states, i.e. they can represent both 0 and 1 at the same time. This phenomenon is called quantum superposition. Such quantum states can be represented by any two-level quantum system and in the experiment be realized by, for example, polarization states or propagation modes of single photons or electronic levels or spin states of atoms. In the same sense, registers made out of several qubits can simultaneously represent many states in quantum superpositions. These initial superpositions of encoded states can then be evolved into different superpositions by so-called quantum processors. During this evolution, each state in the superposition is affected and the result is a massive parallel computation [6, 7, 8]. The laws of quantum mechanics then allow this information to be combined and the desired result to be extracted using quantum measurements, often in fewer computational steps than in the classical case. Quantum algorithms can thus turn a certain class of difficult mathematical problems into easy ones. The factoring of large numbers, which is currently the basis for classical encryption/decryption techniques, is one of the most striking examples so far [9].

Furthermore it is intriguing that quantum computers may not only solve open problems in classical computing but can also be used for genuine quantum simulations. Chemistry, material

---

[1]The following publications can also be regarded as seminal and groundbreaking for this field [2, 3, 4, 5].

sciences, and even microbiology or pharmacology are expected to profit from such simulators. In addition, progress in the science of QIP is redefining our understanding of how "physical systems compute", emphasizing new computational models and architectures.

Single photons that carry the quantum information in their polarization degree of freedom are promising candidates for the realization of such quantum computers. Photons are easily available, they do not tend to interact with their environment and therefore suffer from negligible decoherence. Their excellent manipulability allows for precise execution of single-qubit operations. However, the absence of photon-photon interaction makes two-qubit operations, required for universal quantum computing, very difficult to realize [10, 11]. While schemes to overcome this limitation for linear optics exist, their execution is only of inherently probabilistic nature [12, 13]. More recently, a radical change of perspective in the design of quantum computational protocols has been proposed and formalized in the so-called "one-way" model [14, 15, 16]. In this specific model, the computation is not performed by inducing a sequence of logical gates on the elements of the quantum register, as in the quantum circuit model. One-way computing is based on a multipartite entangled state, the cluster state, on which the actual algorithm is implemented by single-qubit measurements, where the choice of the future measurement basis is dependent on the outcome of preceding measurements. Since the model relies on measurements only, it shifts the difficulty of performing logical gates between quantum particles, to the creation of a suitable entangled resource, the cluster state, and is therefore especially appealing to experimentalists.

The crucial advantage of one-way quantum computation is that it allows for deterministic computation. This requires the possibility to actively change the measurement bases in the course of the computation, a process referred to as *feed-forward*. This classical processing involves fast, active adaptation of subsequent measurements and real-time error correction (feed-forward), so that quantum gates and algorithms can be executed in a deterministic and hence error-free fashion. In Chapter 5 of this Thesis I will discuss techniques for implementing this fast, active feed-forward at the single photon level and we present their application in the context of photonic quantum computing [17]. Dealing with the complex situation of a four-qubit cluster state and three EOMs, we were able to realize an experiment that demonstrates "error-free" single-qubit and two-qubit operations and hence shows for the first time that high-speed, deterministic quantum computation is indeed possible with linear optics [18].

The four-photon cluster state is generated using spontaneous parametric down-conversion (SPDC) and in subsequent experiments I show how this cluster state comprised of four qubits can also be employed to demonstrate basic quantum algorithms consisting of a few gates.

In Chapter 6 I will describe the first experimental demonstration of a one-way based implementation of Deutsch's algorithm [7] which is an important quantum algorithm that is capable of distinguishing whether a mathematical function is constant or balanced. A classical algorithm needs to evaluate the function at least $2^{N-1} + 1$ times, however, in the quantum regime, this can be done with one evaluation of the corresponding quantum algorithm, independent of the size of the input (an N-bit binary string) [19]. This algorithm represents a simple but yet interesting instance of the role that the inherent parallelism of quantum computation plays in the speed-up characterizing quantum versions of classical problems. Using our four-qubit linear

cluster state we were able to demonstrate the algorithm in the two-qubit version [20].

In Chapter 7 I report a different experiment in which we succeeded for the first time in playing an instance of a quantum game — the so-called Prisoner's dilemma — on a one-way quantum computer. The Prisoner's dilemma is a widely known example in classical game theory. It is a two-players non-zero sum game where the players may benefit from unknowing cooperation [21, 22]. Due to the interesting nature of the game and the fact that communication is forbidden, defection turns out to be the unilateral best strategy, however, this strategy does not provide both players with the collective best payoff — which results in the "dilemma". By extending the game into the quantum domain this dilemma can be resolved since superposition and entanglement increase the individual player's strategy space so that eventually the collective best choice for both players and the best individual choices coincide [23]. Playing such a game is essentially the execution of a quantum algorithm made up of a distinct set of one- and two-qubit gates. We translated the required unitary operations into the one-way model of quantum computing which allowed an experimental realization of this quantum game by utilizing a four-photon "box" cluster state. Therefore our demonstration can be seen as playing the game on a one-way quantum computer. Experimentally simulating various different strategy sets and evaluating the associated payoff function of this game we were able to show that the so-called "dilemma", that occurs in the classical version of this game, can indeed be resolved in the quantum domain [24].

Decoherence, the ubiquitous loss of information encoded in a quantum system due to its uncontrollable interaction with an environment, is one of the main obstacles in the grounding of quantum technology for massively parallel information processing. In particular, the accuracy of experimental realizations of quantum algorithms and protocols using cluster states is affected by sources of environmental decoherence and imperfections in the supporting quantum system. It is therefore desirable to design and demonstrate effective schemes that protect the quality of the entangled cluster states and the encoded information within. Quantum error-correction (QEC) [25, 26] and the use of decoherence-free subspaces (DFS) [27, 28, 29] are two well-known methods that offer protection against decoherence-induced loss of information.

In Chapter 8 I describe a setup-independent scheme/method that allows decoherence-free execution of a one-way quantum computation [30]. Our scheme achieves remarkable protection of the encoded quantum information during the performance of a one-way quantum computing protocol while the physical qubits are subject to severe symmetric phase-damping noise. We experimentally demonstrate our concept with our four-qubit linear cluster state, where each logical qubit is encoded in two physical qubits. By doing so we achieved, for the first time, the decoherence-free execution of a one-way quantum computing protocol. Performing quantum process tomography we quantitatively analyze the case of information transfer across a linear cluster state whose physical qubits are affected by phase-damping decoherence. We find remarkable protection of the quantum information during this process, delivering nearly ideal outcomes. In stark contrast, when not using the DFS encoding, the output of the computation is a maximally mixed state. This convincingly shows the superiority of the DFS encoding compared to the standard, i.e. non-DFS situation.

I hope that the experiments presented in this Thesis, although they are only of simple

nature and of proof-of-principle character, will spark further interest in the one-way model of quantum computation, in particular in the realization of simple quantum algorithms and therefore eventually lead to ever more exciting inventions and experimental demonstrations in QIP in the future.

Last but not least, the attentive reader might notice that in most of the experimental Chapters 5-8 some concepts and details are recursively stated, like a brief summary of the concepts and principles of one-way quantum computing or a short description as well as a figure of the experimental setup used to generate the required cluster states. This was done on purpose for the sake of clarity and a self-contained presentation so that each "experimental" chapter can be read individually without the necessity to repeatedly turn the pages.

Chapter 1

Basic concepts of quantum information

Whenever we talk about quantum computation or, in a more general form, of quantum information, we are speaking of information processing tasks that can (only) be accomplished using quantum mechanical systems. In the following chapter, I try to give a not very extensive but hopefully consistent overview of the most important concepts and principles of quantum information that are relevant to this work. An excellent overview is given in [11].

1.1 Classical vs. Quantum bits

1.1.1 The qubit

The fundamental concept of a classical computer is the bit. Quantum information and especially quantum computation rely on a similar concept, the quantum bit, or qubit[1]. But while the classical bit is always in a defined state (either 0 or 1), the qubit can also exist in a superposition of states. In the quantum mechanical picture the state of a qubit is represented as a vector in a two-dimensional *Hilbert*-space and any normalized linear combination of two states is, according to the superposition principle, another valid quantum state. Formally, this can be written as

$$|\psi\rangle = \alpha\,|0\rangle + \beta|1\rangle, \tag{1.1}$$

where α and β are complex numbers (often called *amplitudes*). The states $|0\rangle$ and $|1\rangle$ are also known as *computational basis states* and form an orthonormal basis for this vector space. In contrast to a classical bit the qubit can exist in a continuum of states between $|0\rangle$ and $|1\rangle$, until we observe, i.e. measure it. Quite remarkably however, it is impossible to deduce both α and β at the same time. Instead, whenever we measure a qubit we only get a probabilistic result, either '0' or '1', with probability $|\alpha|^2$ and $|\beta|^2$, respectively. Since the probabilities must sum up to one, i.e. $\langle\psi|\,\psi\rangle = 1$, a natural condition implies $|\alpha|^2 + |\beta|^2 = 1$ (normalization condition).

---

[1]The term "qubit" was first coined by Schumacher [31] in 1995
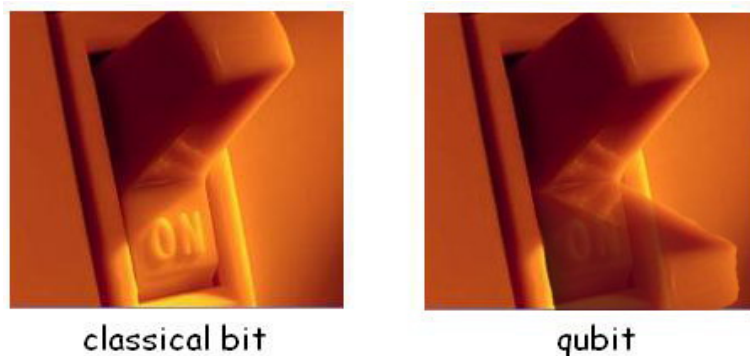
classical bit   qubit

Figure 1.1: Graphical illustration of the difference between classical bits and qubits. While the classical bit, like a switch, is always in a defined state qubits can also exist in a superposition of states.

In principle, any quantum mechanical system composed of two distinct (i.e. orthogonal) states or levels can act as a qubit. These levels can be two different energy levels of a single atom or ion ('ground' and 'excited' state), or the alignment of the nuclear spin in a uniform magnetic field. In this present work we realize the qubit as two different polarizations of a single photon, i.e. horizontal and vertical polarization, $|H\rangle$ and $|V\rangle$ representing the computational states $|0\rangle$ and $|1\rangle$, respectively. Thus from now on, I will use both notations and switch back and forth whenever appropriate.

For illustration purposes, the Hilbert space of one qubit can conveniently be represented graphically by the so-called Poincaré sphere. Since $|\alpha|^2 + |\beta|^2 = 1$, one can rewrite the state in Eqn. 1.1 as

$$|\psi\rangle = \cos\frac{\theta}{2}|0\rangle + e^{i\varphi}\sin\frac{\theta}{2}|1\rangle, \tag{1.2}$$

where the angles $\theta \in [0, \pi]$ and $\varphi \in [0, 2\pi]$ define a point on the three-dimensional unit sphere shown in Fig. 1.2.

Pure states lie on the surface of the sphere while mixed states are found inside the sphere. As we will see later on, many operations on single qubits can be neatly described within this picture.

In order to infer the state of a qubit it has to be measured. In quantum mechanics, measurements are represented as observables, i.e. Hermitian operators $\hat{\Theta}$ (we will come back to this in Section 1.1.3). By measuring $|\psi\rangle$ we project the qubit onto one of the eigenstates of the operator and the measurement outcome is the corresponding eigenvalue (either +1 or -1). Important eigenstates on the Poincaré sphere are those of the Pauli spin matrices[2],

$$\sigma_x \equiv \begin{pmatrix} 0 & 1 \\ 1 & 0 \end{pmatrix}; \; \sigma_y \equiv \begin{pmatrix} 0 & -i \\ i & 0 \end{pmatrix}; \; \sigma_z \equiv \begin{pmatrix} 1 & 0 \\ 0 & -1 \end{pmatrix}. \tag{1.3}$$

and the corresponding orthogonal axes are the so-called **X**-, **Y**- and **Z**-axes (c.f. Fig. 1.2).

---

[2]For the representation of operators acting on the two-dimensional Hilbert space it is convenient to choose the Pauli spin operators $(\sigma_x, \sigma_y, \sigma_z)$ together with the 2x2 identity $\mathbb{1}$ as they form a orthogonal basis in the corresponding operator space.
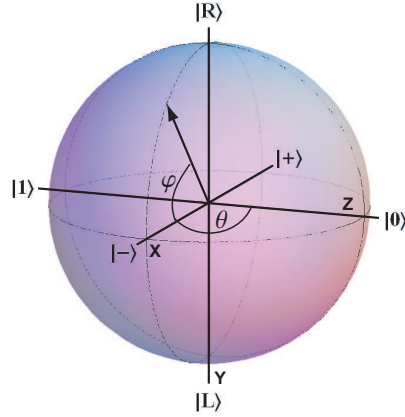
Figure 1.2: Poincaré sphere visualization of a single qubit. A pure qubit state can be represented as a point (θ, φ) on the surface of the three-dimensional sphere with radius one. $|R\rangle$ and $|L\rangle$ lie on the poles of the sphere while $|H\rangle, |V\rangle$ and $|+\rangle$ and $|-\rangle$ are located on the equatorial plane, all those basis states being separated by $\pi/2$. These states lie on the mutually orthogonal **X**-, **Y**- and **Z**-axes, as indicated. θ represents an angle on the equatorial plane while φ is measured off the equator as indicated.

The correspondence between the computational states, their respective polarization as well as their axes on the Poincaré sphere can be inferred from the following table

State	Polarization	axes
$|0/1\rangle$	$|H/V\rangle$	**Z**
$|+/-\rangle$	$1/\sqrt{2}\big(|H\rangle \pm |V\rangle\big)$	**X**
$|R/L\rangle$	$1/\sqrt{2}\big(|H\rangle \pm i|V\rangle\big)$	**Y**

where $|R\rangle$ ($|L\rangle$) denotes right (left) circular polarized light and $|+/-\rangle$ corresponds to $\pm 45°$ linear polarization. Both are coherent superposition of $|H\rangle$ and $|V\rangle$.

1.1.2   The density operator

So far we have only dealt with *pure* states which can be represented by their state vector $|\psi\rangle$. In quantum mechanics, the state vector of a system completely determines the statistical behavior of an observable $\hat{\Theta}$. However, often we are faced with the situation where the quantum state is unknown or composed of a statistical mixture of pure states.

A convenient way to treat these *mixed* states mathematically is the density operator formalism [11, 32]. The density operator of a pure quantum state $|\psi\rangle$ is simply given by its projector

$$\rho = |\psi\rangle \langle \psi|. \tag{1.4}$$

Suppose however we have a quantum system that is in a superposition of pure states $|\psi\rangle_i$ with respective probabilities p_i. Then the density operator for this system can be written as

$$\rho \equiv \sum_i p_i |\psi_i\rangle \langle \psi_i|, \ \text{with} \ \sum_i p_i = 1. \tag{1.5}$$

It is important to note that a density operator ρ is always positive semi definite (i.e.non-negative) and normalized, which implies

$$\mathrm{Tr}(\rho) = 1. \tag{1.6}$$

For many applications it turns out to be practical to express the density operator ρ in form of a matrix, which can be done by choosing a certain orthonormal basis:

$$\rho_{mn} = \langle m | \rho | n \rangle, \tag{1.7}$$

where m and n are the respective basis vectors and $m, n \in \{1, 2, ..., N\}$. A common choice for these basis vectors is the computational basis with $|1\rangle = |00...00\rangle, |2\rangle = |00...01\rangle, ..., |N\rangle = |11...11\rangle$, which requires writing the computational basis states as vectors, i.e.

$$|0\rangle = \begin{pmatrix} 1 \\ 0 \end{pmatrix} \text{ and } |1\rangle = \begin{pmatrix} 0 \\ 1 \end{pmatrix}. \tag{1.8}$$

With this definition, the most important single-qubit states can be written as

$$\rho_H = \begin{pmatrix} 1 & 0 \\ 0 & 0 \end{pmatrix}, \quad \rho_V = \begin{pmatrix} 0 & 0 \\ 0 & 1 \end{pmatrix}, \quad \rho_+ = \frac{1}{2}\begin{pmatrix} 1 & 1 \\ 1 & 1 \end{pmatrix} \text{ and } \rho_R = \frac{1}{2}\begin{pmatrix} 1 & -i \\ i & 1 \end{pmatrix}. \tag{1.9}$$

The density matrix of an arbitrary single qubit can be represented by three independent real parameters (α, γ, and δ):

$$\rho = \begin{pmatrix} \alpha & \gamma e^{i\delta} \\ \gamma e^{-i\delta} & 1 - \alpha \end{pmatrix}, \tag{1.10}$$

where $0 \le \alpha \le 1$ follows from normalization, and $|\gamma| \le \sqrt{\alpha(1 - \alpha)}$ from positive semidefiniteness. Since this is a 2x2 matrix, another equivalent representation is given by a linear combination of Pauli matrices

$$\rho = \sum_{\mu=0}^{3} c_\mu \sigma_\mu, \tag{1.11}$$

where σ_0 is the 2x2 is the identity matrix $\mathbb{1}$ and c_μ are constants. Because of Eqn. 1.6 the trace of the density matrix must be equal to 1 and Eqn. 1.11 can be simplified to:

$$\rho = \frac{1}{2}\big(\mathbb{1} + \vec{r} \cdot \vec{\sigma}\big) \tag{1.12}$$

where $\vec{r} \cdot \vec{\sigma} = \sum_{j=x,y,z} r_j \sigma_j$ and $\vec{r} = (r_1, r_2, r_3)$ is the unit vector in the Poincaré-sphere, s corresponds to the eigenstates $s = 0, 1$ with eigenvalues $\{+1, -1\}$ and $\vec{\sigma} = (\sigma_x, \sigma_y, \sigma_z)$.

The representation of quantum states in form of operators or matrices constitutes a useful tool and allows a quick interpretation of its properties as we will show with the following example. Consider the equally weighted mixture of all basis states, which is more generally known as "white noise". For one qubit this state can be written as $\rho_{mixed} = \frac{1}{2}\left(|0\rangle\langle0| + |1\rangle\langle1|\right)$. However, as we will see by looking at their corresponding density matrices, this is considerably different from the state $\rho_+ = \frac{1}{2}|+\rangle\langle+|$, which is a coherent superposition of the basis vectors:

$$\rho_{mixed} = \frac{1}{2}\begin{pmatrix} 1 & 0 \\ 0 & 1 \end{pmatrix} \text{ and } \rho_+ = \frac{1}{2}\begin{pmatrix} 1 & 1 \\ 1 & 1 \end{pmatrix}. \tag{1.13}$$

The diagonal elements represent the probabilities to observe the different basis states (1/2 in our case) and are often referred to as *populations*. Therefore they are always positive real values. The off-diagonal elements are called *coherences* as they indicate coherence between the corresponding terms and are in general complex numbers.

It should now be obvious that determining the density matrix of an experimentally produced state is of utmost importance if one wants to assess the various properties of a state. In Section 2.4 we will elaborate on different techniques to reconstruct the density matrix of a unknown state or to extract the most relevant properties

Fidelity

The *fidelity* is a useful measure of *distance* between two quantum states, i.e. to which degree two states overlap and are therefore identical. The fidelity between a pure state $|\psi\rangle\langle\psi|$ and an arbitrary state ρ can be written as

$$\mathcal{F} = \langle\psi|\rho|\psi\rangle, \tag{1.14}$$

and is therefore equal to the overlap between $|\psi\rangle\langle\psi|$ and ρ. For a certain mixed state ρ, the fidelity is akin to the expectation value of that state with an operator $\hat{A} = |\psi\rangle\langle\psi|$, i.e. the trace of their product

$$\langle\hat{A}\rangle_\rho = \mathrm{Tr}\left[\hat{A}\rho\right] \tag{1.15}$$

The fidelity between two mixed states ρ and σ was first given in [33] and can be calculated by:

$$\mathcal{F}(\sigma,\rho) = \left(\mathrm{Tr}\left[\sqrt{\sqrt{\sigma}\rho\sqrt{\sigma}}\right]\right)^2 \tag{1.16}$$

Purity

A quantum system whose state $|\psi\rangle$ cannot be represented as a mixture (i.e. a convex combination) of other states is said to be in a *pure state*. In this case the density operator is simply given by a one-dimensional projector, i.e. $\rho = |\psi\rangle\langle\psi|$. Otherwise it is in a *mixed state*. A simple criterion for determining whether a state is mixed or pure is to look at the trace of the corresponding density operator squared. A pure state satisfies

$$\mathrm{Tr}\left(\rho^2\right) = 1 \tag{1.17}$$

while for a mixed state $\mathrm{Tr}\left(\rho^2\right) < 1$.

Entropy

In quantum mechanics, the entropy is a fundamental measure of information and therefore a key concept in quantum information theory. It is a measure for the uncertainty of a quantum state, i.e. its density operators. Von Neumann defined the entropy of a quantum state ρ by [32]

$$S(\rho) \equiv -\mathrm{Tr}\left(\rho\log\rho\right), \tag{1.18}$$

where the logarithm is taken to the base two. If λ_x are eigenvalues of ρ then this definition can be rewritten as

$$S(\rho) = -\sum_x \lambda_x \log \lambda_x. \tag{1.19}$$

The entropy is always non-negative and is zero if and only if the state is pure and is at most $\log d$ in a d-dimensional Hilbert space if the system is completely mixed. If a composite system AB is in a pure state, i.e $\rho_{AB} = |\Psi\rangle\langle\Psi|_{AB}$, then it is given by:

$$\mathcal{E}(\rho) \equiv \mathcal{S}(\rho_A) = \mathcal{S}(\rho_B), \tag{1.20}$$

where $\rho_A = \text{Tr}_B(|\Psi\rangle\langle\Psi|)$ and $\rho_B = \text{Tr}_A(|\Psi\rangle\langle\Psi|)$ are the reduced density matrices. In this case the entropy of the entanglement ranges from 0 for completely separable states to 1 for maximally entangled states, although this definition should be taken with care.

If a measurement is performed on the system, then the state after the measurement can be written as

$$\rho' = \sum_i P_i \rho P_i, \tag{1.21}$$

where P is the *measurement operator* or *projector* (see separate subsection below). The entropy is never decreased by this procedure and remains constant only if the state is not changed by the measurement. Since most measurements are projective, i.e. they effectively change the state of the system, in general $S(\rho') \geq S(\rho)$.

For practical issues it is sometimes more convenient to consider the so-called "*linear entropy*" as its calculation does not require diagonalization of the density operator. The linear entropy[3] is directly related to the von Neumann entropy and for a d-qubit system (n-dim. density operator) it is defined by

$$S(\rho) = \frac{d}{d-1}\left(1 - \text{Tr}\left(\rho^2\right)\right). \tag{1.22}$$

For a pure state $S = 0$ while for a maximally mixed state $S = 1$.

1.1.3 Quantum measurement

Measurements play a significant role in quantum mechanics and especially in quantum information. It can be described as an interaction of the quantum system with a (classical) measurement apparatus, and because it usually destroys the quantum superposition the state might be in it is also referred to as *projective* measurement. Such a projective measurement is characterized by an *observable*, $\hat{\Theta}$, which is a Hermitian operator in Hilbert space, and has a spectral decomposition,

$$\hat{\Theta} = \sum_m m P_m, \tag{1.23}$$

where P_m is the projector onto the eigenstate of $\hat{\Theta}$ with eigenvalue m. The only possible results of the measurement are the eigenvalues m of the observable. The probability of obtaining result m upon measuring the state $|\psi\rangle$ is given by

$$p(m) = \langle\psi| P_m |\psi\rangle, \tag{1.24}$$

and the state of the quantum system is projected onto the final state

$$|\psi_f\rangle = \frac{P_m |\psi\rangle}{\sqrt{p(m)}}. \tag{1.25}$$

---

[3]While the von Neumann entropy (see Eqn. 1.18) is the expectation value of $\log(\rho)$, the linear entropy is the expectation value of the density matrix itself. Hence the name.

Suppose we want to measure a qubit as given in Eqn. 1.1 in the computational basis. If we measure a single qubit, then there are two possible outcomes, defined by two measurement operators, $M_0 = |0\rangle\langle 0|$ and $M_1 = |1\rangle\langle 1|$. Then, according to Eqn. 1.24, the probability of obtaining measurement outcome 0 is given by

$$p(0) = \langle \psi | M_0 | \psi \rangle = |\alpha|^2, \tag{1.26}$$

i.e., the absolute amplitude squared. Similarly, the probability for outcome 1 is $p(1) = |\beta|^2$.

More generally, we can define a measurement projector as

$$P_{\vec{r},s} = \frac{\mathbb{1} + (-1)^s \ \vec{r} \cdot \vec{\sigma}}{2} \tag{1.27}$$

where, again, $\vec{r} \cdot \vec{\sigma} = \sum_{j=x,y,z} r_j \sigma_j$ and $\vec{r} = (r_1, r_2, r_3)$ is the unit vector in the Poincaré-sphere, s corresponds to the eigenstates $s = 0, 1$ with eigenvalues $\{+1, -1\}$ and $\vec{\sigma} = (\sigma_x, \sigma_y, \sigma_z)$. Applying this measurement projector can be thought of as a polarization (spin) measurement along an axis in the Poincaré-sphere defined by $\vec{r}$.

Another important mathematical tool associated with quantum measurements is the *POVM formalism*[4], which is very well adapted to the analysis of measurements. It basically states that one needs a sufficient (complete) set of operators P_m to determine all the different possibilities of measurement outcomes[5].

1.2 Entanglement

The most interesting and puzzling property in quantum information is *entanglement*. In 1935, Erwin Schrödinger wrote [34]:

> *I would not call that one but rather the characteristic trait of quantum mechanics, the one that enforces its entire departure from classical lines of thought.*

Entanglement is the natural consequence of the superposition principle when considering quantum systems composed of two and more subsystems. As a result, the behavior of the system of two or more entangled particles can only be explained by their joint properties[6]. Thus, the total information is not encoded in the state of the individual subsystem but in the relations or correlations which the subsystems possess with respect to each other.

1.2.1 Bell states

Mathematically speaking, an entangled state $|\psi\rangle$ cannot be expressed in terms of a tensor product of its single-qubit states, i.e. $|\psi\rangle \neq |a\rangle |b\rangle$. While two classical bits can only exist in one of four possible states, 00, 01, 10 and 11, a pair of qubits can also exist in a superposition of these states. As an example, consider the following important class of entangled states of

---

[4]Short for "Positive Operator-Valued Measurement".

[5]The interested reader is referred to [11] for a complete introduction into the POVM formalism.

[6]Note that this only holds for maximally entangled states.

two-qubits, the so-called *Bell-states*[7]:

$$|\Phi^{\pm}\rangle = \frac{1}{\sqrt{2}}\Big(|0\rangle_1 \otimes |0\rangle_2 \pm |1\rangle_1 \otimes |1\rangle_2\Big)$$

$$|\Psi^{\pm}\rangle = \frac{1}{\sqrt{2}}\Big(|0\rangle_1 \otimes |1\rangle_2 \pm |1\rangle_1 \otimes |0\rangle_2\Big) \qquad (1.28)$$

These four distinct entangled states form an orthonormal basis for the two-qubit state space, and can therefore be distinguished by appropriate measurements (the subscripts label the qubits). While a joint measurement on both qubits will reveal perfect correlations between the results for the $|\Phi^{\pm}\rangle$ and perfect anticorrelations for $|\Psi^{\pm}\rangle$, a measurement on either qubit of Eqn. 1.28 in the computational basis will always yield a random result, either $|0\rangle$ or $|1\rangle$. In fact, the individual qubit's state is totally mixed and equal to the white noise state ρ_{mixed} we encountered in Section 1.1.2. In order to see this we have to calculate the partial trace over the subsystem not under consideration. For example

$$\text{Tr}_A\big[|\psi^-\rangle_{AB}\langle\psi^-|\big] = \sum_{i=\{0,1\}} {}_A\langle i|\psi^-\rangle_{AB}\langle\psi^-|i\rangle_A = \frac{1}{2}\big(|0\rangle_B\langle 0| + |1\rangle_B\langle 1|\big) = \frac{1}{2}\mathbb{1}_B \qquad (1.29)$$

where A and B denote the various qubits, i.e. subsystem of the bipartite entangled state $|\psi^-\rangle$. Indeed, the state of qubit B is maximally mixed when examined independently from A. This clearly demonstrates that the two qubits in a bipartite entangled state are strongly linked and cannot be described separately.

Entanglement lies at the heart of quantum mechanics and acts as a resource for many tasks in quantum information. Prominent examples of entanglement-based protocols include quantum dense coding [36, 37], which enables more efficient communication than can be accomplished classically, or unconditionally secure quantum key distribution [38, 39, 40, 41] and quantum teleportation [42, 43]. It is also the most important resource for quantum computing and indeed the very resource for the measurement-based or one-way model of quantum computing whose experimental implementation is the main goal of this work.

1.2.2   Entanglement measures

Despite of the straigthforward definition of entanglement, it is not so simple to decide whether a certain state is entangled or not, especially in the case of mixed states. However, the question of how much entanglement is present in a given system is crucial in quantum information theory and of utmost importance in the experiments presented here. In the following, I introduce three different entanglement measures that are widely used within the community. An overview over this topic can be found in [44].

Entanglement of Formation and Tangle

The *tangle* and the *entanglement of formation* [45] are entanglement measures for mixed states and can be interpreted as the "amount" of entanglement between two entangled states. However, they are straightforwardly only defined for a pair of qubits.

---

[7]These states are named in honour of John Bell, who showed that correlations in such entangled states are stronger than could possibly exist between classical systems [35].

If ρ_{AB} is the density operator of two qubits A and B, then the tangle τ_{AB} of the density matrix ρ_{AB} is defined as

$$\tau_{AB} = \left[\max\{\lambda_1 - \lambda_2 - \lambda_3 - \lambda_4, 0\}\right]^2, \tag{1.30}$$

where λ_{1-4} are, in decreasing order, the square roots of the eigenvalues[8] of the product $\rho_{AB}\,\tilde{\rho}_{AB}$, where $\tilde{\rho}_{AB}$ is the bitflipped[9] matrix given by

$$\tilde{\rho}_{AB} = (\sigma_y \otimes \sigma_y)\rho_{AB}^*(\sigma_y \otimes \sigma_y). \tag{1.31}$$

Here, the asterisk denotes complex conjugation and σ_y is one of the Pauli matrices (Section 1.1.1). A tangle of $\tau{=}0$ corresponds to an unentangled state, while $\tau{=}1$ corresponds to a maximally entangled state. For the special case in which the state of AB is pure, the matrix $\rho_{AB}\,\tilde{\rho}_{AB}$ has only one non-zero eigenvalue, and one can show that $\tau_{AB} = 4\det\rho_A$, where ρ_A is the reduced density matrix of qubit A, i.e., the trace of ρ_{AB} over qubit B.

From the tangle we can also easily calculate the *entanglement of formation* which can roughly be interpreted as the amount of quantum resources[10] needed to create a certain state [45, 47]. It is defined as

$$E(\rho) = h\left(\frac{1}{2} + \frac{1}{2}\sqrt{1-\tau}\right), \tag{1.32}$$

where $h(x)$ is the binary entropy function

$$h(x) = -x\log x - (1-x)\log(1-x). \tag{1.33}$$

Note that $E(\rho)$ is a monotonically increasing function of τ.

1.3 Multipartite entanglement

While it should be clear by now what entanglement means for systems composed of two subsystems (bipartite systems), it can easily lead to ambiguities for systems that are composed of more than two qubits. In this case we are speaking of *multipartite* entanglement. The prefix multi may merely mean "more than two" or more generally refer to quantum systems composed of a macroscopic number of subsystems, such as the particles of an interacting manybody system. In contrast to bipartite systems, multipartite systems may feature different types of entanglement which exhibit different characteristics, such as robustness against decoherence.

Multipartite entangled states attract a lot of attention as they serve as the crucial resource for many quantum computation algorithms and protocols. Since the experimental realization of quantum computational tasks forms a primary goal of this work the classification and the fundamental properties of multipartite states shall be further discussed.

---

[8]Note that each λ_i is a non-negative real number.

[9]Note that the bitflip operation on both qubits, though changing the state of each individual subsystem, does not change the correlations (entanglement) which the subsystems posses with respect to each other.

[10]The entanglement of formation is conjectured to be equivalent to the *entanglement cost*, which is the the ratio of the number of maximally entangled input states over the produced output states, minimized over all LOCC operations [46].

1.3.1   Classification via SLOCC

The classification of multi-qubit entanglement based on stochastic local operations and classical communication (SLOCC) is a useful framework and has been studied intensively in the past [48, 49, 50]. In this framework, two states are defined as equivalent (i.e. to belong to the same class) if there is a non-vanishing probability to convert the one into the other (and back) via LOCC (local operations and classical communication). This has its origin in the construction of entanglement measures (c.f. Section 1.2.2), where local operations are being used to identify states with the same amount of entanglement.

Already in the case of three-qubits there is more than one class of entanglement. While for a bipartite system, any two entangled states (such as the ones described in Eqn. 1.28) can be interconverted by local unitary operations or with the help of addtional ancilla photons and classical communication (LOCC), this is not possible for an arbitrary three-qubit entangled state [51]. Instead, there exist two states that cannot be converted by means of LOCC, namely the so called Greenberger-Horne-Zeilinger (GHZ) state $|\text{GHZ}_3\rangle$ [52, 53] and W-state $|\text{W}_3\rangle$ [54, 51, 55], which read[11]:

$$|\text{GHZ}_3\rangle = \frac{1}{\sqrt{2}}\big(|000\rangle + |111\rangle\big), \tag{1.34}$$

$$|\text{W}_3\rangle = \frac{1}{\sqrt{3}}\big(|001\rangle + |010\rangle + |100\rangle\big), \tag{1.35}$$

or in the more general form

$$|\text{GHZ}_n\rangle = \frac{1}{\sqrt{2}}\big(|0\rangle^{\otimes n} + |1\rangle^{\otimes n}\big), \tag{1.36}$$

$$|\text{W}_n\rangle = \frac{1}{\sqrt{n}}\big(|100\ldots 0\rangle + |010\ldots 0\rangle + \cdots + |00\ldots 1\rangle\big). \tag{1.37}$$

Therefore these states also represent two different entanglement classes for genuinly tripartite entanglement, the GHZ- and W- class. In 2000, Dür *et al.* [51] showed that, with respect to the aforementioned SLOCC operations, in total six equivalence classes exist for pure states of three qubits. The remaining four classes are made up of the completely separable state (symbolized by A-B-C) and three so-called biseparable states[12], where two qubits are entangled but separated from the third (A-BC, C-AB and B-AC).

In the case of four qubits, instead of only six, infinitely many SLOCC classes can be distinguished. However, the authors of Verstraete et al. [50] were able to group these classes into nine SLOCC *families* of pure states, corresponding to nine different ways of entangling four qubits. Very recently an alternative and complementary classification of SLOCC-families for four qubits was provided in a publication by Lamata et al. [49]. Common to all the above mentioned attempts of establishing a systematic order of multi-qubit entanglement is the classification of states according to their invariance with respect to local operations.

---

[11]From here on the tensor product sign as well as the subscript that label the individual qubits will be omitted for conciseness.

[12]In general, a n-partite pure state $|\psi\rangle$ is called biseparable, whenever a grouping of the n particles into two groups G_A and G_B can be found such that the resulting state is a product state $|\psi\rangle = |G_A\rangle |G_B\rangle$, otherwise it is a genuine multipartite entangled state.
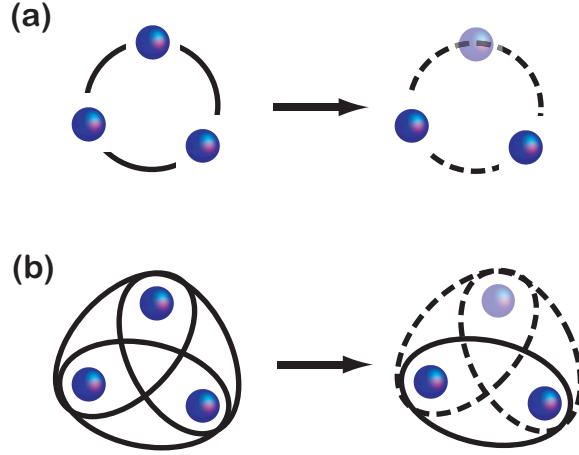
Figure 1.3: Graphical illustration of the GHZ- and W-type entanglement. While the GHZ-state in (a) shows maximum entanglement in the multipartite sense, the remaining state becomes completely disentangled if one qubit is measured or lost. In contrast, the W-state in (b) is more robust against qubit loss and decoherence. There is no genuine three-particle entanglement in W-states, however it contains a maximal amount of two-particle entanglement. If one particle is measured or lost, it leaves an entangled two-qubit Bell state.

1.3.2   Entanglement properties

The states that belong to the GHZ-class and W-class feature fundamentally different behaviors. The three-particle GHZ state of the form in Eqn. 1.45 is known to have the largest amount of entanglement that is distributed evenly between all qubits[13]. Therefore it shows stronger violations of locality and realism than states of the W-class. However, if one of the qubits in a GHZ-state is measured or lost, then the remaining state becomes completely disentangled. In contrast, the W-state maintains some of its entanglement if one of the qubits is traced out. This is graphically shown in Fig. 1.3 for illustration purposes. To see this, consider that, of both GHZ- and W-state, the first qubit is lost:

$$\mathrm{Tr}_A\big(|\mathrm{GHZ}_3\rangle\langle\mathrm{GHZ}_3|\big) \quad = \quad \frac{1}{2}\big(|00\rangle\langle00| + |11\rangle\langle11|\big) = \mathbb{1}/2 \tag{1.38}$$

$$\mathrm{Tr}_A\big(|\mathrm{W}_3\rangle\langle\mathrm{W}_3|\big) \quad = \quad \frac{1}{3}|00\rangle\langle00| + \frac{2}{3}|\Psi^+\rangle\langle\Psi^+| \tag{1.39}$$

This proves the above statement - the GHZ-state "collapses" into a seperable state while bipartite entanglement remains in the W-case. This has important implications for various information processing tasks, e.g. W-states are more robust to the loss of qubits, a feature also known as *entanglement persistency*[14].

---

[13]The GHZ states maximize entanglement monotones and therefore can be called *maximally entangled* in the multipartite sense. A definition of and an excellent overview on entanglement monotones is given in [56]

[14]The persistency of entanglement P_e of an entangled state of n qubits is the minimum number of local measurements such that, for all measurement outcomes, the state is completely disentangled [15].

1.3.3   Graph states

So far we have introduced two distinct multiparite states, the GHZ- and W-state, that exhibit very different entanglement properties. As already mentioned above, in the case of four qubits already infinitely many classes (or families) of entangled states do exist. In the following, a particular family of multiqubit states will be introduced that is of exceptional importance for this work: The *graph states*, a subclass of which is also known as *cluster states*.

Graph states with their unique properties turn out to be extremely fruitful in quantum information science. Graph states are useful for quantum error correcting codes [57], entanglement purification [58] and have provided new insights into studies of multiparty entanglement [59], non-locality [60, 61, 62] and decoherence [63]. However, in 2001 Raussendorf and Briegel [14, 15] discovered that these states can also serve as an essential and universal resource for measurement-based or *one-way* quantum computation, which will become the center of attention in this work.

The graph states are strongly entangled states and can be treated very elegantly with their representation by mathematical graphs and the stabilizer formalism [15, 59]. A graph state is a pure n-qubit state denoted as $G(V, E)$ where V represents the vertices and E is the number of edges that connect the qubits. More intuitively, the vertices of the graph correspond to qubits and the edges to a next-neighbor Ising-type interaction between the connected vertices. In the language of quantum information this interaction can be understood as entanglement or more generally as the application of a two qubit phase gate, as we will see later on in Section 3.1.1.

Mathematically, a graph state obeys the following set of eigenvalue equations [15]:

$$K_G^{(a)} |G\rangle = (-1)^{k_a} |G\rangle, \tag{1.40}$$

with $K_G^{(a)}$ being an operator for each vertex a of G:

$$K_G^{(a)} = \sigma_x^{(a)} \bigotimes_{b \in N(a)} \sigma_z^{(b)}. \tag{1.41}$$

Here $N(a)$ denotes the *neighbourhood* of vertix (particle) a, i.e. all nearest vertices b that are connected to a by an edge. Therefore the Pauli operator corresponding to vertex i is σ_x, the ones corresponding to connected vertices are σ_z and the rest of vertices in a given graph G are described by the identity $\mathbb{1}$. For a N-qubit graph state we therefore find N stabilizing operators that fully characterize the state.

Cluster states are a subclass of graph states that are represented by a periodical two-dimensional lattice. According to the rules above, we can write an arbitrary two-dimensional cluster state $|\mathcal{C}_N\rangle$ as

$$|\mathcal{C}_{2D}\rangle = \bigotimes_{a \in \mathcal{C}} \left(|0\rangle_a \underset{\gamma \in \Gamma}{\otimes} \sigma_z^{(a+\gamma)} + |1\rangle_a \right) \tag{1.42}$$

with $\Gamma = \{(1, 0), (0, 1)\}$ and the convention $\sigma_z^{(a+\gamma)} \equiv 1$ when $a + \gamma \notin \mathcal{C}$ (since qubits cannot be entangled with an empty side) [15].

For the sake of simplicity however, let us first consider an one-dimensional cluster chain of qubits with arbitrary length. It can be written as

$$|\mathcal{C}_N\rangle = \frac{1}{2^{N/2}} \bigotimes_{a=1}^{N} \left(|0\rangle_a \sigma_z^{a+1} + |1\rangle_a \right) \tag{1.43}$$
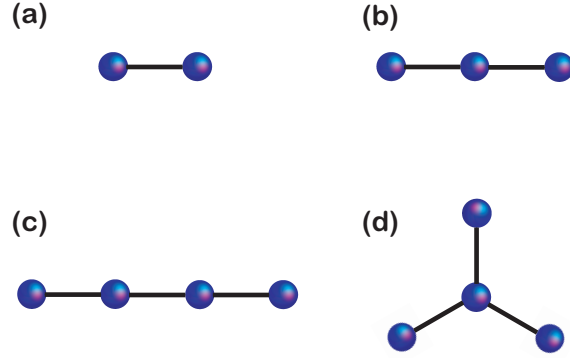
Figure 1.4: Overview of the cluster states for $N = 2, 3, 4$. The two-qubit cluster $|\mathcal{C}_2\rangle$ in (a) is equivalent to the $|\Phi^+\rangle$ Bell state, while the three qubit cluster $|\mathcal{C}_3\rangle$ in (b) is indeed a GHZ_3. In the case of four qubits, we can distinguish between the the linear (c) and star (d) configuration of a cluster. The star cluster represents the GHZ_4 state, while the linear $|\mathcal{C}_4\rangle$ state represents a different entanglement class and is the main subject of this work.

with the convention $\sigma_z^{N+1} \equiv 1$ [15]. For $N = 2$, Eqn. 1.43 becomes

$$|\mathcal{C}_2\rangle = \frac{1}{\sqrt{2}}\Big(|0\rangle_1 \big(|0\rangle_2 - |1\rangle_2\big) + |1\rangle_1 \big(|0\rangle_2 + |1\rangle_2\big)\Big). \tag{1.44}$$

This is a maximally entangled state and locally equivalent to the well-known $|\Phi^+\rangle$ Bell state under the transformation $|\Phi^+\rangle = (1 \otimes \texttt{HAD}) \otimes |\mathcal{C}_2\rangle$ with $\texttt{HAD} = \frac{1}{\sqrt{2}}(\sigma_x + \sigma_z)$. We can thus immediately write down the cluster states for $N = 2, 3, 4$ qubits in the more familiar form as

$$|\mathcal{C}_2\rangle \stackrel{l.u.}{=} \frac{1}{\sqrt{2}}\big(|00\rangle + |11\rangle\big) \tag{1.45}$$

$$|\mathcal{C}_3\rangle \stackrel{l.u.}{=} \frac{1}{\sqrt{2}}\big(|000\rangle + |111\rangle\big) \tag{1.46}$$

$$|\mathcal{C}_4\rangle \stackrel{l.u.}{=} \frac{1}{\sqrt{2}}\big(|0000\rangle + |0011\rangle + |1100\rangle + |1111\rangle\big), \tag{1.47}$$

where the respective local transformations are given by $U_{C_3} = (\texttt{HAD} \otimes 1 \otimes \texttt{HAD})$ and $U_{C_4} = (\texttt{HAD} \otimes 1 \otimes 1 \otimes \texttt{HAD})$. While $|\mathcal{C}_3\rangle$ corresponds to a GHZ state of three qubits, $|\mathcal{C}_4\rangle$ is not equivalent to a 4-qubit GHZ state [64], i.e., they cannot be transformed into each other by LOCC. Therefore these two states yield different entanglement properties.

One of the striking features of cluster states is the fact that they posses *maximum connectedness*[15], as was first discussed in [15]. Here, maximum connectedness means that any two qubits of the cluster can be projected into a pure Bell state by local measurements on a subset of the other qubits where the state obtained may depend on the outcome of the measurements and on the chosen measurement basis. In the case of Z-basis projections the neighboring qubits are disconnected, i.e the cluster will be broken up into two separate pieces. In stark constrast measurements in the X-basis leave the remaining cluster qubits connected, i.e. do not alter the correlations/entanglement of the remaining state (see Fig 1.5).

---

[15]Connectedness is defined as the maximal number of projective measurements that can be performed on a given state such that the residual state is still entangled with certainty.
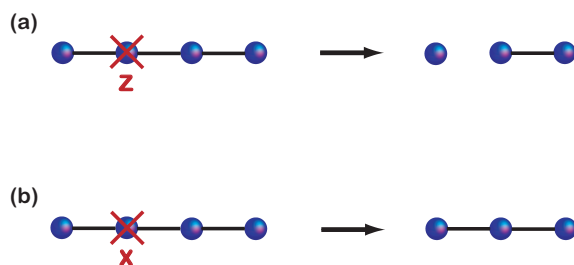
Figure 1.5: Schematic representation of measurements on cluster states in different bases. Shown is a one-dimensional four-qubit cluster state, $\mathcal{C}_4$. (a) If measurements on cluster qubit 2 are performed in the computational, or Z-basis, the neighboring cluster qubits are disentangled. This type of measurements allows to *shape* the form of a graph state. (b) X-basis projections, however, leave the remaining qubits entangled.

Following up on this one might be interested to know how many measurements are necessary to completely disentangle a certain cluster state, i.e. the entanglement persistency P_e, and the answer is straightforward. N/2 measurements[16] are necessary to completely disentangle a cluster state, therefore $P_e(|\mathcal{C}_N\rangle) = N/2$. In contrast, GHZ states become disentangled after projection of only one qubit in the Z-basis. Furthermore, cluster states are characterized by maximal local entropy [50]. This can be calculated by tracing over all but one qubit that make up the cluster - the residual state will be maximally mixed, which is also a indication for genuine multi-partite entanglement

Cluster state generation

A given graph $G(V, E)$, with certain number of vertices (qubits) V and the set of edges E, can be constructed applying the following recipe:

$$|G\rangle = \prod_{(a,b)\in E} U_{\text{CPHASE}}^{\{a,b\}}|+\rangle^{\otimes V} \tag{1.48}$$

This can be understood as first preparing each individual qubit in the $|+\rangle = \frac{1}{\sqrt{2}}(|0\rangle + |1\rangle)$ state and applying an Ising-type interaction which can be described by an entangling operator $U_{\text{CPHASE}}^{\{a,b\}}$ between all connected qubits. Here, $U_{\text{CPHASE}}^{\{a,b\}}$ is the so-called *controlled Phase gate*

$$U_{\text{CPHASE}}^{\{a,b\}} = \begin{pmatrix} 1 & 0 & 0 & 0 \\ 0 & 1 & 0 & 0 \\ 0 & 0 & 1 & 0 \\ 0 & 0 & 0 & -1 \end{pmatrix} \tag{1.49}$$

that will be explained in more detail in Section 3.1.1. There are also other experimental techniques to grow larger cluster states which will be dicussed briefly in Section 3.3.4.

In recent years, several research groups have strived to experimentally produce multipartite graph states due to their appealing features. Many of them have been realized using single

---

[16]This can be achieved by measuring each even numbered qubit $j = 2, 4, 6, ...$ in the chain in the Z-basis.

photons such as the first observation of a $|\mathrm{GHZ}_3\rangle$ [65]. In the meantime, GHZ states of up to six qubits have been demonstrated in multi-photon experiments [66, 67, 68, 69], with trapped ions [70, 71] and in NMR experiments [72]. Recently also other six-photon graph states were created using linear optics and single photons [69]. The first realization of a four-qubit linear cluster state was reported in [73] and subsequently by different groups [74, 75] also by employing additional degrees of freedom [76, 77].

Chapter 2

Tools for optical quantum information processing

Having accustomed ourselves with the basic concepts and principles of quantum mechanics, we now turn our attention to the various tools that allow to make various quantum information processing tasks a reality. In this work, the physical systems of choice are single photons, where we use the polarization as our two-level quantum system to encode the relevant information. This chapter first briefly motivates the use of single photons as our information carriers and discusses various (alternative) possibilities of physical realizations before going in more detail how the single photons are created, manipulated and characterized in the laboratory.

2.1   Why photons?

As we have learned already in Section 1.1.1, any quantum mechanical system composed of two distinct (i.e. orthogonal) states or levels can act as a qubit. However, for many practical applications in QIP it seems reasonable to ask for a qubit architecture in which the coupling to the environment is sufficiently low or at least accurately known. Also, the physical system realizing the qubit should be scalable, i.e. the generation of many qubits at a time should be feasible. Furthermore, initializing, manipulating and reading them out, i.e. detecting the qubit's internal state should be possible in a reliable way with high fidelity and low error. These are some of the requirements also known as the "*DiVincenzo criteria*", named after David DiVincenzo [78], who has classified the main ingredients that a physical system should possess in order to be a candidate for a quantum computer. We will return to and discuss these criteria in more detail at the beginning of the following chapter.

One of the exciting aspects of quantum information science is the fact that several candidates of quite different physical systems exist that fulfill these requirements. Besides single photons, promising candidates are ions, or charged atomic particles, that are trapped by electromagnetic fields and where qubits are stored in stable electronic states [79, 80, 81, 82]. Also qubits can be realized by using the spins of freely floating molecules, where manipulation and detection is performed using nuclear magnetic resonance techniques [83, 84, 85, 86, 87, 87]. Other qubit

architectures are based on flux[1] [88] and charge[2] [89, 90, 91] of micro-meter sized superconducting electrodes coupled through Josephson junctions[3] [92, 93]. All these systems have their own advantages in quantum information processing, however, no physical implementation seems to have a clear edge over others at this point [94].

We choose single photons that carry the quantum information in their polarization degree of freedom and linear optics to experimentally implement quantum information processing for various reasons [95]. First, photons exhibit negligible decoherence, since they tend not to interact with the environment and they can easily be transmitted over long distances using optical glass fibers. Second, single photons can be manipulated in an extremely fast and accurate manner and the existence of a vast photonic industry facilitates access to many already existing technologies such as electro-optic devices. And last but not least, single and entangled photons can be produced in an efficient manner using a process called *spontaneous parametric down-conversion*, as we will see in the following.

2.2   Generating single and entangled photons

The reliable and on-demand generation of single photons in pure quantum states is of utmost importance in photonic QIP. While remarkable effort has been dedicated to the implementation of such single photon sources and subsequently to the heralded generation of entangled states of light [96, 97], it still presents a major technological challenge. At the moment the best method (in terms of intensity and quality) for the generation of such non-classical states of light is still the process of spontaneous parametric down-conversion (SPDC) [98, 99, 100].

2.2.1   Spontaneous parametric down-conversion (SPDC)

Parametric down-conversion and its reverse process, second-harmonic generation (SHG) typically takes place in non-linear optical materials, such as anisotropic or non-centrosymmetric crystals. Technically, the nonlinearity of the materials is reflected in the dielectric polarisation vector, P. When an electromagnetic field such as the light field of a laser interacts with a dielectric medium, it induces electric dipole moments, whose macroscopic sum results in an induced dipole polarization $\vec{P}$ inside the material. Its components P_i are related to the electromagnetic field $\vec{E}$ and can be written as a series expansion [99],

$$P_i = \epsilon_0 \left(\chi_{ij}^{(1)} E_j + \chi_{ijk}^{(2)} E_j E_k + \chi_{ijkl}^{(3)} E_j E_k E_l ... \right), \tag{2.1}$$

where ϵ_0 is the permittivity of the vacuum, $\chi^{(1)}$ is the standard linear coefficient of dielectric susceptibility and E_i denotes the components of the electric field. The contribution of the non-linear second-order term $(\chi^{(2)})$ in Eqn. 2.1 is typically ten orders of magnitude lower than the

---

[1]The computational basis states of the qubit are defined by the circulating currents which can flow either clockwise or counter-clockwise. These currents screen the applied flux limiting it to multiples of the flux quanta and therefore give the qubit its name.

[2]A charge qubit is a superconducting qubit whose basis states are charge states. It is formed by a tiny superconducting island (also known as a Cooper-pair box) coupled by a Josephson junction to a superconducting reservoir. The states are defined as the presence or absence of excess Cooper pairs in the island.

[3]The junction parameters are engineered during fabrication so that a persistent current will flow continuously when an external flux is applied.

one of the linear term in crystalline materials[4]. Therefore it can be usually neglected for weak pump fields. At sufficiently high electric field strength however it becomes significant, eventually leading to oscillator terms which are driven by twice the frequency of the incident fields, so that the reradiated waves have an energy of $2\,\omega$. This is called second-harmonic generation, while spontaneous parametric down-conversion describes the reverse process. In terms of photons, i.e., in the language of second quantization, this corresponds to the spontaneous conversion of a pump photon with energy $\hbar\omega_p$ and momentum $\hbar\vec{k}_p$ into two photons with energies $\hbar\omega_s$, $\hbar\omega_i$ and momenta $\hbar\vec{k}_s$, $\hbar\vec{k}_i$, where the $\vec{k}$ are the wavevectors inside the medium. The downconverted photons are usually, but arbitrarily, referred to as signal and idler photon, hence the subscripts. This process resembles the phenomenon of parametric amplification or three-wave mixing known from classical electrodynamics, where two marginal fields are amplified in a non-linear medium due to the presence of a strong pump field. The spontaneous conversion without the prior presence of a weak field, however, is a pure quantum effect [102].

The process of parametric amplification can also be intuitively understood as follows: As the initial wave associated with the pump field propagates through the crystal, it continues to produce second-harmonic waves which all add up constructively to form a single output wave if they maintain a proper phase relationship. In order to obtain this phase relationship and a good conversion efficiency, one must satisfy so-called *phase matching* conditions, i.e. the relations of the wavevectors $\vec{k}_j$ in the non-linear medium and of the frequencies ω_j of the light involved have to satisfy momentum and energy conservation. In the process of parametric down-conversion, in which a pump photon decays into two photons, the conditions read like [98]

$$\begin{aligned} \omega_p &= \omega_s + \omega i \\ \vec{k}_p &\approx \vec{k}_s + \vec{k}_i. \end{aligned}$$

(2.2)

Most of the times, the crystal is cut such that light impinging perpendicular to the crystal's face forms an appropriate angle Θ with the optic axis so that the down-converted photons obey the momentum conversation, therefore allowing easy phase-matching in the experiments.

Eqns. 2.2 imply that the pairwise generated photons are strongly correlated in their energy and momentum. Especially, the second Eqn. of 2.2 implies that the SPDC emission is rotationally symmetric, which leads to a conic emission (see Fig 2.1). For uniaxial crystals, depending on Θ (i.e. how the crystal is cut) two possible types of phase matching can be distinguished according to the polarization (combinations) of the down converted photons[5]: If we have an extraordinary (*e-*) polarized pump creating two ordinary (*o-*) polarized down-conversion photons, then it is called *type-I*, while an e-polarized pump creating one e- and one o-polarized photon is

---

[4]Although all crystalline materials possess a nonzero $\chi^{(3)}$ coefficient, only anisotropic crystals with no symmetry centre give a nonzero square term in the polarization expansion ($\chi^{(2)} \neq 0$) [101]. As a result, all optical materials with a $\chi^{(2)}$-type nonlinearity are also birefringent.

[5]For negative birefringent crystal, such as BBO (β-barium borate - β-BaB$_2$O$_4$), the ordinary (*o-*) constituent of the beam travels faster than the extraordinary (*e-*) one ($n_o > n_e$), allowing to satisfy the phase matching equations (Eqns. 2.2). Furthermore, extraordinarily polarized means the polarization vector lies in the plane spanned by the principal axis of the crystal and the wave vector of the pump photon. On the other hand, ordinarily polarized indicates the polarization vector is normal to this plane.
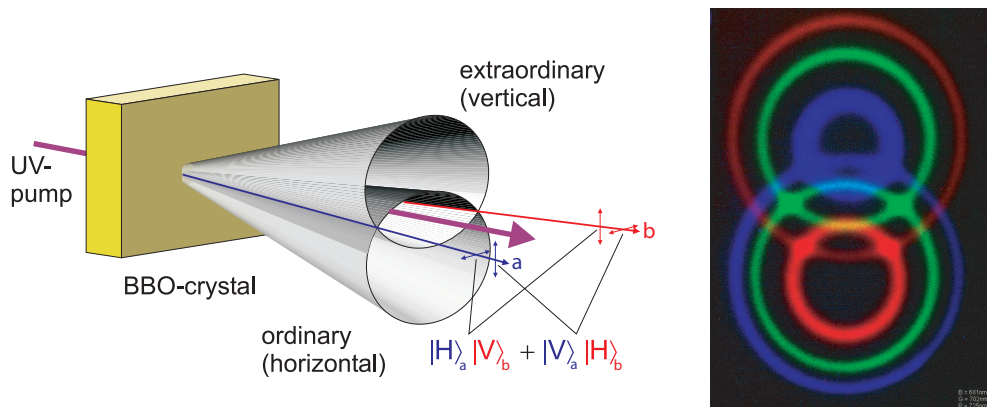
Figure 2.1: Principle scheme of type-II parametric down-conversion. Due to energy and momentum conservation the downconverted photons are orthogonally polarized and emitted into two characteristic emission cones. The intersection lines define two spatial modes a and b. The polarization of the individual photons in these two modes is undefined — since it is impossible to tell which cone they were emitted from. However after proper compensation of walk-off effects caused by birefringence of the crystal the photons are found to be in a polarization-entangled Bell state [103]. On the right hand side, one can see the energy (i.e wavelength) dependent opening of the cones and the respective intersections. Entangled photon pairs are emitted in case where the photons are degenerate in frequency. Picture by P.G. Kwiat and M. Reck.

known as *type-II* phase matching[6]. In the experiments presented in this Thesis we exclusively work with the latter type of SPDC [103]. Since many applications require the photons to be indistinguishable in any degree of freedom other than spatial mode and polarization, we further choose the energies (or wavelengths) of both the signal and idler photons to be degenerate[7], which implies $\omega_s = \omega_i = \omega_p/2$.

The birefringence of non-linear crystals furthermore leads to a polarization dependant non-concentric splitting of the cones, as shown in Fig. 2.1, where the opening angle of each cone depends on the angle enclosed by the pump wave vector and the principal axis of the crystal. This distinct emission geometry of *non-collinear* type-II SPDC is very interesting, since the intersection lines of the cones define two spatial modes a and b. When photons are emitted in these modes, it becomes impossible, in principle, to tell whether the photon was emitted by the o- or e-cone, and because they correspond to different polarization, the photons become polarization entangled. In practice though, due to group velocity mismatch inside the bire-fringent crystal the two photons exhibit slightly different propagation behaviour which renders them partially distinguishable - this has to be compensated in order to obtain genuine and high-quality entangled photons. Experimentally this is done by sending the photons through so-called compensation crystals, usually the same type of birefringent crystal, but of just half

---

[6]Of course it is also possible for an o-polarized pump beam to generate either type of down-conversion.

[7]As we will see later on, this requirement is lessened to the fact that we select only photons which have a certain spectral distribution around the same central wavelength.
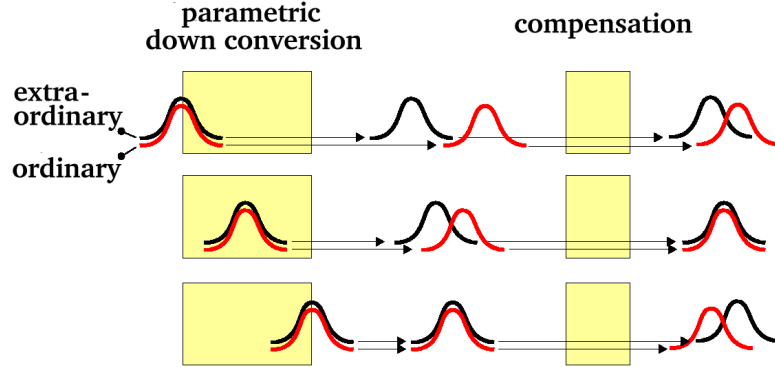
Figure 2.2: Since PDC is a spontaneous process, the down-conversion of the pump photon is equally probable at any point within the crystal. Therefore, the temporal delay between a horizontally and a vertically polarized photon varies depending on the crystal thickness and the point of down-conversion inside the crystal. By inserting compensators of half the thickness, one can, in average, delay the faster photon to erase this timing information. The additional HWPs in front of the compensators are not shown for clarity. (Figure adapted from [104]).

the thickness. If we further interchange the roles of ordinary and extraordinary beam before the compensators by rotating the polarization by 90°, the temporal and spatial walk-off will be canceled on average. One intuitive explanation is that by employing this method the information about the arrival time of the photon is erased, as can be seen schematically in Fig. 2.2.

If this walk-off compensation is properly done, then the SPDC emission along modes a and b is an entangled state of the form

$$|\psi\rangle = \frac{1}{\sqrt{2}} \left(|V\rangle_a |H\rangle_b + e^{i\varphi} |H\rangle_a |V\rangle_b \right). \tag{2.3}$$

The phase φ between the two coherent terms can be easily adjusted by introducing additional birefringent elements, or by slightly tilting one of the compensation crystals. In the experiment, choosing $\varphi = 0$ or $\varphi = \pi$ will result in the maximally entangled Bell states $|\psi^+\rangle$ and $|\psi^-\rangle$, respectively. If additionally the polarization in one mode is rotated by 90°, any of the four distinct Bell states can be generated[8].

Type-II non-collinear spontaneous parametric down conversion

So far the description of how to generate entangled photons in the process of SPDC was rather simplistic. In many situations it is however useful to consider the full quantum mechanical state of the emitted photons.

Employing the notation of second quantization, the overall interaction of the crystal with the pump light can be written as a quantum mechanical Hamiltonian which has an elegant interpretation in the terms of photons:

$$H = g a_p^\dagger a_s a_i + g^* a_p a_s^\dagger a_i^\dagger \tag{2.4}$$

---

[8]For a more detailed description of an entangling type-II photon source, see [103, 104].

Here, g is a coupling constant that contains the non-linear coefficient $\chi^{(2)}$ and $a^{(\dagger)}$ is the annihilation (creation) operator in the Fock formalism, satisfying the conditions

$$a|n\rangle = \sqrt{n}|n-1\rangle \text{ and } a^{\dagger}|n\rangle = \sqrt{n+1}|n+1\rangle, \qquad (2.5)$$

with n being the photon number. The first term in Eqn. 2.4 describes the process of second harmonic generation, while the second refers to SPDC, where a single "harmonic" photon is annihilated and two photons at ω are created.

For the particular case of non-collinear type-II SPDC with modes a and b, we can write the Hamiltonian as

$$H = g\left(a_H^{\dagger}b_V^{\dagger} + a_V^{\dagger}b_H^{\dagger}\right) + h.c. \qquad (2.6)$$

and by expansion the quantum mechanical state that is emitted by the crystal becomes

$$
\begin{aligned}
|\psi\rangle = Ze^{-iH} &= Z\exp\left(-i\alpha\left(a_H^{\dagger}b_V^{\dagger} + a_V^{\dagger}b_H^{\dagger}\right)\right)|0\rangle \\
&= Z\left(1 - \underbrace{i\alpha\left(a_H^{\dagger}b_V^{\dagger} + a_V^{\dagger}b_H^{\dagger}\right)}_{2photons} - \underbrace{\frac{\alpha^2}{2}\left(a_H^{\dagger}b_V^{\dagger} + a_V^{\dagger}b_H^{\dagger}\right)^2}_{4photons} + ...\right)|0\rangle \quad (2.7)
\end{aligned}
$$

where Z is a normalization constant and $|0\rangle$ is the vacuum state. Note that we have replaced the coupling constant g by a new parameter α that is proportional to the non-linearity $\chi^{(2)}$ *and* the intensity of the pump beam.

Obviously, the first order term in Eqn. 2.7 corresponds to the emission of a Bell state as described by Eqn. 2.3. The coefficient in front of the term gives the amplitude of the emission, hence squaring it results in the probability $p_2 \simeq Z^2\alpha^2$ to obtain this 2-photon state. However, the second term leads, with respective probability $p_4 \simeq Z^2\alpha^4$, to the emission of four photons in the following superposition of number states [105]:

$$|\psi_4\rangle = \frac{1}{\sqrt{3}}\left(|2H_a, 2V_b\rangle + |2V_a, 2H_b\rangle + |H_a, V_a, H_b, V_b\rangle\right) \qquad (2.8)$$

It is indeed interesting to note that the probability of emitting equal polarizations in the same mode is enhanced compared to a simple two-pair emission. This is a direct result of the bosonic bunching of the photons. Also, a closer look at the corresponding probabilities p_2 and p_4 reveals the probabilistic nature of the down-conversion and its higher-order contributions. This holds regardless of the fact whether one photon pair each is emitted from two independent crystals pumped by the same laser or two photon pairs being emitted from just one crystal. The latter is called a "double-pair emission" and usually represents a unwanted noisy contribution in experiments that aim at creating multi-photon entangled pairs by interfering photons from separate sources. The usage of higher pump intensities to increase the probability of SPDC is therefore counterproductive as the "signal-to-noise" ratio is getting worse. Therefore the experimentalist typically aims at keeping the *production probability* p of the SPDC low to ensure a good signal to noise ratio, while improving the efficiency of the linear optical setup and of the detection to ensure feasible count rates.

2.2.2 Pulsed SPDC for multi-photon entanglement

So far we have not further remarked on the properties of the light fields that are used to pump the non-linear crystals. As we will see, it is indispensable for the generation of multi-photon entangled states to use pulsed lasers to pump the SPDC sources [106, 107].

First of all, pulsed lasers such as mode-locked Titan-Sapphire oscillators (with pulse lengths of a few hundred femtoseconds) achieve the necessary high energy densities[9] required to observe non-vanishing contributions from the higher-order SPDC emissions described in Eqns. 2.7 and 2.8. Furthermore, for the coherent generation of these emissions or for the possibility of interference, the temporal uncertainty associated with the creation time of the photons has to be smaller than their coherence time[10] [109], which can be achieved by limiting the interaction time of the pump laser with the crystal, i.e. by pulsing the pump laser [106]. Choosing the right pulse length is an important task. Long pulses lead to less tight time correlations of the photons, however, as the laser pulse length gets shorter, the broader its spectral bandwidth becomes, eventually resulting in a shorter coherence time. In practice, experiments have shown that the ideal trade-off is somewhere between 100-200 fs, depending on the central wavelength [107].

However, though being essential to obtain coherence in the second order emission, short pump pulses and their broad spectral bandwidth are also disadvantageous in some respects. To ensure that the coherence time of the emitted photons is larger than the pump pulse duration, the down-conversion has to be spectrally filtered to a suitable bandwidth $\Delta\lambda$, typically a few nm [107]. However, this comes at the cost of precious count rates as these filters usually cut out a large proportion of the emitted spectrum[11] and often suffer from imperfect transmission. This is a consequence of the broad bandwidth of the pump pulse which consists not of a single but a whole range of pump wavevectors that contribute to the down-conversion [110, 111]. Since the phase matching conditions in Eqn. 2.2 are relaxed due to the finite length of the down-conversion crystal this leads to unwanted spectral correlations that differ slightly from the degenerate case [112, 113]. So apparently there is a trade-off between using narrow-band spectral filters to observe high-quality entangled states and the count rates associated with these filters. In our experiment, we typically choose interference filters of $\Delta\lambda = 3\,\text{nm}$ which still yield decent count rates without reducing the quality of the entangled state emitted from the SPDC process too much.

2.3 Manipulating quantum states with linear optics

Quantum information processing is based on state preparation, unitary operations and measurements. In contrast to many other physical implementations of qubits such as the ones based on atoms, ions [79, 80, 81, 82] or superconducting qubits [92, 93], photonic qubits and their respective polarization are in general easy to manipulate with linear optical devices. The

---

[9]Also high intensity cw lasers can generate non-negligible multi-pair emissions due to the finite timing resolution of the detection apparatus. However these emissions are usually incoherent (see e.g. [108, 105]).

[10]The coherence time is defined as the standard deviation of the fourier-transformed light-spectrum, $t_c = \frac{l_c}{c} = \frac{\sqrt{2\ln 2}}{\pi}\frac{\lambda^2}{c\,\triangle\lambda_{FWHM}}$, with λ being the wavelength of the light.

[11]Typically the spectral FWHM (full width at half maximum) bandwidth of down-conversion emitted by a 2mm BBO crystal is 9 and 11 nm for the o- and e-photons, respectively.

design of the linear-optics network used in a particular experiment depends very strongly on the state to be observed or the task to be accomplished. The most prominent examples of linear optical devices used in our experiment are mirrors, waveplates (i.e. phase-shifters) and beam splitters, out of which, in principle, arbitrary complex and powerful linear-optics networks can be built [114].

2.3.1 Waveplates and other birefringent elements

Unitary transformations of single photons can easily be implemented with birefringent crystals that introduce a polarization dependent phase shift. Any light that is incident on such an uni-axial crystal is divided in two coherent constituents of the beam, the ordinary and extraordinary (o- and e-) beam. Typically the crystals are cut so that the optic axis is parallel to the front face. This means that a normally incident beam sees the maximum distinction between the ordinary and extraordinary refractive indices. It also implies that there is no lateral separation between the o- and e-beams. In total, after passing through a crystal of thickness d, there is a relative phase difference of

$$\Delta\varphi = \frac{2\pi}{\lambda}\, d\left(|n_o - n_e|\right) \tag{2.9}$$

between the o- and e-waves, thus resulting in a change of polarization, where n_o and n_e denote the refractive indices for the respective beams. The most important crystals are called *half-* and *quarter-* wave plates since they introduce a phase shift between the linear polarizations parallel to the fast and slow axis of the crystal of $\Delta\varphi = \pi$ and $\Delta\varphi = \pi/2$ respectively, if the thickness of the plate is chosen correctly.[12]

In the single-qubit picture of the Poincaré sphere (c.f. Fig. 1.2) these phase shifts between the linear polarizations correspond to rotations of the polarization vector on the surface of the sphere. Hence, we can write the action of the half- and quarter-waveplates as a unitary matrix [100, 99]:

$$U_{\texttt{HWP}}(\Theta) = e^{i\pi/2} \begin{pmatrix} \cos 2\Theta & \sin 2\Theta \\ \sin 2\Theta & -\cos 2\Theta \end{pmatrix} \text{ and} \tag{2.10}$$

$$U_{\texttt{QWP}}(\Theta) = \frac{1}{\sqrt{2}} \begin{pmatrix} 1 + i\cos 2\Theta & i\sin 2\Theta \\ i\sin 2\Theta & 1 - i\cos 2\Theta \end{pmatrix}, \tag{2.11}$$

where Θ is the angle of the optic axis in physical two-dimensional space. On the Poincaré sphere, this angle is twice as big. A closer look reveals that half- and quarter-wave plates rotate the polarization vector on the Poincaré sphere by 180° and 90° respectively around the optic axis.

Note that any unitary transformation in qubit space can be realized by a proper combination of waveplates. Very often this is achieved by a half-wave plate sandwiched by two quarter-wave plates such that $U = U_{\texttt{QWP}} \cdot U_{\texttt{HWP}} \cdot U_{\texttt{QWP}}$. Furthermore, special transformations worth memorizing are $\texttt{HWP}(0) = \sigma_z$, $\texttt{HWP}(\pi/4) = \sigma_x$ and $\texttt{HWP}(\pi/8) = \texttt{HAD}$. The latter is especially important since it produces a (equal) superposition of the principal polarization states $|H\rangle$ and $|V\rangle$.

---

[12]In practice this thickness would be very small, resulting in very fragile waveplates. We therefore use *zero-order* wave plates, which consist of two orthogonally oriented wave plates cemented together with their thicknesses engineered such that a net phase-shift difference of π or $\pi/2$ is produced.

For some practical implementations[13] it is desirable to have birefringent elements that induce a variable phase shift ϕ between the horizontal and vertical polarizations (a variable phase-shifter). Instead of employing the aforementioned combination of waveplates[14], a pair of strong birefringent crystals can be used, with their optic axes oriented perpendicular with respect to each other and in line with horizontal and vertical polarizations. By rotating one of the crystal around the optic axis the effective thickness of the plate, which determines the phase, can be altered in a continuous fashion. Moreover, the pair configuration allows to compensate dispersion effects that occur due to the finite bandwidth of the photons. In practice, Yttrium-Vanadate crystals (YVO_4) of 200 μm thickness turn out to be a suitable choice. A detailed characterization of these can be found in the Diploma thesis of Christian Schmid [115].

2.3.2 Beamsplitters and PBSs

One of the basic building blocks in (optical) quantum information processing is the ability to let the qubits interact with each other. While for photons the negligible cross-section inhibits the direct interaction between the qubits, it has been shown that the measurement process itself is enough to induce strong nonlinearities at the single-photon level[15]. Generally, these measurements are done after beamsplitters (BS) or polarizing beamsplitters (PBS) that overlap the optical modes — i.e. induce interference.

An ideal beamsplitter is nothing more than a partially silvered piece of glass, which is made such that it reflects a fraction η of the incident light, and transmits (1-η). It is usually made from two prisms with a thin metallic layer sandwiched in between. Most of the times the beamsplitter is chosen to split the incoming light 50/50 into the two outgoing modes, i.e. $\eta = 1/2$. If we parameterize the probability amplitude of reflection and transmission as $\cos\theta$ and $\sin\theta$ respectively, the general action of the beamsplitter in the notation of the second quantization can be written as [95]

$$
\begin{aligned}
a_{out}^\dagger &= \cos\theta a_{in}^\dagger + ie^{-i\varphi}\sin\theta b_{in}^\dagger \\
b_{out}^\dagger &= ie^{i\varphi}\sin\theta a_{in}^\dagger + \cos\theta b_{in}^\dagger,
\end{aligned}
\tag{2.12}
$$

with a_{in} (a_{out}) and b_{in} (b_{out}) being the input (output) modes. The reflection and transmission coefficients R and T of the beamsplitter are given by $R = \eta = \sin^2\theta$ and $T = 1 - \eta = \cos^2\theta$. The relative phase shift $ie^{\pm i\varphi}$ ensures that the transformation is unitary, as was first pointed out in [116]. Note that the beamsplitter transformation is identical to the action of $\mathtt{HWP}(\pi/8) = \mathtt{HAD}$.

If the transmission (reflection) amplitude η becomes polarization dependant then the device becomes a polarizing beamsplitters, or PBS for short. In the usual configuration the PBS perfectly reflects vertically polarized light, while transmitting horizontally polarized light, $\eta_V = 1, \eta_H = 0$. A number of different types of PBSs exist, and they can be used as polarizers in optical experiments. When preceded by quarter- and half-waveplates the PBS can be used for polarization analysis, since it effectively implements a measurement along the Z-basis of

---

[13]For instance, to compensate undesired phase shifts introduced by imperfect optical devices such as beam-splitters.

[14]This would result in tricky operation, since the phase ϕ cannot be tuned continuously by rotation of a single waveplate.

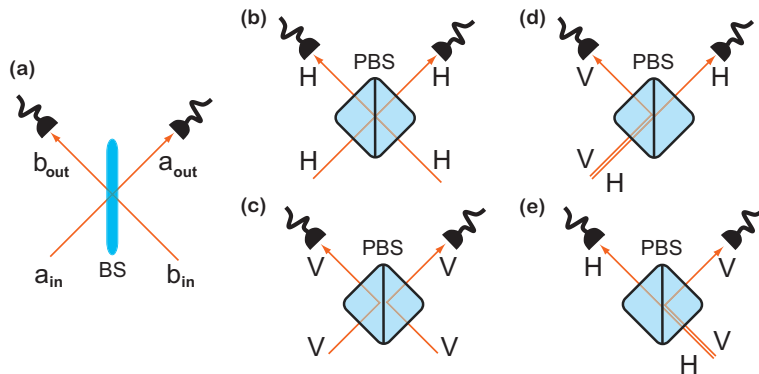[15]This will be discussed in more detail in Chapter 3.

Figure 2.3: In (a) the action of a common beamsplitter (BS) is shown. It can be used to create superposition of the in- and outgoing photons (see main text). In (b) and (c) the function of a polarizing beamsplitter (PBS) is shown. The PBS transmits horizontally polarized photons $|H\rangle$ and reflects vertically polarized photons $|V\rangle$. Therefore, if one photon is found in each of the output modes, four different possibilities exist: Had the two photons entered the PBS from different modes, either both photons were horizontally polarized $|H\rangle|H\rangle$, like depicted in (b) or they were both vertically polarized $|V\rangle|V\rangle$ as in (c). Had the photons entered the PBS from one side only, as in (d) and (e), then the two photons need to be differently polarized, $|HV\rangle$ or $|VH\rangle$, in order to be split up by the PBS and result in a coincidence.

the Poincaré sphere. Furthermore, a PBS allows *targeted* projections on spatial modes and/or polarization which can be used for the conditional preparation of polarization entangled and polarization/path entangled states[16] [117, 118, 119]. In the case of two photons impinging from different input modes, one of these targeted projections is the so-called *parity check*, as further explained in Fig. 2.3. However, the states can be observed only under the condition that after the beam splitter one photon is found in each of the output modes prior to the detection - a requirement that can be met by employing *postselection*, which will be discussed in greater detail later on in this Thesis.

2.4   Characterizing quantum states of light

In the opening paragraph of this chapter, we divided practical implementations of quantum information processing into three distinct stages. So far, we have discussed the creation of single photons using spontaneous parametric down-conversion and their manipulation or processing employing linear optical devices and networks. What is still missing, however, is the description of an appropriate detection system that *reads-out* the quantum information encoded in our photons. Also we will develop the relevant theoretical framework that links the experimental output, which are basically clicks in various detectors, with the concepts reviewed in Chapter 1. This includes the principles of quantum state (and process) tomography which allows the reconstruction of the density (process) matrix of an unknown quantum state (process) by

---

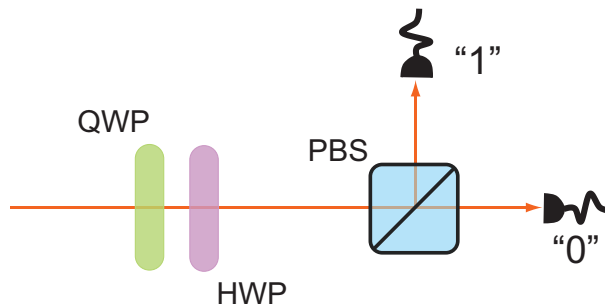[16]This will be explained in Section 4.1.

Figure 2.4: Schematic of the polarization analysis. Any observable $\hat{\mathcal{O}}_{\vartheta,\varphi}$ corresponding to a basis that is spanned by two orthogonal polarization states can be measured with the help of a `PBS` preceded by a `HWP` and `QWP`. The `PBS` effectively measures in the Z-eigenbasis, therefore separating photons with positive and negative eigenvectors of σ_z. To rotate into an arbitrary polarization basis $B_{\vartheta,\varphi}$, the waveplates have to be set at appropriate angles, such that they transform between the eigenstates of $B_{\vartheta,\varphi}$ and σ_z. Each output of the `PBS` is monitored by a fiber-coupled APD.

adequate correlation measurements.

2.4.1   Polarization analysis

In our experiments, we perform polarization analysis with the help of a polarizing beamsplitter preceded by a `HWP` and `QWP`. Each output mode of the `PBS` is monitored by a fiber-coupled detector (APD), as depicted in Fig. 2.4. As discussed above, the `PBS` separates horizontal and vertical polarization and effectively measures the eigenstates of the σ_z operator. By appropriate setting of the preceding waveplates' angles, any arbitrary basis $B_{\vartheta,\varphi}$ in the Poincaré sphere can be analyzed[17]. For instance, setting the `QWP` angle to $\pi/4$ rotates the polarization of a photon that was initially in one of the eigenstates of σ_y, i.e. $|R\rangle$ or $|L\rangle$, to $|H\rangle$ and $|V\rangle$ respectively. Therefore, detecting a photon in the transmitted (reflected) mode of the `PBS` implies that the photon has been in the state $|R\rangle$ or $|L\rangle$ before the waveplates. Analogously, the `HWP` can transform between the eigenstates of σ_x, i.e. $|+\rangle$ or $|-\rangle$, and σ_z if the angle is set to $\pi/8$. Careful attention has to be paid, however, in this case to the setting of the `QWP`. It too has to be rotated by $\pi/4$ (i.e. into the eigenbasis of σ_x) since otherwise it would introduce a undesired phase shift resulting in an unwanted erroneous polarization basis being mapped onto the `PBS`. Table 2.1 summarizes the most important polarization eigenbases and their corresponding waveplate setting.

From the count statistics, that is the (relative) frequency of detection events in the transmitted and reflected output mode of the `PBS` we can infer the respective probabilities $P^+_{B_{\vartheta,\varphi}}$ and $P^-_{B_{\vartheta,\varphi}}$ to find the photon in the corresponding eigenstate of the basis $B_{\vartheta,\varphi}$. In practice, the individual detection efficiencies of the two detectors behind the `PBS` have to be taken into account in order to determine the relative frequencies correctly.

If the quantum information under examination is contained in more than one photon then the measurement of multi-qubit observables, i.e. polarization correlations between the individual

---

[17]Recall that any vector in the Poincaré sphere can be dfined by two angles ϑ, φ, see Fig. 1.2.

Target basis	HWP setting	QWP setting
H/V	0	0
+/-	$\pi/8$	$\pi/4$
R/L	0	$\pi/4$

Table 2.1: Typical wave plate settings for polarisation analysis in the important bases, when the sequence of HWP and QWP combination is as depicted in Fig. 2.4.

photons, is required. In this case a polarization analyzer is placed in each spatial mode of the linear-optics network that can be occupied by a photon. The detection requires then the "simultaneous" detection of two, three or more photons within a given time window. To achieve this, the electronic output (TTL) signal of each APD is fed into an ultra-fast coincidence logic which is capable of registering 64 possible coincidence events for up to twelve input signals. The coincidence time window, within which the signals are considered to be simultaneous, can be arbitrarily set, however one has to take care that it is smaller than the duration between two subsequent pump pulses (less than 13ns in our case).

2.4.2 Quantum state tomography

If we want to extract important properties of a quantum state then we require the state's density matrix (c.f. Section 1.1.2). It gives access to relevant measures such as a state's fidelity with an ideal one or allows to extract the amount of entanglement or entropy that is contained in the state under consideration. Fortunately there exists a mathematical procedure to obtain the density matrix from an unknown, experimentally produced quantum state, namely *quantum state tomography*.

In a nutshell, quantum state tomography is the procedure of experimentally determining an unknown quantum state by reconstructing its density matrix [120]. This can be done by an exact measurement of all the components that make up a particular state. As Stokes [121] showed, the polarization state of a single photonic qubit can be determined by taking a set of four projective measurements which are represented by the operators

$$
\begin{aligned}
\mu_0 &= |H\rangle\langle H|, & \mu_3 &= |+\rangle\langle +|, \\
\mu_1 &= |V\rangle\langle V|, & \mu_4 &= |R\rangle\langle R|,
\end{aligned}
\tag{2.13}
$$

and similarly the state of two qubits can be determined by a set of 16 measurements (represented in the following by $|\psi\rangle_\nu$, $\nu = 1, 2, ..., 16$), which are all possible combinations of the above operators $\mu_i \otimes \mu_j$, where i,j=0,1,2,3. In general, a n-qubit system requires 4^n measurements. The average number of counts in the detector is given by the formula $n_i = \mathcal{N} \operatorname{tr}(\rho \cdot \mu_i)$, where ρ is the density matrix representing the state of the qubit and $\mathcal{N}$ is a constant that can be determined from the experimental data (includes light intensity, detector efficiency).

In order to develop a better understanding of how state tomography works let us consider a two-qubit system. The density operator representing an arbitrary two-qubit state is a 4x4
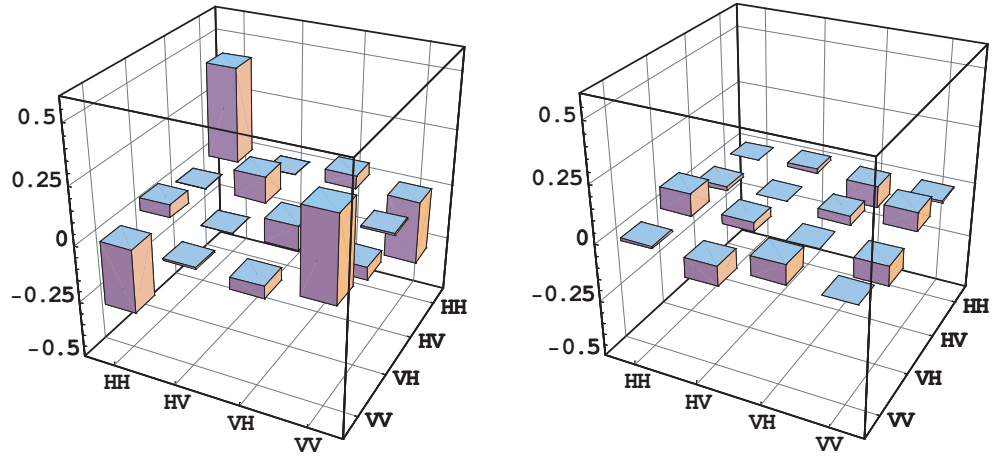
Figure 2.5: An example for a two-qubit density matrix reconstructed by quantum state to-mography employing maximum-likelihood estimation. The left plot shows the real part of ρ, the right plot the imaginary part. This plot shows a density matrix of an experimentally prepared and entangled state $|\Phi\rangle^{-} = \frac{1}{\sqrt{2}}(|HH\rangle - |VV\rangle)$.

density matrix with 16 real parameters (of which 15 are independent). For the density matrix to be physical, we want it to be:

- **hermitian**, i.e. $\rho = \rho^{\dagger}$

- **non-negative**, i.e. $\langle\psi|\,\rho\,|\psi\rangle \geq 0 \quad \forall\,|\psi\rangle$

- **normalized**, i.e. $\mathrm{Tr}(\rho) = 1$

This implies that for every density matrix ρ, there exists a matrix T such that ρ can be written as $\rho = \frac{T^{\dagger}T}{\mathrm{Tr}(T^{\dagger}T)}$. As mentioned above, ρ is a function of 16 real variables, which we will denote as $t_1, t_2, ..., t_{16}$. For various reasons [120], it is useful and convenient to choose a tridiagonal form for T:

$$T(t) = \begin{pmatrix} t_1 & 0 & 0 & 0 \\ t_5 + i\,t_6 & t_2 & 0 & 0 \\ t_{11} + i\,t_{12} & t_7 + i\,t_8 & t_3 & 0 \\ t_{15} + i\,t_{16} & t_{13} + i\,t_{14} & t_9 + i\,t_{10} & t_4 \end{pmatrix} \tag{2.14}$$

To quantify how good the density matrix $\rho(t_1, t_2, ..., t_{16})$ is in agreement with the measured experimental data (i.e. coincidence rates), we introduce the so-called "likelihood-function", which represents the deviation of the density matrix ρ from the measurement. Since the expected number of coincidence counts in a given experimental run is given by

$$n_\nu = \mathcal{N}\langle\psi_\nu|\rho|\psi_\nu\rangle. \tag{2.15}$$

The likelihood P that ρ reproduces the data, given the coincidence measurements have a Gaus-

sian probability distribution, is

$$P = \prod_{\nu=1}^{16} \exp\left[-\frac{(n_\nu - \mathcal{N}\langle\psi_\nu|\rho|\psi_\nu\rangle)^2}{2\mathcal{N}\langle\psi_\nu|\rho|\psi_\nu\rangle} \right],$$ (2.16)

where the standard deviation is given approximately by Poissonian noise, i.e. $\sqrt{n_\nu}$. But it is actually easier to find the minimum of the logarithm of this function P, which leads us to

$$\Delta f = \sum_{\nu=1}^{16} \frac{(n_\nu - \mathcal{N}\langle\psi_\nu|\rho|\psi_\nu\rangle)^2}{2\mathcal{N}\langle\psi_\nu|\rho|\psi_\nu\rangle}$$ (2.17)

with Δf being the likelihood-function that indicates the deviation from the observed νth coincidence measurement. Note that ρ is a function of $t_1, t_2, ..., t_{16}$ and $\mathcal{N} = \sum_{\nu=1}^{4} n_\nu$ (see [120]). Fortunately, mathematic computer packages like `Mathematica` are able to execute an algorithm which finds the minimum of Δf and all corresponding values of $t_1, t_2, ..., t_{16}$, and therefore the desired density matrix which represents our two-qubit system. An example of such a reconstructed density matrix using experimental data can be seen in Fig. 2.5.

2.4.3 Quantum process tomography

In addition to the reconstruction of quantum states, it is often necessary to have precise knowledge of a particular process that acts on the quantum states under examination. Formally, a quantum process can be described by a function $\mathcal{E}$ that describes the evolution of states during a given quantum process. The experimental determination of a full description of such a process is called quantum process tomography (QPT) [122, 123, 11, 124]. It aims at the reconstruction of the process operator which is a superoperator in Hilbert space. This constitutes an important part of the analysis of the decoherence-free subspace experiment that is presented in Chapter 8.

To determine a quantum process operator, we have to determine the linear map $\mathcal{E}$, which completely describes the dynamics of the quantum system, so that the state change experienced by the process can be written as

$$\rho \rightarrow \mathcal{E}(\rho),$$ (2.18)

where we have to obey the condition that the trace $\text{Tr}(\mathcal{E}(\rho))$ is always equal to one. Any quantum operation $\mathcal{E}$ can also be written in the so-called *operator sum representation* for an arbitrary input state ρ

$$\mathcal{E}(\rho) = \sum_k E_k \rho E_k^\dagger,$$ (2.19)

where E_k are the *operation elements* and have to obey the completeness relation,

$$\sum_k E_k^\dagger E_k = 1,$$ (2.20)

to ensure that ρ remains hermitian with trace one. The set of operation elements $\{E_k\}$ completely describes the action of the gate process and with process tomography we want to experimentally determine some of the E_k matrices. If one now chooses a fixed basis $\{\tilde{E}_m\}$ for the operators on the state space then we can express the operation elements in this basis as $E_i = \sum_m a_{im} \tilde{E}_m$ and Eqn. 2.19 becomes

$$\mathcal{E}(\rho) = \sum_{mn} \chi_{mn} \tilde{E}_m \rho \tilde{E}_n^\dagger,$$ (2.21)

where χ_{mn} is a positive hermitian matrix $\chi_{mn} = \sum_i a_{im}a_{in}^*$ that now completely describes the process in the chosen basis.

The process matrix χ can be determined by sending a certain set of *probe states* into the process and recording their respective output state under the action of the quantum process $\mathcal{E}$. Usually the basis of input states is chosen such that the matrices $\rho^{(jk)}$ representing them all have a 1 in the jth row and k^{th} column and zeros elsewhere. A suitable set for the experiment are the operators $|H\rangle\langle H|$, $|V\rangle\langle V|$, $|+\rangle\langle +|$, and $|R\rangle\langle R|$, which are related to some other basis $\rho^{(\alpha\beta)}$ by $\rho^{(jk)} = M^{-1}\rho^{(\alpha\beta)}$. The complex and nontrivial 16x16 matrix M^{-1} can be found in [125].

The complete set $\{\rho^{(\alpha\beta)}\}$ of input states for a process acting on two qubits consists of 16 two-qubit states given by all the tensor products of the single-qubit states[18],

$$\{\rho^{(\alpha\beta)}\} = \{\rho^{(\alpha)} \otimes \rho^{(\beta)}\}, \quad \alpha,\beta \in \{H,V,D,R\}, \tag{2.22}$$

and performing tomography on each of them one obtains a set of output matrices $\{\mathcal{E}\rho^{(jk)}\}$ using the inverted M matrix of Reference [125]. It is then possible to reconstruct the 16x16 χ matrix in block form:

$$\chi = K^T \begin{pmatrix} \mathcal{E}\rho^{(11)} & \mathcal{E}\rho^{(12)} & \cdots \\ \mathcal{E}\rho^{(21)} & \mathcal{E}\rho^{(22)} & \cdots \\ \vdots & \vdots & \ddots \end{pmatrix} K, \tag{2.23}$$

where K is a particular matrix written as $K = P \cdot \Lambda$ with the permutation matrix $P = \mathbb{1} \otimes [\rho^{(11)} + \rho^{(23)} + \rho^{(32)} + \rho^{(44)}] \otimes \mathbb{1}$ and $\Lambda = [Z \otimes \mathbb{1} + X \otimes X] \otimes [Z \otimes \mathbb{1} + X \otimes X]/4$. Unfortunately, this procedure does not allow the incorporation of experimental uncertainties for a full error analysis. But still there exists a measure which tells how much the obtained process matrix resembles the ideal process, namely the *process fidelity* $\mathcal{F}_g$ between the ideal, target unitary process U and the actual process $\mathcal{E}$

$$\mathcal{F}_p(U,\mathcal{E}) = \min\langle\psi|U^\dagger\mathcal{E}(|\psi\rangle\langle\psi|)U|\psi\rangle, \tag{2.24}$$

where the minimum is over all input states $|\psi\rangle$.

An alternative approach to the process fidelity is to calculate the *average process fidelity*, i.e. the average overlap of the predicted output states with the measured output states (from the individual state tomography results), which is the average of the usual state fidelity defined as [11, 126]

$$\mathcal{F}(\rho,\sigma) = \left(\mathrm{Tr}\sqrt{\sqrt{\sigma}\rho\sqrt{\sigma}}\right)^2, \tag{2.25}$$

where ρ, σ are the density matrices under consideration. The average process fidelity $\mathcal{F}_{avg}$ then becomes

$$\mathcal{F}_{avg} = \frac{d \cdot F_p + 1}{d + 1}, \tag{2.26}$$

with d the dimension of the Hilbert space.

---

[18]Recall the relevant single-qubit states' density matrices:
$\rho^{(H)} = \begin{pmatrix} 1 & 0 \\ 0 & 0 \end{pmatrix}$, $\rho^{(V)} = \begin{pmatrix} 0 & 0 \\ 0 & 1 \end{pmatrix}$, $\rho^{(D)} = \frac{1}{2}\begin{pmatrix} 1 & 1 \\ 1 & 1 \end{pmatrix}$ and $\rho^{(R)} = \frac{1}{2}\begin{pmatrix} 1 & -i \\ i & 1 \end{pmatrix}$.

The process purity is defined as the purity of all output states averaged over all pure inputs,

$$\mathcal{P}_p = \overline{\mathrm{Tr}(\rho^2)} = \frac{d \cdot \mathrm{Tr}(\chi_{exp}^2) + 1}{d + 1} \tag{2.27}$$

and also allows to extract an average normalized linear entropy of the process.

However, similar to QST, the process matrix χ can give unphysical results in certain cases and numerical optimization methods have been developed which account for this, very much equal to the maximum-likelihood approach in QST [125, 126].

Chapter 3

Quantum computing with linear optics

As we have already seen in the opening chapter, a quantum computer can generally be described as a machine that can perform certain calculations by using the laws of quantum mechanics. Already in 1982, R.P. Feynman put forward the idea that certain computations could be performed much more efficiently with quantum mechanical systems than with classical computation machines [1]. This was subsequently proven with the discovery of the first few quantum algorithms [7, 9, 8] and eventually started a whole new field of research [127, 128]. Quantum computing has attracted increasing attention because of its promise to perform certain tasks such as factoring of a large integer more efficiently than any classical computer [9], and due to its potential use to efficiently simulate large quantum systems and their dynamics - a feat that seems intractable with current or future classical machines.

There are different architectures for quantum computers based on many different physical systems, some of which I have already discussed in Section 2.1 of Chapter 2. From here onwards I will solely concentrate on linear-optics quantum computing with single photons (LOQC). After giving a short introduction into the basic concepts and principles of quantum computing I will present and explain the two cornerstone models of LOQC: The standard or *circuit model*, more widely known as the Knill-LaFlamme-Milburn (KLM) scheme [12, 13] and its measurement based alternative, the *one-way model*, which was put forward by Raussendorf and Briegel [14, 15, 16].

3.1 The power of quantum computing - a short introduction

Whenever a computer performs a computation, it processes a given input information according to definite pre-programmed rules and finally delivers an output that contains the desired information. From a physical point of view, this computation is associated with a time evolution of the initial input state to the final output state. When extending this concept from the
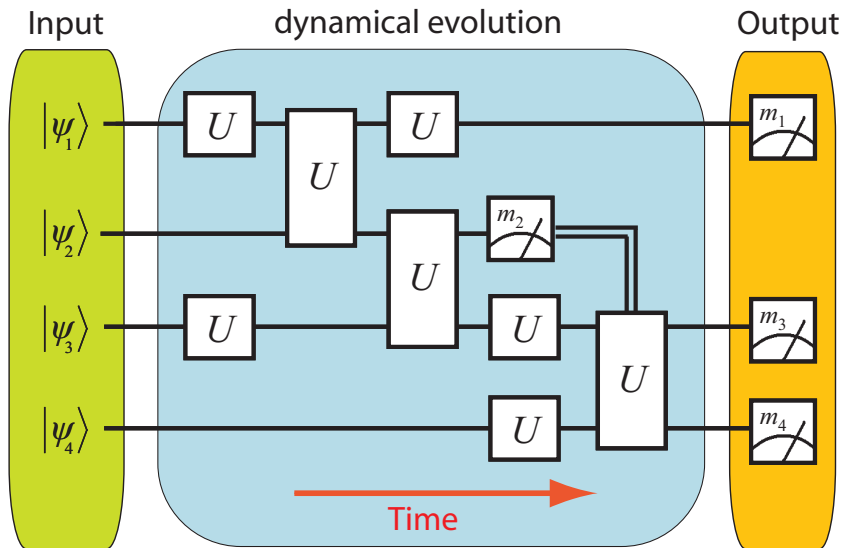
Figure 3.1: Schematic representation of a basic quantum computation in the notation of the quantum circuit model. The computation proceeds as follows: (1) The input state is prepared as a tensor product of pure single-qubit states, $|\psi_1\rangle \otimes |\psi_2\rangle \otimes \ldots \otimes |\psi_n\rangle$; (2) The computation itself proceeds as a dynamical evolution of the input states through a circuit of single- and two-qubit gates which are element of a universal set of gates, e.g. $U \in \{R(\alpha, \beta, \gamma), \texttt{CNOT}\}$. Single horizontal lines represent quantum wires or logical qubits that are processed in time from left to right. Double lines denote classical communication, i.e. feed-forward of the measurement results during the computation, so that later actions (e.g., quantum gates) may depend on the results of earlier measurement outcomes. (3) The read out is performed by measurements in an any orthonormal single-qubit basis, since this is equivalent to applying a single-qubit unitary operation followed by a computational basis measurement. The output of the computation is then a classical bit string of the form "0100 . . . 10".

classical to the quantum domain, it turns out that the time evolution of the initial state can be described by a unitary process. In analogy to classical computers where the transformations are implemented by logical gates, unitary operations acting on qubits can be thought of as quantum gates.

It has been shown that any arbitrary unitary process that acts on a finite number of qubits can be decomposed to a product of one- and two-qubit operations. In fact, any entangling two-qubit gate when combined with arbitrary single-qubit operations is sufficient to implement any quantum algorithm [10, 129, 130]. In the language of quantum information, we say that this is a *universal* set of gates[1] and we will return to this in the following Section.

Although shortly discussed in Section 2.1 it seem sensible to again list the essential requirements that a physical system supporting a quantum computer has to fulfill[2]. They were first

---

[1]In the theory of quantum computational networks, a gate is considered to be universal if instances of it are the only computational components required to build a universal quantum computer. A set of gates is said to be universal, if any arbitrary unitary operation can be performed by these gates alone.

[2]These are often known as the DiVincenzo criteria, or the five "commandments" for quantum computation.

put forward by David P. DiVincenzo in [78] and read:

1. A scalable physical system with well characterized qubits.

2. The ability to initialize the state of the qubits to a simple fiducial state, such as $|000\rangle$.

3. Long relevant decoherence times, much longer than the gate operation time.

4. A "universal" set of quantum gates.

5. A qubit-specific measurement capability.

The physical system supporting the qubit should be scalable, i.e., it should have the capacity for numerous qubits, as a single qubit is hardly useful for any reasonable application. Furthermore, it should be possible to initialize the qubit in a well defined state and apply to it the previously mentioned set of universal quantum gates. Also, the time scales on which the gates act on the qubits should be sufficiently small compared to the decoherence time of the qubit system in order to allow for any "useful" computation. Finally, any computation requires the ability to measure specific qubits to obtain the final result. Here it is necessary to have reliable, i.e. fast and efficient (ideally with 100% quantum efficiency) measurement capabilities. Photons do meet almost of all of the aforementioned — with the restriction that both state initialization and detection is currently a probabilistic process. Nevertheless, linear optics allows scalable and deterministic quantum computing as we will see in Section 3.2 and it allows proof-of-principle demonstration of many exciting ideas.

3.1.1   Single- and two-qubit gates - a universal set

Just like a conventional computer is made up of numerous distinct logical gates, unitary transformations are the building blocks of any quantum computer. Unlike many classical logic gates however, quantum logic gates are reversible [131]. Since any arbitrary unitary transformation can be decomposed into a set of single-qubit gates and one distinguished two-qubit gate it seems reasonable at this point to briefly review the relevant gates and their respective action [10, 11].

Single-qubit gates

Quantum gates acting on single qubits can be be described by 2x2 matrices, with the constraint that the gate or matrix be *unitary*, therefore satisfying the normalization condition before and after the gate (i.e. particle conservation). Since this unitary operations are elements of the special unitary group $SU(2)$, their action can be written in terms of the Pauli operators[3]

$$\mathcal{U}(\alpha, \gamma) = \exp(i\alpha)\exp(-\frac{\gamma}{2}\vec{r} \cdot \vec{\sigma}) \tag{3.1}$$

There also exist two extra requirements relating to the communication of quantum information: The ability to interconvert stationary and flying qubits and the ability faithfully to transmit flying qubits between specified locations.

[3]The Pauli operators are (up to a constant factor) the generators of $SU(2)$.

In the single qubit picture this corresponds to a rotation of the polarization vector on the surface of the Poincaré sphere by an angle γ around the axis given by $\vec{r}$ and the application of a phase α.

Important single-qubit gates are the X-, Y-, Z-gates that correspond to the already known Pauli matrices

$$X \equiv \begin{pmatrix} 0 & 1 \\ 1 & 0 \end{pmatrix}; \quad Y \equiv \begin{pmatrix} 0 & -i \\ i & 0 \end{pmatrix}; \quad Z \equiv \begin{pmatrix} 1 & 0 \\ 0 & -1 \end{pmatrix}. \tag{3.2}$$

The X-gate, for example, acts like a quantum NOT-gate, performing a bit flip on the input state $\alpha|0\rangle + \beta|1\rangle \rightarrow \alpha|1\rangle + \beta|0\rangle$, so that the roles of $|0\rangle$ and $|1\rangle$ are interchanged. The Z-gate, on the other hand, performs a sign flip, since it does nothing to $|0\rangle$, but flips the sign of $|1\rangle$ to give $-|1\rangle$, therefore $\alpha|0\rangle + \beta|1\rangle \rightarrow \alpha|0\rangle - \beta|1\rangle$. This can be written as a circuit diagram, which is a graphical representation of the above gates:

$$\alpha|0\rangle + \beta|1\rangle \quad \boxed{X} \quad \alpha|1\rangle + \beta|0\rangle$$

$$\alpha|0\rangle + \beta|1\rangle \quad \boxed{Z} \quad \alpha|0\rangle - \beta|1\rangle$$

Pauli matrices, when exponentiated, give rise to *rotation operators* about the $\hat{x}$-, $\hat{y}$-, $\hat{z}$-axes on the Poincaré sphere, and can be defined by

$$R_x(\theta) \equiv \exp^{-i\Theta X/2} = \mathbb{I} \cos \frac{\theta}{2} - iX \sin \frac{\theta}{2} = \begin{pmatrix} \cos \frac{\theta}{2} & -i \sin \frac{\theta}{2} \\ -i \sin \frac{\theta}{2} & \cos \frac{\theta}{2} \end{pmatrix}, \tag{3.3}$$

and similarly for the other rotation operators $R_y(\theta)$, $R_z(\theta)$.

In circuit notation[4] this becomes

$$\boxed{X(\theta)} \quad \equiv \quad \exp(-i\theta X/2), \tag{3.4}$$

$$\boxed{Y(\theta)} \quad \equiv \quad \exp(-i\theta Y/2), \tag{3.5}$$

$$\boxed{Z(\theta)} \quad \equiv \quad \exp(-i\theta Z/2). \tag{3.6}$$

Another important example gate[5] is the *Hadamard*-gate (denoted H), which transforms between the eigenstates of σ_z and σ_x. It is one of the most useful single-qubit gates in quantum information, since it creates superposition states, turning $|0\rangle$ into $(|0\rangle + |1\rangle)/\sqrt{2} = |+\rangle$ and $|1\rangle$ into $(|0\rangle - |1\rangle)/\sqrt{2} = |-\rangle$. A Hadamard-gate can be constructed out of X- and Z-gates, such that $H = (X + Z)/\sqrt{2}$. The transformation matrix reads:

$$H \equiv \frac{1}{\sqrt{2}} \begin{pmatrix} 1 & 1 \\ 1 & -1 \end{pmatrix} \tag{3.8}$$

---

[4]From here onwards we will use both the notations $X(\theta)$ and $R_x(\theta)$ to describe an rotation around the x-axis by an angle θ and will switch between these descriptions whenever appropriate.

[5]For the sake of completeness, other frequently used single-qubit gates are the phase gate (denoted S) and the $\pi/8$ gate (denoted T), whose corresponding matrices read

$$S = \begin{pmatrix} 1 & 0 \\ 0 & i \end{pmatrix}; \quad T = \begin{pmatrix} 1 & 0 \\ 0 & e^{i\pi/4} \end{pmatrix}. \tag{3.7}$$

$$\alpha|0\rangle + \beta|1\rangle \quad \boxed{H} \quad \alpha|+\rangle + \beta|-\rangle$$

When visualizing the Hadamard operation on the Poincaré-sphere, it turns out that it is just a rotation of the sphere about the $\hat{y}$-axis by $90°$, followed by a rotation about the $\hat{x}$-axis by $180°$. This gate is often encountered in quantum algorithms since it generates equally weighted superpositions of the computational basis states. A prominent and very illustrative example is the Deutsch algorithm [7, 19], which will be encountered in Chapter 6.

Two-qubit gates

Two-qubit gates are essential for quantum computing, since they allow individual qubits to interact with one another, conditional on the state of one or more qubit(s). Therefore two-qubit gates can be employed to create entanglement between previously unentangled qubits in a controlled fashion.

One of the cornerstone two-qubit quantum logic gates is the *controlled*-NOT or CNOT-gate. It acts on two input qubits, called the *control* and *target qubit*, respectively, and has the following circuit representation:

$$|c\rangle \quad \boxed{\text{CNOT}} \quad \equiv \quad \bullet \quad \equiv \quad \bullet \quad |c\rangle$$
$$|t\rangle \quad \oplus \quad \boxed{X} \quad |t \oplus c\rangle \tag{3.9}$$

The action of the gate is $|c, t\rangle \rightarrow |c, t \oplus c\rangle$, where $\oplus$ denotes addition modulo two. The top line represents the control qubit $|c\rangle$, while the bottom line denotes the target qubit $|t\rangle$. The gate's action can be summarized as follows. If the control qubit is set to 0, then the target qubit is unchanged. If the control qubit is set to 1, then the target qubit is flipped, thus resulting in the following, so-called truth table:

$$|00\rangle \rightarrow |00\rangle$$
$$|01\rangle \rightarrow |01\rangle$$
$$|10\rangle \rightarrow |11\rangle$$
$$|11\rangle \rightarrow |10\rangle \tag{3.10}$$

Yet it is also possible to give a matrix representation of the CNOT, with respect to the basis states $|00\rangle$, $|01\rangle$, $|10\rangle$ and $|11\rangle$, in that order.

$$\text{CNOT} = \begin{pmatrix} 1 & 0 & 0 & 0 \\ 0 & 1 & 0 & 0 \\ 0 & 0 & 0 & 1 \\ 0 & 0 & 1 & 0 \end{pmatrix} \tag{3.11}$$

As we have shortly mentioned before, a CNOT-gate can be employed to create entanglement between two initially independent particles, as was shown in [132]. Suppose we have the control qubit in a superposition state, i.e. $|+\rangle = \frac{1}{\sqrt{2}}(|0\rangle + |1\rangle)$, while the target qubit is in the state $|0\rangle$. According to the CNOT truth table of Eqn. 3.10, we end up with the state

$$|+\rangle \quad \boxed{H} \quad \bullet \quad \Bigg\} \quad \Rightarrow \quad \frac{1}{\sqrt{2}}\left(|00\rangle + |11\rangle\right) = |\Phi^+\rangle, \tag{3.12}$$
$$|+\rangle \quad \oplus$$

which is one of the maximally entangled Bell-states, as in Eqn. 1.28. Thus, the following circuit transforms between the Bell- and the product basis of two qubits and can therefore effectively entangle, but also disentangle any two qubits. It is of utmost importance in quantum computation to experimentally realize such a two-qubit gate, as has been achieved by various research groups [133, 134, 91, 135, 136].
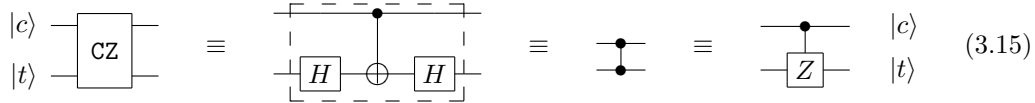
Further inspection reveals that the `CNOT`-gate is not the only two-qubit gate capable of entangling two particles. Another very useful gate in quantum computations turns out to be the *controlled*-`Z`-gate, or `CZ`-gate for short. The gate's action in the computational basis is specified by the following unitary matrix

$$\mathtt{CZ} = \begin{pmatrix} 1 & 0 & 0 & 0 \\ 0 & 1 & 0 & 0 \\ 0 & 0 & 1 & 0 \\ 0 & 0 & 0 & -1 \end{pmatrix}, \tag{3.13}$$

it therefore changes the sign on the $|11\rangle$ element to $-|11\rangle$ which is equivalent to the application of a Z-gate to the target qubit, hence the name. It turns out that the `CZ`-gate is closely related to the `CNOT`. By applying additional Hadamard gates acting on the target qubit before and after the `CZ`-gate, results in the same action as the `CNOT`,

$$\mathtt{CZ} = (\mathbb{1} \otimes H) \ \cdot \ \mathtt{CNOT} \ \cdot \ (\mathbb{1} \otimes H) \tag{3.14}$$

This can also be seen in the circuit representation:

$$\tag{3.15}$$

where a pair of controls (i.e dots) connected by a wire denote the controlled-`Z`-gate.

Therefore we can create an entangled state by initializing two separable qubits in the $|+\rangle$ state and applying the `CZ`-gate. In circuit notation this becomes

$$\Rightarrow \frac{1}{\sqrt{2}} \left(|0+\rangle + |1-\rangle \right) \overset{L.U.}{=} |\Phi^+\rangle. \tag{3.16}$$

3.2   The standard quantum circuit model

The most widely used model of quantum computation at present is the *quantum circuit* model — or standard model of quantum computation [131]. It is intuitively easy to understand since it is basically a generalization of the well-known classical circuit model based on Boolean logical operations such as `AND` and `NOT` in to the quantum regime. Of course the Boolean operations are substituted by appropriate one- and two-qubit gates as explained in the previous Section. The circuit model turns out to be very helpful when trying to reinterpret abstract algorithmic concepts into physical operations. Often in the case of linear optics, the circuit model is a synonym for the Knill, LaFlamme and Milburn (KLM) scheme of quantum computing, since these authors showed in a much celebrated paper how the constituents of the circuit model can be implemented with linear optical devices in a scalable manner [13].

3.2.1   The KLM scheme

From an experimental point of view, the implementation of single-qubit gates for photonic qubits that carry the quantum information in their polarization state is not a challenge at all. As we have seen in Section 2.3 these operations correspond to simple polarization rotations and can be implemented with suitable birefringent crystals such as waveplates. Because photons do not tend to interact with the environment they have exceptionally long decoherence times. However, this represents a serious challenge when it comes to the experimental realization of two-qubit gates since they are based on some sort of (nonlinear) interaction between the qubits. In principle one could harness non-linear effects in solid state materials, such as the optical Kerr effect[6], but in practice they turn out to be much too weak [95]. While it is possible to realize any discrete unitary operation with linear optics only [114] these linear operations cannot make two photons interact, they can only make them interfere. Therefore the unitary transformation U_L is separable in the sense that it can be written in terms of a unitary operation U over each photon, i.e. $U_L = U \otimes U$, and of course a CNOT cannot be performed by these means.

As a consequence, linear-optics quantum computation (LOQC) was thought to be utterly impossible. This however changed dramatically with a seminal work by Emanuel Knill, Raymond LaFlamme and Gerard Milburn (KLM) in 2001 [13]. The authors introduce a scheme that achieves the required non-linearity and interaction between photons in the form of auxiliary entangled states, ancillary modes, photon counting and conditional detection. Here, conditional detection implies that actions are performed on photons occupying different modes or particular events are selected, conditioned on the detection of a photon in a given mode. Using these tools it was shown that LOQC can be made near deterministic, i.e. given sufficient resources in terms of ancilla photons/modes, the success probability of a two-qubit gate can be made arbitrarily high. The neat fact here is that even if these auxiliary resource states can be generated only probabilistically, the overall computation can still be deterministic. To understand this, let's go into some more detail:

Basically, the KLM scheme induces the effective interaction between photons by projective measurements with photo-detectors. The difficulty with this technique is however that such optical quantum gates turn out to be inherently probabilistic [138, 10, 139]. When some gates in a computational circuit succeed only with a certain probability p, then the overall computation that is based on N such gates succeeds with probability p^N. For realistic and practical circuits, N is quite large and p rather small, therefore the calculation has to be repeated on the order of p^{-N} times, or has to run on p^{-N} such systems in parallel [95]. Either way, the resources (time or circuits) scale exponentially with the number of gates — undoing the advantage that many quantum algorithms have over classical protocols. Knill, LaFlamme and Milburn however succeeded in taking probabilistic elements out of the actual computation by employing, and improving upon, a clever *teleportation trick* invented by Gottesman and Chuang in 1999 [12].

---

[6]The *Kerr* effect, often also called the *quadratic electro-optic effect* is a change in the refractive index of a material in response to an electric field. In the optical Kerr effect the electric field is due to the light itself. This causes a variation in the index of refraction which is proportional to the local irradiance of the light. This variation of the refractive index is responsible for nonlinear optical effects such as self-focusing and self-phase modulation. This effect however only becomes significant with very intense beams, e.g. from lasers. For more information, see [137, 95].
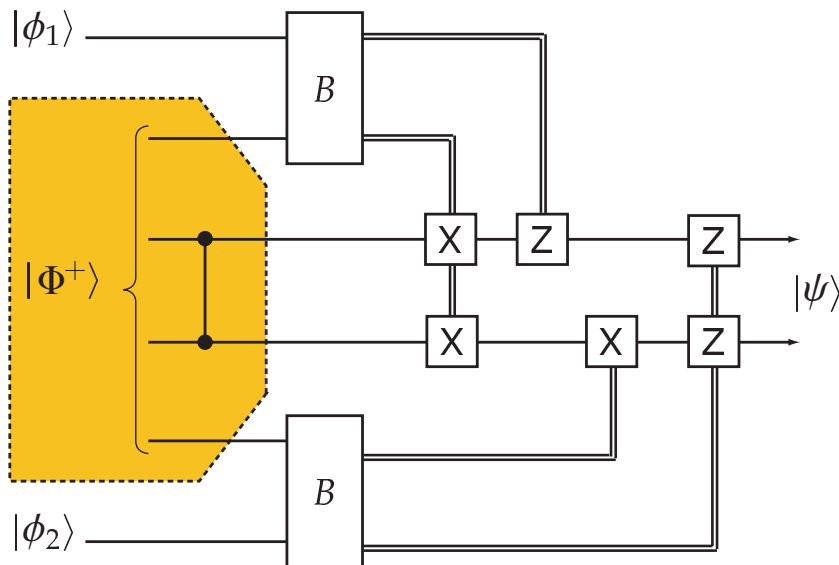
Figure 3.2: The Gottesman-Chuang gate. Here $|\phi_1\rangle$ and $|\phi_2\rangle$ are the input qubits onto which we wish to apply the two-qubit CZ-gate U_{CZ} at the end of the circuit. The teleportation trick can explained as follows: The input qubits $|\phi_1\rangle$ and $|\phi_2\rangle$ are teleported into the main circuits by employing Bell-state measurements (B) and by applying corresponding Pauli-operations. At the end of the circuit we perform the CZ-gate U_{CZ} i.e. $\psi = U_{\text{CZ}}|\phi_1\rangle|\phi_2\rangle$. Then we commute the U_{CZ} operation from the right to the left, through the corrective Pauli operations of the teleportation into the shaded box. Since the CZ-gate is part of the Clifford group the commutation does not induce any new two-qubit gates. This allows to perform the CZ-gate operation *off-line*, together with the preparation of the entanglement channel for teleportation (denoted by $|\Phi^+\rangle$). This total resource can be prepared off-line with a probabilistic protocol, however there are no more probabilistic elements in the actual computational circuit. Fig. adapted from [12, 95]

This trick removes the probabilistic gate from the actual quantum circuit by including it in the resources that can be prepared *offline* and teleports it into the actual circuit whenever it succeeds. This is explained in greater detail in Figure 3.2.

While this trick in principle removes all probabilistic elements in the computational circuit, there is a problem when we try to realize it with linear optics. That is because the Bell-state measurements that are essential to the teleportation trick can again only be performed probabilistically, i.e. they succeed only half of the time [140]. To overcome this, KLM designed a teleportation protocol that uses $2n$ additional photons and succeeds with a success probability $n/(n+1)$. Since the Gottesman-Chuang gate requires two teleportation events, the success probability of the two-qubit gate is $[n/(n+1)]^2$. The more ancilla photons the more reliable the whole computation. However, this is a very resource intensive scheme. To achieve 99% success probability of the two-qubit gate we require already on the order of 200 ancilla photons. The main aim, of course, is to achieve scalable LOQC, which can be done by lowering the error probability ε below the *fault-tolerant threshold*, which is on the order of a few percents [141]. Failure of the two-qubit gate can also be minimized by using *error correction* in the quantum

circuit, however this too is resource intense. Either way, the resource requirements for scalable optical quantum computing — though possible theoretically – seem daunting for practical implementations.

While several simplifications of this scheme have been proposed in recent years [142, 143, 144, 145, 146], the main crux remains — the KLM variant of the Bell measurement always has a small error probability ε, and therefore a perfect and deterministic teleportation and with it deterministic computation is not possible with linear optics in a realistic manner.

This believe radically changed with the advent of a new and in many ways entirely different model of quantum computation which is based on single-qubit measurements on highly entangled multi-particle states [14, 15, 16]. In this specific model, quantum computation is deterministic even when performed with linear optics and a small number of qubits. To see how this works we will explain this model and discuss the implementation of single- and two-qubit gates in the following Section.

3.3 The measurement-based or "one-way" model

The *measurement-based* model of quantum computing is an exciting alternative approach to LOQC since it allows to prepare the resource for the quantum computation *offline* prior to any logical operations. Furthermore this model has the remarkable property that all the basic dynamical operations and the evolution of quantum states are performed by non-unitary quantum measurements — hence the name *measurement-based* or *one-way* — and still be used to simulate arbitrary complex quantum mechanical dynamics through a set of universal gates. Moreover it allows for deterministic quantum computing with linear optics through a process called feed-forward. In the following we will focus on a class of measurement-based models proposed by Raussendorf and Briegel [147], the so-called *cluster-state* model, or *one-way quantum computer*.

The cluster-state model thus differs substantially from the conventional unitary model of quantum computing and these differences have led to new insights into quantum computational complexity [148], and to dramatic simplifications in experimental proposals for quantum computation [16, 149]. It also challenges our conventional understanding of quantum measurement as a process that produces irreducible randomness and that inherently destroys quantum coherence.

3.3.1 Introduction & simple algorithms

The very heart of measurement-based quantum computing can be summarized by the following statement. First a sufficiently large and highly entangled resource — the cluster state — is created; then the actual computation is performed by single-qubit measurements on these cluster qubits and by feed-forwarding the results of the individual measurements. Since the "hard work" of creating all the necessary entanglement can be performed offline and since single-qubit measurements are particularly easy to implement in the experiment, this constitutes a powerful approach to quantum computing with single photons and linear optics.

A cluster state is a network of entangled qubits and represents a universal state for quantum computing. Universal means that any quantum logic operation can be carried out on a sufficiently large and appropriately structured cluster state. These states arise when individual qubits are prepared in the superposition state $|+\rangle = (|0\rangle + |1\rangle)/\sqrt{2}$, where $|0\rangle, |1\rangle$ denote the computational basis states, and connected by applying a controlled-PHASE operation $|j\rangle|k\rangle \rightarrow (-1)^{jk}|j\rangle|k\rangle$ with $(j, k \,\epsilon\, 0, 1)$ between neighboring qubits, effectively generating entanglement, as we have already seen in Section 1.3.3.

But how can single- and two-qubit gates or even whole quantum circuits be simulated with these cluster states? To see this, we first focus on a particular single-qubit rotation and show how this can implemented by a simple circuit identity that is often known as one-bit teleportation [150]. Let's consider the following circuit diagram that describes this process[7]:

$$
\begin{array}{ll}
|\psi\rangle \quad\bullet\!\!-\!\!\boxed{H}\!\!-\!\!\boxed{\angle} & \text{``}m\text{''} \\
|0\rangle \quad\oplus\!\!-\!\!\!-\!\!\!-\!\!\!- & Z^m|\psi\rangle
\end{array}
\qquad (3.17)
$$

Here, the measurement is represented by a "meter" and it is always performed in the computational basis. "m" is the outcome of this measurement and hence takes the value 0 or 1. Depending on this value, we apply a Pauli Z (σ_z) operation to the other qubit. It is easy to show that the state of this qubit is identical to the input state $|\psi\rangle$, therefore we can say it was teleported through the circuit.

Next we translate the CNOT gate into the CZ gate, since the CZ gate also naturally occurs in the generation of cluster states. This can be done by applying Eqn. 3.15, i.e. by adding a Hadamard gates before and after the CNOT in the lower line. When we absorb the first Hadamard into the state of the ancilla ($|0\rangle \rightarrow |+\rangle$) and the second into the teleported qubit then the circuit becomes:

$$
\begin{array}{ll}
|\psi\rangle \quad\bullet\!\!-\!\!\boxed{H}\!\!-\!\!\boxed{\angle} & \text{``}m\text{''} \\
|+\rangle \quad\bullet\!\!-\!\!\!-\!\!\!-\!\!\!- & HZ^m|\psi\rangle = X^m H|\psi\rangle
\end{array}
\qquad (3.18)
$$

Here we used the identity $X = HZH$. Let's consider now we implement a single-qubit rotation around the Z axis by an angle α to the input qubit $|\psi\rangle$:

$$
\begin{array}{ll}
|\psi\rangle \quad\boxed{Z(\alpha)}\!\!\bullet\!\!-\!\!\boxed{H}\!\!-\!\!\boxed{\angle} & \text{``}m\text{''} \\
|+\rangle \quad\!\!-\!\!\!-\!\!\bullet\!\!-\!\!\!-\!\!\!- & X^m HZ(\alpha)|\psi\rangle
\end{array}
\qquad (3.19)
$$

Note that now the rotation $Z(\alpha) \equiv \exp(i\alpha Z/2)$ also appears on the output side of the circuit. This is analogous to remote state preparation. Since the rotation around the z-axis commutes with the CZ gate (they are both diagonal in the computational basis), we can also write:

$$
\begin{array}{ll}
|\psi\rangle \quad\bullet\!\!-\!\!\boxed{HZ(\alpha)}\!\!-\!\!\boxed{\angle} & \text{``}m\text{''} \\
|+\rangle \quad\bullet\!\!-\!\!\!-\!\!\!-\!\!\!- & X^m HZ(\alpha)|\psi\rangle
\end{array}
\qquad (3.20)
$$

This however is remarkable because we can reinterpret this diagram as an entangled state $|\Psi\rangle = \text{CZ}|\psi, +\rangle$, followed by a single-qubit measurement on the first qubit that performs the

---

[7]Parts of the following explanation of cluster state quantum computing are based on an excellent lecture given by P. Kok [150]

single-qubit gate $HZ(\alpha)$ on the state $|\psi\rangle$ of the second qubit! Also, although we measure the first qubit no quantum information is lost, instead it is teleported to the second qubit under the action of a known unitary transformation X and H.

The measurement that induces this state transfer is preceded by a single-qubit rotation followed by a Hadamard and is equivalent to a measurement along an axis given by α on the $X-Y$ plane of the Poincaré sphere.

An arbitrary rotation $R(\theta)$ on the Poincaré sphere can be implemented by concatenating rotations around the z-axis and Hadamard gates

$$R(\theta) = Z(\gamma)X(\beta)Z(\alpha) = H\,HZ(\gamma)\,HZ(\beta)\,HZ(\alpha) \tag{3.21}$$

where $X(\beta) \equiv \exp(i\beta X/2)$ and $H^2 = \mathbb{1}$. In circuit language, this becomes

$$\boxed{HZ(\alpha)} - \boxed{HZ(\beta)} - \boxed{HZ(\gamma)} - \boxed{H} \tag{3.22}$$

hence we can perform arbitrary single-qubit operations via concatenated measurements on an sufficiently large cluster state [150]:

$$\tag{3.23}$$

This circuit leaves us with the output state

$$|\psi_{\text{out}}\rangle = (X^m HZ(\gamma))\,(X^l HZ(\beta))\,(X^k HZ(\alpha))\,|\psi\rangle \tag{3.24}$$

The operators X^k, X^l, and X^m depend on the measurement outcomes, however we can get rid of them by commuting them through the Pauli gates and Hadamards. By using the relation $ZX = -XZ$ it is possible to show[8] that

$$Z(\beta)X = XZ(-\beta)\,, \tag{3.25}$$

which allows to rewrite Eqn. 3.24 in the following circuit form

$$- \boxed{HZ(\alpha)} - \boxed{HZ((-1)^k\beta)} - \boxed{HZ((-1)^l\gamma)} - \boxed{X^k} - \boxed{Z^l} - \boxed{X^m} -$$

This therefore gives rise to an adjustment of the measurement bases depending on the previous measurement outcomes[9], a process that is generally referred to as *feed-forward*. It results in a definite temporal direction in the computation hence the name "one-way model" of quantum computing[10]. Note that if we restrict ourselves, instead of an arbitrary input state $|\psi_{in}\rangle =$

---

[8]The prove goes as follows [150]: $Z(\beta)X = \sum_{n=0}^{\infty} \left(\frac{i\beta}{2}\right)^n \frac{Z^n}{n!} X = \sum_{n=0}^{\infty} \left(\frac{-i\beta}{2}\right)^n \frac{XZ^n}{n!} = XZ(-\beta)$.

[9]Note that every measurement depends at most on the previous measurement outcome.

[10]Remember that all the elements in the traditional circuit model are unitary operators, and therefore reversible.

$\alpha \ket{0} + \beta \ket{1}$ to an input state of the form $\ket{\psi_{in}} = \ket{+}$ which is intrinsic in the cluster, then an arbitrary single-qubit operation can be accomplished by an three-qubit linear cluster state and two measurements only (see Section 3.3.3, Fig. 3.5 and Chapter 5).

So far, we have not incorporated the feed-forward process that takes care of the actual measurement result during the computation. It is clear from Eqn. 3.24 that the desired output state is only obtained if the outcome of each measurement $s_j = 0, 1, \forall j = k, l, m$ is as desired, say $s_j = 0$. Due to the intrinsic randomness of the quantum measurement, it happens with equal probability that the measurement yields the unwanted result $s = 1$. In that case, well known Pauli-errors ($\sigma_x = -\boxed{X}-$) are introduced in the computation, and can be eliminated by adapting the measurement bases of subsequent measurements [151]. This will be discussed in more detail and with example circuits in Chapter 5.

It is important at this point to understand that we are able to process our quantum circuit and thereby our quantum algorithm deterministically, even though only local measurements and classical feed-forward procedures are employed, which are well within technological reach. The major difficulty is left to produce the highly entangled cluster state. However, since it is prepared before the actual computation, we can generate it off-line, i.e. we can use as many trials as we need to make sure we have succeeded with our task.

Also at this point, it makes sense to incorporate the single-qubit rotation $Z(\alpha)$ and the Hadamard gate H before each measurement (c.f. Eqn. 3.20) into the actual measurement basis $B(\alpha)$ by defining the following:

$$B_j(\alpha) = \{\ket{\alpha_+}, \ket{\alpha_-}\} \text{ with } \ket{\alpha_\pm} = (\ket{0} \pm e^{-i\alpha}\ket{1})/\sqrt{2} \tag{3.26}$$

where $\alpha \in [0, 2\pi]$ and j denotes the qubit. These measurements perform the actual quantum information processing, while measurements in the computational basis $\{\ket{0}_j, \ket{1}_j\}$ have the effect of disentangling, i.e., removing the physical qubit j from the cluster. This leaves a smaller cluster state and thus gives the ability to shape the cluster to the specific algorithm. Confer our discussion of cluster state properties in Section 1.3.3.

Let us now consider a two-qubit gate. For simplicity, we again first assume that the outcome of all measurements corresponds to $s = 0$, thus not requiring active compensation. The following circuit

$$\ket{\psi_{in}}_{a,b} \quad \begin{array}{c} \ket{+} -\boxed{HZ(\alpha)} - \bullet - \boxed{HZ(\gamma)} - \\ \ket{+} -\boxed{HZ(\beta)} - \bullet - \boxed{HZ(\delta)} - \end{array} \quad \ket{\psi_{out}}_{a,b} \tag{3.27}$$

is a two-qubit gate that implements the computation

$$\ket{\psi_{out}}_{a,b} = \left[H^a Z^a(\gamma) \otimes H^b Z^b(\delta)\right] U_{\text{CPHASE}}^{a,b} \left[H^a Z^a(\alpha) \otimes H^b Z^b(\beta)\right] \ket{\psi_{in}}_{a,b} \tag{3.28}$$

The correction rules applied in Eqn. 3.24 generalize in a straight forward manner to the two-qubit case.

$$\begin{aligned} U_{\text{CPHASE}}^{a,b} \left[\mathbb{1}^a \otimes X^b\right] &= \left[Z^a \otimes X^b\right] U_{\text{CPHASE}}^{a,b} \\ U_{\text{CPHASE}}^{a,b} \left[\mathbb{1}^a \otimes Z^b\right] &= \left[\mathbb{1}^a \otimes Z^b\right] U_{\text{CPHASE}}^{a,b} \end{aligned} \tag{3.29}$$

For an input state of $|\psi_{in}\rangle_{a,b} = |+\rangle_a |+\rangle_b$ the circuit generates entanglement between the logic qubits a and b depending on the measurement settings α, β, γ and δ. Note that the `CPHASE` gate between the logical qubits a and b is already inherently built into a two-dimensional cluster.

At this point it becomes important to understand that, while the actual quantum circuit acts on and processes the logical qubits a and b, the actual measurements and read out to implement the circuit are performed on physical qubits. This shall be discussed in more detail in the following.

Logical vs. physical qubit

The one-way quantum computer does not perform quantum logic on the individual qubits of the cluster state. In order to describe the computational circuit, we need to distinguish between the physical qubits, in our case the photons and their respective polarization state, which make up the cluster state and on which actual measurements are performed, and the logical qubits on which the actual computation is carried out [73]. Whenever not obvious, the latter will be denoted by the letter L in the subscript, e.g. $|+\rangle_L$. It is important to note that the entire information of the logical input state is initially stored in the multiparticle correlations of the cluster, with the individual physical qubits being completely undefined and therefore not carrying any information about the input at all. Single-qubit measurements on the cluster process the encoded logical input from one qubit to another analogous to remote state preparation and the output is finally transferred onto physical readout qubits, usually the remaining qubits of the cluster. A specific example is given in Fig. 3.3. Interestingly, while the entanglement between the physical qubits in general decreases as a result of the measurement sequence, the entanglement between encoded qubits may increase [119].

3.3.2   Summary of one-way quantum computing

This concludes our introduction of the one-way model of quantum computing. At this point it seems reasonable to again summarize the most important features of this model and give an overview and recipe of how to perform an arbitrary computation. The list below is complemented by Fig. 3.4 which gives a graphical interpretation of the summary.

Cluster state generation

- Cluster qubits are always initialized in the $|+\rangle$ state.

- All nearest neighbors are connected by applying `CPHASE` operations between them.

- The cluster is *shaped* to the specific algorithm by measurements in the computational basis $\{|0\rangle_j, |1\rangle_j\}$. These measurements that have the effect of disentangling, i.e., removing the physical qubit j from the cluster — therefore leaving a smaller cluster state.
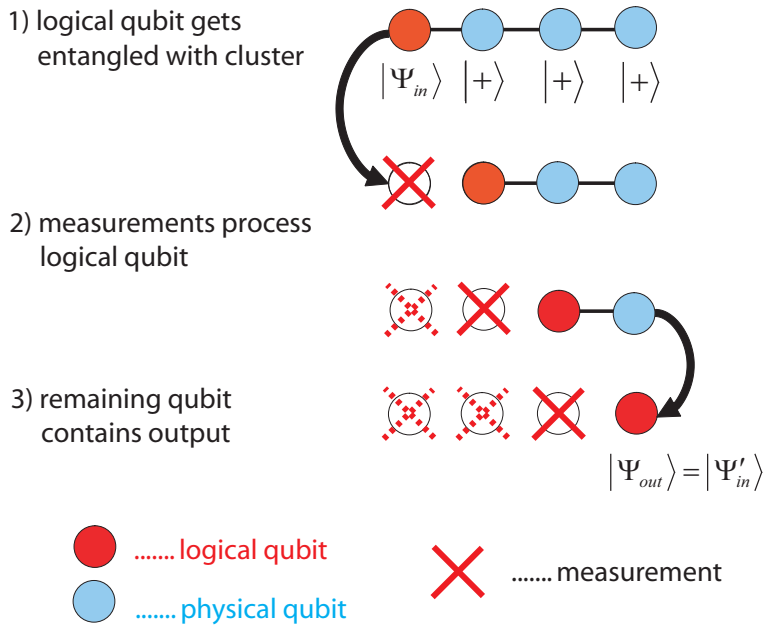
Figure 3.3: The distinction between logical and physical qubits in the general scheme of one-way quantum computation. The very left qubit denotes the logical input qubit, which is usually prepared to be in the $|\psi_{in}\rangle = |+\rangle_L$. The input qubit becomes entangled with the neighboring qubits via `CPHASE` operations, yielding a linear cluster state in this specific example. The input qubit is thus encoded non-locally into the cluster state. The encoded input qubit is processed by consecutive measurements from "left to right". The output of the computation is finally left on the physical readout qubit $|\psi_{out}\rangle_L$, whose state is obtained by measuring the following, subsequent qubit in the Z-basis, or by reaching the end of the cluster [119].

Processing information on a cluster state

- Logical qubits are mediated along one-dimensional cluster chains (i.e. the horizontal lines of the cluster).

- Measurements in basis $B(\alpha)$ perform a single-qubit gate of the form

$$R_z(\alpha)H|\psi_{in}\rangle \quad \Rightarrow \quad |\psi_{in}\rangle - \boxed{R_z^{(\alpha)}} - \boxed{H} - |\psi_{out}\rangle \tag{3.30}$$

- Two-qubit gates are implemented by vertical bonds connecting the one-dimensional (horizontal) cluster chains and are thus inherent in the cluster.
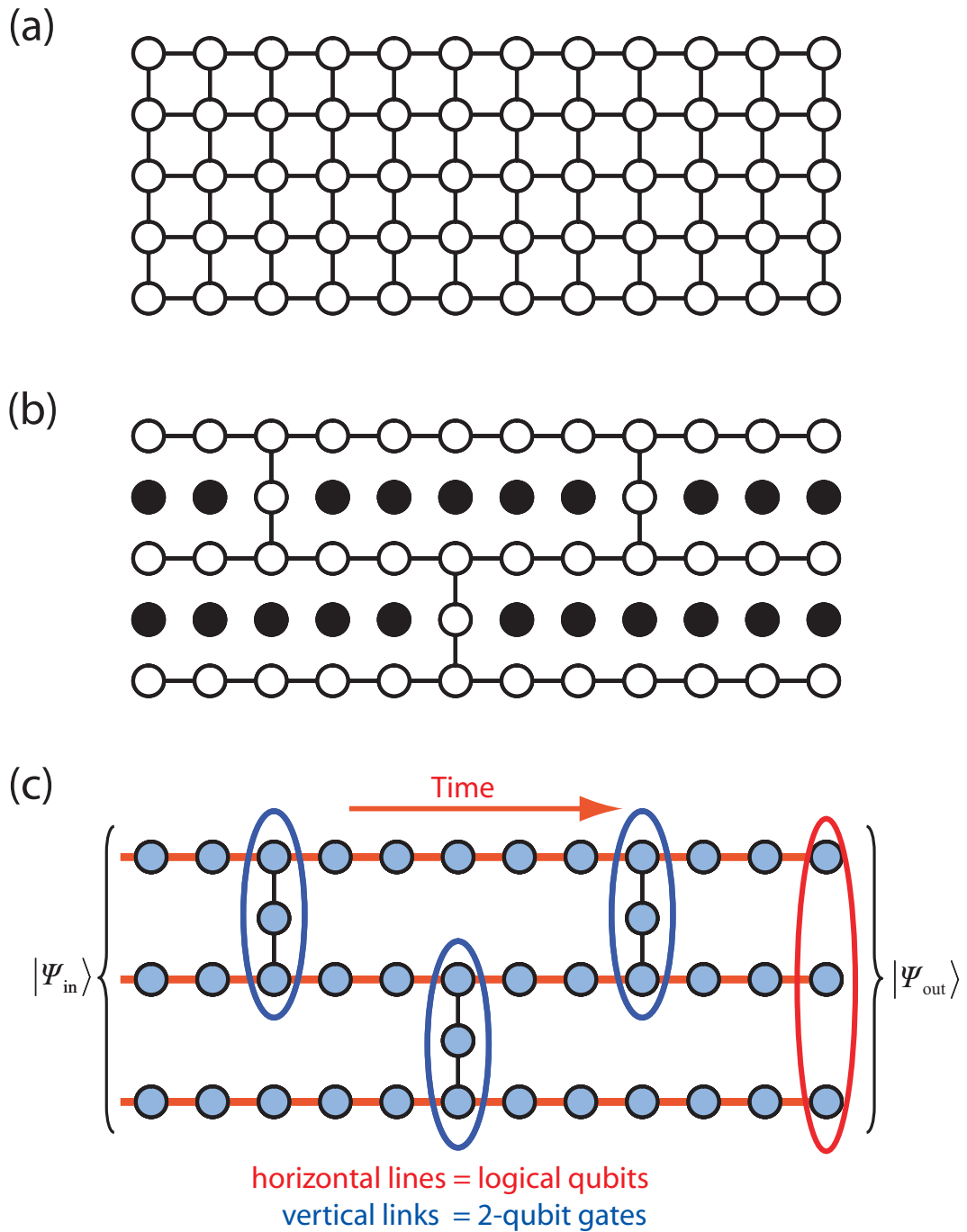
Figure 3.4: Recipe for one-way quantum computing on an arbitrary cluster state. a) Prepare 2D-cluster by initializing all qubits in $|+\rangle$ and entangle qubits by applying CZ gates to nearest neighbors. b) Remove unwanted qubits by performing Z-basis measurements, thereby shaping the quantum circuit. c) The actual computation proceeds via measurements in the X-Y plane of the Poincaré sphere and by feed-forwarding the results to adapt future measurement settings. Finally, the output is stored on the remaining qubits and read out by single-qubit measurements.

3.3.3   Quantum circuits with 4-qubit cluster states

Naturally one might ask at this point how feasible the one-way model is under practical, i.e. experimental considerations. At first sight, although the processing of information is largely simplified due to the single-qubit measurements, it seems very resource intensive, i.e. for every gate, even single-qubit ones, we require one physical qubit. For fundamental and proof-of-principle purposes it is interesting to know how large the cluster state resource has to be in order to demonstrate an universal set of quantum gates in the one-way model. The answer is quite surprising, namely it is sufficient to generate a linear cluster state of four qubits to simulate an arbitrary single-qubit operation and one two-qubit gate [73].

While we have already learned that a four-qubit linear cluster state is sufficient to implement an arbitrary single-qubit operation (Eqn. 3.23) it is not straightforward to see how two-qubit gates can be realized on this one-dimensional state. After all, we have learned that two-dimensional clusters are required for this purpose. The trick here is that a particular circuit that is to be implemented also depends on the order of the measurements performed. To be more precise, we can choose both qubits 2 & 3 as our logical input qubits, thereby *folding* the cluster state to shape a two-dimensional *horseshoe* structured cluster (see Fig. 3.5). Choosing both input qubits in the $|+\rangle_L$ state, the choice of measurement basis $B_2(\alpha)$ and $B_3(\beta)$ determines the output that is left on qubits 1 & 4 and also whether those become entangled or not — the basic action of an two-qubit gate. Also, by local Hadamard rotations and by swapping (i.e., relabeling) the physical qubits 2 and 3 a so-called four qubit *box* cluster can be generated out of the linear four-qubit cluster. An overview over the possible quantum circuits with linear four-qubit cluster states is presented in Fig. 3.5.

3.3.4   Experimental techniques for cluster state generation

Now that we have established the relevant theory, let us focus on the experimental techniques that can be employed to turn one-way quantum computing with photons into a reality. The vital single-qubit measurements that process the quantum information directly translate into polarization analysis in an arbitrary basis $B(\alpha)$ and has been discussed in detail previously (see Section 2.4.1). They are easily implemented using linear polarizers or polarizing beam splitters and do not constitute a challenge in the experiments.

Measurement based quantum computing is such an exciting alternative to conventional model because it shifts the difficulty of performing the dynamical unitary evolution of the quantum state during the computation to the generation of a sufficiently large cluster state. While the procedure is clear-cut in theory, there exist at least three different and distinct approaches in linear optical experiments that shall be briefly discussed in the following.

Realization of optical `CZ`-gate

The most intuitive and straightforward method to generate cluster states in the optical laboratory is to realize the essential two-qubit gate that is required to entangle the individual qubits in the cluster. In recent years there have been numerous proposals [152, 153] and experimental demonstrations of all-optical `CNOT` gates most notably by Pittman *et al.* [154, 155], O'Brien *et*

al. [133] and Gasparoni *et al.* [134] as well as Zhao *et al.* [156]. More recently, specific `CZ`-gates have been realized by Langford *et al.* [157], Hoffmann *et al.* [158] and Kiesel *et al.* [159]. Latter have also explicitly used this gate to generate four-qubit linear cluster states [74]. All of the above schemes are probabilistic and require postselection and deterministic single-photon sources to operate efficiently.

Making cluster states with fusion gates

The KLM-type optical quantum computing approach heavily relies on the well-known Hong-Ou-Mandel (HOM) effect [160] in which photon bunching occurs when two indistinguishable photons are incident on a 50:50 beamsplitter. This process generates entanglement in the photon number states[11]. The same interference effect can lead to entanglement in polarization if we replace the beamsplitter with a polarizing beamsplitter (`PBS`). To understand this consider two photons impinging on a `PBS` such as depicted in Fig. 2.3. When we erase polarization information in the output modes by 45° rotations and perform single-photon detection, we can construct so-called *fusion gates*. These turn out to be extremely useful for optical quantum computing since they effectively project onto an entangled state and can therefore be used to *fuse* two cluster states. There are two types of fusion gates, aptly named type-I and type-II [161]. In type-I, only one of the output ports is detected, while in type-II both output ports are detected. Because of this detection, if we want to create entanglement we cannot start with single photons. The basic building block that is to be used with fusion gates is a two-qubit cluster state or Bell state, e.g., $1/\sqrt{2}(|H,V\rangle + |V,H\rangle)$. Since fusion gates have not been employed in our experiments I refer the interested reader to [161, 95, 150] for more details. Experimentally, fusion gates have been realized and employed to build three-photon cluster states in an experiment by Zhang *et al.* [68].

A "straightforward" source of cluster states

The techniques discussed above are theoretically sound but already require several two-qubit (fusion) gates to generate even moderately large clusters of 3-5 qubits. Therefore it is legitimate to ask whether a more *straightforward* or *direct* method can be employed to circumvent many of the stringent experimental conditions that need to be met for such a concatenation of gates to work. As it turns out, there exists a clever method to generate four-qubit linear cluster states directly with the help of type-II non-collinear spontaneous down-conversion [73]. In this method that shall be explained in great detail in the following chapter the various single- and double-pair emission amplitudes of SPDC occurring in a single crystal that is pumped in a double-pass configuration are superposed to directly emit the four-qubit cluster into four distinct output modes of an optical interferometer.

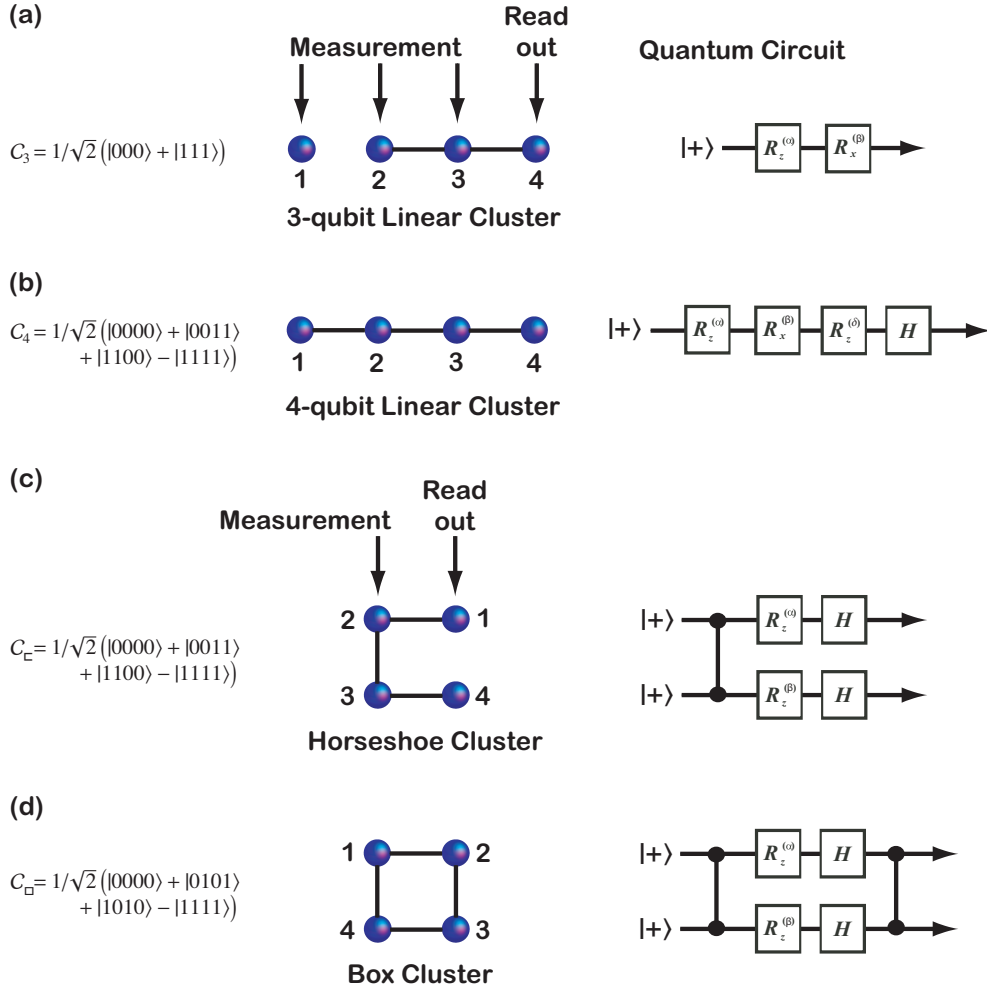[11]For a detailed explanation and derivation of this process see e.g. [150].

(a)

$C_3 = 1/\sqrt{2} \left(|000\rangle + |111\rangle \right)$

(b)

$C_4 = 1/\sqrt{2} \left(|0000\rangle + |0011\rangle + |1100\rangle - |1111\rangle \right)$

(c)

$C_{\llcorner} = 1/\sqrt{2} \left(|0000\rangle + |0011\rangle + |1100\rangle - |1111\rangle \right)$

(d)

$C_{\square} = 1/\sqrt{2} \left(|0000\rangle + |0101\rangle + |1010\rangle - |1111\rangle \right)$

Figure 3.5: Four-qubit cluster states and the quantum circuits they can implement. For the case of the linear clusters a) and b) consecutive measurements on the qubits (1), 2, and 3 will perform a computation as a series of one-qubit rotation gates. The encoded input state undergoes single-qubit rotations with controllable angles and the output is left on physical qubit 4. In contrast, the horse-shoe cluster c) and the box cluster d) perform both single-qubit and two-qubit gates, as indicated by the respective circuits. Both single- and two-qubit gates are essential for universal quantum computation. Note that here we have chosen the notation $R_z(\alpha)$ for single-qubit rotation around the z-axis. This is equivalent to the notation $Z(\alpha)$ that was previously used in this Section. We will encounter this new notation again in Section 3.3. Details about the experimental realization of the depicted cluster states follow in the subsequent Chapter(s). Fig. adapted from [73].

Chapter 4

Experimental all-optical one-way quantum computing

This chapter tries to bridge the gap between the theoretical concepts we have been developing so far and their actual experimental implementation. First I will briefly describe the basic outline of the (optical) setup and of the relevant equipment that is being used. A simplified scheme of the setup can be seen in Fig 4.1 and I will often refer to it in the following. Then I will give a detailed tutorial in how to efficiently align the setup so that the desired cluster state is produced with high quality. In the remainders of the chapter I give results on the characterization of the experimentally generated cluster state, which has been performed using quantum state tomography.

4.1 The cluster state setup

As already stated before, all experiments described in this Thesis require the generation of two-, three- and four-photon cluster states where the quantum information is encoded in the polarization state of the individual photons. The principal source for single and entangled photons in our experiment is the process of spontaneous parametric down-conversion (SPDC). In particular, we employ SPDC type-II in the non-collinear configuration, as already discussed in Sections 2.1 and 2.2.1. As SPDC is a spontaneous process, we have to ensure that variations in the creation time of the photons are smaller than their coherence time. The best way to do so is by limiting the interaction time of the pump laser with the PDC-crystal (BBO), which can be achieved by pulsing the pump laser (see Section 2.2.2).

In our experiments we use a laser system from the company Coherent, in particular a 10 W, 532 nm solid state laser, Verdi-V10, that pumps a mode-locked Ti:sapphire laser, Mira 900F, to generate ultra-short laser pulses of 200 fs at a central wavelength of 789 nm. The Mira produces an average output power of 2.3 W cw-averaged at a repetition rate of $\sim$76 MHz, which corresponds to a temporal separation of 13 ns in between subsequent pulses.

The near-infrared output of the Mira laser has to be up-converted to half the wavelength in order to allow for parametric down-conversion in the near-infrared where commercially available

single-photon detectors have their peak efficiency. This is done by focusing the output with a 40 mm lens onto a nonlinear LBO-crystal (2 mm, lithium triborate, LiB_3O_5), which is cut for type-I collinear second-harmonic generation (SHG). SHG converts a fraction[1] of the incident light, resulting in approximately 1 W of 394.5 nm blue light. Three subsequent dichroic mirrors[2] placed at 45° off normal incidence, separate the residual fundamental 789 nm light from the desired UV-light and direct the pump laser onto the SPDC-crystal (2 mm BBO - βbarium-borate). Due to imperfections of these mirrors some UV-light will still leak through, which, together with the near-infrared, is used for spectral measurements and adjustment of the laser system. Due to the birefringence of the LBO-crystal, the up-converted beam profile is elliptical, which can be corrected with the help of two cylindrical lenses, mounted perpendicular to each other. A Gaussian beam profile is essential for high-efficiency down-conversion [103, 162], and the right geometry of the pump light at the PDC-crystal can be verified in situ by a CCD-camera. Following the method developed by R. Kaltenbaek [163], we achieve a circular spot with a waist of roughly $300\mu m$ at the BBO crystal.

To generate the cluster states that serve as a resource for our one-way quantum computing experiments, we employ the "railway-cross" - scheme that was employed by our group in recent years [164, 43, 117]. This scheme and the basic setup which was used for all experiments, is shown in Fig. 7.3. The UV laser pulse makes two passages through a single BBO crystal which probabilistically emits entangled pairs into the forward-oriented pair of modes, a1 & b1, and the backward-oriented pair of modes, a2 & b2. To counter the effect of birefringence in the BBO crystal, the polarization in each mode is rotated by 90° with half wave plates (HWPs) and the photons pass through compensation crystals which erase transverse and longitudinal walk-off (c.f. Section 2.1). Final HWPs, one for each photon pair, and the tilt of the compensation crystals allow for the production of any of the four Bell states. These pairs are coherently combined and overlapped at the two PBSs by adjusting the position of the retroreflecting pump mirror $\Delta 1$ as well as of an additional mirror $\Delta 2$ in mode a1— thereby realizing a complex interferometer. The output modes of the PBS are coupled into single-mode fibers [162] that guide the photons to the detection stage where polarization analysis and, if necessary, fast active switching of the polarization can be implemented. Eventually, the photons are detected by single-photon counting modules (SPCM) and their electronic output signal amplified, processed and registered by a coincidence logic. This logic is configured and read-out by a personal computer. In the following as we will go along I will spend more time on each of the individual components described above.

The construction of the interferometric setup allows us to generate the required four-photon cluster state and, in general, can produce up to four photons which are entangled either in polarization or in in their spatial modes. To see this, consider the situation where the pump pulse creates exactly one photon pair of the entangled state $|\Phi^+\rangle$ during the two passes through the crystal.

The two possible emissions of only one single pair in either forward or backward direction

---

[1] The up-conversion efficiency in our experiment is approximately 40-45 %, depending on alignment and quality of the crystal.

[2] Dichroic mirrors consist of a dielectric layer which, when placed at the right angle, perfectly reflect UV-light while most of the remaining near-infrared light is transmitted.
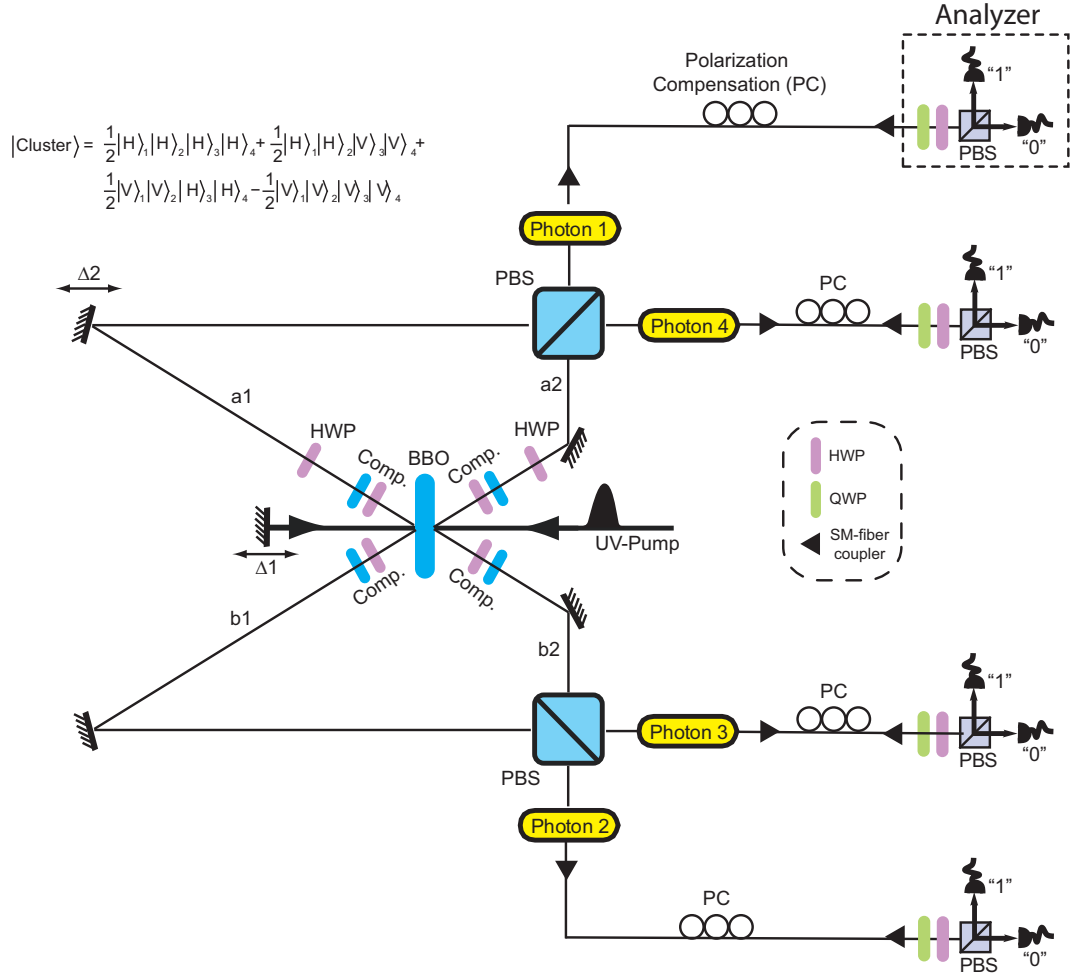
$$|\text{Cluster}\rangle = \frac{1}{2}|H\rangle_1|H\rangle_2|H\rangle_3|H\rangle_4 + \frac{1}{2}|H\rangle_1|H\rangle_2|V\rangle_3|V\rangle_4 +$$
$$\frac{1}{2}|V\rangle_1|V\rangle_2|H\rangle_3|H\rangle_4 - \frac{1}{2}|V\rangle_1|V\rangle_2|V\rangle_3|V\rangle_4$$

Figure 4.1: Schematic drawing of the setup used to generate the four-photon linear cluster state of Eqn. 4.5. The 200 fs UV laser pulse makes two passages through a single BBO crystal emitting entangled pairs into the forward-oriented pair of modes, a1 & b1, and the backward-oriented pair of modes, a2 & b2. To counter walk-off effect in the BBO crystal, half wave plates (HWPs) and compensation crystals are used. Additional HWPs, one for each photon pair, and the tilt of the compensation crystals allow for the production of any of the four Bell states. In our specific configuration, they are aligned such that $|\Phi^-\rangle$ and $|\Phi^+\rangle$ states are emitted in the forward and backward direction, respectively. These pairs are coherently combined at the two PBSs by adjusting the position of the retroreflecting pump mirror $\Delta 1$ as well as of an additional mirror $\Delta 2$ in mode a1. Lenses in modes a2, b2 just before the PBSs allow for mode-matching and aid in aligning the backwards pair. The output modes of the PBS are coupled into single-mode fibers that guide the photons to the detection stage. After proper polarization compensation (PC) polarization analysis is performed with a QWP, HWP and PBS. Eventually, the photons are detected by single-photon counting modules (SPCM).

is approximately described by the Hamiltonian [165]

$$H \propto \left(a_{1H}^\dagger b_{1H}^\dagger + a_{1V}^\dagger b_{1V}^\dagger \right) + re^{i\Delta\phi} \left(a_{2H}^\dagger b_{2H}^\dagger + a_{2V}^\dagger b_{2V}^\dagger \right) + h.c. \tag{4.1}$$

Here $a_{1H}^\dagger$ describes the creation operator that produces an horizontally polarized photon in the spatial mode a1, etc. and r denotes the relative probability of emission of photons into the modes a2 & b2 compared to modes a1 & b1. ϕ is the relative phase between the two emission possibilities and can be set by the pump mirror position[3] Δ1. Applying the Hamiltonian once to the vacuum state gives rise to a single-pair production and yields

$$H|0\rangle = \left(|H\rangle_{a_1} |H\rangle_{b_1} + |V\rangle_{a_1} |V\rangle_{b_1} \right) + re^{i\Delta\phi_2} \left(|H\rangle_{a_2} |H\rangle_{b_2} + |V\rangle_{a_2} |V\rangle_{b_2} \right) \tag{4.2}$$

which is, as expected, a superposition of a $|\Phi^+\rangle$ state in either way of emission direction. The same state can be written, in a different notation, as

$$\left| \Phi_{hyper}^+ \right\rangle \propto \left(|a_1\rangle |b_1\rangle + re^{i\Delta\phi_2} |a_2\rangle |b_2\rangle \right) \left(|H\rangle_a |H\rangle_b + |V\rangle_a |V\rangle_b \right) \tag{4.3}$$

where $|a_1\rangle|b_1\rangle$ and $|a_2\rangle|b_2\rangle$ denote the spatial modes of the photon pair. In this notation it is immediately clear that the photon pairs are entangled both in their polarization as well as in their spatial modes. Such a state is commonly referred to as a two-photon four-dimensional entangled state [165, 117, 166]. As we will see, it is of great importance to the experiments, especially for the initial alignment.

However, we are mainly interested in the simultaneous production of four entangled photons. The four-photon state that is produced by our source in the interferometric setup can be obtained by applying the Hamiltonian in Eqn. 4.1 twice to the vacuum:

$$\begin{aligned} H^2 |0\rangle &= \left[\left(a_{1H}^\dagger b_{1H}^\dagger + a_{1V}^\dagger b_{1V}^\dagger \right)^2 + r^2 e^{i2\Delta\phi} \left(a_{2H}^\dagger b_{2H}^\dagger + a_{2V}^\dagger b_{2V}^\dagger \right)^2 \right. \\ &\quad \left. + 2re^{i\Delta\phi} \left(a_{1H}^\dagger b_{1H}^\dagger + a_{1V}^\dagger b_{1V}^\dagger \right) \left(a_{2H}^\dagger b_{2H}^\dagger + a_{2V}^\dagger b_{2V}^\dagger \right) \right] |0\rangle \end{aligned} \tag{4.4}$$

This four-photon state obviously contains the situation where one photon occupies each spatial mode a_1, a_2, b_1, and b_2. However, it also has components of comparable magnitude with two photons each in the forward-oriented pair of modes, a_1 & b_1, or two photons each in backward-oriented pair of modes, a_2 & b_2. This is a direct consequence of the quasi-thermal nature of down-conversion: Considering two down-conversion sources, the probability that each source emits a pair is of the same order of magnitude as the probability that one of them emits four photons while the other does not emit any photons at all.

Usually, the latter situation which is also often called a *double-pair emission* is undesired in quantum optics experiments and causes unwanted spurious detection events. However in our scheme this emission amplitude actively contributes to the generation of the cluster state, which is one of the advantages of our scheme.

Remember that our goal is to create a four-photon linear cluster state of the form

$$\begin{aligned} |\Phi_{Cluster}\rangle &= \frac{1}{2} \left(|H\rangle_1 |H\rangle_2 |H\rangle_3 |H\rangle_4 + |H\rangle_1 |H\rangle_2 |V\rangle_3 |V\rangle_4 \right. \\ &\quad \left. + |V\rangle_1 |V\rangle_2 |H\rangle_3 |H\rangle_4 - |V\rangle_1 |V\rangle_2 |V\rangle_3 |V\rangle_4 \right), \end{aligned} \tag{4.5}$$

---

[3]The phase ϕ can be set arbitrarily with the help of a piezo positioning system that features a resolution of 25 nm.

in the spatial output modes 1, 2, 3, 4 of the PBSs with the setup at hand. In the following we will see how this can be achieved by clever engineering of the various SPDC emission amplitudes that are present in our setup configuration.

The preparation of the cluster state $|\Phi_{Cluster}\rangle$ is based on postselection, i.e the simultaneous emission of four photons and the detection of one and only one photon in each of the output modes 1, 2, 3, 4 of the PBSs (see Fig. 4.1 and [73]). The construction of the setup allows for four photon events to come from either two entangled pairs, one forward and one backward, or from double-pair emission into the modes a1 & b1 or a2 & b2. Remember that the PBS transmits horizontally-polarized light and reflects vertically-polarized light.

Postselection implies that after every single PBS, in each mode one photon has to be detected. If (a) the photons come from different input modes, both incoming photons must have the same polarization, or (b) they must have orthogonal polarizations when entering along the same input mode in order to be split up by the PBS (c.f. Fig. 2.3)).

If we align the SPDC source such that it produces into the forward pair of modes a $|\Phi^-\rangle_{a1b1}$ state, while simultaneously emitting a $|\Phi^+\rangle_{a2b2}$ state in the backwards direction, only the state

$$|\phi_{SP}\rangle \propto \frac{1}{2} \left(|H\rangle_1|H\rangle_2|H\rangle_3|H\rangle_4 - |V\rangle_1|V\rangle_2|V\rangle_3|V\rangle_4 \right), \tag{4.6}$$

results in a four-photon coincidence since condition (a) has to be fulfilled.

However, with equal probability, there is the chance that a double-pair is emitted in the forward direction, which will result in the four-mode contribution $-|H\rangle_1|H\rangle_2|V\rangle_3|V\rangle_4$ in the output modes of the two PBS; likewise, if the a double-pair is emitted in the backward modes a2-b2, we will end up with the four-mode contribution $|V\rangle_1|V\rangle_2|H\rangle_3|H\rangle_4$. These are actually the two terms that appear in Eqn. 4.4 and if we fix the position of the reflection mirror $\Delta 1$ then the amplitudes of these two four-mode contributions arrive at the two PBS simultaneously, and are thus in a coherent superposition

$$|\phi_{DB}\rangle \propto \frac{1}{2} \left(-|H\rangle_1|H\rangle_2|V\rangle_3|V\rangle_4 + e^{i2\Delta\phi_4}|V\rangle_1|V\rangle_2|H\rangle_3|H\rangle_4 \right). \tag{4.7}$$

The total state that is emitted by our setup is a superposition of all four terms that appear in Eqns. 4.6 and 4.7. Note that in order to produce the desired cluster state the phase of the double-pair emission $-|H\rangle_1|H\rangle_2|V\rangle_3|V\rangle_4$ has to be shifted by π. Fortunately this can be done using a HWP in one mode [73], where according to a rotation by an angle Θ the state after the PBSs evolves to $-\cos(2\Theta)|H\rangle_1|H\rangle_2|V\rangle_3|V\rangle_4$. Thus any HWP rotation larger than $\Theta = \pi/8 = 22.5°$ results in a sign flip. At the same time however, the Bell state $|\Phi^-\rangle_{a1b1}$ is rotated to $|\Phi^-\rangle_{a1b1} \rightarrow \cos(\Theta)|\Phi^-\rangle_{a1b1} + \sin(\Theta)|\Psi^+\rangle_{a1b1}$, where the amplitude of the desired state $|\Phi^-\rangle_{a1b1}$ is decreased by a factor of $\cos(\Theta)$. Thanks to the intrinsic property of the PBS only the amplitudes for the terms $|H\rangle_1|H\rangle_2|H\rangle_3|H\rangle_4 + |V\rangle_1|V\rangle_2|V\rangle_3|V\rangle_4$ are affected, while the Bell state $|\Psi^+\rangle_{a1b1}$ does not contribute to any four-fold coincidence after the PBS. The HWP rotation together with the ratio r of the relative probability of emission of photons into the forward and backward modes allow us to match the various emission amplitudes that contribute to the cluster state

$$\begin{aligned}
|\Phi_{Cluster}\rangle &= \frac{1}{2} \left(r\cos(\Theta)e^{i\Delta\phi_2}|H\rangle_1|H\rangle_2|H\rangle_3|H\rangle_4 + \cos(2\Theta)|H\rangle_1|H\rangle_2|V\rangle_3|V\rangle_4 \right. \\
&\quad \left. + r^2 e^{i2\Delta\phi_4}|V\rangle_1|V\rangle_2|H\rangle_3|H\rangle_4 - r\cos(\Theta)e^{i\Delta\phi_2}|V\rangle_1|V\rangle_2|V\rangle_3|V\rangle_4 \right) \tag{4.8}
\end{aligned}$$

if $\Theta > \pi/8$. That implies that $r > \cos(\pi/4) > \sqrt{2}$ in order for the amplitudes and phases to match up. In the experiments, typical emission rates of the forward- and backwards-emitted pair were 30000 s^{-1} and 10000 s^{-1} two-photon coincidences, respectively ($r = \sqrt{1/3}$). Taking this into account a numerical optimization yields that a `HWP` setting of approximately $27.5°$ results in the generation of the maximally entangled cluster state in Eqn. 4.5. Note that also the phase of the back-reflected pair $\Delta\phi = \Delta\phi_2 = \Delta\phi_4$ has to adjusted to a multiple of 2π and kept fixed during the experiment. This will be explained in the next section together with a brief alignment tutorial.

4.1.1   Alignment tutorial

The cluster state creation is based on the superposition of all the second order emission amplitudes of our SPDC process. Therefore we require quantum interference of the photons at the two central `PBS`s, as described and depicted in Fig. 2.3. This interference can only take place when the participating photons are indistinguishable in every degree of freedom. To select SPDC-photons of equal wavelength from the down-conversion, we employ 3 nm bandwidth interference filters. This also stretches their coherence length to approximately 700 fs ($\sim 110\mu m$), effectively longer than the pump pulse length which renders both entangled photon pairs indistinguishable in time, an important prerequisite for interfering photons from independent down-conversion processes, as was pointed out in Section 2.2.2 and Ref. [106]. An increase in coherence length is also desirable when matching the photon paths to equal length. The temporal delay between the photons can be varied by a delay mirror $\Delta 1$ mounted on a motorized translation stage as well as with an additional mirror $\Delta 2$. Single-mode fiber coupling after the `PBS` ensures that only photons propagating along a perfectly defined spatial mode[4] are selected, therefore allowing for high-fidelity interference. Also the small numerical aperture[5] of a single-mode fiber in combination with an achromatic microscope lens (f=14mm) assures that only photons within a small angular distribution emitted along the vertices of the cones are select, resulting in a high quality of the polarization entangled photon pairs.

Temporal overlap

To meet the condition of temporal overlap at the `PBS`, the two photons must arrive at their `PBS` within their coherence length to allow for interference. To achieve this we apply the following procedure [117, 166]: we first translate $\Delta 1$ in small steps to search for the position where the two photons in b1 and b2 have traveled the same path length. When two indistinguishable photons are incident on the beamsplitter, photon bunching also known as the two-photon Hong-Ou-Mandel dip is observed after the `PBS` [160]. To ensure indistinguishability, we insert polarizers at $45°$ into each of the modes b1 and b2 while performing polarization analysis in both output modes 3 and 4 of the `PBS` in the $+/-$ basis. The dip indicates the region of maximum interference and we denote it by p_b. Note however, that unlike in [160] here the

---

[4]The single- mode fibers only allow propagation of the Gaussian TEM00 mode and therefore serve as spatial mode filters.

[5]Single-mode fibers at 790 nm have a core diameter of approximately $5\mu m$.

photons are emitted in a pseudo-thermal state[6] [163], which results in a maximum dip visibility of only $V = 1/3$. In spite of the low expected dip visibility this technique suffices in practice to roughly find the position p_b.

Analogously, we can repeat the procedure for the opposite PBS and input modes a1, b1 and find the position p_a. Generally, p_a and p_b will not coincide — however we can fix $\Delta 1$ at p_b and move the mirror $\Delta 2$ by a distance $p_b - p_a$ to achieve simultaneous temporal overlap at both PBSs.

After this preliminary alignment, we can fine adjust the path lengths by employing the polarization-path entangled state from Eqn. 4.3. Therefore we remove the polarizers from the input modes and restrict our measurements to two-fold coincidence $+/-$ basis between the output modes 1 and 2 (or 3 and 4). Then a coincidence[7] will be produced by the two-photon four-dimensional state

$$|\Phi_{hyper}\rangle \propto \frac{1}{2} \left(|H\rangle_{a1} |H\rangle_{b1} + e^{i\Delta\phi_2} |V\rangle_{a2} |V\rangle_{b2} \right), \tag{4.9}$$

which is entangled in both path and polarization[8]. By scanning the position of $\Delta 1$ with an envelope-like curve can be observed for the two-fold coincidence (see Fig.4.3). Outside the coherent region, no interference occurs since $|H\rangle_{a1} |H\rangle_{b1}$ and $|V\rangle_{a2} |V\rangle_{b2}$ are distinguishable. The best visibility is obtained inside the coherent region, where perfect temporal overlap is achieved. Therefore we perform fine adjustment of the position of $\Delta 2$ and repeat the scan of $\Delta 1$ until the best visibility is obtained[9]. (see Fig.4.3).

Next, we have to set the phase $\Delta\phi$ to a multiple of 2π to generate the desired cluster state. For this purpose we fine scan the envelope center of Fig. 4.3, i.e the region of optimal temporal overlap, using the piezoelectric translation stage of the pump mirror $\Delta 1$. By setting the phase $\Delta\phi$ to a position where a maximum of two-fold coincidence in $|+\rangle_1 |+\rangle_2$ between modes 1 and 2 is observed, we ensure that ϕ_2 equals a multiple of 2π. At the same position we should then observe a minimum in the two-fold coincidence $|+\rangle_3 |+\rangle_4$ between modes 3 and 4, since we have aligned the SPDC to produce $|\Phi^-\rangle_{a1b1}$ and $|\Phi^+\rangle_{a2b2}$ states in the forwards and backwards direction, respectively. This is in general not the case due to birefringent effects in PBSs. Therefore the terms $|H\rangle_{a1} |H\rangle_{b1}$ and $|V\rangle_{a2} |V\rangle_{b2}$ accumulate a different phase ϕ_2' during their passage through the PBS when they exit in the modes 3 and 4.

To compensate for this in the experiment we can introduce an additional phaseshift in the output modes 3 and 4 [117, 166]. In practice we inserted QWPs at $0°$ which almost perfectly compensated the unwanted phase shifts [119]. After this compensation, the two coincidence

---

[6]This is due to the fact that we can not discern whether the two photons originated both from double-pair emission in either forward or backward direction, or whether one photon was emitted in either direction.

[7]This corresponds to the case where, after the pump pulse has passed through the BBO crystal twice, one and only one entangled pair is created. This entangled photon pair is thus emitted into a superposition of the mode pairs a1–b1 and a2–b2.

[8]This can intuitively be explained by following example: Analyzing in the $+/-$ basis erases the polarization information, therefore if we observe a coincidence it could have come from a forward-emitted pair that was horizontally polarized or by vertically polarized pair from the backward mode. These probabilities interfere at the PBS and give rise to the interference fringes in Fig. 4.3.

[9]Note that the right position of $\Delta 1$ can alternatively be found by measuring the four-fold polarization correlation in the $+/-$ basis. However, in the real experiment, this is very challenging due to the low four-fold coincidence rate.
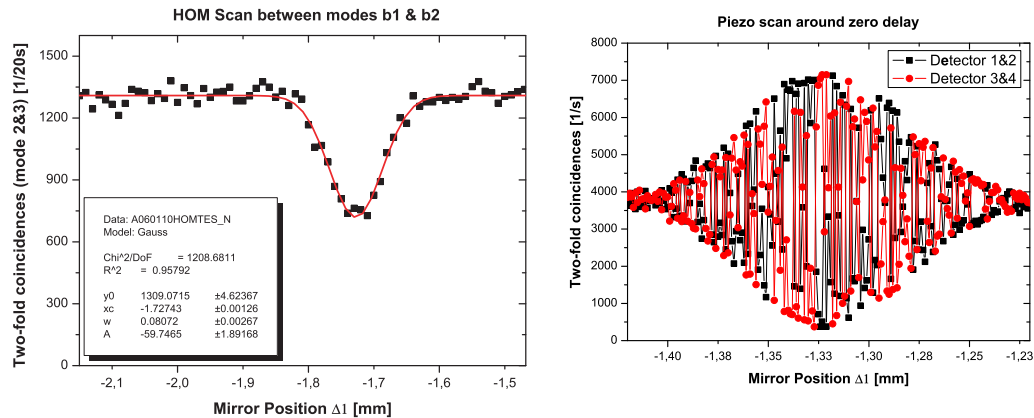
Figure 4.2: Achieving perfect temporal overlap. First we move $\Delta 1$ and and perform a Hong-Ou-Mandel dip scan to find the position p_a where the two photons in a1 and a2 travel the same path length (see main text for details). The left plot shows a typical experimental result of such a scan. Note that the limited dip visibility of 30% is due to the fact that we are dealing with a pseudo-thermal source which would lead to a maximum expected visibility of $V = 1/3$. Nevertheless this suffices to roughly find the position of temporal overlap. The same procedure is repeated for the modes b1 and b2, thereby finding p_b. By fixing $\Delta 1$ at p_b and moving the mirror $\Delta 2$ by a distance $p_b - p_a$, we can thus roughly achieve temporal overlap. To fine tune the temporal delay we scan the position of $\Delta 1$ with a step size of 1μm while measuring the two-fold coincidences between the output modes 1 & 2, 3 & 4 in the $+/-$ basis. The resulting envelope-like curve for the two-fold coincidences is shown in the right plot. Fine adjustment of the position of $\Delta 2$ and and repeated scans of $\Delta 1$ are performed until the best visibility is achieved ($\sim 90\%$ in our experiment)

.

sine-curves of 1 & 2 and 3 & 4 exhibit perfect anti-synchronization (i.e. they differ by a factor of π), i.e. $\phi_2 = \phi_2' + \pi$, see Fig. 4.3.

Setting the piezo-system again to a position where a maximum of two-fold coincidences in $|+\rangle|+\rangle$ ($|-\rangle|-\rangle$) is observed in modes 1 & 2 (3 & 4) achieves $\phi_2 = \phi_4 \propto 2\pi$ and therefore leads to the generation of the maximally entangled cluster state of Eqn. 4.5.

In order to maintain a fixed phase throughout the course of the experiments, perfect phase stabilization on the scale of the wavelength is required. Therefore the setup was built onto a aluminum platform to avoid sound resonance and a feedback air-condition avoids thermal expansion of the interferometer. Furthermore a plastic housing surrounding the setup prevents air flow [117]. During the experiments we also use the two-fold coincidences between modes 1 & 2 as a phase monitor allowing us to keep the phase stable for several hours.

Polarization compensation

Single-mode fibers offer the benefit that the photons remain in a perfectly defined spatial mode which not only allows high-fidelity interference as discussed above but also facilitates their
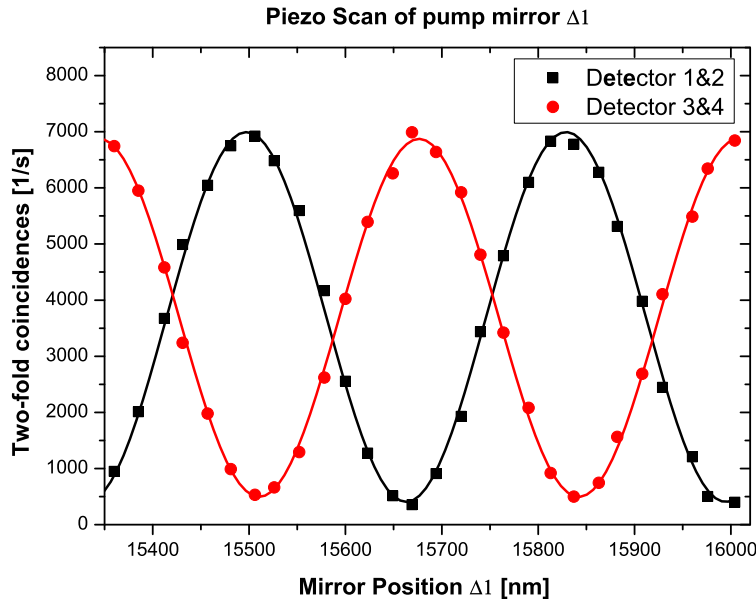
Piezo Scan of pump mirror Δ1

Figure 4.3: Fine scan around the region of zero delay by translating $\Delta 1$ using the piezoelectric translation stage. After proper birefringence compensation, the two-fold coincidence curves $|+\rangle_1 |+\rangle_2$ between modes 1 and 2, and $|+\rangle_3 |+\rangle_4$ between modes 3 and 4 exhibit perfect anti-synchronization. By setting the piezo to a peak in the coincidences we ensure that ϕ_2 is a multiple of 2π.

distribution. In our experiment we fiber-couple the photons to guide them to our analysis and feed-forward stage. This stage consists of four polarization analyzers each consisting of a `QWP` followed by a `HWP` and `PBS` whose outputs are multimode fiber-coupled to single-photon detectors. For more details concerning the polarization analyzers see Section 2.4.1. The feed-forward apparatus will be decribed in Chapter 5.

While the single-mode fibers come in handy for the distribution of photons, stress-induced and, in general, randomly distributed birefringence in optical fibers leads to rotations of the photon's polarization during their propagation. These rotations need to be actively compensated since otherwise the polarization analyzer would not perform polarization measurements in the desired basis. For the active compensation we use so-called Polarization Controllers[10], which deliberately squeeze and twist the fibers in a controllable way such that the unwanted rotations can be undone. The polarization controller implements a tunable wave plate via an actuator (e.g. screw), which presses the fiber and induces birefringence. The strength of the birefringence can be controlled by turning the screw in or out, and the axis of the birefringence is adjusted by rotating the screw mount — effectively realizing an all fiber Babinet-Soleil compensator.

To compensate for any fiber induced polarization rotation, we proceed as follows: First horizontally aligned polarizers are inserted into the modes 1,2,3 and 4 just after the main setup `PBS`s and the polarization analyzer is prepared to project in the H/V basis (c.f. Table 2.1). Then

---
[10] We use in-line PolaRITE™-Controllers F-POL-IL manufactured by Newport.

the polarization controllers are tuned such that all the light exits at the corresponding horizontal port of the analyzer. However successful compensation in one basis does not automatically imply universal polarization compensation, since any point on the Poincaré-sphere[11] is defined by two angles θ and φ (see Fig. 1.2). Therefore polarization compensation has to be performed for two orthogonal bases, such as the H/V- and +/− basis. The compensation in the +/− basis is performed independently from the H/V basis by rotating a `HWP` that succeeds a `QWP` oriented at 45°. The `HWP` is rotated as long until maximum polarization contrast is achieved at the analyzers. Employing this technique typical contrasts of 100:1 could be obtained. Since the single-mode fibers were taped down to the optical table, upholstered by foam, the polarization compensation turned out to be very stable and did not require readjustment during the experiments.

Detection stage

Silicon Avalanche Photo Diodes, or Si-APD for short, are most suitable for the detection of single photons at our selected wavelength of 789 nm because of their high quantum efficiency in this regime. In our experiment, we use Perkin Elmer Single Photon Detector Modules (SPCM AQ4C Four Channel Counting Module) with less than 500 dark counts per second. These are silicon avalanche photon detectors which have an overall detection efficiency of approximately 40-45%. The semiconductor silicon is operated at 20 Volts above breakdown voltage, called the Geiger-mode, so that the energy of a single incident photon triggers a electron "avalanche", that is further amplified and converted to a 35 ns wide TTL pulse of 2.5 Volts (minimum) height in a 50 Ω load. There is a "dead time" of 50 ns in between pulses and the modules require a +5 Volt power supply.

The electronic output signals of the APDs are fed into a coincidence logic were the signals are registered and processed. The logic is capable to register and store up to 64 coincidence patterns composed of up to 12 input signals. The coincidence window, within which two or more incoming signals are considered to be coincident, can be varied in steps of 1.56 ns. In the experiment we adjusted it to be less than 6 ns to ensure that photons generated in subsequent pump pulses cannot lead to a coincidence event. Finally the logic is read-out by a personal computer over a USB connection.

4.1.2 Summary: How to align the setup

Aligning the interferometric setup shown in Fig. 4.1 is by far not a straightforward task. Both intersection lines of the down-conversion have to be coupled efficiently into single-mode fiber to obtain high quality polarization entangled photon pairs while at the same the spatial and temporal overlap at the two `PBS` has to be accomplished. In the following I give a brief summary of the detailed alignment tutorial I presented above. I hope that future researchers find it helpful in aligning the setup.

1. Provided that the laser is already mode-locking and the upconversion crystal is properly aligned (i.e tilted) and positioned after the focusing lens, start aligning the cylindrical

---

[11]One might think of this polarization compensation procedure as trying to match the respective Poincaré-spheres of the qubits such that they become identical.

lenses by closely following the procedure explained in [163]. Choose the focus position of the UV-light at the position of the backreflection mirror and aim for a circular beam waist of approximately 2-300μm.

2. Roughly prealign the fibercouplers of the setup by shining with visible laser light in the reverse direction onto the SPDC crystal. The right opening angle of the SPDC emission ($\sim 3°$) can be set by positioning irises in the beampath.

3. Block the backwards SPDC emission of the BBO crystal. Walk the dichroic mirrors until some down-conversion signal is picked up by the fibercouplers. Continue walking the mirrors or start walking all four fibercouplers.

4. Once coincidences and a good polarization contrast in H/V ($\sim$50:1) is achieved in the forward pair, set the Bell state ($|\Phi^-\rangle$) by properly rotating the additional `HWP` in mode a1 and tilt the compensation crystal until a good contrast in $+/-$ basis is achieved (usually 30:1). Note that the `PBS` of the setup can analyze in the $+/-$ basis when preceded by a `HWP` set to an angle of $\pi/8$.

5. Align the backwards pair by first blocking the forward emission. Then proceed by walking both the mirrors and lenses in the backwards arm a2, b2. Do not touch the fibercouplers as those are already aligned for the forward emission. Again set the desired Bell state ($|\Phi^+\rangle$) analogously to Point 4.

6. Scan the backreflection pump mirror $\Delta1$ to find the HOM dips in both arms a1, b1 as well as in a2, b2. Once found, note the position of the dips (denoted by p_a and p_b) and translate the mirror $\Delta2$ by the amount $p_a - p_b$.

7. Again scan pump mirror $\Delta1$ around the region of overlap with a step size of 1μm — the envelope shaped curve is observed for two-fold coincidence in $+/-$ basis in e.g. modes 1& 2. Improve visibility by fine-adjustments of $\Delta2$ and repeated scans.

8. Compensate the additional phaseshifts of the `PBS` by inserting proper birefringent elements (crystals, waveplates) in the output modes 3 and 4. Perform fine scans with the piezo-system around the center of the envelope curve. Vary the strength of the birefringence until the two coincidence sine-curves of 1 & 2 and 3 & 4 exhibit perfect anti-synchronization (i.e. they differ by a factor of π).

9. Perform short measurements and slightly vary Θ of the `HWP` in mode a1 to achieve equal four-fold coincidences for the individual terms appearing in Eqn. 4.8. Additionally fine tune fiber couplers to achieve equal two-fold coincidence rates in modes 1 & 2 and 3 & 4.

10. Set the correct phase for the cluster state by setting $\Delta1$ with the piezo to a maximum of the two-fold coincidence in $+/-$ basis in e.g. modes 1& 2.

4.2 Characterization of the cluster state

Once we have properly aligned the optical setup we are of course interested in the quality of the experimentally generated state. Due to various imperfections the state will have a non-unit fidelity, i.e. overlap, with the ideal cluster state given in Eqn. 4.5.

The most precise estimation of the fidelity can be performed by reconstructing the density matrix of the experimental state. This is done by performing quantum state tomography, whose theory has been explained in detail in Section 2.4.2.

4.2.1 State tomography

Since we are dealing with a four-qubit state this implies we have to base the density matrix reconstruction on a set of 256 local measurements, i.e. all combinations of $\{|0\rangle, |1\rangle, |+\rangle, |R\rangle\}$ for the individual qubits [120]. However, since our polarization analysis stage gives access to both outcomes of a measurement, we can break this number down to 81 measurement settings, since we are recording both the H and V outcomes simultaneously. Therefore we are able to record all 1296 combinations of $\{|0\rangle, |1\rangle; |+\rangle, |-\rangle; |R\rangle, |L\rangle\}$, which results in a so-called "over-complete" state tomography [157]. This over-complete state tomography has the experimental advantage of providing a more precise state estimation and significantly smaller error bars. Using the maximum-likelihood technique developed in [120, 167] and discussed in Section 2.4.2 we can reconstruct the density matrix. The experimentally obtained density matrix ρ of our cluster state has a typical fidelity of $\mathcal{F} = \langle \Phi_{Cluster} | \rho | \Phi_{Cluster} \rangle = 0.62 \pm 0.01$ with the ideal four-qubit cluster[12]. There are several different influences that are responsible for a non-unit fidelity of the experimental state. Mainly, obtaining a higher fidelity is limited by higher order SPDC emissions as well as by partial distinguishability of the photons that interfere at the PBS. Also, phase instability during the lengthy process of state tomography and non-ideal optical elements employed in the setup, such as the birefringence inducing PBSs decrease the fidelity value. However, a fidelity of $\mathcal{F} = 0.62$ is well-above the limit $\mathcal{F} = 0.5$ for any biseparable four-qubit state [168] and therefore demonstrates the presence of genuine four particle entanglement in the produced state. A plot of the ideal as well as the experimental density matrix can be found in Fig. 4.5.

4.2.2 Entanglement properties of projected states

Cluster states feature the unique property that projective measurements on at least $N/2$ qubits are required to completely disentangle the cluster state, i.e. they exhibit a high entanglement persistency P_e (see Section 1.3.2 and [15]). In the case of four qubits these measurements can be performed on two different types of qubit pairs, depending on the measurement basis. If we want the residual state to be maximally entangled, Z-basis measurements on either qubits 1 & 2 or 3 & 4 can be performed. Alternatively, we can perform X-basis measurements on qubits 1 & 3, 1 & 4, 2 & 3 or 2 & 4. For demonstration purposes, we restrict ourself here

---

[12]The error bar of this result was estimated by performing a 100 run Monte Carlo simulation of the whole state tomography analysis, with Poissonian noise added to the count statistics in each run [120].
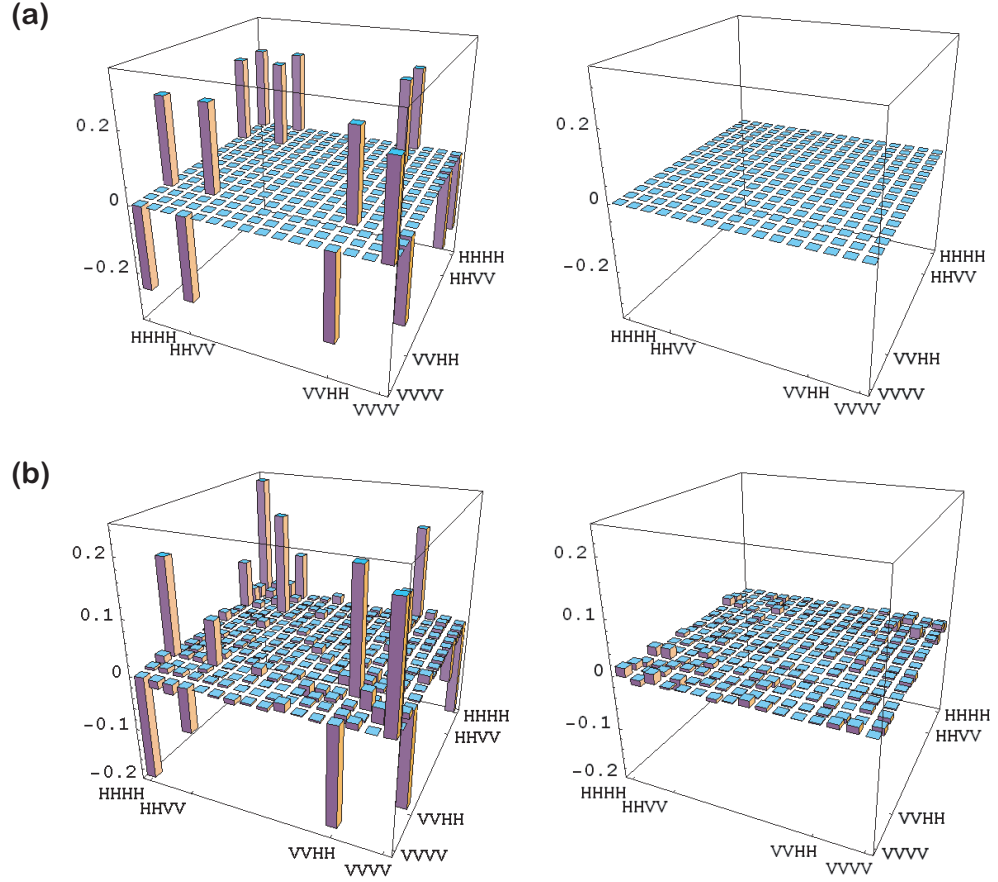
Figure 4.4: Density matrix plots of the four-qubit cluster state with the real (left) and imaginary (right) parts of the matrix. In a) the ideal cluster state plots are shown while b) gives the tomographic reconstructed experimental density matrix ϱ. The experimental state exhibits the desired characteristic correlations which show up as coherences (i.e. off-diagonal contributions) between the main diagonal cluster terms HHHH, HHVV, VVHH and VVVV. The experimental density matrix was reconstructed using a maximum likelihood technique based on 1296 polarization projection measurements, each acquired within a time window of 500 s. The decrease in coherence of the HHVV term is likely due to higher order pair emission which is more pronounced in the forward direction of the setup as well as imperfect interference of the photons at the PBS. Nevertheless we compute a fidelity (i.e. state overlap with the ideal cluster state) of $\mathcal{F} = \langle\Phi_{Cluster}|\varrho|\Phi_{Cluster}\rangle = 0.62 \pm 0.01$ which is well-above the limit $\mathcal{F} = 0.5$ for any biseparable four-qubit state.

exemplarily to Z-basis measurements[13]. Note that in this case, only identical measurement results (i.e. parallel polarizations) lead to the projection onto an entangled state. Particularly, projections of qubits 1 & 2 onto $|HH\rangle_{12}$ ($|VV\rangle_{12}$) result in the maximally entangled Bell state

---

[13]In Chapter 8, Fig. 8.4(b) we show the resulting density matrix when qubit 1 & 4 are measured in the X-basis. In this case we find a state fidelity of 0.74 ± 0.02 with the ideal, expected state $|\Phi_C\rangle_{23} = 1/\sqrt{2}(|0,+\rangle + |1,-\rangle)_{23}$.
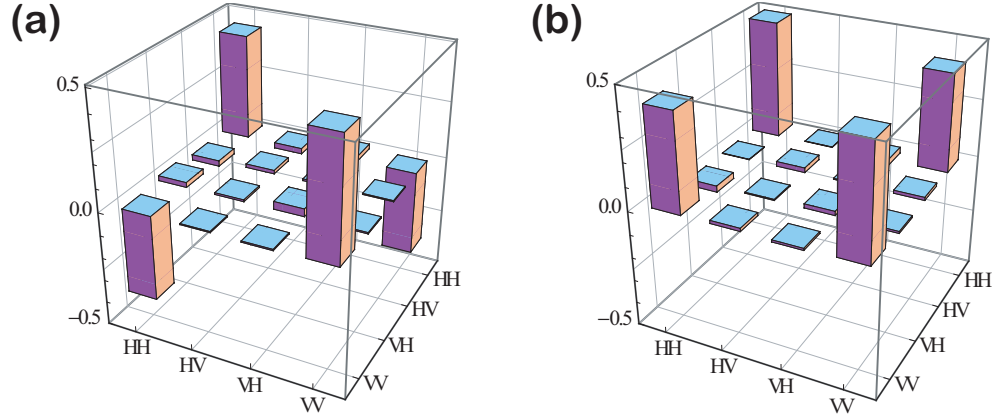
Figure 4.5: Experimentally observed four-fold count rates in the computational basis, i.e. $Z_1 Z_2 Z_3 Z_4$ or H/V (left plot), as well as in the $+/-$ basis (right plot). Ideally, in the H/V basis, only the term corresponding to HHHH, HHVV, VVHH and VVVV should be occupied, with all others zero. In the $+/-$ basis, all outcome combinations should occur with equal probability in the ideal case (the corresponding height is denoted by the dashed black line). The deviations from the ideal are largely due to higher-order emissions from the SPDC, which have different effects on the various detector combinations.

$|\Phi^+\rangle_{34}$ ($|\Phi^-\rangle_{34}$). Likewise, if we choose the measurements to be performed on qubits 3 & 4 we obtain $|HH\rangle_{34} \rightarrow |\Phi^+\rangle_{12}$ ($|VV\rangle_{34} \rightarrow |\Phi^-\rangle_{12}$).

In order to analyze the residual states we perform quantum state tomography and reconstruct the density matrices of the remaining qubit pairs after the described projective measurements. This allows to determine the fidelity as well as various entanglement measures. Two exemplary density matrices together with their respective fidelity and entanglement measures are shown in Fig. 4.6. The projected states feature a good qualitative agreement with the ideal, expected states and hence demonstrate that our cluster state indeed possesses the desired entanglement properties.

Figure 4.6: Real parts of the density matrices of the residual, entangled states after Z-basis measurements on qubits 1 & 2 and 3 & 4 of the four-qubit linear cluster state. In a) qubits 1 & 2 were measured to be in $|VV\rangle_{12}$ resulting in a highly entangled $|\Phi^-\rangle_{34}$ Bell state. The fidelity with the ideal, expected state is $\mathcal{F} = 84 \pm 1.6\%$ and the tangle was computed as $\tau = 0.55 \pm 0.05$. Similarly, in b) qubits 3 & 4 were measured to be in $|HH\rangle_{34}$ thereby projecting the remaining qubits onto a $|\Phi^+\rangle_{12}$ Bell state. In this particular case we extract a fidelity of $\mathcal{F} = 89.3 \pm 1.3\%$ and the tangle was computed as $\tau = 0.69 \pm 0.05$ from the reconstructed density matrices. Furthermore, our reconstructed density matrices imply a maximum CHSH Bell parameter [169, 170] of $S=2.46\pm0.05$ and $S=2.60\pm0.03$, for a) and b) respectively, which is clearly above the $S = 2$ upper limit for local realistic theories [35]. Noise on real and imaginary parts are comparable for both matrices.

Chapter 5

High-speed LOQC using active feed-forward

In this chapter I will describe an experiment that, based on the recent successful demonstration of one-way quantum computing [73] in our research group, realizes the required implementation of active feed-forward and error-correction in real time on a 4-photon cluster state. This constitutes a proof-of-principle demonstration of *deterministic* quantum computing and therefore conceptually presents a crucial step towards realizing scalable optical quantum computing. Also from a fundamental point of view our work shows that it is indeed possible to build a deterministic quantum computer which uses both entanglement and the intrinsically random measurement outcomes of quantum mechanics as an essential feature.

For the sake of a clear and self-contained presentation, I will first briefly recall the basic concepts of quantum information processing on linear cluster states that are already found in Section 3.3. Then I will generalize on these working principles to also account for undesired measurement results that require feed-forward techniques to adapt subsequent measurement settings and give explicit single- and two-qubit operations as an example. After this theoretical introduction I will bridge the gap from theory to experiment and discuss the technical requirements and experimental realization of feed-forward techniques before presenting the results showing that one-way quantum computing using fast-active feed-forward is possible with gate times of less than 150 ns [18].

5.1   Introduction

Single qubit measurements are essential in cluster state quantum computing. The shape of the cluster state and the nature of these measurements, i.e. the order of measurements and the individual measurement bases determine the algorithm that is computed. The input state $|\psi_{in}\rangle$ in our demonstrations is always initialized as $|+\rangle_L$. It is important to note that the entire information of the input state is initially stored in the multi-particle correlations of the cluster, with the individual physical qubits being completely undefined and therefore not carrying any information about the input state. In this sense, namely that properties of individual subsys-

tems are completely undefined, the cluster state is a maximally entangled state. Well-known examples include 2-qubit Bell states and 3-qubit GHZ states. Single qubit measurements on the cluster process the encoded input from one qubit to another analogous to remote state preparation. In principle, two basic types of single-particle measurements suffice to operate the one-way quantum computer. Measurements in the computational basis $\{|0\rangle_j, |1\rangle_j\}$ have the effect of disentangling, i.e., removing the physical qubit j from the cluster. This leaves a smaller cluster state and thus gives the ability to shape the cluster to the specific algorithm. The measurements which perform the actual quantum information processing are made in the basis $B(\alpha) = \{|\alpha_+\rangle, |\alpha_-\rangle\}$, where $|\alpha_\pm\rangle = (|0\rangle \pm e^{-i\alpha}|1\rangle)/\sqrt{2}$ with $\alpha \in [0, 2\pi]$. The choice of measurement basis determines the single-qubit rotation[1], $R_z(\alpha) = \exp(-i\alpha\sigma_z/2)$, followed by a Hadamard operation, $H = (\sigma_x + \sigma_z)/\sqrt{2}$, on the input state ($\sigma_x$, σ_y, σ_z, being the Pauli matrices).

$$R_z(\alpha)H|\psi_{in}\rangle \quad \Rightarrow \quad |\psi_{in}\rangle \longrightarrow \boxed{R_z^{(\alpha)}} \boxed{H} |\psi_{out}\rangle \tag{5.1}$$

The order and choices of these measurements determine the unitary gates that are implemented and therefore the algorithm that is computed. Remember that logical input states are by construction always $|\psi_{in}\rangle = |+\rangle_L$ unless the cluster is part of a larger cluster state. Rotations around the z-axis can be implemented through the identity $HR_z(\alpha)H = R_x(\alpha)$ so that two consecutive measurements on a linear 3-qubit cluster can rotate the input state to any arbitrary output state on the Poincare-sphere (c.f. Fig. 3.5)

$$R_z(\alpha)HR_z(\beta)H|\psi_{in}\rangle = R_z(\alpha)R_x(\beta)|\psi_{in}\rangle \quad \Rightarrow \quad |\psi_{in}\rangle \longrightarrow \boxed{R_z^{(\alpha)}} \boxed{R_x^{(\beta)}} |\psi_{out}\rangle \tag{5.2}$$

Up until now, we have not incorporated the actual measurement result in our analysis. Eqn. 5.1 only holds if the outcome of the measurement s is as desired, say $s = 0$. Due to the intrinsic randomness of the quantum measurement, however, it happens with equal probability that the measurement yields the unwanted result $s = 1$. In that case, a well known Pauli-error ($\sigma_x = \boxed{X}$) is introduced in the computation, so that the single measurement in basis $B_j(\alpha)$ rotates the qubit to:

$$R_z(\alpha)H\sigma_x|\psi_{in}\rangle \quad \Rightarrow \quad |\psi_{in}\rangle \longrightarrow \boxed{R_z^{(\alpha)}} \boxed{H} \boxed{X} |\psi_{out}\rangle \tag{5.3}$$

As we have learned in Section 3.3.1, Eqn. 3.25 these Pauli X errors can be eliminated by adapting the measurement bases of subsequent measurements. In the following, let us consider the general case of a single-qubit operation by taking into account the feed-forward rules. If we choose consecutive measurements in bases $B_1(\alpha)$ and $B_2(\beta)$ on physical qubits 1 and 2 of a 3-qubit cluster, then we rotate the encoded input qubit $|\psi_{in}\rangle$ to the output state

$$|\psi_{out}\rangle = \sigma_x^{s_2}HR_z((-1)^{s_1}\beta)\sigma_x^{s_1}HR_z(\alpha)|\psi_{in}\rangle = \sigma_x^{s_2}\sigma_z^{s_1}R_x((-1)^{s_1}\beta)R_z(\alpha)|\psi_{in}\rangle \tag{5.4}$$

which is stored on qubit 3. The measurement outcome, $s_i = \{0, 1\}$, on the physical qubit i determines the measurement basis for the succeeding qubit and indicates any introduced Pauli errors that have to be compensated for. This idea can schematically be depicted as a circuit

---

[1]Note that the notation $R_z(\alpha)$ is equivalent to the notation $Z(\alpha)$ that was previously used in Section 3.3.

diagram:

$$(5.5)$$

Cluster   Error Correction
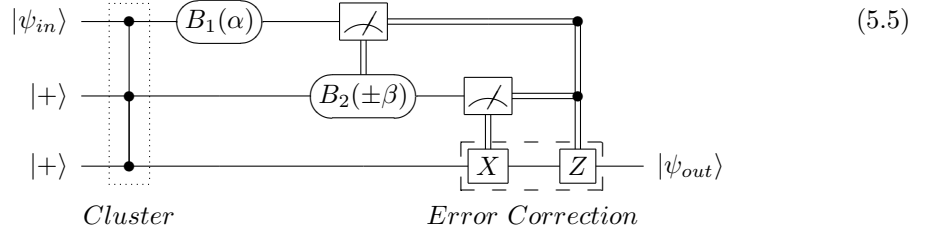
Single wires represent quantum channels, while double lines denote classical communication. The circles in front of the measurement meters show the measurement basis. Note that this circuit is almost identical to the one presented in Eqn. 3.23, however only requires a 3-qubit cluster state. This is because here we restrict ourselves to the specific logical input state $|\psi_{in}\rangle = |+\rangle_L$.

No error correction is required for the specific case where the outcomes of the first and second qubit are $s_1 = s_2 = 0$ and hence, as expected,

$$|\psi_{out}\rangle = R_x(\beta)R_z(\alpha)|\psi_{in}\rangle. \qquad (5.6)$$

However, if the outcome of the second qubit is $s_1 = 1$ ($s_2 = 0$) the measurement basis of the third qubit has to be changed from $B_2(\beta)$ to $B_2(-\beta)$ and finalized by a Pauli error correction, i.e. σ_z on the output qubit, to get the desired output of the computation. This yields

$$|\psi_{out}\rangle = \sigma_z R_x(-\beta)R_z(\alpha)|\psi_{in}\rangle \qquad (5.7)$$

Similar corrections are required in the cases when the third qubit's outcome is $s_2 = 1$ ($s_1 = 0$) and hence

$$|\psi_{out}\rangle = \sigma_z R_x(\beta)R_z(\alpha)|\psi_{in}\rangle. \qquad (5.8)$$

Finally, if an unwanted projection occurs to both qubits, ($s_1 = s_2 = 1$), two Pauli errors, σ_z and σ_x, have to be compensated for on qubit 3 yielding

$$|\psi_{out}\rangle = \sigma_x \sigma_z R_x(-\beta)R_z(\alpha)|\psi_{in}\rangle. \qquad (5.9)$$

This is summarized in the following table:

Outcome Qubit 1	Outcome Qubit 2	Basis Adaptation	Error Correction
$s_1 = 0$	$s_2 = 0$	no: $B_2(\beta)$	no
$s_1 = 0$	$s_2 = 1$	no: $B_2(\beta)$	σ_z
$s_1 = 1$	$s_2 = 0$	yes: $B_2(-\beta)$	σ_x
$s_1 = 1$	$s_2 = 1$	yes: $B_2(-\beta)$	$\sigma_x\sigma_z$

Let us now consider a two-qubit gate. For simplicity, we again first assume that the outcome of all measurements corresponds to $s = 0$, thus making no active compensation necessary. However, the correction rules developed in Eqn. 3.29 can be applied in a straight forward

manner. If we choose to perform measurements on the physical qubits 2 and 3 of a four-qubit linear cluster (as in Fig. 3.5) in the basis $B_2(\alpha)$ and $B_3(\beta)$, we effectively implement the following circuit

$$|\psi_{in}\rangle_{a,b} \quad \begin{array}{c} |+\rangle \longrightarrow \bullet \boxed{HZ(\alpha)} \\ |+\rangle \longrightarrow \bullet \boxed{HZ(\beta)} \end{array} \quad |\psi_{out}\rangle_{a,b} \tag{5.10}$$

which is a two-qubit gate with the output

$$|\psi_{out}\rangle_{a,b} = H^a Z^a(\alpha) H^b Z^b(\beta) U_{\texttt{CPHASE}}^{a,b} |\psi_{in}\rangle_{a,b} \tag{5.11}$$

For an input state of $|\psi_{in}\rangle_{a,b} = |+\rangle_a |+\rangle_b$ the circuit generates entanglement between logic qubits a and b. This is one of the strengths of cluster state quantum computing! Single- and two-qubit gates can be implemented by the same resource (in this case a one-dimensional linear cluster) by just changing the order and sequence of measurements. The CPHASE gate between the logical qubits a and b is already inherently built into the cluster. In total, the circuit of Eqn. 5.10 performs a CPHASE gate followed by the usual single-qubit rotations and Hadamard gate for both qubits.

Experimentally, feed-forward can only be achieved by recording both measurement outcomes simultaneously, $s_i = \{0, 1\}$. The recent photonic realization of a one-way quantum computer [73] employed single-port polarizers, which are, although sufficient to demonstrate the working principle, not suited for this purpose. Simultaneous recording of the measurement results can be achieved with polarizing beamsplitters (PBSs), preceded by half- and quarter-wave plates to chose arbitrary measurement bases. The basis of the measurements can be adapted by employing fast-switching and low-loss electro-optical modulators (EOMs), which, depending on the applied voltage, change the photon's state of polarization and therefore the measurement basis of the analyzer. Analogously, error-correction can be performed on the output qubit if the EOMs are aligned to apply σ_x and σ_z rotations, respectively.

In an experimental implementation of this scheme, the individual photonic qubits must be delayed just long enough so that the classical feed-forward process can be carried out, i.e., that an individual outcome can adapt the measurement basis for the next measurement. The most rudimentary "quantum memory" that can be used for such purpose is a single-mode fiber of a specific length, which has negligible photon loss over moderate distances. Every single feed-forward process includes detection of a photon, processing of the measurement result and finally switching of the modulator to adapt the measurement basis in real time and/or performing error correction on the output qubit. A major advantage of optical quantum computation is the achievable high speed of the gate operation. Various types of EOMs achieve low-loss and high contrast switching with fidelities above 99%. Switching times are well below 100 ns when combined with custom built drivers and such devices have successfully been implemented in early demonstrations of feed-forward control [171, 172, 173, 174]. Currently available logic boards and single-photon detectors have response times of around 10 ns and 30 ns, respectively, so that feed-forward cycles of less than 150 ns seem experimentally feasible. This time-scale corresponds to a single-mode fiber delay line of approximately 30 m. A gate time of 150-300 ns for one computational step is about two orders of magnitude faster than achievable in other

physical realizations of quantum computers such as in ion-traps [135] or in NMR [175].

5.2 Implementation of the feed-forward apparatus

In this Section, we will give a detailed account of the technical devices required for the implementation of the feed-forward apparatus and present the results of its characterization. While feed-forward techniques have been previously realized in a different context [171, 172, 173, 174], the system at hand here is optimized for quantum computation.

The feed-forward apparatus required for the demonstrations of deterministic single- and two-qubit operations on a four-photon cluster state consist of three custom-built EOMs (to perform the error correction) and of fast electronic logic boards and single-photon detectors. Together they allow for gate operations on the order of 150 ns, as we will see. While the feed-forward operations are carried out, the remaining photons are delayed in optical fibers.

The rest of this Section is structured as follows. First we describe the EOMs (i.e. Pockels cells) and their custom-built drivers - giving details about their electronics - and the self-designed, fast logic boards and their relevance in the feed-forward circuit. Then we present experimental results characterizing the performances of the EOMs, in particular at the single-photon level. Finally we discuss possible improvements of the feed-forward system before we discuss the actual quantum computing experiment in the following Section.

5.2.1 Technical realization

In order to implement the feed-forward system, drivers for the Pockels cells are required that are not only fast but whose characteristics are also very reproducible. Additionally, to decide which Pockels cells to switch - depending on previous measurements outcomes - we need fast switching logics.

Pockels cells and their high-voltage switches

The Pockels effect, being the lowest order electrically induced refractive-index changing effect, works accurately and at comparatively low voltages (compared with Kerr cells) with short response times (typically less than 10 ns [100]). We use commercially available Pockels cells based on *KD*P* (potassium dideuterium phosphate, *Cleveland Crystals Inc.*, type *QX1020*). Those crystals have an aperture diameter of 9.25 mm, a capacitance of 6 pF (at 1 kHz) and a 10%-90% risetime of 0.8 ns. With such crystals the voltage required to obtain a full phase shift of π between the 2 principal polarizations at our working wavelength of 789 nm is about 6-7 kV. In order to apply such a voltage on a Pockels cell within just tens of nanoseconds, fast switching electronics (drivers) as well as suitable high-voltage supplies are required.

Our Pockels cell drivers (custom-built by *Bergmann Messgeräte*) include single or double push-pull switches whose maximal repetition rates are as high as 10 and 100 kHz, respectively (see Fig. 5.1). The push-pull devices have some restrictions imposed by their electrical circuits: The time between an on and off event (i.e. the effective on-time) for an individual push-pull

switch must not be much shorter than 50 ns in order to not damage the device, limiting the minimum on-time window duration. For a double push-pull driver, there is no such restriction since both included circuits only have to switch once each in order to get an effective on-off cycle. After this, the switch requires a few μs to fully recharge again. Not allowing for this dead time results in an unstable operation characteristic. Therefore, an electronic circuit ("splitter box") acts as a filter for the trigger signals, monitoring the aforementioned timing restrictions for each Pockels cell driver. If a trigger occurs during the dead time, the signal will not get routed to the driver, but instead a "veto" signal is sent to the data acquisition system. In addition, the splitter box generates a suitable on-off scheme for the double push-pull device. Also note that, because ion wandering effects can occur and damage the KD*P crystals if it is operated in a continuous fashion, on-times should not exceed a few μs.

Fast switching logics

For active feed-forward applications it is necessary to perform a real-time analysis of the photon detection events since their outcomes set the electro optical modulators acting on the remaining photons [18]. A block diagram of the logical combination required to perform deterministic single-qubit operations in one-way quantum computing is shown in Fig. 5.2. In our experimental implementation and in the following, a $|0\rangle$ state corresponds to $|H\rangle$, i.e. a horizontally polarized photon, while the state $|1\rangle$ denotes $|V\rangle$, a vertically polarized photon. Moreover, when per-
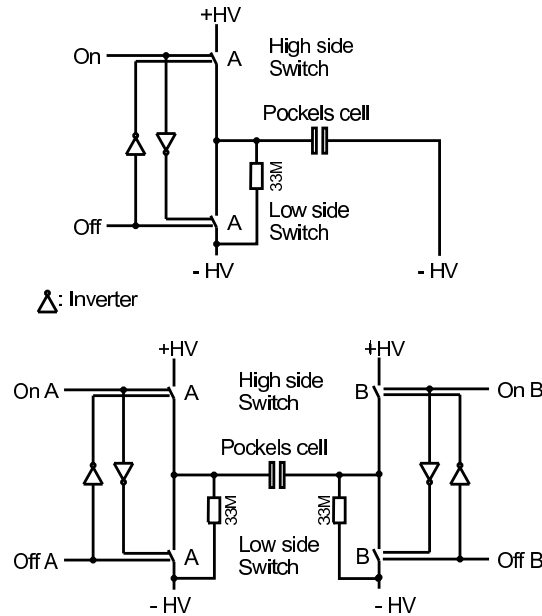
Figure 5.1: Electronic schematics of the single- (up) and double push-pull driver (down). High voltages (HV) and Pockels cells are indicated. In order to perform an on-off cycle using a single push-pull driver, the included switch (type Bergmann pp7d) has to be activated twice. In the case of a double push-pull driver, both included switches (type Bergmann pp7c) have to be switched just once.
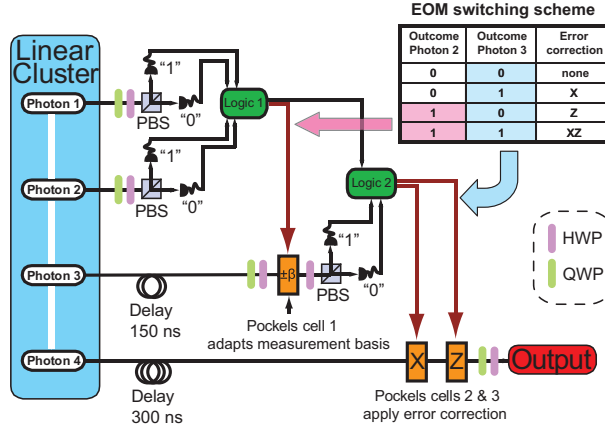
Figure 5.2: Overview of the switching scheme for the Pockels cells used to perform deterministic single qubit preparation. Depending on the measurement outcome for photon 2 (after successfully disentangling photon 1 from the linear cluster state), the measurement basis for photon 3 has to be adjusted (i.e. finding a "1"-outcome in the measurement of photon 2, Pockels cell 1 has to be activated for the third photon, cf. table in the upper-right corner). After measurement of photon 3, a final error correction has to be applied on the output photon (X=σ_x, Z=σ_z, Y=XZ=$\sigma_x\sigma_z$ or none). σ_x corresponds to exchanging state $|0\rangle$ with $|1\rangle$ and vice-versa and σ_z to a phase shift of π between states $|0\rangle$ and $|1\rangle$. Pockels cell 1 is driven by a double push-pull device, cells 2 & 3 by single push-pull devices.

forming measurements in the $B(\gamma) = \{|\gamma_+\rangle, |\gamma_-\rangle\}$ basis (defined as $|\gamma_\pm\rangle = (|0\rangle \pm e^{-i\gamma}|1\rangle)/\sqrt{2}$), a projection onto state $|\gamma_+\rangle$ will be denoted as a "0"-outcome (desired outcome - no correction necessary) while a projection onto state $|\gamma_-\rangle$ will be denoted as a "1"-outcome (undesired outcome - correction required). For example, if the measurement of photon 1 leads to a projection onto $|\gamma_+\rangle$ (thereby disentangling photon 1 from the linear four-qubit cluster [73, 18]), and finding a projection for the second photon onto state $|\alpha_-\rangle$ (instead of the desired $|\alpha_+\rangle$-state), the measurement basis of photon 3 has to be adapted, i.e. changing it from $|+\beta\rangle$ to $|-\beta\rangle$, which is done by a σ_{x3} operation (i.e. exchange of the state $|0\rangle$ and $|1\rangle$ of photon 3) and a combination of waveplates (cf. Fig. 5.2). If after that, a projection of photon 3 onto state $|\beta_-\rangle$ occurs, the polarization of the remaining photon has to be changed by a σ_{z4} operation (additional phase shift of π between states $|0\rangle$ and $|1\rangle$) followed by a σ_{x4}. The full logical functions for triggering the Pockels cells in the experiment is given in Table 5.2.1.

Since the overall delay time is crucial, it is necessary to design a logic circuit that operates as fast as possible. In order to realize throughput delays of less than 10 ns, we utilize the fastest available digital logic electronics, the ECLinPS™ family. The elements have propagation delays of about 1ns per element. Standard coincidence detection circuits based on TTL (transistor logic) or FPGAs (field programmable gate array) only achieve a signal propagation delay of about 100 ns. The logic circuit units provide two-fold combinations of the four input signals A,B,C,D as (A and D), (B and C) as well as ((A and D) or (B and C)) and the OR combination of the two-fold signals. The overall insertion delay of the units is only 7 ns. Using two units in

Outcome qubit 2	Outcome qubit 3	Logical functions for triggering the Pockels cells
0 @ α	0 @ β	PC 1=0, PC 2=0, PC3=0
0 @ α	1 @ β	PC1=0, PC2=(0PH2 AND 1PH3), PC3=0
1 @ α	0 @ $(-\beta)$	PC1=1PH2, PC2=0, PC3=(1PH2 AND 0PH3)
1 @ α	1 @ $(-\beta)$	PC1=1PH2, PC2=(1PH2 AND 1PH3), PC3=(1PH2 AND 1PH3)

Table 5.1: The logic function that actually triggers the Pockels cells 1, 2 and 3 (PC1, PC2, PC3) is shown here. The measurement results of the photons are denoted as 0PH2, 1PH2, respectively, for the 0 and 1 measurement outcomes of photon 2, and likewise for photon 3. In addition, in the real experiments all logical functions are in coincidence with detection of the previous photons 1, 2 (and 3).

combination realizes the required switching logic (see Fig. 5.2).

The circuit details of the coincidence logic are shown in Fig. 5.3, 5.4 and 5.5. The electronics is based on positive-emitter-coupled-logic (PECL), where VCC = +5V, VTT = VCC-2V, and every PECL output is terminated by 50 Ohm resistors into VTT. The input pulses coming from detectors or other logic stages are TTL levels (2.5 V into 50 Ohm termination), and are shortened with a pulse former to 1-2 ns. The internal pulse width leads to the coincidence window of about 1 ns. The output coincidence pulses must be prolonged to about 100 ns, so they can be suitably processed as TTL pulses by the subsequent data acquisition software.

5.2.2 Characterization of Pockels cells and their drivers

We characterized the performance of the Pockels cells and their drivers electrically by capacitive measurements as well as optically by measuring the switching fidelity with laser light and at the single photon level by employing a SPDC source of time-correlated photons.

High-voltage switches

Capacitive measurements have been performed by measuring the induced voltage of a probe head placed between the electrodes of an attached Pockels cell. We use a function generator (SRS DS345) to simultaneously trigger the Pockels cell drivers and an oscilloscope. We measured a delay-time of approx. 47 ns, which is the time until a stable voltage is applied to the Pockels cell (cf. Fig. 5.6). Series of capacitive measurements show a very reproducible behavior with jitter below 2 ns.
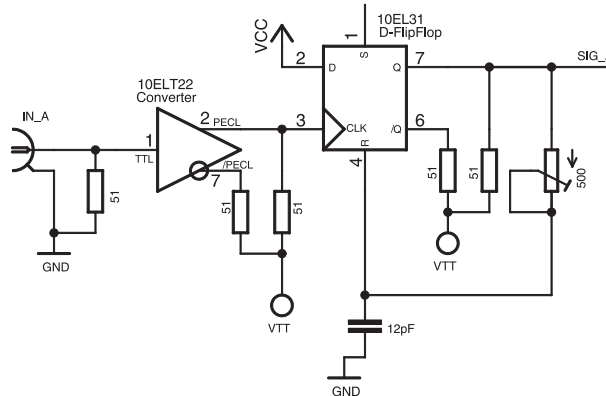
Figure 5.3: The input stage constitutes a TTL/PECL converter (10EL31) and a Monoflop for pulse shaping. The Monoflop is based on a D-Flipflop (10EL31) with a feedback from the output to the reset input with an adjustable resistor-capacitor combination. When the Flipflop senses a positive edge, it will generate a short pulse of about 1-2 ns.
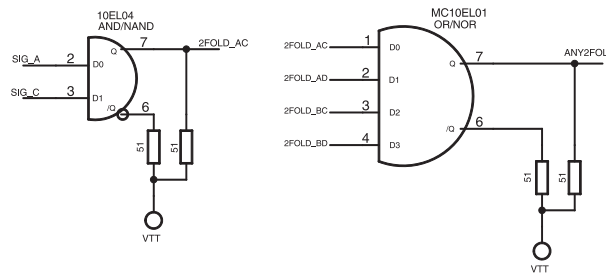

Figure 5.4: (Left) The two-fold coincidence logic (shown is the example for "A and C"). (Right) The OR gate for one out of the four two fold logics. The circuits are based on standard ECLinPS boolean elements.
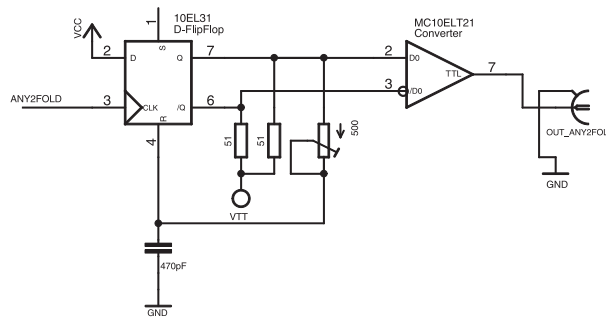
Figure 5.5: The output stage for the coincidence signals. These must first be prolonged to a useful pulse width, which is achieved with a Monoflop, based on a 10EL31, to generate a pulse width of about 100 ns. This PECL-level pulse is converted to TTL levels for output and further use in the experiment.

Optical characterization

Straightforward optical measurements of our Pockels cells show a transmittance of more than 96 % (including AR coating) at 830 nm, for all incoming polarizations.

Contrast and reproducibility

In order to minimize imperfections in the course of the computation, high contrast and reproducibility are essential for a feed-forward stage. Therefore we place the cell between two orthogonal polarizers (horizontal and vertical), with the Pockels cell's principal axis forming an angle of 45° with the polarizers' axes. Measuring with a cw-diode laser at 830 nm, we typically achieve a contrast exceeding 500:1, where the contrast (or extinction ratio) is defined as the light intensity measured in a certain polarization after the Pockels cell over the orthogonal one (which was originally fed into the stage). Furthermore, we record the performance of a Pockels cell as a function of time - indicating the temporal stability of the system. A single push-pull switch driver is used for these measurements and the right plot of Fig. 5.6 shows 181 subsequent measurement traces recorded over 1 second. The temporal stability of succeeding switching events also agrees with the capacitively measured ones and shows a very low jitter of less than 2 ns. This reproducibility is not dependent on the applied voltage. By comparing capacitive and optical measurements, we are able to infer a Pockels cell crystal response time of less than 5 ns.

Switching fidelity for single photons

Eventually the Pockel cells have to be used at the single photon level. In order to characterize their performance in this regime, we use a BBO type-II down-conversion setup [103, 176] (cw pumped at 405 nm) as a source of single photons, where one of the two downconverted photons acts as a trigger for the Pockels cell in the optical path of the other photon (see Fig. 5.7). In order to compensate for the various electronic delays, the other photon is delayed in an optical single mode fiber loop whose length is 35 m (approximately 175 ns). Finally the coincidence events between the trigger event and the detection of the second photon are measured, yielding a coincidence rate of about 600 Hz with the single count rate being approximately 20 kHz.

The switching fidelity is measured by feeding horizontal / vertical polarized photons through the Pockels cell stage and detecting them behind the Pockels cell in the different ports of a fiber-coupled polarizing beam-splitter (PBS) oriented in the H/V basis. The results are shown in Fig. 5.8 and 5.9, where the coincidence count rate at each output of the PBS is plotted versus the Pockels cell voltage. The good agreement of the measured data with sinusoidal fits shows the linearity of the phase with the voltage being applied and the high peak switching contrast demonstrates the good performance of these devices. The switching contrast has been calculated as the ratio of photons detected having the polarization orthogonal to the input polarization divided by the number of photons detected in the input polarization.

Finding similar measurement results as in Fig. 5.8 for arbitrary input polarizations shows that the Pockels cells are capable of applying the desired phase shifts at the single photon level.

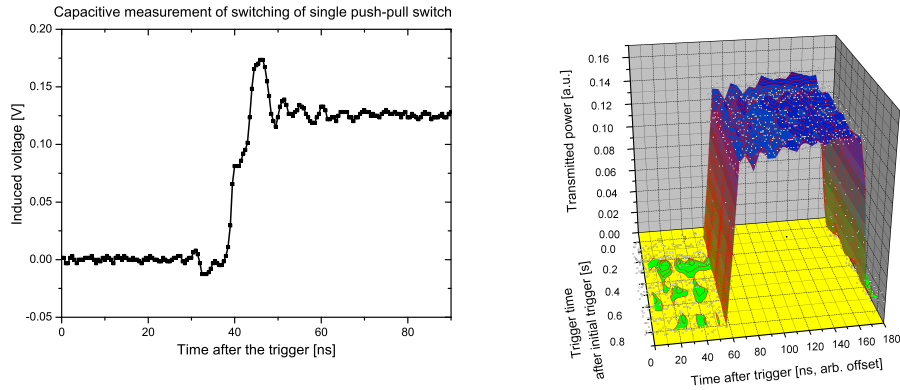Interestingly, the achievable switching contrast is dependant on the duration of the on-time

Figure 5.6: Left plot: Capacitive measurement (performed using a probe head, placed close to the Pockels cell) of the voltage signal of a single push-pull switch Pockels cell driver. From this plot we can infer a response time of ~5 ns (the relative height of the overshooting is decreasing with an increasing voltage applied). After a delay time of approximately 47 ns, a sufficiently stable voltage across the Pockels cell is achieved.

Right plot: Optical measurement of the temporal stability of succeeding switching events measured with cw IR laser light at 830 nm. Laser light is fed onto a Pockels cell put in between two crossed polarizers, with the polarizer's axes forming an angle of 45° with the Pockels cell's principal axes. The light intensity after the second polarizer is monitored using a photodetector. During the Pockels cell's on-time window, light is shining onto the photodetector. Note the low jitter (< 2 ns).
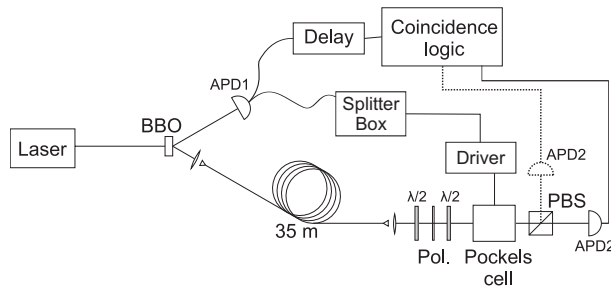
Figure 5.7: Sketch of the setup used to measure the Pockels stage switching fidelity at the single photon level. While one photon of a downconverted photon pair acts as a trigger, the second one is delayed in an optical fiber before being fed into a Pockels cell. Finally, coincidences between detection events at an avalanche photo diode (APD1) and the different ports of a fiber-coupled polarizing beam-splitter (PBS) after the Pockels cell (APD2) are measured.

window which can be seen in Fig. 5.9. The difference between both measurements in this Fig. is the chosen on-time duration, where in both cases, the photons arrive approximately in the middle of the on-time window. For an on-time window of 22 ns we observe a low peak contrast of only 200:1, instead of more than 3000:1 in the case of a 46 ns on-time window (note that a
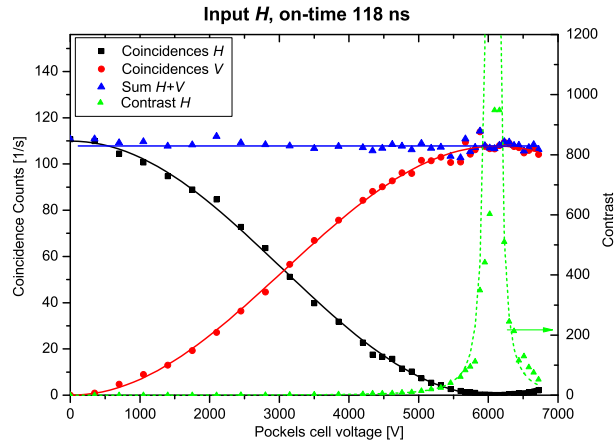
Figure 5.8: The polarization of a horizontal input-photon is rotated by a Pockels cell. The number of coincidence counts per second (each point corresponds to a 30 seconds average) in the different ports of a fiber coupled `PBS` behind the Pockels cell are plotted in this graph as a function of the voltage being applied. For these measurements, the on-time of the Pockels cell is 118 ns (driven by a single push-pull device). The photons arrive approximately in the middle of the on-time window, resulting in a peak-contrast exceeding 900:1. The coincidence data are fitted with sinusoidal functions. Dashed: the $\tan^2$ function resulting from the coincidence fit parameters that is theoretically expected for the contrast. Note here that $\tan^2$ is a diverging function and therefore does not fit the experimental data well.

22 ns on-time window is only possible with a double push-pull driver). For an on-time window duration greater than 46 ns, we find that the switching contrast always exceeds a ratio of 500:1 (up to more than 1000:1) regardless of the input polarization and the chosen driver. Because we use three Pockels cells in our final setup, a contrast ratio of more than 500:1 for each Pockels cell corresponds to an overall feed forward fidelity of more than 99 % $((1 - 1/500)^3)$ in our chosen configuration. For the final feed-forward experiment (Section 5.3 and [18]), we choose an on-time window duration of 46 ns for the double push-pull driver and 118 ns for the single ones. Pockels cell 1 (cf. Fig. 5.2) has to switch at a rate of about 2 kHz while the other two are switched at below 1 kHz. The Pockels cells are operated at a voltage of 6.3 kV. We choose dead-times of 3.2 μs for the single push-pull drivers and 1.6 μs for the double push-pull driver. Two photons of the four-photon cluster are delayed in optical single mode fibers having lengths of 30 m and 60 m - allowing 150 ns for the execution of each feed-forward step. Experimentally, we find that a single feed-forward operation takes on average 145±3 ns, where this value is composed of the following contributions: propagation time of photons 1 and 2 in single-mode fibres leading to detector (15 ns), delay of the single-photon detectors (35±3 ns), processing time of the logic (7.5 ns), switching delay of the EOM driver (65 ns - this includes an offset of the photon in the on-time window of about 18 ns - which is necessary to get a good contrast), rise time of the Pockels cell (5 ns), and miscellaneous coaxial cables employed in the set-up
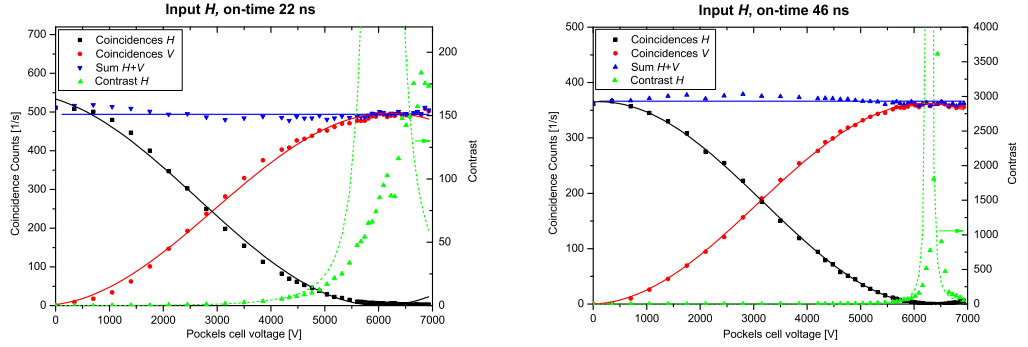
Figure 5.9: Comparison of the EOM switching contrasts for different on-times at the single-photon level - in this case for a horizontal input polarization. Measurements are performed using a double push-pull driver. A much higher contrast is achievable if an on-time of 46 ns (right graph) is chosen instead of 22 ns (left graph). Each data-point corresponds to an average taken over 30 s and the coincidence data are fitted with sinusoidal functions. The expected $\tan^2$ function for the contrast is shown as a dashed line.

(17.5 ns).

The ordinary single mode delay fibers that serve as storage devices for the photons are taped down to the optical table, upholstered by foam. The polarization rotation in the fibers is compensated by polarization controllers (see Section 4.1.1). Once aligned, the polarization turned out to be stable and did not require readjustment during the experiment.

5.3 Feed-forward experiment and results

So far we have discussed the relevant techniques for the implementation of fast, active feed-forward in the context of photonic quantum computing. This included a detailed description and the characterization of fast EOMs for the active switching of the polarization state of single photons and a description of the switching logics. We will now proceed to describe the actual experiment in which this feed-forward system is employed on a four-photon cluster state, thus allowing the deterministic execution of single- and two-qubit operations as well as Grover's search algorithm.

In our experiment the four-photon linear cluster state was produced in the interferometric down-conversion setup that is explained in Chapter 4. Successful state generation provides us with a linear cluster of the form,

$$|\Phi_{Cluster}\rangle = \frac{1}{2}(|0\rangle_1|0\rangle_2|0\rangle_3|0\rangle_4 + |0\rangle_1|0\rangle_2|1\rangle_3|1\rangle_4 + |1\rangle_1|1\rangle_2|0\rangle_3|0\rangle_4 - |1\rangle_1|1\rangle_2|1\rangle_3|1\rangle_4) \quad (5.12)$$

where $|0\rangle$ and $|1\rangle$ is the computational basis and, in the actual experiment, denotes horizontal and vertical polarization, respectively (the subscript labels the photon). The state of Eqn. 5.12 is equivalent to the four-qubit linear cluster $|\Phi_{lin3}\rangle$ and to the horseshoe cluster (Fig. 3.5) $|\Phi_{\subset 4}\rangle$ under the local unitary operation $H_1 \otimes \mathbb{1}_2 \otimes \mathbb{1}_3 \otimes H_4$ on the physical clus-
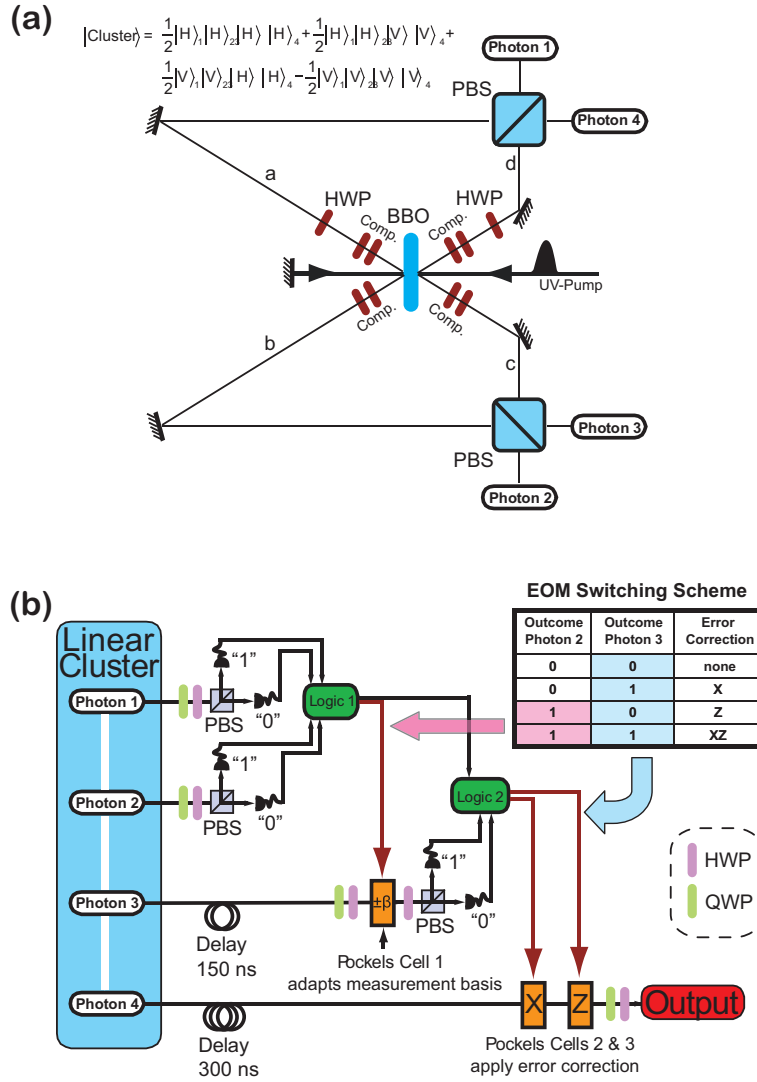
(a)

$$|\text{Cluster}\rangle = \frac{1}{2}|H\rangle_1|H\rangle_2|H\rangle_3|H\rangle_4 + \frac{1}{2}|H\rangle_1|H\rangle_2|V\rangle_3|V\rangle_4 +$$
$$\frac{1}{2}|V\rangle_1|V\rangle_2|H\rangle_3|H\rangle_4 - \frac{1}{2}|V\rangle_1|V\rangle_2|V\rangle_3|V\rangle_4$$

(b)

Outcome Photon 2	Outcome Photon 3	Error Correction
0	0	none
0	1	X
1	0	Z
1	1	XZ

Figure 5.10: Schematic drawing of the interferometric cluster-state preparation in **(a)**, and its extension ,**(b)**, to achieve active feed-forward of the one-way quantum computation (namely, a single-qubit rotation). An ultra-violet laser pulse passes twice through a non-linear crystal to produce polarization-entangled photon pairs in both the forward and backward direction. Compensators (Comp) are half-wave plates (`HWP`) and BBO crystals used to counter walk-off effects in the down-conversion crystal. They are aligned such that $|\Phi^-\rangle$ and $|\Phi^+\rangle$ states are emitted in the forward and backward direction, respectively. Taking into account the possibility of double-pair emission and the action of the polarizing beam splitters (`PBS`s), the four amplitudes of the linear cluster state can be generated with an additional `HWP` in mode a. Once this is achieved, the computation proceeds by consecutive polarization measurements on photons 1-4. Dependent on the outcomes of photons 1-3, three fast electro-optical modulators (EOMs) are employed to implement the active feed-forward. One EOM adapts the measurement basis of photon 3, while two EOMs, aligned for σ_x and σ_z operation, apply the error-correction on output photon 4. Two single-mode fibres, 30m and 60m long, serve to locally delay the photons during the detection stage, logics operation and switching/charging process of the EOMs.

ter state (H is the Hadamard and $\mathbb{1}$ is the Idenity operation). In the experiment, the state creation is verified by over-complete state tomography in which the density matrix of the cluster state is reconstructed from a set of 1296 local measurements using a maximum-likelihood technique [120, 167] and all combinations of mutually unbiased basis sets for individual qubits, i.e. $\{|0\rangle, |1\rangle; |+\rangle, |-\rangle; |R\rangle, |L\rangle\}$, where $|+/-\rangle = (|0\rangle \pm |1\rangle)/\sqrt{2}$ denote $\pm 45°$ polarization and $|L/R\rangle = (|0\rangle \pm i|1\rangle)/\sqrt{2}$ stands for right and left circular polarization. The experimentally obtained density matrix has a fidelity of $\mathcal{F} = \langle \Phi_{Cluster}|\rho|\Phi_{Cluster}\rangle = 0.62 \pm 0.01$ with the ideal four-qubit cluster, which is sufficiently above the threshold of 50% to prove genuine multiparticle entanglement [168].

Using the technical realization outlined in the previous Section, we were able to realize fast active switching with duty cycles of less than 150 ns, which to our knowledge, is about two orders of magnitude faster than in other physical realizations of quantum computers [177, 135, 178, 175] (cf. Section 5.2.1).

For the active switching, we employ KD*P (potassium dideuterium phosphate) crystals with a measured transmission greater than 96%, a half-wave voltage of 6.3 kV and a high switching contrast[2] of approximately 500:1. From the high switching contrast of 500:1, one can infer that the total feed-forward accuracy of the three EOMs for detected photons is at least $(1-1/500)^3 > 0.99$. Other errors apart from photon loss, such as mode mismatch and unwanted phase shifts at the interferometric setup only result in non-ideally prepared input cluster states. However, the performance of the feedforward stage is unaffected by these imperfections. In the present configuration, the custom-built EOM drivers can be operated up to 20 kHz; this is compatible with our trigger-rate requirement, which is set by our photon pair production rates (2 kHz). During recharge cycles, the EOM drivers are "disabled" for an effective dead time of 1.6 ms, which is short enough, considering our average two and four-photon production rate (of the order of 2 kHz and 1 Hz, respectively). The overall detection efficiency of the experiment — bearing in mind the nonideal collection of photons in single-mode fibres (20%), quantum efficiency of the detectors (55%) and various losses in fibres, optical elements and EOMs (5%) — is roughly 10% per detector, which is a standard figure in many multi-photon down-conversion experiments.

The measurement device for an arbitrary basis consists of a quarter-wave and a half-wave plate followed by a polarizing beam-splitter (PBS), which transmits horizontally polarized light ("0") and reflects vertically polarized light ("1"). Quantum computation on a cluster state is performed by consecutive measurements on qubits 1-4. It is therefore necessary to locally delay photons 3 and 4 if active feed-forward of measurement results is desired. While qubit 1 and qubit 2 are measured without any delay, qubit 3 and qubit 4 are delayed in optical single-mode fibres with lengths of 30m (150 ns) and 60m (300 ns), respectively. The active switching itself is achieved via Pockels cells; one for qubit 3 to adapt the measurement basis, i.e. from $B_3(\beta)$ to $B_3(-\beta)$, and two in the channel of output-qubit 4 to correct introduced Pauli-errors, σ_x and

---

[2]The switching contrast is defined as the ratio of photons that are measured to obtain a well-defined polarization rotation due to the operation of the EOM divided by the photons that remain in the original state due to malfunctioning of the device. This was measured at the single photon level for various input polarizations employing time-correlated photons emitted by a down-conversion source, triggering on one photon and thereby rotating the polarization state of the other photon.
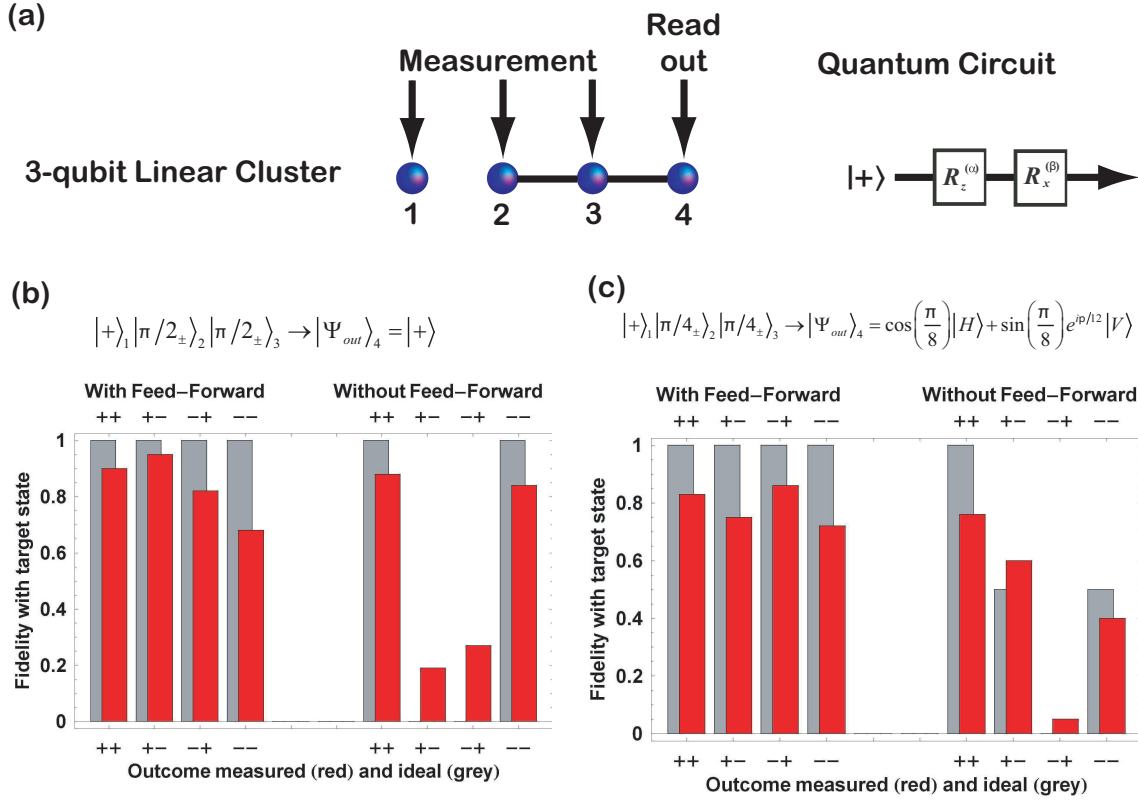
(a)

Figure 5.11: Active feed-forward of two different single-qubit rotations. (a) The linear three-qubit cluster state (obtained from our four-qubit cluster state) and the quantum circuit it implements. The operation $R_x(\alpha) = \exp(-i\alpha\sigma_x/2)$ can be implemented through the matrix identity $R_x(\alpha) = HR_z(\alpha)H$. (b) and (c) Fidelity of the output state with the desired state in the case of active feed-forward and without feed-forward of measurement results. Both the experimentally measured fidelities (red bars) and the theoretically expected, ideal fidelities (grey bars) are given. It is immediately clear that, with feed-forward, the computation theoretically always produces the desired outcome with certainty, even if measurement outcomes in the $|\alpha\rangle_2$, $|\beta\rangle_3$ basis deviate from the desired $s_2 = s_3 = 0$ event ("++"). In (b, α and β were both set to $-\pi/2$, resulting in the output state $|\Psi_{out}\rangle_4 = |+\rangle$, while, in (c), the measurement angles were set to $\alpha = \pi/4$ and $\beta = \pi/12$. In that specific case the angles lie outside the Clifford group and produce the complex output state $|\Psi_{out}\rangle = \cos(\pi/8)|H\rangle + \sin(\pi/8)e^{i\pi/12}|V\rangle$. Averaged over all possible measurement outcomes, the overlap of the measured one-qubit density matrix with the ideal state with feed-forward is 0.84 ± 0.08 in (b) and 0.79 ± 0.07 in (c), respectively. Without feed-forward, theory predicts an average fidelity of 0.5. In the experiment, we find 0.55 ± 0.06 and 0.45 ± 0.05, for (b) and (c), respectively.

σ_z (see Fig. 5.10).

As an example, consider the general case of a three-qubit linear cluster state $|\Phi_{lin3}\rangle$, such as the one depicted in Fig. 5.11(a). This state can be obtained from our four-qubit cluster by removing qubit 1, i.e. measuring this qubit in the computational basis for the linear cluster, $\{|+\rangle_1, |-\rangle_1\}$. Consecutive measurements in bases $B_2(\alpha)$ and $B_3(\beta)$ on the physical qubits 2 and 3 implement an arbitrary single-qubit rotation of the encoded input qubit $|\Psi_{in}\rangle = |+\rangle_L$. These measurements rotate the encoded input qubit to the output state

$$|\Psi_{out}\rangle = \sigma_x^{s_3} H R_z((-1)^{s_2}\beta)\sigma_x^{s_2} H R_z(\alpha)|\Psi_{in}\rangle = \sigma_x^{s_3}\sigma_z^{s_2} R_x((-1)^{s_2}\beta)R_z(\alpha)|\Psi_{in}\rangle, \qquad (5.13)$$

which is stored on qubit 4. The measurement outcome, $s_i = 0, 1$, on the physical qubit i, (1) determines the measurement basis for the succeeding qubit and (2) indicates any introduced Pauli errors that have to be compensated for. For the specific details concerning the adaptation of the measurement basis and the respective error correction on the output qubit see the introductory part of this Chapter (Section 5.1).

Experimental results of single-qubit rotations with feed-forward are shown in Fig. 5.11, together with the outcomes of the same computation in the case when no feed-forward is applied. In each case the output of the single-qubit rotation is stored in qubit 4 and completely characterized by single-qubit tomography. Fig. 5.11(a) shows a schematic of the implemented quantum algorithm; Fig. 5.11(b) shows the output of the computation $|\Psi_{out}\rangle = R_x(-\pi/2)R_z(-\pi/2)|\Psi_{in}\rangle = |+\rangle_4$, in the laboratory basis, with and without active feed-forward. We find an average fidelity of 0.84±0.08 with the ideal state when active feed-forward is implemented. This is a considerable improvement over the case of no feed-forward, which produces the target state with an average fidelity of only 0.55±0.06. See the caption of Fig. 5.11 for more detail.

In order to prove universal quantum computing we need to demonstrate single-qubit rotations outside the Clifford group [11]. This special example is shown in Fig. 5.11(c), where we perform polarization projections in the basis $\alpha = \pi/4$ and $\alpha = \pi/12$ which results in the more complex computation $|\Psi_{out}\rangle = R_x(\pi/4)R_z(\pi/12)|\Psi_{in}\rangle = \cos(\pi/8)|H\rangle + \sin(\pi/8)e^{i\pi/12}|V\rangle$ in the error-free case. Here we find an average fidelity of 0.79±0.07 with active feed-forward, but only 0.45±0.05 without (see Fig. 5.11). We find similar results for other measurement angles and hence other single-qubit rotations.

It is a specific strength of the cluster-state computation that the adaptation of the measurement basis, $B_j(\alpha)$, caused by the measurement outcome of the preceding qubit, can be carried out without active switching when the eigenstates of the measurement basis are identical to the eigenstates of σ_x, σ_y or σ_z. In that case logical feed-forward results in a reinterpretation of the measurement outcome. Outcome "0" would then correspond to the measurement outcome $|\alpha_-\rangle$ and "1" to the outcome $|\alpha_+\rangle$. We demonstrate this specific feature within the two-dimensional four-qubit cluster-states, the horse-shoe cluster, $|\Phi_{\subset 4}\rangle$, and the box cluster, $|\Phi_{\square 4}\rangle$, which we use to realize an entangling gate and an efficient implementation of Grover's quantum search algorithm, as follows.

Universal quantum computing requires a universal set of one- and two-qubit operations such as the controlled-NOT (CNOT) or controlled-PHASE (CPHASE) gates which can be realized using either horseshoe- or box cluster. These gates can be implemented on our linear
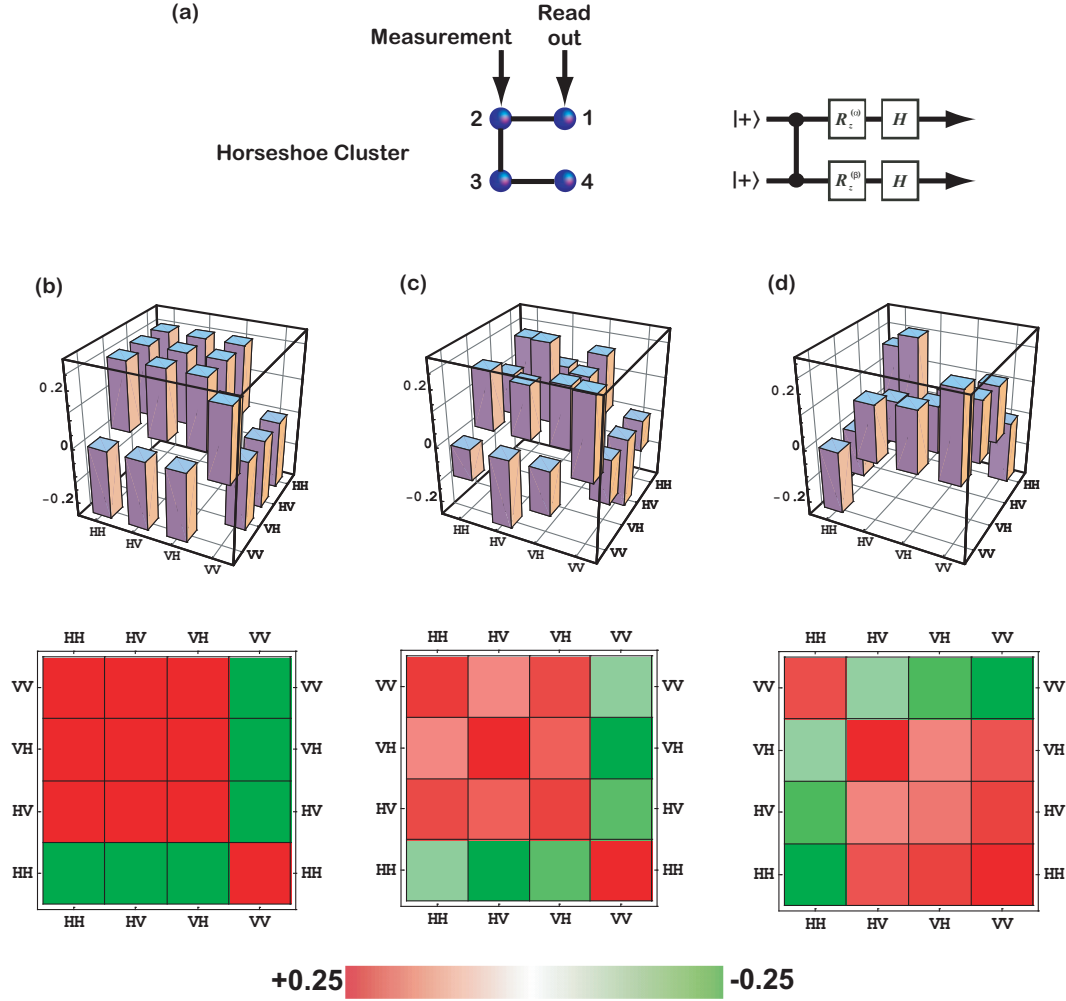
Figure 5.12: Feed-Forward of the two-qubit operation $|+\rangle_1|+\rangle_2 \rightarrow \frac{1}{\sqrt{2}}(|H\rangle_1|+\rangle_4 + |V\rangle_1|-\rangle_4)$,,, with single-qubit measurements in $B_2(0)$ and $B_3(0)$ carried out on photons 2 and 3 on the horseshoe cluster state . (a) The algorithm implemented by the horseshoe cluster. (b) The ideal, expected density matrix, with the real part of the density matrix shown. The imaginary components of the density matrices are zero in theory and negligible in the experiment. (c) In the case were photon 2 and 3's outcome was $s_2 = s_3 = 1$ instead of the desired "00" event, the logical feed-forward relation $\sigma_x \otimes \sigma_x$ has been applied by relabeling the analyzer output ports. Fidelity and measures of entanglement of the reconstructed the state can be inferred from the main text. In (d) we show the output of the same quantum computation when no feed-forward is applied. The experimental density matrix in this case differs remarkably from the ideal one, which is reflected in the low state fidelity (see main text).

cluster by changing the order of measurements, e.g. by measuring qubits 2 and 3 and thus transferring the two-qubit quantum state onto the remaining qubits 1 and 4. This quantum circuit can also be written as $|\Psi_{out}\rangle = (\sigma_x^{s_2} \otimes \sigma_x^{s_3})(H_1 \otimes H_2)[R_z(\alpha) \otimes R_z(\beta)]\texttt{CPHASE}|\Psi_{in}\rangle$ where $|\Psi_{in}\rangle = |+\rangle_1|+\rangle_2$ is our encoded two-qubit input state. Note that the Pauli errors have to be compensated for in the case where $s_2 = 1$ and/or $s_3 = 1$. In principle, feed-forward relations in the case of two-qubit gates are more complex, as measurement errors in one "rail" influence the state of the qubit in another rail [151]. In particular, for polarization projections $|\alpha_+\rangle_2|\beta_+\rangle_3, |\alpha_+\rangle_2|\beta_-\rangle_3, |\alpha_-\rangle_2|\beta_+\rangle_3, |\alpha_-\rangle_2|\beta_-\rangle_3$, (i.e. for measurement outcomes $s_2 = s_3 = 0; s_2 = 0, s_3 = 1; s_2 = 1, s_3 = 0; s_2 = s_3 = 1$), the operation $I_1 \otimes I_4, I_1 \otimes \sigma_{x4}, \sigma_{x1} \otimes I_4, \sigma_{x1} \otimes \sigma_{x4}$ has to be fed-forward to the output qubits 1 and 4, respectively. In Fig. 5.11, we explicitly show the case where both photons 2 and 3 are measured to $s_2 = s_3 = 1$ be instead of the desired "0" outcomes $s_2 = s_3 = 0$ in the bases $B_2(0)$ and $B_3(0)$. Those "errors" rotate the input state $|\Psi_{in}\rangle = |+\rangle_2|+\rangle_3$ to the maximally entangled output state

$$|\Psi_{out}\rangle_{1,4} = \frac{1}{\sqrt{2}}(|+\rangle_1|V\rangle_4 - |-\rangle_1|H\rangle_4). \tag{5.14}$$

However, to obtain the desired state

$$|\Psi_{out}\rangle_{1,4} = \frac{1}{\sqrt{2}}(|H\rangle_1|+\rangle_4 + |V\rangle_1|-\rangle_4), \tag{5.15}$$

the operation $\sigma_{x1} \otimes \sigma_{x4}$ has to be fed-forward on qubits 1 and 4. Density matrices of the ideal two-qubit output state and the experimentally reconstructed state are shown in Fig. 5.11, together with the measured output state obtained without feed-forward. We compute a state fidelity of 0.79±0.04 for the overlap of our experimental fed-forward state with the ideal one. The tangle [45, 179] of this output state is τ =0.42±0.09, confirming the generation of entanglement between the output qubits as a result of the computation. Furthermore, our reconstructed density matrix implies a maximum CHSH Bell parameter [170] of S=2.40±0.09, which is more than four standard deviations above the S =2 upper limit for local realistic theories. For comparison, if the feed-forward relation is not applied to this specific computation, the measured fidelity is only 0.09±0.03, in agreement with the theoretical prediction of 0 - no overlap with the desired state.

Quantum algorithms [11, 8, 9] are fascinating applications of quantum computers. Grover's quantum search algorithm is considered as one of the milestone in the field of quantum computing. The algorithm can search for a single match in a database with N records in $O(\sqrt{N})$ steps which is a quadratic speedup over the best known classical algorithm. Interestingly, Grover's quantum search algorithm [180] can be implemented on a four-qubit box cluster, such as the one depicted in Fig. 3.5 and 5.13. It is worth mentioning that in the case of a two-bit function ($N = 4$), the difference is even more dramatic since Grover's search will find the marked entry with certainty using only a single oracle query.

For the two-qubit algorithm, two input qubits, 1 and 2, are prepared in the state $|+\rangle_1|+\rangle_2$, which is a superposition of all four computational basis states, $|0\rangle|0\rangle, |0\rangle|1\rangle, |1\rangle|0\rangle$ and $|1\rangle|1\rangle$. The algorithm itself can be separated into two basic operations. First the "black box" labels the correct element, which can be set by a proper choice of α and β, specifically, it tags one of the four computational basis states $|0\rangle|0\rangle, |0\rangle|1\rangle, |1\rangle|0\rangle$ and $|1\rangle|1\rangle$ by changing its sign, e.g.
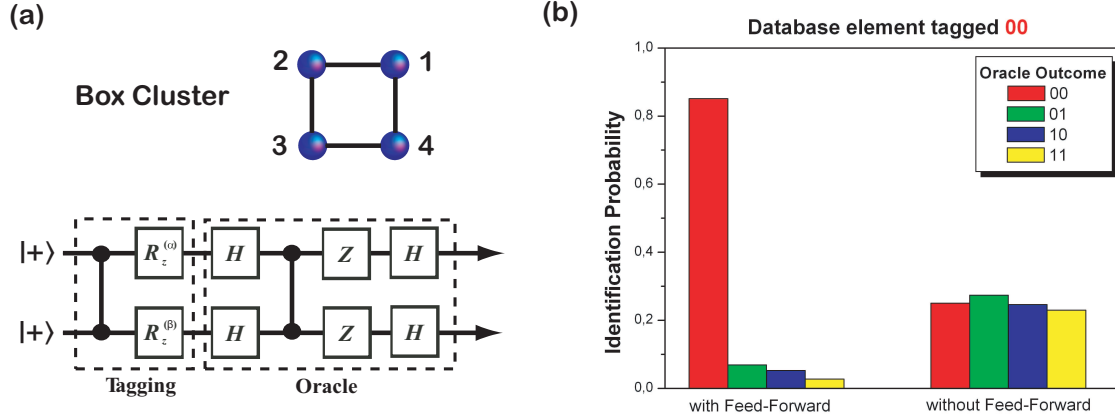
(a)

(b)

Figure 5.13: Deterministic demonstration of Grover's search algorithm where we chose to tag the $|0\rangle|0\rangle$ entry. (a) The algorithm is implemented on a box cluster state and consists of two distinct operations: The "black box" tags the database element by measuring physical qubits 2 and 3 in the bases $B_{2,3}(\pi)$, while the quantum oracle finds the desired database entry with certainty after a single query. Owing to intrinsic measurement randomness, however, it happens with equal probability that other database entries become tagged. Without feed-forward, this results in a balanced output of the oracle, as can be seen from the experimental data in (b). Applying the feed-forward procedure leads to an unambiguous search result, so that, on average, the oracle finds the correct outcome with a probability of 85±3%. In the case without feed-forward, we find each possible result with equal probability of 25±2%.

$|0\rangle|0\rangle \rightarrow -|0\rangle|0\rangle$. Then the quantum oracle finds the labelled element with an inversion-about-the-mean operation [8, 73] which inverts the amplitudes for each computational state about the mean value. This process amplifies the labeled amplitude and reduces the rest. In the two-qubit case, theory predicts that after a single application of this inversion, the computer outputs the labeled state with unit probability.

Grover's algorithm circuit contains extra fixed single-qubit operations, specifically a σ_z followed by a Hadamard transformation, H, on each qubit before the readout in the computational basis (c.f. Fig. 5.13). However this is equivalent to direct final readout measurements made in the basis $B_{1,4}(\pi)$, i.e., we can absorb these additional fixed single-qubit operations into the readout stage. The quantum circuit implemented by the box cluster can be seen as precisely that one required for Grover's algorithm provided the final readout measurements are made in $B_{1,4}(\pi)$ on physical qubits 1 and 4.

Our demonstration of Grover's algorithm on our four-qubit box cluster proceeds as follows. The encoded qubits are initialized in the state $|+\rangle_1 |+\rangle_2$. By choosing the measurement angles α and β as $\pi\pi$, $\pi 0$, 0π, and 00 we can tag the database entries $|0\rangle|0\rangle$, $|0\rangle|1\rangle$, $|1\rangle|0\rangle$ and $|1\rangle|1\rangle$, respectively. In principle, these settings remain hidden. Incorrect measurement outcomes at the "black box" qubits 2 and 3, however, introduce Pauli-errors, which effectively cause a wrong database element to be tagged. Feed-forward compensates for these errors such that the

algorithm produces the right search result with certainty, i.e. deterministically. Remarkably, the inversion-about-the-mean process is already hard-wired into the structure of the cluster state and is automatically implemented. The output of the computation, including feed-forward, are two bits identifying the marked database element. In Fig. 5.13(b), we show the experimental results of this quantum algorithm with and without feed-forward. The difference in performance is quite obvious, with feed-forward the right database element is identified in one query with a probability of 85±3%, which compares favorably with the case when the feed-forward relation is not applied, which we find to be 25±2%, just as good as with an classical random search algorithm.

5.4   Conclusion and outlook

In summary, we have shown that in the absence of photon loss, a one-way quantum computer with active, concatenated feed-forward would operate with high fidelity. As in all current photonic quantum computation experiments, the input cluster state is produced conditional on detecting all constituent photons. Because the efficiency of producing cluster states is low at present, this is not yet scalable. However, the technique is insensitive to photon loss due to absorption, reflection, fibre coupling and photodetector inefficiency. Thus our experiments show that except for photon loss, the feed-forward procedure operates with a quality and speed at present unmatched by other quantum computation methods. Conceptually, the most interesting result of our work is that it is indeed possible to build a deterministic quantum computer that has intrinsically random quantum measurements as its essential feature. Eventual large-scale implementations will need significant improvement of state preparation quality and photon detection efficiency, and reduction of photon losses. This will certainly be fostered by recent developments of highly efficient single-photon detection methods [181, 182, 183, 184, 185] as well as "on demand" single-photon sources [96, 186, 187, 188, 189, 190, 97, 191]. Given large and high-fidelity cluster states as well as low photon loss and significantly improved detectors, promising future applications of one-way quantum computers include important tasks such as the quantum Fourier transform [59] which is at the heart of Shor's factorizing algorithm.

The feed-forward apparatus that was developed for our experiment can easily be adapted for the use in other existing schemes of quantum computing, both in the one-way and standard circuit model [13, 68, 69]. Also, feed-forward techniques based on our apparatus might be used for the construction of heralded multi-photon states, which in turn, can be utilized for the deterministic creation of photonic cluster states. Using smaller apertures or even going into the integrated optics regime and/or by employing different crystal types, we believe that the overall switching operation can be improved to less than 50 ns, since the small scale results in faster charging of the EOM driver [192]. Such improvements will certainly pave the way to deterministic demonstrations of even more complex quantum algorithms and strengthen linear optics as a perfect test-bed for quantum computation.

Chapter 6

Demonstration of Deutsch's algorithm

In this Chapter, I will describe the first experimental demonstration of a one-way based implementation of Deutsch's algorithm [7, 20]. It represents a simple but yet interesting instance of the role that the inherent parallelism of quantum computation plays in the speed-up characterizing quantum versions of classical problems. Using a four-qubit linear cluster state and the all-optical setup described in previous Sections, we were able to demonstrate the algorithm in the two-qubit version.

The chapter is structured as follows. First, a short introduction to the mathematical problem that is at the heart of Deutsch's algorithm is given before I describe how the required unitary operations for various oracle settings can be implemented in the one-way quantum computer model. Finally we present the experimental realization and corresponding results that show a very good overall performance of the algorithm when compared with the theoretical expectations.

6.1 Introduction

First of all, let us get accustomed with the underlying problem of the Deutsch algorithm[1]. Often it is translated to the following, classical situation drawn from everyday life:

Consider you were given a coin. Determining whether this coin is fair (i.e. head on one side, tail on the other) or fake (heads or tails on both sides) requires an examination of each side of the coin in the classical case. However, there exists an analogous procedure in the quantum domain, the Deutsch–Jozsa algorithm [7, 19], that accomplishes this examination in a single step.

Mathematically, the above situations translates to the question whether a function is balanced or constant. To further illustrate this let us represent the four possible coins by four Boolean functions f_j with $j = 1, ..., 4$ that map one input bit $x = 0, 1$ (denoting the side of the

---

[1]The problem has first been defined by Deutsch [7] and is therefore commonly referred to as "Deutsch's problem".

coin) onto one output bit $f_j(x) = 0, 1$ (denoting "head or tail"). There exist altogether four such functions, which can be summarized by the following truth table

x	$f_1(x)$	$f_2(x)$	$f_3(x)$	$f_4(x)$
0	0	1	0	1
1	0	1	1	0

These functions can be divided into two groups: $f_1(x) = 0$, $f_2(x) = 1$ are *constant* functions since they returns the same value (either 0 or 1) for all possible inputs of x, while $f_3(x) = x$, $f_3(x) = \text{NOT}x$ are *balanced* functions since they return 0 for half of the inputs and 1 for the other half. The former represent the fake coins, while the latter stand for the fair coins. An unknown function is characterized as constant or balanced by evaluating $f(0) \oplus f(1)$ which yields 0 (or 1) for a constant (or balanced) function ($\oplus$ denotes addition modulo 2). This evaluation classically requires two function calls, whereas the Deutsch–Jozsa quantum algorithm allows us to obtain the desired information with a single evaluation of the unknown $f(x)$. The generalized version of Deutsch's problem, also known as the Deutsch-Josza algorithm [19], takes an N-bit binary input x and still allows to distinguish between the two different types of function $f(x)$ with only one query [19], while classically one needs to evaluate the function as many as $2^{N-1}+1$ times in some cases to obtain the desired result.

The action of the algorithm in the two-qubit version can be written as a circuit diagram [7]

$$(6.1)$$

where the middle operation is the "black box" (also called an *oracle*) representing the function evaluation $U_f : |x\rangle |y\rangle \rightarrow |x\rangle |y \oplus f(x)\rangle$. In the two qubit version, the algorithm implements the oracle as a function f on a single query bit x using an input ancilla bit y. The algorithm proceeds as follows:

The qubits in the quantum network are initialized as $|0\rangle_x$ and $|1\rangle_y$. After the first Hadamard, they evolve to $|+\rangle_x |-\rangle_y$, where $|\pm\rangle = (|0\rangle \pm |1\rangle)/\sqrt{2}$ and $\{|0\rangle, |1\rangle\}$ is the single-qubit computational basis. To determine the effect of the function evaluation on this state, first note that, for each $x \in \{0, 1\}$,

$$|x\rangle (|0\rangle - |1\rangle) \mapsto (-1)^{f(x)} |x\rangle (|0\rangle - |1\rangle). \tag{6.2}$$

Therefore, the state of the qubits after the function evaluation becomes

$$(1/\sqrt{2}) \left[(-1)^{f(0)} |0\rangle + (-1)^{f(1)} |1\rangle \right] (|0\rangle - |1\rangle). \tag{6.3}$$

That is, for each x the $|x\rangle$ term acquires a phase factor of $(-1)^{f(x)}$ which corresponds to the eigenvalue of the state of the auxiliary qubit under the action of the operator that sends $|y\rangle$ to $|y + f(x)\rangle$. Note that the state of the second (ancilla) qubit has not changed during the function evaluation. However, from the state of the first (query) qubit we can infer the properties of $f(x)$. That is, if $(1/\sqrt{2})[(-1)^{f(0)} |0\rangle + (-1)^{f(1)} |1\rangle$ is equal to $\pm(|0\rangle + |1\rangle) = \pm|+\rangle$ then $f(0) = f(1)$ and hence the function is constant. Analogously, if we find the query qubit in $\pm(|0\rangle - |1\rangle) = \pm|-\rangle$ then $f(0) \neq f(1)$, i.e. the function is balanced. By measuring the

query qubit in the $\{|\pm\rangle\}$ basis, one can determine which type of function $f(x)$ corresponds to. This can be achieved by applying another Hadamard gate to the query qubit followed my a measurement in the computational basis. Then $|0\rangle$ corresponds to a constant function while $|1\rangle$ indicates a balanced function and a single bit-value measurement on this qubit can distinguishes these cases with certainty!

6.2 Experiment and results

The steadily increasing interest in topics of quantum information processing (QIP) and quantum computation has stimulated considerable efforts in the realization of *quantum hardware* based on various kinds of experimental settings. These efforts have resulted in the realization of promising one and two-qubit logical gates [11, 95], even though the networking of these basic building blocks is still far from being practical. Nevertheless, investigations in this direction, both at the experimental and theoretical level are vital for the advancement of QIP. The ultimate aim is the realization of multi-qubit quantum algorithms with the ability to outperform their classical analogues [11, 8, 9]. In this context, the implementation of few-qubit quantum algorithms represents a step forward in the construction of working processors based on quantum technology [85, 86, 87, 193, 194, 195, 69].

Here we report the first experimental demonstration of a one-way based implementation of Deutsch's algorithm [7]. We have used an all-optical setup, where the construction of cluster states has been successfully demonstrated [73, 18, 159, 68, 69]. Negligible decoherence rates affecting qubits embodied by photonic degrees of freedom ensure the performance of the protocol in a virtually noise-free setting. Although Deutsch's algorithm has been implemented in a linear optical setup before [196], our protocol represents its first realization in the context of one-way quantum computation. It is based on the use of an entangled resource locally equivalent to the cluster state used previously for performing a two-qubit search algorithm [73], thereby reinforcing the idea of the high flexibility of cluster resources. We show that four qubits in a linear cluster configuration are sufficient to realize all the possible configurations of a function acting on a logical two-qubit register. Two of the possible configurations are the result of an application of an entangling gate to the elements of the register. In principle, this gate can be realized by inducing an interaction between the photonic qubits. In our cluster state-based approach, the required entangling operations are realized by using the entanglement present in the cluster resource and the nonlinearity induced by the detection. There is no necessity for *engineering* it in a case by case basis [196], which is a very important advantage. The reconstructed density matrix of the logical output qubits shows excellent performance of the algorithm in our setup when compared with the ideal, expected outcome.

The action of the oracle in Deutsch's algorithm is either preset or dictated by the outcome of another algorithm. In order to implement all possible configurations that the oracle might take in the two qubit version, we must be able to construct them using a combination of quantum gates. In Fig. 6.1 we show all possible oracles in terms of their quantum network. By describing the oracle simply as a "black box", it is easy to see that all four black boxes given in Fig. 6.1 by BB(i)-(iv) implement their respective oracle operation. In order to carry out Deutsch's
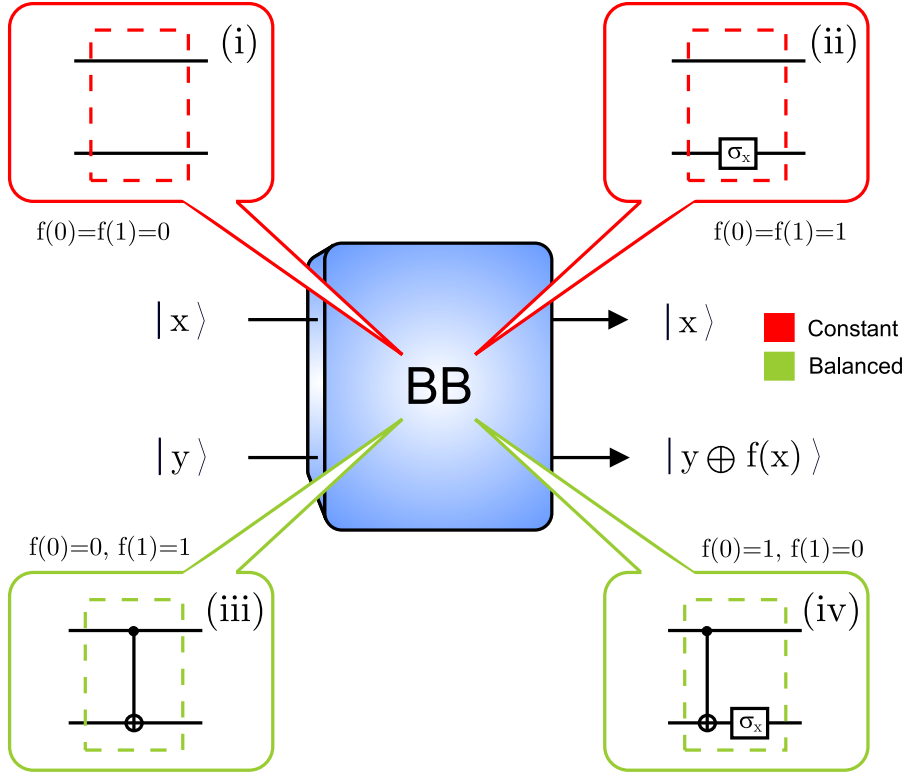
Figure 6.1: Network diagrams for each black box (BB) operation in Deutsch's algorithm. In order to implement all possible configurations that the oracle might take in the two qubit version, we must be able to construct them using a combination of quantum gates. Here we have BB(i)=$\mathbb{1} \otimes \mathbb{1}$, BB(ii)=$\mathbb{1} \otimes \sigma_x$, BB(iii)=CNOT and BB(iv)=($\mathbb{1} \otimes \sigma_x$)CNOT, where CNOT denotes a Controlled-NOT gate.

algorithm using these quantum gates, we use a cluster state resource and carry out one-way quantum computation on it. This allows the implementation of the algorithm by performing a correct program of measurements. No adjustment to the experimental setup is necessary.

Given a cluster state, there are two types of single-qubit measurements that allow a one-way quantum computer to operate. First, by measuring a qubit j in the computational basis $\{|0\rangle_j, |1\rangle_j\}$ it can be disentangled and removed from the cluster, leaving a smaller cluster state of the remaining qubits. Second, in order to perform actual QIP, qubits must be measured in the basis $B_j(\alpha) = \{|\alpha_+\rangle_j, |\alpha_-\rangle_j\}$, where $|\alpha_\pm\rangle_j = (|0\rangle \pm e^{i\alpha}|1\rangle)_j/\sqrt{2}$ ($\alpha \in \mathbb{R}$). Choosing the measurement basis determines the rotation $R_z(\alpha) = \exp(-i\alpha\sigma_z/2)$, followed by a Hadamard operation $H = (\sigma_x + \sigma_z)/\sqrt{2}$ being simulated on an encoded logical qubit in the cluster residing on qubit j ($\sigma_{x,y,z}$ are the Pauli matrices). With a large enough cluster, any quantum logic operation can be performed with a proper choice for the $B_j(\alpha)$'s.

For the entangled resource, in an ideal case, the following four-photon state is produced by means of the set-up shown in Fig. 6.3(a)

$$|\Phi_c\rangle = \frac{1}{2}(|0000\rangle + |0011\rangle + |1100\rangle - |1111\rangle)_{1234} \qquad (6.4)$$
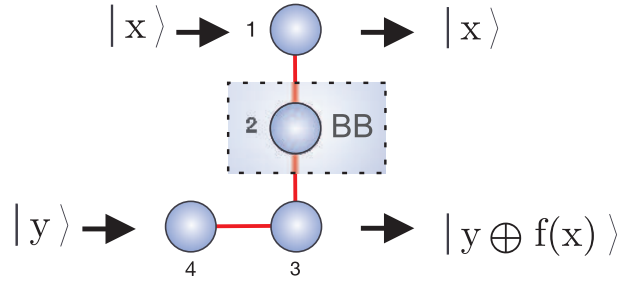
Figure 6.2: Sketch of the cluster-state configuration used for the algorithm. Qubit 1 embodies the logical input for $|x\rangle$ and its output. Qubit 4 is the logical input for $|y\rangle$ with qubit 3 as its output, which is always found to be $|-\rangle_3$.

with $|0\rangle_j$ ($|1\rangle_j$) embodied by the horizontal (vertical) polarization state of one photon populating a spatial mode $j = 1, .., 4$. The preparation of the resource relies on postselection: a four-photon coincidence event at the detectors facing each spatial mode witnesses the preparation of the state. This state is locally equivalent to a four-qubit linear cluster state (the required local operation being $H_1 \otimes \mathbb{1}_2 \otimes \mathbb{1}_3 \otimes H_4$). The experimentally produced state ϱ is verified by means of a maximum-likelihood technique for tomographic reconstruction [120, 167] performed over a set of 1296 local measurements, each acquired within a time-window of 500 s. This provides useful information about the overall quality of the experimental state on which the algorithm is performed. We have used all the possible combinations of the elements of the mutually unbiased single-qubit basis $\{|0\rangle, |1\rangle, |+\rangle, |-\rangle, |R\rangle, |L\rangle\}_j$ with $|\pm\rangle_j$ embodied by the polarization state at $\pm 45°$ and $|L/R\rangle_j = (|0\rangle \pm i\,|1\rangle)_j/\sqrt{2}$ corresponding to left and right-circularly polarized photons. This over-complete state tomography has the experimental advantage of providing a more precise state estimation and significantly smaller error bars. The reconstructed density matrix of ϱ is shown in Fig. 6.3(c) & (d) and has a fidelity with the ideal state in Eqn. 6.4 of $\mathcal{F} = \langle \Phi_c | \varrho | \Phi_c \rangle = 0.62 \pm 0.01$. The error bar of this result was estimated by performing a 100 run Monte Carlo simulation of the whole state tomography analysis, with Poissonian noise added to the count statistics in each run [120, 167]. Obtaining a higher fidelity is mainly limited by higher order pair emission and phase instability during the lengthy process of state tomography as well as due to non-ideal optical elements employed in the setup. However, it is well-above the limit $\mathcal{F} = 0.5$ for any biseparable four-qubit state [168] and demonstrates the presence of genuine four particle entanglement in the produced state.

In order to perform Deutsch's algorithm on the cluster resource given in Eqn. 6.4, we have used a specific set of measurement bases for the qubits in each black box case. In Table 6.1 we provide these measurement basis sets (BB_c) and feed-forward operations used to carry out the black boxes on $|\Phi_c\rangle$ and also its locally equivalent (LE) cluster state (BB basis sets). As BB(ii) and BB(iv) are obtained from BB(i) and BB(iii) by using alternative feed-forward operations (which correspond to adaptive measurements on the output qubits [18]), in what follows we explicitly describe BB(i) and BB(iii). Fig. 6.2 shows the in-out logical states of the algorithm, where the logical input state corresponding to $|x\rangle = |+\rangle$ is encoded on qubit 1. The state $|y\rangle = |-\rangle$ will be encoded on qubit 3 by measuring qubit 4 in the $B_4(\pi)$ basis during the
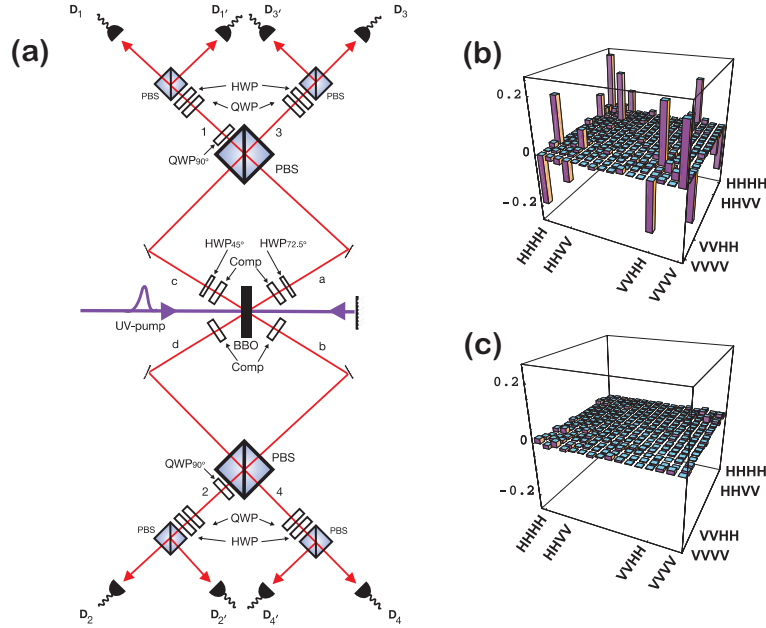
Figure 6.3: (a): Setup for the experimental implementation of Deutsch's algorithm. An ultraviolet pump-laser performs two passages through a nonlinear Beta-Barium-Borate crystal (BBO) aligned to produce entangled photon pairs of the form $(|00\rangle - |11\rangle)_{ab}/\sqrt{2}$ and $(|00\rangle + |11\rangle)_{cd}/\sqrt{2}$. Compensators (Comp) are half-wave plates (HWP) and BBO crystals used in order to counteract walk-off effects at the BBO. By considering the possibility of obtaining a double-pair emission into the same pair of modes and the action of the polarizing-beam splitters (PBS's), the four terms entering Eqn. 6.4 are obtained and their amplitudes and respective signs adjusted [73] with an additional HWP in mode a. The algorithm is executed by using quarter-wave plates (QWPs), HWP's, PBS's and photocounter pairs $\{D_j, D_{j'}\}$ for the performance of polarization measurements in arbitrary bases of the photons in mode j. (b) & (c): Real and Imaginary plots respectively of the tomographic reconstructed experimental density matrix ϱ.

implementation of the algorithm (described next). This gives

$$|x\rangle |y\rangle \equiv (\mathbb{1} \otimes R_z(\pi)) |+\rangle |+\rangle . \tag{6.5}$$

Qubit 2 in the LE cluster state of Eqn. 6.4 plays the pivotal role of the oracle as it performs a two-qubit quantum gate on the logical input states $|x\rangle$ and $|y\rangle$. For BB(i), measuring qubit 2 in the computational basis disentangles it from the cluster and the LE state of Eqn. 6.4 is transformed into

$$|\pm\rangle_1 (1/\sqrt{2})(|0\rangle |+\rangle \pm |1\rangle |-\rangle)_{34} \tag{6.6}$$

with $+$ $(-)$ for outcome $|0\rangle_2$ $(|1\rangle_2)$. The effective operation performed by this choice of the oracle's measurement basis is $\mathbb{1} \otimes \mathbb{1}$. By including the H operation applied to the input state $|y\rangle$ from the measurement of qubit 4, the overall computation results in

$$(\mathbb{1} \otimes \mathbb{1})(\mathbb{1} \otimes HR_z(\pi)) |+\rangle |+\rangle \tag{6.7}$$

	Measurement basis
BB(i)	$\{B_1(0), \{|0\rangle_2, |1\rangle_2\}, \{|0\rangle_3, |1\rangle_3\}, B_4(\pi)\}$
BB$_c$(i)	$\{\{|0\rangle_1, |1\rangle_1\}, \{|0\rangle_2, |1\rangle_2\}, \{|0\rangle_3, |1\rangle_3\}, \{|1\rangle_4, |0\rangle_4\}\}$
BB(iii)	$\{B_1(\pi/2), B_2(\pi/2), \{|0\rangle_3, |1\rangle_3\}, B_4(\pi)\}$
BB$_c$(iii)	$\{B_1(3\pi/2), B_2(\pi/2), \{|0\rangle_3, |1\rangle_3\}, \{|1\rangle_4, |0\rangle_4\}\}$

Table 6.1: Measurement bases for the black boxes in the experiment. The feed-forward operations are $(\sigma_x^{s_2})_1 (\sigma_x^{s_4})_3$ for BB$_c$(i) and $(\sigma_z^{s_2 \oplus s_4})_1 (\sigma_x^{s_4})_3$ for BB$_c$(iii). Here, s_j is 0 (1) if the measurement outcome is $|\alpha_+\rangle_j$ ($|\alpha_-\rangle_j$) on qubit j.

which is equivalent to

$$|x\rangle |y \oplus f(x)\rangle = (\mathbb{1} \otimes \mathbb{1}) |+\rangle |-\rangle \tag{6.8}$$

up to a local rotation H on physical qubit 3, applied at the feed-forward stage. Qubits 1 and 3 can now be taken as the output $|x\rangle |y \oplus f(x)\rangle$. For BB(iii), upon measuring qubit 2 in the $B_2(\pi/2)$ basis, the oracle applies the gate

$$[R_z(\pi/2) \otimes R_z(\pi/2)] \, \mathsf{CPHASE} \, |x\rangle |y\rangle, \tag{6.9}$$

where CPHASE shifts the relative phase of the state $|1\rangle |1\rangle$ by π. This produces the computation

$$|x\rangle |y \oplus f(x)\rangle = \mathsf{CNOT} |+\rangle |-\rangle \equiv [R_z(\pi/2) \otimes R_z(\pi/2)] \, \mathsf{CPHASE} \, [\mathbb{1} \otimes H R_z(\pi)] |+\rangle |+\rangle \tag{6.10}$$

up to local rotations $R_z(-\pi/2) \otimes H R_z(-\pi/2)$ on qubits 1 and 3, applied at the feed-forward stage. The measurements and outcomes of qubits 1, 3 and 4 constitute the algorithm. The additions to the feedforward stages described above, together with the measurement of qubit 2 should be viewed as being carried out entirely by the oracle.

The results of our experimental demonstration are shown in Fig. 6.4, where we provide a full characterization of the output state of our quantum computer by repeating the algorithm a large number of times. A single run of the algorithm (measuring the output qubit 1 in a specific basis only once) is sufficient in our setup to carry out the quantum computation with success rates as large as 90% (78%) for BB(i) (BB(iii)). However, repeating it several times allows us to verify the density matrix for the quantum state of the output qubits 1 and 3 reconstructed through a maximum likelihood technique [120, 167]. Although only the logical state residing on qubit 1 provides the outcome of the algorithm, it is useful for the purposes of characterizing the performance of the quantum computer to also determine the state residing on qubit 3. Ideally, the joint state of qubits 1 and 3 should be the product state $|x\rangle |y \oplus f(x)\rangle$. By obtaining both correct logical output states in our setup, we can confirm that the algorithm will run correctly if it is included as part of a larger algorithm. Fig. 6.4 shows the density matrices for BB(i) and BB(iii) being implemented. Both the no-feed-forward (no-FF) and feed-forward (FF) situations are shown on the left and right hand sides respectively. In the latter case, the state of the output qubits is corrected from the randomness of the measurements performed on the physical qubits 2 and 4. From the analysis performed in the previous Section, we know that the expected outcome from a single run, when a constant (balanced) function is applied is $|+, -\rangle_{13}$
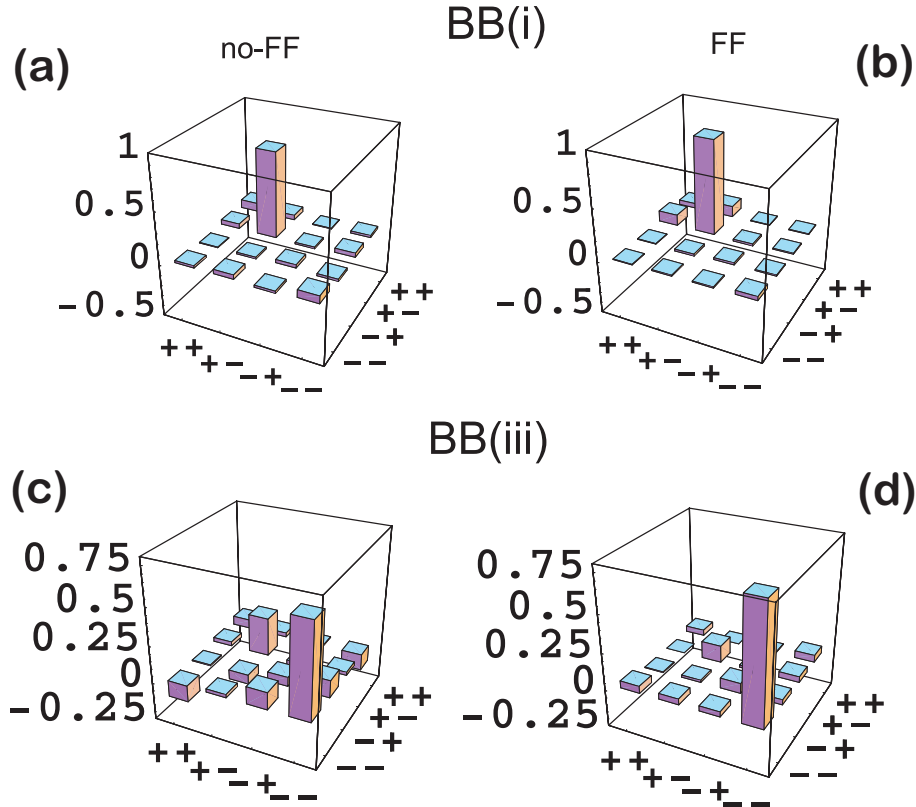
Figure 6.4: The output density matrices for cluster qubits 1 and 3 when BB(i) and BB(iii) are implemented. Panels (a) and (c) show the real parts of the two-qubit density matrix elements as obtained from a maximum likelihood reconstruction for the no-FF cases of BB(i) and BB(iii) respectively. Panels (b) and (d) show the corresponding plots for the FF case, due to the randomness of measurement outcomes for qubits 2 and 4. In all four cases the imaginary parts are zero in theory and negligible in the experiment (average values < 0.02).

$(|-,-\rangle_{13})$. Evidently, the reconstructed density matrices, both in the FF and no-FF cases, show a very good overall performance of the algorithm when compared with the theoretical expectations. The real parts are dominated by the correct matrix elements, while no significant imaginary parts are found. Quantitatively, the fidelity with the desired state in the case of a constant (balanced) function is found to be as large as 0.90 ± 0.01 (0.78 ± 0.01) for the FF case and 0.82 ± 0.01 (0.63 ± 0.01) for the no-FF one.

Moreover, no entanglement is found in any of the joint output states, as witnessed by the negativity of partial transposition criterion [197, 170]. The small admixture of the undesired $|+,-\rangle_{13}$ to the expected $|-,-\rangle_{13}$ state when a balanced function is applied (Fig. 6.4(c)) is due to the relatively low fidelity of the experimental cluster state with Eqn. 6.4. This effect is more pronounced for BB(iii) than for BB(i), where the measurement basis of qubit 2 is chosen to break the channel between $|x\rangle$ and $|y\rangle$, and results in a protocol-dependent *noise-inheritance* effect for imperfect cluster states (see Tame *et al.* in [198]).

6.3   Conclusion

We have designed, demonstrated and characterized the performance of the first experimental realization of Deutsch's algorithm on a cluster state using only four qubits. Our experiment is based on an all-optical setup where we encode the relevant quantum information into the polarization states of four photons and our demonstration is one of the few quantum algorithms entirely implemented within the framework of the one-way computational model [73, 199]. The agreement between the experimental data and theory is excellent and only limited by the overall quality of the entangled resource in the experiment. Realizations of the Deutsch-Jozsa algorithm with more than two qubits only require a larger cluster state and their demonstration should be feasible with ongoing improvements in state preparation quality and photon detection efficiency.

Chapter 7

Realization of a quantum game

In this chapter I will describe an experiment that shows how to simulate or "play" an instance of a quantum game — the so-called Prisoner's dilemma — on our one-way quantum computer. Playing such a game is essentially the execution of a quantum algorithm made up of a distinct set of one- and two-qubit gates. This allows the individual players to increase their strategy space, as they can also choose between superposition of classical input states while their choices get entangled. Evaluating the payoff function of this game for different strategy sets, we were able to show that the so-called "dilemma", that occurs in the classical version of this game, can be resolved in the quantum domain.

The subsequent parts of this Chapter are structured as follows. A brief explanation of the Prisoner's dilemma in the classical as well as in the quantum domain is given in Section 7.1 followed by a succinct introduction into the paradigm of one-way quantum computing and the formulation of the game in its context. In the remaining parts we describe our experimental demonstration as well as the results of our investigation. We find good agreement between the experimentally measured and expected payoff values for various strategy sets which allowed us to "solve" the Prisoner's dilemma.

7.1   Introduction and motivation

In the past, classical game theory has been extensively used to study problems such as stock market development, human as well as animal behavior or even the evolution of viruses at the microbiological level [22, 21, 200]. Quantum versions [201, 23, 202] of existing games offer additional strategies to the players - and resolve dilemmas that occur in the classical versions. As it is possible to recast any algorithm (classical or quantum) as a game characterized by strategies and rules, it is reasonable to believe that the quantum mechanical formulation of existing games can also be helpful in gathering a deeper understanding of quantum algorithms and quantum information processing. It has even been argued that performing experiments in physics can be viewed as simply playing a "game" against nature in which the observer tries to maximize the information obtained from the system under consideration. Eventually, such studies may even shed light on the great divide between classical and quantum physics [203].

The Prisoner's dilemma is a widely known example in classical game theory. It is a two players non-zero sum game where the players may benefit from unknowing cooperation. Due to the interesting nature of the game and the fact that communication is forbidden, defection turns out to be the unilateral best strategy, making it a *Nash*-equilibrium [22]. The dilemma arises because this strategy does not provide both players with the collective best payoff (which would be cooperation). However, extending the game into the quantum domain resolves the dilemma, as was first pointed out by Eisert *et al.* [23]. In the quantum version of the game, entanglement introduces some sort of cooperativity between the players and changes the Nash-equilibrium, so that the collective best choice for both players and the best individual choices are equal.

The quantum version of the Prisoner's dilemma has recently been experimentally demonstrated using a nuclear magnetic resonance (NMR) quantum computer [204]. Here we present the first optical implementation within the one-way model of quantum computation. By employing an all-optical system where the qubits are encoded in the polarization degree of freedom of the photons, the quantum states are subject to negligible decoherence and can easily be distributed among distant players. Moreover, in stark contrast to NMR quantum computing [84], in an all-optical implementation the observed entanglement can always be described as pure - and since the introduction of entanglement gives rise to the interesting features of quantum games we consider it important to report on an experimental realization which is free of any ambiguity in this respect.

Our implementation of the quantum version of the Prisoner's dilemma follows a recent proposal [199] which uses optical cluster states to realize the quantum game's circuit. Since cluster states are the resource states for one-way quantum computing [15, 16, 14, 205], our demonstration is equivalent to playing the game on a quantum computer. The choice of a photonic system guarantees the externally-controlled implementation of the player's strategy to a high degree. Additionally, the underlying principles of one-way quantum computing along with demonstrations of simple quantum algorithms [73, 18, 20] as well as the generation of cluster states [159, 68, 69] have recently been successfully demonstrated using linear optics.

7.1.1 The Prisoner's dilemma

The Prisoner's dilemma is a non zero-sum two players game. In the classical version, each player $j \in \{A, B\}$ independently chooses a strategy s_j which is a binary choice $s_j \in \{d, c\}$. The choices are sent to a supervising referee who computes the payoff of each player $\$_j(s_A, s_B)$ according to a payoff table. Since both players aim to maximize their individual payoff, the game is known to have a non-cooperative and selfish character.

The payoff table for player A is shown in Table 7.1 and as it is a symmetric game, player B's payoffs are given by the transposed table. With the strategy profile (d, d) neither player can increase his/her individual payoff regardless of the opposition, making it a *Nash equilibrium* [22]. However the cooperative profile $s = (c, c)$ is *Pareto-optimal* [21] since no player can increase their payoff by changing strategy, without reducing the payoff of the opponent. Classically, the dilemma arises since (d, d) is a dominant profile (rational reasoning causes both players to choose this strategy) but the associated payoff is not the overall best available to them.

A\B	c	d
c	$\$_A(c,c) = 3$	$\$_A(c,d) = 0$
d	$\$_A(d,c) = 5$	$\$_A(d,d) = 1$

Table 7.1: Payoff table of player A for the classical Prisoner's dilemma. Since this is a symmetric game, player B's payoffs are given by the transposed table.

In the quantum version of this game, however, this dilemma can be solved. Introducing entanglement provides both players with the ability to cooperate and therefore with an increased strategy space, effectively changing the Nash-equilibrium [23]. Suppose the strategy is realized by qubits, on which each player can perform their strategy by applying unitary operations. Following [23], the new strategy space is spanned by the unitary operator

$$U_j\left(\theta_j, \phi_j\right) = \begin{pmatrix} e^{-i\phi_j}\cos(\theta_j/2) & -\sin(\theta_j/2) \\ \sin(\theta_j/2) & e^{i\phi_j}\cos(\theta_j/2) \end{pmatrix}, \tag{7.1}$$

where $\theta \in [0, \pi]$ and $\phi \in [0, \pi/2]$. The respective classical strategies c and d are realized by $U_j(0,0)$ and $U_j(\pi,0)$. Before and after the operation of the players, the two qubits are subjected to entangling operations denoted P and M (see Fig. 7.1), which in our specific game, are a combination of Hadamard and `CPHASE` (`CZ`) operations (a `CPHASE` operation is a two-qubit entangling gate, which in the logical basis adds a π phase shift to the $|11\rangle$ term). Without those entangling steps the quantum version would not differ from a probabilistic, classic game. The corresponding quantum circuit is shown in Fig. 7.1. To compute the payoffs in the quantum version the referee projects the two qubit state onto the computational basis $\{|0\rangle, |1\rangle\}$ and distributes the payoff according to the payoff table.

Depending on the player's actual choice of strategy (i.e. the unitary U_j), the cooperativity due to the shared entanglement is preserved, giving rise to a Pareto optimal point that coincides with the Nash-equilibrium [23]. However, it should be noted at this point that Eisert *et al.* have chosen an artificial constraint on the set of strategies available to the players. As was shown in Ref. [202], when the players are permitted free choice of any unitary strategy, the behavior of the game is completely different and the resolution of the dilemma disappears[1].

7.1.2 Playing the game on a one-way quantum computer

The entangling stages (P and M) that are introduced in the quantum version of the game can be engineered by two-qubit gates. Two-qubit gates are crucial elementary gates for quantum computation [10] and have recently been demonstrated in the all-optical regime [133, 134, 155, 157, 159, 158]. In the one-way model of computation, such gates can be implemented by a proper measurement pattern on a sufficiently large entangled resource state (cluster state) [14, 73]. A specific way to implement the Prisoner's dilemma on an all-optical one-way quantum computer was proposed by Paternostro *et al.* [199]. The main advantage of the one-way model is that the entangling gates are already intrinsically implemented in the structure of the cluster state,

---

[1]Indeed, were both players allowed access to the full set of unitary strategies, then the game would not exhibit any Nash equilibria, since then every strategy has a perfect counterstrategy [202].
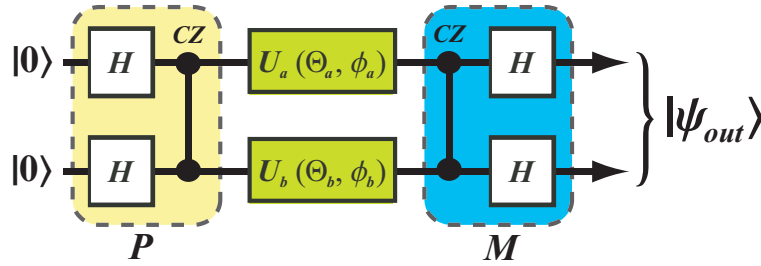
Figure 7.1: Quantum circuit of the two-player Prisoner's dilemma quantum game, H is a Hadamard gate and CZ a `CPHASE` gate. The output state of the circuit is sent to a referee who computes the payoffs.

such that the actual game can easily be carried out by single-qubit rotations only. The theory of one-way quantum computing was already established in Chapter 3 of this Thesis and the experimental generation of cluster states was discussed in great detail in Chapter 4. However for the sake of clarity and a self-contained presentation we will briefly summarize both in the following.

In the alternative and elegant model of one-way quantum computing the information processing is achieved by performing single-qubit measurements on a highly-entangled multi-particle cluster state [14]. This shifts the difficulty of realizing unitary gates to the generation of an appropriately designed multi-particle entangled state — the cluster state — which serves as a resource for the computation. The processing of information is accomplished by sequential single-qubit measurements on the cluster qubits, greatly facilitating the computation itself. Given a cluster state, measurements in the computational basis $\{|0\rangle, |1\rangle\}$ have the effects of disentangling the qubit, while leaving the remaining qubits entangled. Measurements performed in a different basis denoted $\{|\alpha_+\rangle, |\alpha_-\rangle\}$, where $|\alpha_\pm\rangle = (|0\rangle \pm e^{i\alpha}|1\rangle)/\sqrt{2}$, also effectively rotate the logical qubit that undergoes the computation. In our case, the rotation is around the z-axis $R_z(\alpha) = \exp(i\alpha\sigma_z/2)$ and followed by a Hadamard gate H. Rotations around the x-axis, i.e. $R_x(\alpha) = \exp(i\alpha\sigma_x/2)$ can be implemented through the matrix identity $R_x(\alpha) = HR_z(\alpha)H$. An elaborated and detailed introduction to experimental one-way quantum computing is discussed in Chapter 3 as well as in [73, 18]. Any complex operation (consisting of one- and two-qubit gates) can be carried out by a suitable choice of measurement patterns on a sufficiently large cluster state, so that, literally, the specific sequence of measurements forms the algorithms that is computed.

A special cluster state configuration, the box-cluster, is depicted in Fig. 7.2. It allows the implementation of a given set of unitaries U_j on two logical qubits as defined in the quantum circuit in Fig. 7.1, by measurement of qubits 1 and 4 in appropriate basis. This processes the input states, which are initialized as the logical $|+\rangle_L$ states, and transfers them across the cluster to qubits 2 and 3. During this process, which is often referred to as *one-bit teleportation*, the logical qubit undergoes the unitary U_j, depending on the measurement basis and its outcome.

However, closer investigation reveals that measurements performed in the $\{|\alpha_+\rangle, |\alpha_-\rangle\}$ basis would only allow $R_z(\alpha)H$ operations, which do not belong to the strategy space defined by Eqn.(7.1) apart for $\alpha = \pi/2$, consequently limiting the strategy space to $\{c, q\}$ where
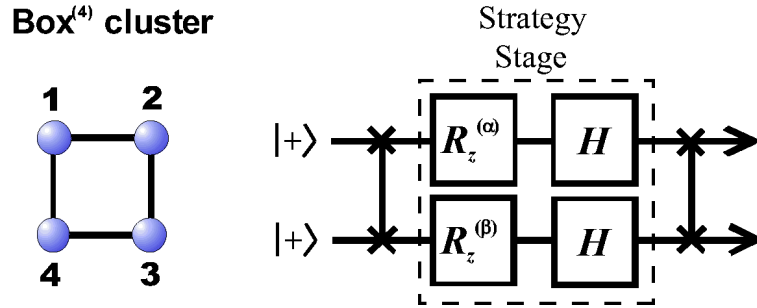
Box$^{(4)}$ cluster   Strategy
                                                Stage

Figure 7.2: Left: Schematic representation of a box-cluster state. Physical qubits (blue spheres) are entangled to their nearest neighbors (indicated by a black line) by applying `CPHASE` gates between them. Right: The quantum circuit realized by the box-cluster state. Note that the input states are initialized as the logical $|+\rangle_L$ state, which is equivalent to a Hadamard gate acting on the $|0\rangle$ state. Therefore the box-cluster implements, up to single-qubit rotations, the desired quantum circuit depicted in Fig. 7.1.

$q = U_j(0, \pi/2)$. Therefore we have to introduce an additional single-qubit rotation before the measurements, as described in [199]. Then the strategy space can be increased to $\{c, d, q(\alpha)\}$ where $q(\alpha) = U_j(0, \alpha)$, which allows an experimental realization of the quantum version of the game, as will be discussed in the following section.

7.2 Experimental realization

The cluster state creation is based on a interferometric method employing entangled photon pairs produced by spontaneous parametric down-conversion [103]. An ultra-violet laser pulse (1 W, 150 fs, $\lambda = 394.5$ nm) passes twice through a non-linear crystal (BBO), thereby generating polarization-entangled photon pairs in both the forward (modes a and b) and backward (modes c and d) direction (see Fig. 7.3). Half-wave plates (`HWP`) and BBO crystals are used to counteract walk-off effects in the down-conversion crystal [103]. They are aligned such that $|\Phi^-\rangle$ and $|\Phi^+\rangle$ states are emitted in the forward and backward direction, respectively. Taking into account the possibility of double-pair emission into each direction and the action of the polarizing beam splitters (`PBS`) mixing modes $a - d$ and $b - c$, the four amplitudes of the cluster state can be generated by rotating an additional `HWP` in mode a (see Ref. [73] for further details). Subsequently, the photons pass narrowband interference filters ($\Delta\lambda = 3\,nm$), and are then coupled into single-mode fibres and guided to the detection stage, where the photon's polarization is detected in an arbitrary basis using a combination of quarter-wave plates (`QWP`), `HWP` and `PBS` (see Fig. 7.3). A multichannel coincidence unit allows simultaneous detection of all relevant 16 four-fold coincidence events, therefore significantly speeding up the analysis process. The relative phase between the forward and backward emission in the setup sets the phases of the four individual terms of the cluster state. In the experiment, this is achieved with a piezo actuator translating the pump mirror. In the experiment, generation of the cluster state is retrodictive: it is known to have been prepared when one photon in each output port of the `PBS`'s is detected. This postselection technique is well established in linear optics and ensures
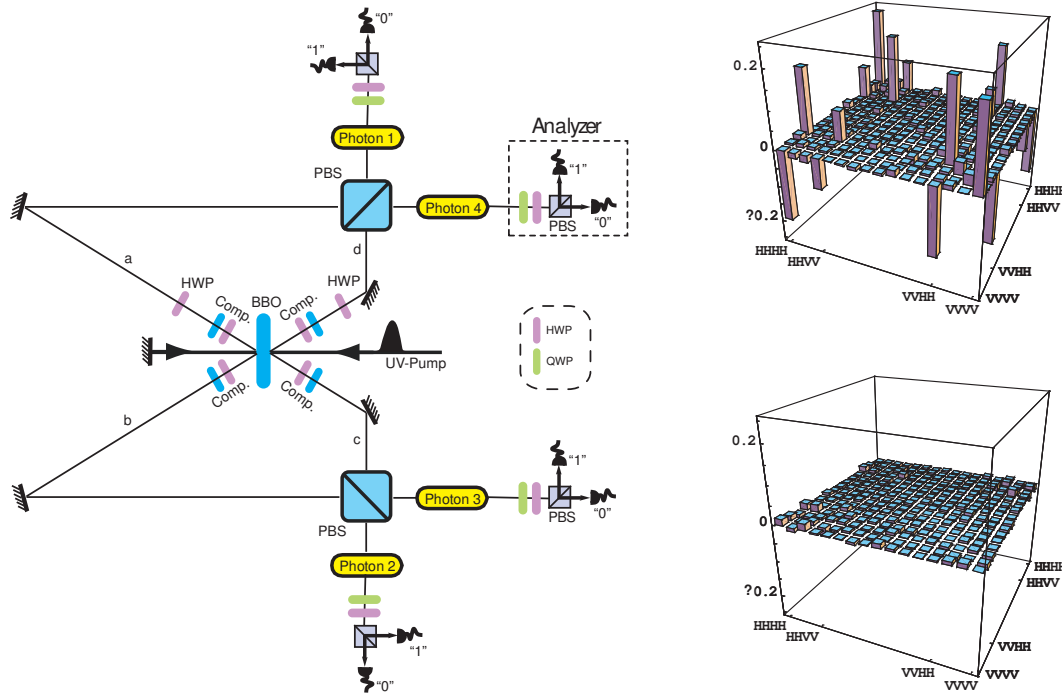
Figure 7.3: Left: Schematic drawing of the experimental setup that is employed to realize the quantum version of the Prisoner's dilemma. Whenever one photon is emitted into each of the four output ports of the PBSs (mixing modes $a - d$ and $b - c$), a photonic 4-qubit cluster state is generated. The analyzers, which consist of QWP, HWP and PBS, allow measurements in an arbitrary polarization basis and therefore the implementation of the quantum game. Details are discussed in the text. Right: Tomographic plot of the generated cluster state with the real part (upper plot) and imaginary part (lower plot) of the density matrix.

that photon loss and photodetector inefficiency do not affect the experimental results.

In an ideal case, the following four-photon state is produced by the experimental set-up:

$$|\Phi_c\rangle = \frac{1}{2}(|0000\rangle + |0011\rangle + |1100\rangle - |1111\rangle)_{1234} \tag{7.2}$$

with $|0\rangle_j$ ($|1\rangle_j$) embodied by the horizontal (vertical) polarization state of one photon populating a spatial mode $j = 1, .., 4$. The state $|\Phi_c\rangle$ can be converted to the box cluster state (Fig. 7.2) by the local unitary operation $H_1 \otimes H_2 \otimes H_3 \otimes H_4$ and a swap (or relabeling) of qubits 2 and 3 [73].

The quality of the generated cluster state is quantified by performing full quantum state tomography [120]. The reconstructed density matrix of the experimentally produced state, ϱ, is presented in Fig. 7.3 and has a fidelity with the ideal state in Eqn. (7.2) of $\mathcal{F} = \langle\Phi_c|\varrho|\Phi_c\rangle = 0.62 \pm 0.01$. The error bar of this result was estimated by performing a 100 run Monte Carlo simulation of the whole state tomography analysis, with Poissonian noise added to the count statistics in each run [157]. Higher fidelities are difficult to achieve due to phase instability during the lengthy process of state tomography and non-ideal optical elements employed in the setup. However, it is well-above the limit $\mathcal{F} = 0.5$ for any biseparable four-qubit state [168].

This demonstrates the presence of genuine four particle entanglement and confirms that such an experimental state can be used for the quantum protocol under consideration.

Starting from the state in Eqn. 7.2 the game is implemented by projecting the photons 1 and 4 onto the state $|\theta_{1,4}\rangle_{1,4} = \cos(\theta_{1,4})|0\rangle_{1,4} + \sin(\theta_{1,4})|1\rangle_{1,4}$ resulting in the state $|\psi(\theta_1;\theta_4)\rangle_{23} = {}_1\langle\theta|_4\langle\theta_4|\Phi_c\rangle_{1234}$ where θ_1 and θ_4 determine the strategies of players A and B, respectively, up to a rotation on the remaining photons. This projection in the laboratory basis is equivalent, up to a Hadamard rotation, to the box cluster state. The final state $|\Psi\rangle_{23}^{out}$, after the projection and any relevant σ_y operations are applied to them, resides on qubits 2 and 3 which are sent to the referee who calculates the payoff. The experimental parameters for the chosen strategies can be inferred from Table 7.2. In the Appendix we give a detailed derivation of this table.

A \ B	c	d	$q(\alpha_B)$
c	$\mathbb{1}\otimes\mathbb{1}\,\vert\psi(0;0)\rangle$	$\sigma_y\otimes\mathbb{1}\,\vert\psi(0;-\pi/2)\rangle$	$\mathbb{1}\otimes\mathbb{1}\,\vert\psi(0;\alpha_B)\rangle$
d	$\mathbb{1}\otimes\sigma_y\,\vert\psi(-\pi/2;0)\rangle$	$\sigma_y\otimes\sigma_y\,\vert\psi(-\pi/2;-\pi/2)\rangle$	$\mathbb{1}\otimes\sigma_y\,\vert\psi(-\pi/2;\alpha_B)\rangle$
$q(\alpha_A)$	$\mathbb{1}\otimes\mathbb{1}\,\vert\psi(\alpha_A;0)\rangle$	$\sigma_y\otimes\mathbb{1}\,\vert\psi(\alpha_A;-\pi/2)\rangle$	$\mathbb{I}\otimes\mathbb{1}\,\vert\psi(\alpha_A;\alpha_B)\rangle$

Table 7.2: Table of the states after the players implemented their strategies. $|\psi(\alpha_A,\alpha_B)\rangle$ is the state after both player applied their projections with angles α_A and α_B as described in the text. The final state $|\Psi\rangle_{23}^{out}$ is obtained by applying an additional rotation σ_y if necessary.

Experimentally the payoffs are determined as follows. We project the remaining two photons onto the $\{|0\rangle, |1\rangle\}$ basis and measure the probabilities $p_{ij} = \left|\langle ij|\,\Psi\rangle_{23}^{out}\right|^2$. The payoff of player A is then computed using

$$\$_A^{\exp}(s_A, s_B) = \$_A(c,c)p_{00} + \$_A(c,d)p_{01} + \$_A(d,c)p_{10} + \$_A(d,d)p_{11} \tag{7.3}$$

For each player we have chosen the following 4 strategies $\{c, d, q(\pi/4), q(\pi/2)\}$ and Fig. 7.4 shows the experimental payoffs for all possible combinations of the implemented strategies. For comparison, the expected, ideal payoff function is also shown as a surface plot. We find good agreement between the measured and expected values. The discrepancies are due to the non-ideal cluster state resource at hand. Unwanted correlations are known to affect the computation performed according to the one-way model in a protocol-dependent fashion [206]. Moreover, some of the payoffs corresponding to specific strategic moves played by A and B, suffer from the imperfect resource more than other, due to the specific nature of the measurement being performed. We emphasize that although we cannot implement $U(\alpha, 0)$ strategies with arbitrary α, our strategy space is still large enough to resolve the dilemma.

7.3   Discussion and outlook

We have experimentally demonstrated the application of a measurement-based protocol to realize a quantum version of the Prisoner's dilemma. Our implementation is based on entangled photonic cluster states and constitutes the first realization of a quantum game in the context of one-way quantum computing. Furthermore, our particular realization is especially suited for
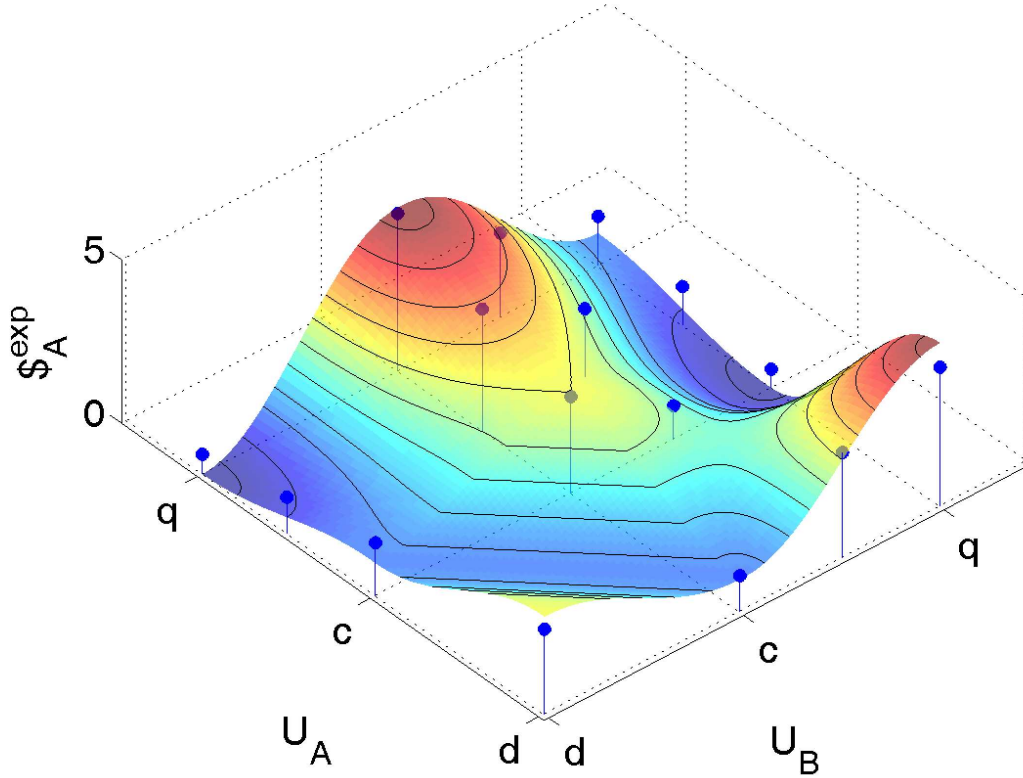
Figure 7.4: Graphical representation of the theoretical (surface) and measured (dots) payoffs of player A as a function of both players' strategies. The interval [d,c] is defined by the strategies $U_j(\theta,0)$ with $\theta \in [\pi,0]$ and [c,q] by the strategies $U_j(0,\phi)$ with $\phi \in [0,\pi/2]$. The strategy profile (d,d) is Pareto-optimal and a Nash equilibrium thus resolving the dilemma occuring in the classical version of the game.

playing between distant parties. Because all the entangling operations preparing the cluster state are done locally by the referee, it is easy to distribute the entangled photons, even over large distances. Here we note that, of course, the game can also be played using an ancillary entangled pair for the realization of the disentangling `CPHASE` gate. In this scenario, initially both players share one particle of an entangled photon pair and apply a polarization rotation on their respective photon $U_j(\theta_j,\phi_j)$ (corresponding to their chosen strategy). The photons are then sent to the referee who applies the disentangling operation with an ancillary, entangled pair [134]. However such an operation experimentally requires interferometric stability between the initial and the ancilla pairs, a very difficult experimental challenge if the players reside at distant locations.

Another interesting feature is that, in our demonstration, the entanglement generation is decoupled from the actual processing of the quantum mechanical information. It remains an open question whether applications of few qubit cluster states could facilitate some kind of remote quantum information processing, e.g. multi-party quantum communication protocols [207].

Nonetheless, we also expect that the simple nature of our demonstration will trigger further interest in the one-way model of quantum computation, in particular in the realization of simple quantum algorithms.

7.4 Appendix

In order to find the correspondence between the quantum circuit which describes the game, as depicted in Fig. 7.1, and the sequence of measurements on the cluster state, we compare the output state of the circuit for each chosen strategy to the corresponding output state of the one-way computation sequence. The output state of the circuit for the input state $|00\rangle$ is

$$|\psi\rangle_{out} = [H \otimes H] \cdot \texttt{CZ} \cdot [U_a(\theta_a, \phi_a) \otimes U_b(\theta_b, \phi_b)] \cdot \texttt{CZ} \cdot [H \otimes H] |00\rangle$$

where the `CPHASE` gate (`CZ`) is defined by

$$\texttt{CZ} = \begin{pmatrix} 1 & 0 & 0 & 0 \\ 0 & 1 & 0 & 0 \\ 0 & 0 & 1 & 0 \\ 0 & 0 & 0 & -1 \end{pmatrix}.$$

Table 7.3 shows the output states as a function of the player's local strategies. Projecting these states onto the computational basis leads to the payoffs shown in Table 7.4. When the (dis)entangling operations are removed from the circuit this payoff table reduces to the original Table 7.1.

A\B	c	d	$q(\alpha_B)$
c	$|00\rangle$	$-|11\rangle$	$\cos(\alpha_B)|00\rangle - i\sin(\alpha_B)|01\rangle$
d	$-|11\rangle$	$-|00\rangle$	$i\sin(\alpha_B)|10\rangle - \cos(\alpha_B)|11\rangle$
$q(\alpha_A)$	$\cos(\alpha_A)|00\rangle$ $-i\sin(\alpha_A)|10\rangle$	$i\sin(\alpha_A)|01\rangle$ $-\cos(\alpha_A)|11\rangle$	$\cos(\alpha_A)\cos(\alpha_B)|00\rangle - i\cos(\alpha_A)\sin(\alpha_B)|01\rangle$ $-i\sin(\alpha_A)\cos(\alpha_B)|10\rangle - \sin(\alpha_A)\sin(\alpha_B)|11\rangle$

Table 7.3: Output states from the game circuit as a function of players' A and B strategies. Although these states are separable, they cannot be obtained by local unitary operations and without the action of (dis-)entangling operations between the players.

A\B	c	d	$q(\alpha_B)$
c	$\$_A(c,c)$	$\$_A(d,d)$	$|\cos(\alpha_B)|^2\,\$_A(c,c) + |\sin(\alpha_B)|^2\,\$_A(c,d)$
d	$\$_A(d,d)$	$\$_A(c,c)$	$|\sin(\alpha_B)|^2\,\$_A(d,c) + |\cos(\alpha_B)|^2\,\$_A(d,d)$
$q(\alpha_A)$	$|\cos(\alpha_A)|^2\,\$_A(c,c)$ $+ |\sin(\alpha_A)|^2\,\$_A(d,c)$	$|\sin(\alpha_A)|^2\,\$_A(c,d)$ $+ |\cos(\alpha_A)|^2\,\$_A(d,d)$	$|\cos(\alpha_A)\cos(\alpha_B)|^2\,\$_A(c,c)$ $+ |\cos(\alpha_A)\sin(\alpha_B)|^2\,\$_A(c,d)$ $+ |\sin(\alpha_A)\cos(\alpha_B)|^2\,\$_A(d,c)$ $+ |\sin(\alpha_A)\sin(\alpha_B)|^2\,\$_A(d,d)$

Table 7.4: Payoffs for player A computed using the states from Table 7.3.

Next we show how a cluster state can be used to simulate the quantum circuit corresponding to the quantum game. The cluster state $|\Phi_c\rangle = \frac{1}{2}(|0000\rangle + |0011\rangle + |1100\rangle - |1111\rangle)_{1234}$ is projected onto a two photon state by projecting the qubit 1 and 4 onto the states $\cos(\theta_{1,4})|0\rangle_{1,4} + e^{i\varphi_{1,4}}\sin(\theta_{1,4})|1\rangle_{1,4}$. We verify that the remaining two-photon state is equivalent to the circuit outcome up to a local rotation on each remaining qubit. Before the rotation the state is

$$
\begin{aligned}
|\psi(\theta_1, \varphi_1; \theta_4, \varphi_4)\rangle_{23} \ = \ & \cos(\theta_1)\cos(\theta_4)|00\rangle_{23} + e^{i\varphi_4}\cos(\theta_1)\sin(\theta_4)|01\rangle_{23} \\
& + e^{i\varphi_1}\sin(\theta_1)\cos(\theta_4)|10\rangle_{23} - e^{i(\varphi_1+\varphi_4)}\sin(\theta_1)\sin(\theta_4)|11\rangle_{23}
\end{aligned}
$$

When Player A and B apply a rotation $R_j(\alpha_j, \beta_j, \gamma_j)$ on qubit 3 and qubit 2 respectively, the final output state is

$$
|\psi\rangle_{23}^{out} = R_B(\alpha_B, \beta_B, \gamma_B) \otimes R_A(\alpha_A, \beta_A, \gamma_A) |\psi(\theta_1, \varphi_1; \theta_4, \varphi_4)\rangle_{23}
$$

where

$$
R(\alpha, \beta, \gamma) = R_z(\alpha) R_x(\beta) R_z(\gamma) = \begin{pmatrix} e^{i(\alpha-\gamma)}\cos(\beta/2) & -e^{i(\alpha+\gamma)}\sin(\beta/2) \\ e^{i(\alpha-\gamma)}\sin(\beta/2) & e^{i(\alpha+\gamma)}\cos(\beta/2) \end{pmatrix}
$$

Table 7.5 shows the final states as a function of the strategies. Although they are not strictly equal to the output of the quantum circuit, those states lead to the same payoffs when measured in the computational basis. This proves the equivalence of both approaches and shows that it is necessary, in order to span the entire strategy space, to extend the cluster state scheme by allowing arbitrary one-qubit rotations. However, we note that the strategies $m = U(\alpha, 0)$ are not accessible because the output of the circuit for the strategy $(s_A, s_B) = (q(\alpha), c)$ is $\cos(\alpha/2)|00\rangle - \sin(\alpha/2)|11\rangle$. Such an output cannot be achieved using a cluster state of the form of Eqn. 7.2 for any α different from 0 or π. A six photon cluster state [69] would be required to implement the whole space of strategies $U_j(\theta_j, \phi_j)$.

A \ B	c	d	$q(\alpha_B)$
c	$\mathbb{1} \otimes \mathbb{1} \, |\psi(0;0)\rangle$	$-i\sigma_y \otimes \mathbb{1} \, |\psi(0;-\pi/2)\rangle$	$\mathbb{1} \otimes \mathbb{1} \, |\psi(0;\alpha_b)\rangle$
d	$-i \cdot \mathbb{1} \otimes \sigma_y \, |\psi(-\pi/2;0)\rangle$	$-\sigma_y \otimes \sigma_y \, |\psi(-\pi/2;-\pi/2)\rangle$	$-\mathbb{1} \otimes i\sigma_y \, |\psi(-\pi/2;\alpha_B)\rangle$
$q(\alpha_A)$	$\mathbb{1} \otimes \mathbb{1} \, |\psi(\alpha_A;0)\rangle$	$-i\sigma_y \otimes \mathbb{I} \, |\psi(\alpha_A;-\pi/2)\rangle$	$\mathbb{1} \otimes \mathbb{1} \, |\psi(\alpha_A;\alpha_B)\rangle$

Table 7.5: Table of the projected states and rotation angles corresponding to different strategies, with $\mathbb{1} = R_j(0,0,0)$, $-i\sigma_y = R_j(0,\pi,0)$ and $|\psi(\alpha_A;\alpha_B)\rangle = |\psi(\alpha_A,0;\alpha_B,0)\rangle_{23}$.

Chapter 8

Quantum computing in a decoherence-free subspace

Decoherence, the ubiquitous loss of information encoded in a quantum system due to its uncontrollable interaction with an environment, is one of the main obstacles in the grounding of quantum technology as a realistic scenario for ultra-fast and massively parallel information processing. It is easy to imagine that the accuracy of QIP protocols using cluster states is greatly affected by environment-induced decoherence and imperfections in the supporting quantum system. One possible approach to overcome this challenge is to perform QIP in a so-called decoherence-free subspace (DFS). In this Chapter a novel fault-tolerant scheme for the one-way quantum computing model is introduced that builds on previous work on concepts of DFS [208, 29, 28, 209, 210]. We have been able to theoretically adapt these concepts to the model of one-way quantum computing, which allowed us to demonstrate for the first time the decoherence-free execution of a one-way quantum computing protocol while the photons were exposed to severe symmetric phase-damping noise.

This chapter is organized as follows. First we introduce the concept of a special decoherence-free subspace (DFS) and develop a scheme that effectively uses this DFS in the one-way model to protect the quality of the entangled cluster states and the encoded information against random symmetric phase noise. We then proceed and experimentally implement our scheme by demonstrating a decoherence-free information transfer across a linear cluster state whose physical qubits are affected by phase-damping decoherence. Evaluating the performance of our DFS scheme using quantum process tomography, we find remarkable protection of the quantum information in the experiment, delivering nearly ideal outcomes, which convincingly shows the superiority of the DFS encoding.

8.1 Introduction

In the quest for the realization of accurate and efficient quantum information processing (QIP), protection from potentially destructive environmental effects is of the utmost importance [11]. There is no evidence in nature of a physical system which can be said to be totally immune

from some sort of decoherence mechanism. The design of fault-tolerant protocols is therefore necessary in order to achieve reliable QIP.

In a coarse-grained but yet effective picture, we can distinguish two relevant strategies to tackle this issue. The first, known as quantum error correction (QEC), deals with the correction of errors in computational processes by means of appropriate codewords [11, 211], in complete analogy with classical error correction. The second strategy, known as the decoherence-free subspace (DFS) approach, is intended to prevent or reduce the effects of a specific decoherence mechanism [29, 28, 209, 210]. It is based on the use of particular symmetries in the system-environment coupling and the search for a region of the Hilbert space inaccessible to the environment. Information can be encoded within such a robust subspace, which is usually spanned by entangled states of the system's constituents. In practice, a DFS approach is most effective whenever there is a dominant class of decoherence. It has been theoretically shown that DFS's can be efficiently concatenated with QEC codewords [212], the quantum Zeno effect [213] and methods of dynamical decoupling [214].

In the next Section we will show that it is possible to protect an entangled cluster state resource from symmetric phase-damping decoherence therefore allowing decoherence-free one-way quantum computing.

8.1.1   The DFS scheme

As briefly stated in the introductory part, in general certain symmetries in the system-environment interaction are required to effectively decouple the DFS from the environment and therefore to provide appropriate protection. One particular example of such a symmetry is that the qubits under consideration are subject to *collective* decoherence, i.e. the disturbances or noise that affect the qubits are identical, which can be seen as each individual qubit coupling to the environment in the same way [208]. This special decoherence model is applicable to experimental situations where the qubits are physically very close to each other and the environment cannot distinguish them. Whenever the system-environment interactions possess this sort of symmetry, the decoherence-free states that make up the DFS also exhibit this type of permutation symmetry. Indeed this particular type of symmetry is a often encountered condition for a DFS. Whenever quantum states display permutation symmetry they are in general also maximally entangled, such as e.g. the well-known Bell states $|\Psi^{\pm}\rangle$.

To illustrate[1] these concepts, let us consider a pair of qubits that is subject to an decoherence-inducing environment which adds random, but collective phase shifts ϕ_j to each qubit j. In the computational basis $\{0, 1\}$ the action of the environment can be written as [208]

$$
\begin{aligned}
|0\rangle &\rightarrow e^{i\phi_0} |0\rangle \\
|1\rangle &\rightarrow e^{i\phi_1} |1\rangle
\end{aligned}
\tag{8.1}
$$

If the two qubits under consideration display permutation symmetry, i.e. they are in a maximally entangled state of the form

$$
\left|\Psi^{-}\right\rangle_{12} = \frac{1}{\sqrt{2}} \left(|01\rangle - |10\rangle\right)_{12}
\tag{8.2}
$$

---

[1]Note that formally the density matrix formalism is required to describe the interaction of a state with its environment.

then the environment will induce the following phase shifts on the qubits of the Bell state

$$\left|\Psi^-\right\rangle_{12} \quad \rightarrow \quad \frac{1}{\sqrt{2}}\left(e^{i\phi_0}\left|0\right\rangle e^{i\phi_1}\left|1\right\rangle - e^{i\phi_1}\left|1\right\rangle e^{i\phi_0}\left|0\right\rangle\right) \tag{8.3}$$

$$= \quad \frac{1}{\sqrt{2}}e^{i(\phi_0+\phi_1)}\left(\left|01\right\rangle - \left|10\right\rangle\right)_{12}. \tag{8.4}$$

The global phase is unobservable therefore the initial state is preserved and effectively decoupled from the action of the environment. However, if the phase shifts for qubit 1 and 2 are not identical, i.e. not collective, then the phase shifts will not factor out. In this case the qubit will be left in a mixed state and the off-diagonal elements of the density matrix will vanish because of averaging over the random phases [208].

A closer investigation reveals that the state $\left|\Psi^-\right\rangle$ is not the only decoherence-free state. As already stated above, also the $\left|\Psi^+\right\rangle = 1/\sqrt{2}\left(\left|01\right\rangle + \left|10\right\rangle\right)$ exhibits permutation symmetry. However, the $\left|\Psi^+\right\rangle$ is only antisymmetric in the computational basis $\{0,1\}$. If the noise or phase shifts also act on the superposition basis $\{+,-\}$ then the phase shifts result in bit-flip errors. This can be seen by rewriting $\left|\Psi^+\right\rangle$ in the diagonal basis, $\left|\Psi^+\right\rangle = 1/\sqrt{2}\left(\left|++\right\rangle - \left|--\right\rangle\right)$. This state is no longer antisymmetric and the phases will therefore not factor out. Nevertheless, for a "pure dephasing" environment that only acts in the $\{0,1\}$ basis, $\left|\Psi^-\right\rangle$ and $\left|\Psi^+\right\rangle$ span a two-dimensional DFS that can be used to encode a logical qubit [208].

This concludes our introduction and exemplary illustration of a decoherence-free subspace. In the following we will show how the developed concepts of DFS can be applied to the one-way model of quantum computing in order to allow for noise-resilient measurement-based quantum information processing.

Applying the DFS scheme to the one-way model of quantum computing

The structure and operation of a DFS-encoded cluster state are different to the standard one in many respects. The first is that each physical qubit j initially prepared in the state $\left|+\right\rangle$ in the standard model, is replaced by a pair of qubits prepared in the state $\left|\Psi^-\right\rangle_{j_1 j_2} = 1/\sqrt{2}\left(\left|01\right\rangle - \left|10\right\rangle\right)_{j_1 j_2}$. The key step here is the use of the logical encoding

$$\begin{aligned}\left|0_L\right\rangle &\rightarrow \left|01\right\rangle \\ \left|1_L\right\rangle &\rightarrow \left|10\right\rangle\end{aligned} \tag{8.5}$$

which pairs two *physical* qubits into a single *effective* one. For ease of notation, we label each qubit pair as an effective qubit j'. Next, instead of the standard entangling CPHASE gates $\left|m\right\rangle_{q_1}\left|k\right\rangle_{q_2} \rightarrow (-1)^{mk}\left|m\right\rangle_{q_1}\left|k\right\rangle_{q_2}$ applied between all nearest-neighbour qubits q_1 and q_2 in the cluster, in the DFS-encoded scenario only the first or top level of qubits of all nearest-neighbour pairs are involved, as depicted in Fig. 8.1(a). The resulting entangled resource has an effective structure exactly the same as a cluster state [215]. Thus, one can use it for one-way QC, with the added benefit that it provides DFS protection from phase-damping (PD) decoherence, as will be see in the following.

The physical assumption we have made here concerning the noise affecting the so-prepared cluster state is that qubits along the z-axis are physically very close together, while qubits in
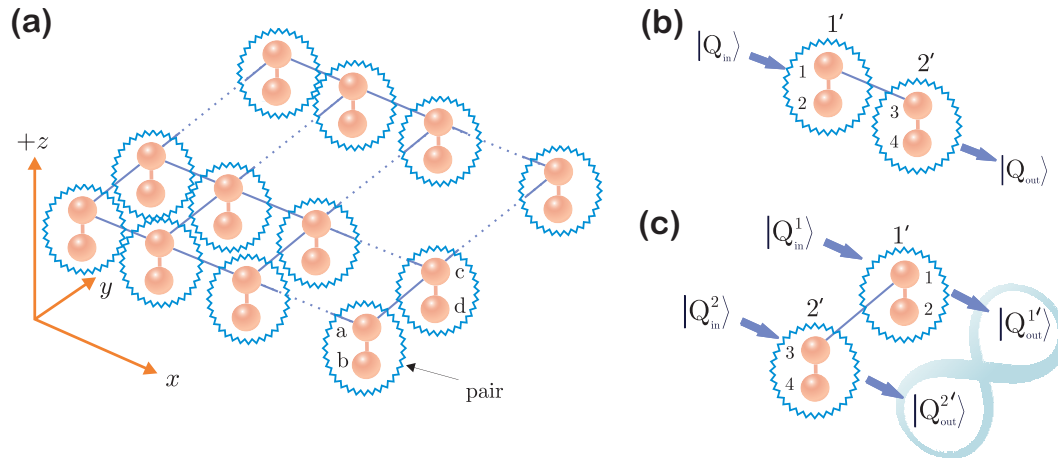
(a)

(b)

(c)

Figure 8.1: (a): The effective two-dimensional cluster state layout with each pair of physical qubits representing an encoded effective qubit. The pair of qubits that makes up the logical qubit reside physically very close to each other so that they couple to the environment in the same way, which is graphically depicted by the jagged surroundings. (b): Schematics for information transfer of a logical qubit $|Q_{\mathrm{in}}\rangle$ through the process of genuine one-bit teleportation. (c): Schematics for the simulation of a gate operation on two logical qubits $|Q^1_{\mathrm{in}}\rangle$ and $|Q^2_{\mathrm{in}}\rangle$.

the x-y plane across the lattice structure are at a larger and fixed distance from each other (see Fig. 8.1(a)). This way, each qubit in a pair couples to the same environment.

The encoded qubit state $|+\rangle_{j'}$ (equivalent to $|\psi^-\rangle_{j_1 j_2}$), before entanglement generation on the top layer, is invariant under phase-damping decoherence on the physical qubits, $|k_j\rangle \rightarrow e^{i\phi_k}|k_j\rangle$ $(j = 0, 1)$. Since any random phase shifts of this form commute with the entangling CPHASE operations on the top layer that produces the encoded cluster state, the final DFS state $|\phi\rangle_{\mathcal{C}'}$ is also unaffected by such environment-induced phase-damping [215]. This so-called *dual-rail* encoding [29] is well-known in providing robust protection against phase-damping decoherence, or more generally, against symmetrical multi-qubit environmental noise [216]. Combining this encoding technique with the entangling operations described above rotates the encoded cluster state $|\phi\rangle_{\mathcal{C}'}$ in a DFS for the phase-damping class of noise considered here. Such a protection is even robust against slight asymmetries in the system-environment coupling for qubits in a pair [217]. Phase damping is a major source of noise affecting many quantum systems such as trapped ions [218], NMR [219], optical lattices [220] and various photon-based communication systems [221, 222, 176]. The state $|\psi^-\rangle$ is insensitive to this noise in the symmetrical way mentioned above and can therefore be used to perform phase-damping resilient QIP in specially engineered registers [29, 28, 210, 209].

For a DFS-encoded cluster state to act as a one-way quantum computer requires the adaptation of the single-qubit measurements that enables it to process the quantum information. The key insight here is that every single-qubit measurement in the standard cluster state model has to be replaced with a measurement of two physical qubits in the DFS-case [215].

In order to show how information can be transferred across the effective cluster lattice shown in Fig. 8.1 (a), let us consider the prototypical configuration shown in Fig. 8.1 (b). In this case,

a normalized logical qubit $|Q_{\text{in}}\rangle = \mu |0_L\rangle_{1'} + \nu |1_L\rangle_{1'}$ is encoded on the effective qubit $1'$ which is represented by the physical qubits 1 and 2. After the entangling operations are performed on the top layer, the total state of the effective qubits $1'$ and $2'$ can be written as

$$|\phi\rangle_{\text{DFS}} = \mu |0_L, +_L\rangle_{1'2'} + \nu |1_L, -_L\rangle_{1'2'} \tag{8.6}$$

with $|\pm_E\rangle = (1/\sqrt{2})(|0_L\rangle \pm |1_L\rangle)$. Propagating information across these effective sub-clusters can be accomplished via two strategies. Depending on the physical setup, one strategy may be preferable to the other. The first is to perform a joint measurement on a pair of qubits comprising an effective qubit j' in the basis $B_{j'}(\alpha) = \{|\psi^{+\alpha}\rangle_{j'}, |\psi^{-\alpha}\rangle_{j'}\}$ with outcomes $s_{j'}^{\alpha} = \{0, 1\}$ and $|\psi^{\pm\alpha}\rangle_{j'} = (1/\sqrt{2})(|01\rangle \pm e^{i\alpha} |10\rangle)_{j_1' j_2'}$. In the case of $j' = 1'$ in Eqn. 8.6 this strategy simulates the transformation [215]

$$|Q_{\text{out}}\rangle = \sigma_x^{s_{1'}^{\alpha} \oplus 1} H R_z^{-\alpha} |Q_{\text{in}}\rangle \tag{8.7}$$

on the logical qubit $|Q_{\text{in}}\rangle$, where $R_z^{-\alpha}$ is a single-qubit z-rotation in the Bloch sphere by an angle $-\alpha$.

In linear-optics experiments, an alternative method turns out to be preferable since it relies on single-qubit measurements only and is therefore easier to implement. The strategy is to perform single-qubit measurements on j_1' and j_2' in the bases $B_{j_1'}(\alpha) = \{|+\alpha\rangle_{j_1'}, |-\alpha\rangle_{j_1'}\}$ and $B_{j_2'}(0) = \{|+\rangle_{j_2'}, |-\rangle_{j_2'}\}$ with outcomes $s_{j_{1,2}'}^{\alpha} = \{0, 1\}$ and $|\pm\alpha\rangle_{j_k'} = (1/\sqrt{2})(|0\rangle \pm e^{i\alpha} |1\rangle)_{j_k'}$ $(j = 1, 2)$. For $j' = 1'$, $i_k' = k$, this simulates the transformation

$$|Q_{\text{out}}\rangle = \sigma_x^{s_{j_1'}^{\alpha} \oplus s_{j_2'}^{0} \oplus 1} H R_z^{-\alpha} |Q_{\text{in}}\rangle \tag{8.8}$$

on the logical qubit [215].

Let us now consider the situation depicted in Fig. 8.1 (c). Here we have two logical input qubits, denoted $|Q_{\text{in}}^1\rangle$ and $|Q_{\text{in}}^2\rangle$. If no measurements are performed on the qubit pairs and the two-qubit gate CPHASE^{13} is applied to the top-layer physical qubits 1 and 3, a state that simulates the outcome of the effective gate CPHASE$^{1'2'}$ being applied to the logical qubits $1'$ and $2'$ is obtained [215]. These two examples represent the DFS-encoded version of the basic building blocks of any quantum computation, namely a universal set of single- and two-qubit gates. From the above discussions, one can clearly see how similar the simulations on encoded cluster states are to the original one-way model.

All the computational steps can be performed within the DFS and at no point during the computation is the effective cluster state exposed to phase-damping type decoherence. In the case of an ideal cluster-resource being produced, this allows the noise effects to be canceled exactly. However in a real experiment, due to imperfections at the cluster generation stages, we only obtain a state having non-unit overlap with the ideal resource $|\phi\rangle_{C'}$. This results in an effective resource that is partially residing outside the DFS and it is only this fraction that is prone to environmental effects. The benefits of this proposal should now be clear: Encoding in a protected DFS provides us with a method of reducing greatly decoherence processes (ideally, their complete cancelation) in such a way that avoids the use of *a posteriori* procedures for correcting the resulting errors.

8.1.2   Characterization and evaluation of the scheme

In the experiment it seems natural to determine and characterize the effectiveness of our DFS encoding when compared to a standard, non-DFS computation. Below we describe a general operative way to evaluate the effectiveness of the noise protection for one-way quantum computing when utilizing the DFS encoding outlined above. This can be efficiently done by characterizing the effective transformation the logical state of undergoes during the computational process in the presence of a noisy environment. This characterization requires the use of *quantum process tomography* [11], which has already been introduced in Section 2.4.3.

A general formalism frequently used for describing the effect of noise on a quantum system relies on the so-called Kraus operators[2] $\{\hat{K}_i\}$ which are used to describe the interaction of quantum systems in an operational way. According to the operator-sum representation [11], a trace-preserving completely positive map $\mathcal{E}$, also called "channel", which transforms a single-qubit input state ϱ into the output density matrix $\mathcal{E}(\varrho)$ can be formally written as

$$\varrho \to \mathcal{E}(\varrho) = \sum_i \hat{K}_i \varrho \hat{K}_i^\dagger, \tag{8.9}$$

Here the Kraus operators $\{\hat{K}_i\}$ satisfy the completeness relation $\sum_i \hat{K}_i^\dagger \hat{K}_i = \mathbb{1}$.

The characterization of the channel then reduces to the determination of the $\hat{K}_i$'s. By choosing a complete set of orthogonal operators $\{\hat{\mathcal{K}}_m\}$ over which we expand $\hat{K}_i = \sum_m e_{im} \hat{\mathcal{K}}_m$ we can write Eqn. 8.9 as

$$\mathcal{E}(\varrho) = \sum_{m,n} \chi_{mn} \hat{\mathcal{K}}_m \varrho \hat{\mathcal{K}}_n^\dagger \tag{8.10}$$

with $\chi_{mn} = \sum_i e_{im} e_{in}^*$ being the *channel matrix*. Therefore it is sufficient to consider a fixed set of operators $\{\hat{\mathcal{K}}_m\}$, which characterize a channel through the process matrix χ. The χ matrix elements can be found by performing quantum process tomography as outlined in Section 2.4.3.

Formal introduction to the phase-damping channel

To test the DFS protection and to evaluate the efficacy of our scheme in the experiment, phase-damping noise is applied to the physical qubits (i.e. photons) during information transfer in both the standard and DFS-encoded cases. For the DFS-encoded cluster, symmetric noise is applied to qubit pairs $1' = (1a, 1b)$ and $2' = (2a, 2b)$, while for the standard cluster, noise is applied to qubits 1 and 2 (see Fig. 8.2).

For a phase-damping channel acting on a single qubit, a detailed calculation leads to the non-zero Kraus operators

$$\begin{aligned}
\hat{K}_1 &= 1/\sqrt{2} \left(1 + e^{-\Gamma t}\right)^{1/2} \mathbb{1} \\
\hat{K}_2 &= 1/\sqrt{2} \left(1 - e^{-\Gamma t}\right)^{1/2} \sigma_z
\end{aligned} \tag{8.11}$$

with Γ the strength of the system-environment coupling and t the interaction time. In our experiment, we simulate symmetric phase-damping noise for the worst case scenario, i.e. for

---

[2]The so-called *quantum operation formalism* was introduced in 1983 by K. Kraus [223]. It allows to express (quantum) operations such as measurements or interactions of a quantum system with an environment as a mapping from density states to density states.
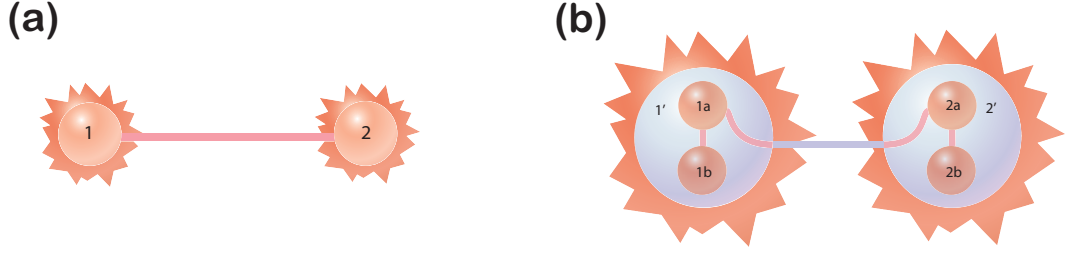
Figure 8.2: Cluster state configuratiosn. In (a) a two-qubit standard cluster state is shown, while in (b) we present the DFS-encoded cluster state. Each effective qubit (blue sphere) is represented by two physical qubits prepared in $|\Psi^-\rangle_{ja,jb}$. Since is locally equivalent to a standard two-qubit cluster state (the local rotations being $\mathbb{1}_1 \otimes (\sigma_x \sigma_z H)_2$, the pairwise entanglement operations that build up larger clusters commute with each other. Therefore, an arbitrary sized DFS-encoded cluster state can be created.

the limit $\Gamma t \to \infty$ which corresponds to a channel with $\hat{K}_1 = \left(1/\sqrt{2}\right)\mathbb{1}$, $\hat{K}_2 = \left(1/\sqrt{2}\right)\sigma_z$ and therefore to a full destruction of coherences in a single-qubit state. In this limit, the noise experienced by each qubit pair (a, b) is the same but still *independent*. The noise can be different in general, making our DFS encoding suitable for other setups such as optical lattices and ion traps [215].

In the DFS-encoded case, the action of symmetric noise on the state of the entire system $\rho_{DFS} = |\Phi_{DFS}\rangle \langle \Phi_{DFS}|$ can be written by applying the map defined by the Kraus operators of Eqn. 8.11 to each physical qubit of the cluster. The output state is then given by

$$\varepsilon(\rho_{\text{DFS}}) = \frac{1}{4}\left[\rho_{\text{DFS}} + \sigma_z^{1a} \otimes \sigma_z^{1b} \otimes \mathbb{1}^{2a,2b} \rho_{\text{DFS}} \, \sigma_z^{1a} \otimes \sigma_z^{1b} \otimes \mathbb{1}^{2a,2b}\right. \tag{8.12}$$

$$+ \quad \mathbb{1}^{1a,1b} \otimes \sigma_z^{2a} \otimes \sigma_z^{2b} \rho_{\text{DFS}} \, \mathbb{1}^{1a,1b} \otimes \sigma_z^{2a} \otimes \sigma_z^{2b} \tag{8.13}$$

$$+ \quad \left. \sigma_z^{1a} \otimes \sigma_z^{1b} \otimes \sigma_z^{2a} \otimes \sigma_z^{2b} \rho_{\text{DFS}} \, \sigma_z^{1a} \otimes \sigma_z^{1b} \otimes \sigma_z^{2a} \otimes \sigma_z^{2b}\right]. \tag{8.14}$$

and in the standard cluster state scenario, for the density matrix $\rho_C = |\Phi_C\rangle \langle \Phi_C|$ of a two-qubit cluster $\rho_C = 1/\sqrt{2}\left(|0, +\rangle + |1, -\rangle\right)_{12}$ by

$$\varepsilon(\rho_C) = \frac{1}{4}\left[\rho_C + \sigma_z^1 \otimes \mathbb{1}^2 \rho_C \sigma_z^1 \otimes \mathbb{1}^2 + \mathbb{1}^1 \otimes \sigma_z^2 \rho_C \mathbb{1}^1 \otimes \sigma_z^2 + \sigma_z^1 \otimes \sigma_z^2 \rho_C \sigma_z^1 \otimes \sigma_z^2\right]. \tag{8.15}$$

A logical state $|Q_{in}\rangle$ encoded into ρ_C and transferred across the cluster under the action of the channel described by Eqn. 8.15 will result in the maximally mixed output state $(1/2)\,\mathbb{1}$. On the other hand, Eqn. 8.12 will perfectly preserve the coherences of the state $|Q_{in}\rangle$ encoded into ρ_{DFS} during the transfer.

By means of quantum process tomography (QPT) [122, 11] we can experimentally determine the *logical* transfer channels $\varepsilon_{\text{L}}(\rho_{in})$ (with $\rho_{in} = |Q_{in}\rangle \langle Q_{in}|$) while the physical qubits are exposed to noise. With this apparatus, the reconstruction of the effect of ε_{L} on the set of logical input states (*probe states*) $\{|0\rangle, |1\rangle, |+\rangle, |L\rangle\}$ is enough for a full characterization of the physical process encompassed by the logical channel. Thus, we have implemented the DFS protocol by encoding the probe states onto photons $1a$ and $1b$ of the four-photon DFS cluster depicted in Fig. 8.2(b). Although arbitrary logical inputs are not possible in our setup, through

tailored measurement patterns (as described below) it is possible to encode all probe states. We remark that in principle, arbitrary encoding is not necessary for sufficiently large clusters [14].

8.2 Experimental demonstration and results

8.2.1 Introduction

Despite the existence of a threshold for fault-tolerance and its quantitative estimate for the case of linear-optics implementations [224], there has so far been no experimental realization of noise-resilient one-way computation. This constitutes a vital step toward the upgrading of the model as a viable route for scalable quantum computation. Here we perform such an important step by designing and experimentally demonstrating the encoding of a four-qubit photonic entangled resource into a DFS cluster state. We show that the combination of measurement-based QIP and passive protection from noise is effective in manipulating information, shielded from the action of an undesired symmetric phase-damping mechanism. The model, which is complementary to the proposed use of QEC in a one-way scenario [225], has the potential to be scaled to larger cluster states [215]. In our experiment we successfully demonstrate an encoded version of the key building block on which the one-way model is built—i.e. genuine teleportation [14, 205] in the form of a one-way information transfer protocol—across a photonic cluster state protected from multi-qubit symmetric phase-damping noise. The experimental linear-optics realization we have employed in order to verify our theoretical predictions demonstrates processing outcomes strikingly close to the ideal situation where decoherence is not present. Linear optics is at the forefront of experimental implementations of the one-way model, therefore representing the most appropriate and accessible test-bed for the DFS one-way model. The inherent manipulability of a linear-optics setup guarantees the successful controlled engineering of the decoherence mechanism we wish to test. However the DFS scheme is independent of the physical implementation and the theoretical model is effective in any other physical setup affected by the phase damping described here.

Experimentally, DFS's have been tested in setups of linear optics [208, 196, 226], trapped ions [218] and nuclear magnetic resonance [219, 227] (NMR). Here, in contrast to most of the earlier implementations which focused on the generation and verification of a DFS, and in line with the work of Refs. [208, 227], we utilize DFS states in a scheme to successfully process quantum information in a controlled system explicitly subject to noise.

8.2.2 Experimental implementation

To perform the information transfer protocol, we start by creating a linear cluster state

$$|\Phi_{lin}\rangle = \frac{1}{2}(|0000\rangle - |0011\rangle - |1100\rangle - |1111\rangle)_{1a1b2a2b} \qquad (8.16)$$

by using the setup illustrated in Fig. 8.3(a) (the subscripts label the photon modes). This technique was extensively discussed in previous Chapters (4 and 5) and is a standard tool for the generation of four-photon clusters [73, 228]. The cluster state creation is based on a

postselection technique that ensures that photon loss and detector inefficiency do not affect the experimental results.

The cluster state $|\Phi_{lin}\rangle$ is rotated into the DFS cluster

$$|\Phi_{DFS}\rangle = \frac{1}{2}(|0101\rangle - |0110\rangle - |1001\rangle - |1010\rangle)_{1a1b2a2b} \qquad (8.17)$$

by applying $\sigma_x\sigma_z$ to qubits $1b$ and $2b$, where $|0\rangle$ ($|1\rangle$) is embodied by the horizontal (vertical) polarization of a photon. The DFS state creation is verified by performing an over-complete state tomography [120] thereby reconstructing the density matrix of the DFS cluster. We use 1296 measurements (each taking 350 sec) and a maximum-likelihood (ML) function on all combinations of polarization-projections on the qubits, *i.e.* $\{|0/1\rangle; |\pm\rangle; |L/R\rangle\}$, where $|\pm\rangle$ denote $\pm 45°$ polarization and $|L/R\rangle$ stand for left/right circular polarization. The experimental state ρ_{exp} has a state fidelity[3] of $F_{DFS} = \langle\Phi_{DFS}|\rho_{exp}^{DFS}|\Phi_{DFS}\rangle = 0.70 \pm 0.01$ with the ideal DFS-cluster. During the tomography process, we simultaneously monitor and correct phase drifts in our setup which results in an increased cluster state fidelity as compared to previous experiments.

We also utilize a two-qubit standard cluster state ρ_{exp}^C to perform the non-DFS scenario. This standard cluster arises out of the 4-qubit cluster resource ρ_{exp}^{lin} which is produced within our setup, by measuring photons 1a and 2b in the σ_x-eigenbasis (i.e. $B_{1a}(0), B_{2b}(0)$). This transfers the initial input state to the remaining photons $1b$ and $2a$, which form an entangled two-qubit cluster state $|\Phi_C\rangle = (1/\sqrt{2})(|0,+\rangle + |1,-\rangle)_{12}$. Since this cluster is composed of only two qubits, 36 instead of 1296 local polarization measurements are sufficient to experimentally reconstruct the state's density matrix. The tomography data yields a maximum likelihood density matrix that has a state fidelity of $F_C = \langle\Phi_C|\rho_{exp}^C|\Phi_C\rangle = 0.74 \pm 0.02$ with the ideal two-qubit cluster. Tomographic plots of both the DFS-encoded as well as of the standard cluster resources are shown in Fig. 8.4.

For a standard cluster state, there are two types of single-qubit measurements that enable a one-way quantum computer to operate [14, 73]. First, by measuring the state of qubit j in the computational basis $\{|0\rangle_j, |1\rangle_j\}$, we disentangle it and shape the resource, leaving a smaller cluster. Second, in order to perform QIP, qubits must be measured in the basis $B_j(\alpha) = \{|\alpha_\pm\rangle_j = \frac{1}{\sqrt{2}}(|0\rangle \pm e^{i\alpha}|1\rangle)_j\}$ ($\alpha \in \mathbb{R}$). This applies a single-qubit rotation $R_z(\alpha) = \exp\left(-\frac{i}{2}\alpha\sigma_z\right)$, followed by a Hadamard operation H to a logical qubit residing on site j in the cluster ($\sigma_{x,y,z}$ are the Pauli matrices). With proper choices for the $B_j(\alpha)$'s, any quantum gate can be performed on a large enough cluster state.

We use the scheme in Fig. 8.1 to demonstrate DFS quantum information transfer. Recall that the structure and operation of a DFS cluster state are significantly different from the standard one. A logical qubit $|Q_{in}\rangle = \mu|0\rangle + \nu|1\rangle$ (with $|\mu|^2 + |\nu|^2 = 1$) is encoded on effective qubit $1'$ embodied by qubits $j_a = 1a$ and $j_b = 1b$. After the entangled resource is prepared, we obtain the DFS state $|\Phi_{DFS}\rangle = \mu|0_L, +_L\rangle_{1'2'} + \nu|1_L, -_L\rangle_{1'2'}$. Information is transferred across $|\Phi_{DFS}\rangle$ by measuring the state of the qubits in $B_{1a}(\alpha)$ and $B_{1b}(0)$, where α determines the operation $HR_z(\alpha)$ on $|Q_{in}\rangle$. This can be compared to the case of a standard cluster (see Fig. 8.2(b) with $B_1(\alpha)$).

---

[3]The uncertainties in the state fidelities is from a 100 run Monte Carlo simulation of the tomography analysis with Poissonian noise added to the count statistics in each run.
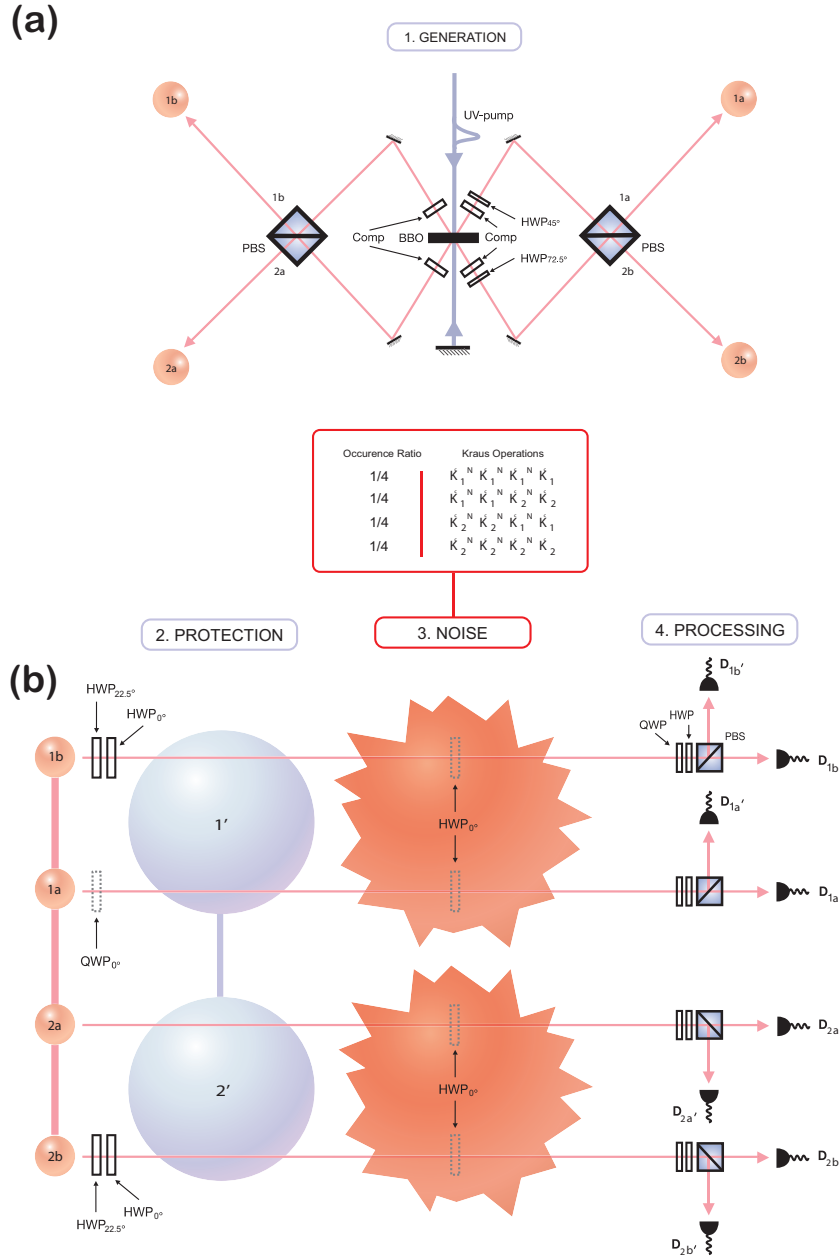
(a)

(b)

Figure 8.3: Experimental scheme. The optical *generation* stage is shown in (a), while (b) depicts the *protection*, *noise* and *processing* stages that create and manipulate the protected DFS cluster state. A UV femto-second laser pulse with 1 W of cw-power pumps a non-linear crystal (BBO) in a double-pass configuration. Compensation of walk-off effects in the crystal leads to the emission of Bell states ($|\Phi^-\rangle$ and $|\Phi^+\rangle$ in the forward and backward direction, respectively). Coherent combination of these states on polarizing beam-splitters (PBS) and postselection yields a cluster state with a rate of ~ 1 Hz in output modes $1a, b$ and $2a, b$. This linear cluster is rotated into a DFS cluster by $\sigma_x\sigma_z$ operations on modes $1b$ and $2b$ using HWP's. Probe state $|L\rangle$ is encoded with an additional QWP in mode $1a$. Phase-damping noise is implemented by inserting HWPs at $0°$ (σ_z operation) between the *protection* and *processing* stages. Polarization measurements in arbitrary bases are performed using analyzers consisting of a PBS, preceded by a HWP and QWP.
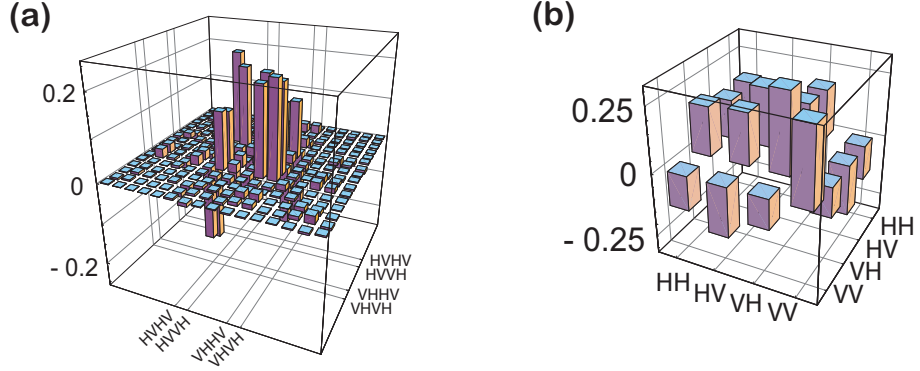
Figure 8.4: Tomographic plots of the real parts of the experimental density matrices for four-qubit DFS cluster state in (a) and for the two-qubit standard cluster state in (b). Imaginary parts are on average < 0.05 and therefore not shown. The density matrices were reconstructed using a maximum likelihood method from data obtained in 1296 (36) different measurement settings for the four-qubit DFS (two-qubit standard) cluster state. Their respective state fidelities with the ideal states are 0.70 ± 0.01 and 0.74 ± 0.02 for (a) and (b).

To test the scheme, phase-damping noise is applied to the physical qubits (i.e. photons) during the information transfer in both the standard and DFS-encoded cases. For the DFS-encoded cluster, we consider symmetric noise on qubit pairs ($1a, 1b$ and $2a, 2b$), while for the standard cluster, noise is applied to qubits 1 and 2 which results in the overall dynamics $\mathcal{E}(\varrho)$ undergone by the state as given in Eqns. 8.12 and 8.15.

As we have already seen in Section 8.1.2 a logical input state $|Q_{in}\rangle$ encoded into Φ_C will result in the maximally mixed output state $(1/2)\,\mathbb{1}$. On the other hand, encoding the state into Φ_{DFS} will perfectly preserve the coherence of the quantum information during the transfer.

We aim for an experimental determination of the logical transfer channels $\mathcal{E}_L(\varrho_{in})$ where $\varrho_{in} = |Q_{in}\rangle\langle Q_{in}|$, while the qubits are exposed to severe phase-damping noise. To achieve this task, we use quantum process tomography (QPT) [122, 11, 126], as described in Section 8.1.2 (and in more detail also in Section 2.4.3). Again we stress at this point that a certain set of logical input states (the probe states) $\{|0\rangle, |1\rangle, |+\rangle, |L\rangle\}$ is enough for a full characterization of the physical process encompassed by such a logical channel.

For the DFS cluster, by measuring photon $1b$ in $|1\rangle$, we encode the probe state $|0\rangle$ on effective qubit $1'$. Then measuring photon $1a$ in $|+\rangle = |(\alpha = 0)_+\rangle$ we transfer the logical state across the cluster to $2'$ (embodied by $2a$ and $2b$). Analogously the other probe states are encoded and transferred by the measurement patterns $B_{1a}(0), |0\rangle_{1b}$ for $|1\rangle$, $B_{1a}(0), B_{1b}(0)$ for $|+\rangle$ and $B_{1a}(0)R_z(\pi/2), B_{1b}(0)$ for $|L\rangle = |(\alpha = \pi/2)_-\rangle$. Note that for the logical $|L\rangle$ input, a quarter-wave plate (QWP) at $0°$ has been placed in mode $1a$, effectively realizing the rotation $R_z(\pi/2)$. For each of these input states, we perform an over-complete two-qubit state tomography [120] of the output qubits $2a$ and $2b$. This is then repeated with phase damping noise added to the system, i.e. by applying half-wave plates (HWP's) at $0°$ (realizing $\hat{K}_2 = \sigma_z$) to the photons. As the occurrence-ratio in time of $\hat{K}_i$'s is dictated by the state given in Eqns. 8.12 and 8.15, we

apply the HWP combinations in sequence, each for 1/4 of the duration of the tomography process (as shown in the box of Fig. 8.3(b)). This full realization of complete symmetric phase-damping noise is in striking contrast with simpler phase-flip mechanisms frequently adopted in previous experimental characterizations of photonic DFS's [208].

8.2.3   Results

From this set of data (1728 measurements in total), we are able to reconstruct the complete effect of the transfer channel $\mathcal{E}_L(\varrho_{in})$ using QPT. This study allows us to determine the state onto which each transfer channel maps an arbitrary pure logical input state $|Q_{in}\rangle = \mu|0\rangle + \nu|1\rangle$ ($|\mu|^2 + |\nu|^2 = 1$). The action of the channel can be visualized by considering the correspondence between a single-qubit density matrix and its Bloch vector [11]. Taking $|Q_{in}\rangle$ from a large set of values for μ and representing their output states from the QPT-reconstructed transfer channel in a three-dimensional space, allows us to depict the deformation of the single-qubit Bloch sphere induced by the experimental logical channel. We believe this technique to be very useful in order to clearly visualize the overall effect of the channels. The results of this visualization process are shown in Fig. 8.5(a) for the case of a DFS-encoded channel with and without noise. The protection from phase-damping effects is striking: the Bloch sphere for the noise-affected DFS-encoded state is almost identical to the case without phase-damping noise. An informative way to quantify the closeness of two experimental channels is to consider the output state fidelity averaged over μ. We find an average state fidelity[4] of 0.991±0.003.

The benefit of the DFS-protocol should of course be evaluated with respect to the standard case. Therefore, we have run an experiment where a two-qubit cluster state (generated out of the four-photon resource, as described above) is used for the information transfer protocol. As before, the input state is transferred across the cluster with and without phase-damping noise applied. We have chosen the measurement pattern $B_{1a}(0), |0\rangle_{1b}, |+\rangle_{2a}$ for the probe state $|0\rangle$, $B_{1a}(0), |1\rangle_{1b}, |+\rangle_{2a}$ for $|1\rangle$, $B_{1a}(0), |+\rangle_{1b}, |+\rangle_{2a}$ for $|+\rangle$ and $B_{1a}(0), |+\rangle_{1b}, |+\rangle_{2a}$ for $|L\rangle$ with an extra QWP, as in the DFS case. This time, the single-qubit operations that rotate the cluster into the DFS are not present. The output state—that is the remaining photon—is analyzed using single-qubit state tomography while the channels with and without noise being applied are analyzed using QPT. The resulting deformation of the Bloch sphere is shown in Fig. 8.5(b). By comparison with Fig 8.5(a), it is evident that the standard noise-free channel is very close to the analogous DFS-encoded situation. However, we now see that if the information is not shielded by a DFS encoding, the induced environment is affecting the quantum information in a severe way. The output states in the presence of noise suffer strong decoherence effects, resulting in a significant shrinking of the Bloch sphere and an almost complete loss of coherence. This is even more evident by closely analyzing the output density matrix resulting from an input state $|Q_{in}\rangle$, whose average state fidelity with the maximally mixed state $(1/2)\mathbb{1}$ (resulting from an ideal full phase-damping process) is 0.994 ± 0.002. Clearly, the information initially encoded in the standard cluster resource has almost entirely been "washed away" by the noise.

We can also complement such a comparison by means of the reconstructed process matrices

---

[4]Again, the uncertainties associated with this parameters were estimated by performing a 100 run Monte Carlo simulation of the QPT analysis, with Poissonian noise added to the count statistics in each run.
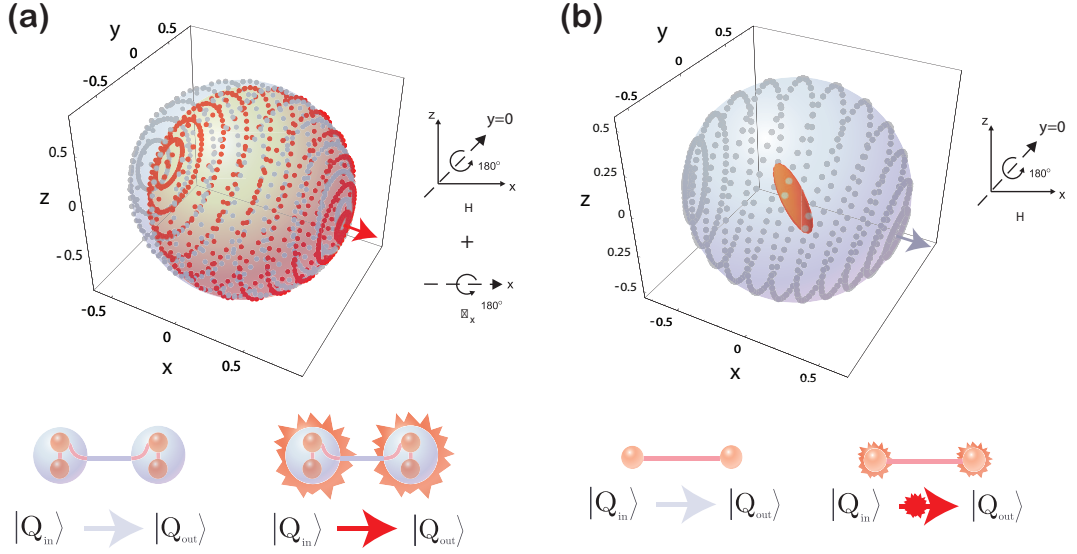
Figure 8.5: Quantum process tomographic plots of the information transfer protocol. In (a) ((b)) we show the QPT-reconstructed Bloch spheres corresponding to the use of a DFS-encoded (standard) cluster state and the information transfer protocol we experimentally realize for measurement outcomes $|+, +\rangle_{1a1b}$ ($|+\rangle_1$). Underneath, we show the corresponding configuration for the protocol (noise is represented by the jagged red surroundings). The light-blue sphere shows the case of no noise being applied to the system, while the inner red one is for an environment-exposed channel. While the comparison in (a) reveals striking protection of the processed quantum information (the *quantum process fidelity* is 0.95 ± 0.02), (b) shows that in a non-protected scenario information is almost completely lost, which is reflected in the low process fidelity of 0.53 ± 0.02, which consistent with the value for a maximally mixed output state of a noise-affected standard resource $(1/2)\mathbb{1}$. The shape of the inner ellipsoid in (a) is due to small coherences in the reconstructed density matrix stemming from noise affecting the encoding of $|L\rangle$ and leads to non-zero x and y components of the Bloch vectors. This coherences can be reduced by simulating a better encoding of $|L\rangle$. Therefore a better quality cluster state would help in obtaining an increased overlap of the two experimental Bloch spheres. The orientation of the pole of the Bloch sphere corresponding to the logical $|0\rangle$ input state, shown by an arrow in (a) ((b)), is in agreement with the expected transformation $\sigma_x H$ (H) being applied during the computation of the protocol (see insets). The dots represent output states corresponding to the action of the channel on pure input states $|Q_{in}\rangle$ for various choices of μ.

of these two channels. Indeed, an informative quantity is the *process fidelity* [11] which measures the closeness of generic processes characterized by the matrices χ_1 and χ_2 and is given by

$$\mathcal{F}(\chi_1, \chi_2) = \text{Tr}\left(\sqrt{\sqrt{\chi_1}\chi_2\sqrt{\chi_1}}\right)^2 \tag{8.18}$$

The process fidelity between the DFS-encoded information transfer with and without noise is $\mathcal{F}(\chi_{noise}^{DFS}, \chi_{no-noise}^{DFS}) = 0.95 \pm 0.02$, in excellent agreement with the large state fidelity mentioned above. On the other hand, an analogous calculation involving the cases where standard cluster states are used for the realization of the protocol leads to the value $\mathcal{F}(\chi_{noise}^{standard}, \chi_{no-noise}^{standard}) =$

0.53 ± 0.02. This is only slightly different from 0.52, the value for the process fidelity that we would have obtained if the output state resulting from the use of a standard cluster state affected by noise was maximally mixed. This analysis confirms the closeness of a non-protected channel, exposed to environmental decoherence, to a maximally mixed state and thus provides strong evidence regarding the effectiveness of the noise-protection the DFS cluster provides.

8.3   Conclusion and outlook

In summary, we have designed and experimentally demonstrated a strategy to protect a one-way quantum protocol from symmetric, multi-qubit phase-damping noise. We have combined, for the first time, one of the most promising models for quantum computing and an effective strategy for information protection. Our DFS technique represents an important simplification with respect to other current proposals for noise-resilient measurement-based quantum computing. The effectiveness of the proposed DFS one-way model has been established in a proof-of-principle experiment conducted in a linear optics setting, where excellent shielding of information processed in a genuine quantum mechanical way has been found. This successful experimental verification and the setup-independent nature of the model [215] guarantee its applicability to any physical situation where symmetric phase-damping noise is a dominant source of error. Conceptually, the model also holds the promise of a generalization to any form of symmetric noise, i.e. where the decoherence that affects the individual qubits is identical [208].

So far, we have only considered phase-damping mechanisms in our scheme. However it is possible to extend our ideas and construct a DFS which offeres protection from all types of from symmetric noise [215, 219]. The encoding in this case is then given by

$$
\begin{aligned}
|0_L\rangle_{1'} &:= (1/\sqrt{2})(|10\rangle - |01\rangle)_{12} |0\rangle_3 \\
|1_L\rangle_{1'} &:= (2/\sqrt{6}) |0\rangle_1 (|10\rangle - |01\rangle)_{23} + (1/\sqrt{6})(|10\rangle - |01\rangle)_{12} |0\rangle_3
\end{aligned} \tag{8.19}
$$

where now three entangled physical qubits (instead of two) embody a single effective cluster qubit. However, it is important to note that in this scheme encoding and decoding stages are required to protect and recover the information encoded in the cluster state [215]. Therefore, it remains to be seen whether this is the most economical or optimal method. Developments of similar schemes with minimal possible resource requirements would represent a powerful and novel technique for the protection of one-way quantum computers exposed to environmental effects. The associated resource overheads in terms of physical qubits could be bypassed by using additional degrees of freedom within the same physical information carrier, e.g. hyper-entangled states [77, 76]. An extension to more general forms of environment will require the integration of DFS's with other tools for environmental protection [212, 214] and is most certainly a stimulating challenge.

8.4 Appendix

8.4.1 Determination of a physical process matrix

Quantum Process tomography (QPT) [11, 123, 229, 230] is a well-established mathematical apparatus allowing for the faithful reconstruction of the action of a channel $\mathcal{E}$ through the experimental determination of its effects on the set of probe states $\{|0\rangle, |1\rangle, |+\rangle, |L\rangle\}$. By using the linearity of $\mathcal{E}$ and the experimentally acquired data, we can infer the action of the channel over any generic single-qubit input $\varrho_{in} = |Q_{in}\rangle \langle Q_{in}|$. The output state of the logical qubit as determined by the channel can be written as

$$\mathcal{E}_L(\varrho_{in}) = \sum_{m,n} \chi_{mn} A_m \varrho_{in} A_n^\dagger \tag{8.20}$$

with the process matrix χ and the standard set of operations $\{A_1 = \mathbb{1}, A_2 = \sigma_x, A_3 = -\sigma_y, A_4 = \sigma_z\}$ that spans the space of all allowed single-qubit operations and thus constitutes a basis upon which the map can be decomposed. The determination of the process matrix χ is equivalent to a full characterization of $\mathcal{E}$, i.e. in our case, of the channel resulting from the information transfer protocol being applied to the information-encoded cluster state resource.

We experimentally determine the process matrix χ following the technique described in the main text. As $\mathcal{E}$ is completely positive, the corresponding process matrix must be Hermitian and positive semi-definite. However, quantum noise affecting the measurements being performed could lead to some non-physicality in the experimentally inferred process matrix. This is typically witnessed by the appearance of one or more negative eigenvalues of χ. Any conclusion derived from such an unphysical process should be regarded as not trustful. The problem can be bypassed by means of maximum-likelihood-function techniques similar to those employed for quantum state tomography [120, 167]. In those cases where the experimentally inferred process matrix is unphysical, we must look for the positive semi-definite Hermitian matrix η closest to the experimental one that respects the constraint imposed by the completeness relation. In a more formal way, such an estimate is found by minimizing the functional [231]

$$\delta(\chi) = \left| \sum_{m,n=1}^{4} \chi_{mn} - \eta_{mn} \right|^2 + \lambda \left| \sum_{m,n=1}^{4} \eta_{mn} A_n^T A_m - \mathbb{1} \right|^2 \tag{8.21}$$

where λ is a Lagrange multiplier and we have used the fact that the elements of the standard set of operations $\{A_i\}$ are real. The physical nature of the estimated process matrix is guaranteed by assuming the decomposition of η in terms of a complex lower-diagonal matrix analogous to the one used in quantum state tomography. With a faithful reconstruction of the process matrix, the corresponding set of Kraus operators is determined following the recipe of standard QPT [122, 229]. For the DFS-encoded cluster state in the presence of the phase-damping noise

implemented in our experiment, the set of non-zero Kraus operators is found to be

$$
\begin{aligned}
\hat{K}_1^{DFS} &= \begin{pmatrix} 0.585 + 0.054i & -0.693 + 0.007i \\ 0.601 + 0.133i & 0.662 + 0.054i \end{pmatrix}, \\
\hat{K}_2^{DFS} &= \begin{pmatrix} 0.296 - 0.137i & -0.071 - 0.044i \\ -0.317 + 0.185i & -0.062 - 0.138i \end{pmatrix}, \\
\hat{K}_3^{DFS} &= \begin{pmatrix} -0.118 + 0.050i & -0.152 + 0.148i \\ -0.132 + 0.030i & 0.050 + 0.050i \end{pmatrix}.
\end{aligned}
\tag{8.22}
$$

On the other hand, the reconstruction of the channel determined by the use of a noise-affected standard two-qubit cluster state leads to the following Kraus operators

$$
\begin{aligned}
\hat{K}_1^{standard} &= \begin{pmatrix} -0.218 + 0.222i & -0.518 + 0.076i \\ -0.106 + 0.425i & -0.118 + 0.222i \end{pmatrix}, \\
\hat{K}_2^{standard} &= \begin{pmatrix} -0.324 - 0.307i & 0.075 - 0.346i \\ -0.126 + 0.293i & 0.260 - 0.307i \end{pmatrix}, \\
\hat{K}_3^{standard} &= \begin{pmatrix} 0.119 - 0.114i & -0.238 - 0.277i \\ -0.419 + 0.175i & -0.183 - 0.114i \end{pmatrix}.
\end{aligned}
\tag{8.23}
$$

Chapter 9

Conclusion and outlook

In summary, we have designed, implemented and characterized algorithms and new techniques for all-optical one-way quantum computing. The underlying resource for the computation, a four-photon linear cluster state, has been generated using spontaneous parametric down conversion (SPDC), linear optics and conditional detection. Taking advantage of the curious equivalence of a number of cluster states which gives access to a universal set of single- and nontrivial two-qubit quantum logic gates in the one-way quantum computer model, we were able to implement various quantum algorithms. The fact that all these have been realized with the same experimental setup and with the same four-qubit linear cluster state underlines in a striking way the flexibility, potency and simplicity of the one-way approach.

Through tailored measurement patterns we were able to realize the first one-way based implementation of Deutsch's algorithm — an algorithm that highlights in a fascinating way the advantages of quantum algorithms in speeding-up classical processes through inherent quantum parallelism [20].

In a different experiment we realized a quantum algorithm that effectively simulates (or "plays") an instance of a quantum game, the so-called Prisoner's dilemma. The Prisoner's dilemma, which, for its applicability to countless classical situations, is a popular and widely known example in classical game theory, offers an interesting backdoor when extending its concept into the quantum domain that allows the resolution of the "dilemma" which occurs in the classical version. The experimental realization of this quantum game marks the first demonstration of a quantum game on a one-way quantum computer and will hopefully trigger further interest in the design of new quantum algorithms and in the application of quantum mechanical concepts to situation which, up to now, have been treated strictly classical [24].

Furthermore we designed and experimentally tested a novel, noise-resilient scheme for one-way quantum information processing (QIP) which is based on decoherence-free subspace (DFS) concepts. With a special encoding structure, we showed that it is possible to protect the cluster states from certain types of decoherence. The scheme is setup independent and can readily applied to larger systems or other physical realizations of quantum computers, such as ion traps or optical lattices. In our linear-optics experiment we have found excellent protection of the encoded quantum information when applying this DFS scheme, even though the qubits were exposed to severe phase-damping noise. Our demonstration represents the first realization of a

decoherence-free protocol in the context of one-way quantum computing and therefore marks an important step toward the construction of reliable large-scale one-way quantum computers [30].

One of the main challenges at the time when I started my research on linear-optics realizations of one-way quantum computers was the implementation of fast, active feed-forward where earlier measurement outcomes actually change the setting of a future measurement in real time — therefore correcting for the intrinsical randomness of measurement outcomes. This feed-forward technique is crucial for achieving deterministic linear-optics quantum computing and has not been achieved in the appropriate fashion back then[1]. Employing custom-built, ultra-fast electro-optical modulators as well as a specially developed classical logic boards we succeeded in realizing this active feed-forward with overall gate times below 150 ns, which at the time was unmatched by any other physical realization of quantum computers by two orders of magnitude. We applied this feed-forward technique to demonstrate a universal set of single- and two-qubit gates as well as a quantum search algorithm. Our feed-forward apparatus can easily be adapted for the use in other existing small- and potentially large-scale implementations of linear-optics quantum computers, both in the one-way and standard circuit model. However, the probably most interesting result of this experiment from an conceptual point of view was that it is indeed possible to build a deterministic quantum computer that has intrinsically random quantum measurements as its essential feature [18, 232, 17].

Given the various alternatives for their creation, such as linear optics, ion traps, and optical lattices, and the recent advances in the preparation of multi-particle entangles states, cluster states are promising candidates for future quantum computers. The most important challenges that remain for the optical approach are

(a) realization of cluster states on demand,

(b) generating cluster states with more qubits and

(c) the experimental demonstration of cluster state operations with fidelities that fall below of error-correction and fault-tolerant thresholds.

All of the above can be achieved by developing and incorporating new techniques for the efficient generation and detection of single photons, such as deterministic single-photon sources and high-efficiency, photon-number resolving single-photon detectors.

Alternatively, the latter requirement (c) can be met by theoretically designing new, more efficient architectures or inherently fault-tolerant schemes for one-way quantum computing, such as discussed in [95, 215].

9.1 Quo vadis photonic quantum computing?

The future will certainly show which computational model and which physical system will be best suited for the future implementation of quantum computaters. One has to admit though, that while linear optics quantum computing can be made deterministic in principle, it

---

[1]Experiments involving single-step feed-forward had been demonstrated, e.g. see [172, 173, 171]. However, these experiments did not realize quantum computational tasks.

is questionable whether large scale quantum information processing based on photonic qubits will be feasible. Photons are, however, certainly the best quantum system for a fast information transfer at low decoherence. Therefore photons might provide the ideal "quantum-bus" between different quantum information processing and storage units in a "hybrid" quantum computer architecture.

Currently, spontaneous parametric down-conversion (SPDC) is the gold standard and predominantly used for the generation of single- and entangled states of light that serve as the resource for photonic quantum information processing. Despite the recent realization of up to six photon cluster states [69] and the demonstration of ten-qubit hyper-entangled states [233], a further increase of multi-photon states with SPDC, linear optics and conditional (inefficient) detection faces severe challenges: The necessity to increase the photon creation probability in SPDC inevitably leads to an increase in noise because of higher order emissions which are due to the probabilistic nature of SPDC. This fact quickly renders the generation of high-quality multi-photon states infeasible. Furthermore, the probabilistic character of linear-optics schemes cause large-scale experimental setups to become increasingly inefficient. Therefore these techniques cannot be considered scalable, at least not in the present form. Only further development in respect to a more efficient creation, interaction and detection of single-photons will open the way to large-scale photonic QIP.

9.1.1 Promising future techniques for large scale QIP with photons

Throughout this Thesis we have learned that the negligible photon-photon interaction or more generally the absence of a sufficiently strong nonlinearity prohibits deterministic two-qubit gates between individual photons. Recent work, however, has shown that coupling the photons with other media might induce the required nonlinearity. For example, electromagnetically induced transparency (EIT) offers nonlinearities that are on the threshold of becoming practical [234, 235]. Alternatively, relatively large nonlinearities can be obtained in photonic bad-gap materials [236].

Progress is also made on the single-photon "on demand" source side for which several candidates are currently investigated. Among others[2], these are nitrogen-vacancy colour centers in diamond [186, 187, 188], atoms [190] and ions [189] in the gaseous phase as well as optical transitions in various assembled quantum dots [97]. Especially the broad research field of the latter promises practical, deterministic single-photon emitters. An excellent overview is given by Santori et al. [96]. Recent achievements include the on-demand emission of entangled photons from a biexciton quantum dot [191] but the main difficulty with quantum dots is that they interact with a solid state environment, necessitating cryogenic operation temperatures, and environment-induced decoherence is a problem. Alternatively it has been proposed by Franson et al. [239] to use atoms with a two-photon transition placed in optical fibers to knock out two-photon contributions of the photon states which, in a more general way, can be used to get rid of unwanted, noise-inducing higher order terms in the SPDC emission.

---

[2]Note that proposals for heralded single- and entangled photon sources exist which are again based on SPDC, e.g. [237] or [238]. However due to the large resource overheads and the fact that these are again based on SPDC we do not seriously consider them here.

Quantum memories might provide a work around in the absence of practical single-photon sources and naturally they are interesting in their own right as future large-scale quantum computers will most certainly require such devices in order to store their internal quantum states. For such purposes, the use of mere fiber loops for the storage of single photons becomes problematic, as the photon can not be recovered after arbitrary storage times and the fibers induce photon losses ($0.17\,\mathrm{dbkm}^{-1}$ at 1550 nm). Single photons can be stored up to milliseconds in ground states of atomic ensembles using magnetic sublevels [240, 241, 242, 243, 244] or as dark state polaritons using EIT processes [245, 246, 247]. Alternatively, other proposals include single-photon cavity QED [248]. One of the main challenges in all of the above schemes is the efficient coupling of the photon into and out of the quantum memory.

Currently the most common, because commercially available, single-photon detectors are avalanche photo-diodes (APDs) and they have also been used for the experiments presented in this Thesis. Unfortunately these detectors are quite inefficient ($\sim$70% at 660 nm) and do not allow photon-number resolution. This feature can be approximated by detector cascading in the spatial [249] and time domain [250, 251] although this is often impractical and inefficient in experiments. Full-fledged number-resolving detectors such as the Visible Light Photon Counter (VLPC) are currently being developed [181, 182, 252]. Since the active area of the detector is divided into many independent regions a multiple photon detection generates a current that is proportional to the number of photons. However, VLPCs do not offer much higher quantum efficiencies but come with higher dark count rates compared to ordinary APDs. An alternative and very promising technique uses superconducting transition-edge sensors (TES) that act as calorimeters, i.e. the photon is detected by an absorption-induced rise in temperature [253]. These sensors feature photon-number resolution and a very high detection efficiency greater than 95% at 1550 nm [185]. Unfortunately this devices require cryogenic temperatures below 100 mK to operate and the repetition rate is rather slow (on the order of 10 kHz) preventing their use in current linear-optics experiments aimed at the generation of multi-photon states with pulsed SPDC. Using superconducting nanowires (made of NbN or similar materials), the timing resolution of these detectors can be increased to few tens of picoseconds [183, 184]. Although number-resolution is not possible and the quantum efficiency is still in the range of $\sim$1-2% these detectors could potentially allow multi-photon experiments with cw-SPDC. Future progress will show which of these types of superconducting detectors is best suited for photonic QIP with an increased photon number.

In addition to these experimental developments, theoretical proposals for number-resolving detectors exist that are based on atomic vapours [254] and EIT [255]. Alternatively, there is the possibility to detect the photon's state without destroying it in the process. This is called quantum non-demolition (QND) measurement and several schemes for single-photon QND measurements have been proposed [256, 257, 258] and experimental proof-of-principle demonstrations have been reported [259, 260].

Very recently, advances have been achieved in the integrated optics realization of photonic QIP with experimental demonstrations of high-fidelity quantum operations utilizing silica-on-silicon waveguides [261]. The monolithic nature of these devices results in improved mode-matching and stability and the miniaturization permits scalability. Furthermore the confine-

ment of the light field inside the waveguide leads to higher SPDC efficiency. Additionally it becomes possible to directly "write" sophisticated photonic quantum circuits onto a waveguide chip, which certainly will be of benefit to future quantum technologies based on photons. This technique has recently attracted attention from several research groups and is currently actively pursued.

Nevertheless, despite the numerous imperfections of current state-of-the-art linear-optics experiments it is remarkable that so far the most demonstrations of quantum computational concepts have been achieved in photonic systems. Currently they seem to provide the most flexible testbed for the investigation of quantum computing concepts such as the demonstrations of quantum algorithms on a small scale. When combined with the techniques and concepts presented above, and with ongoing developments and improvements in these respective fields, there is certainly a "bright" future for linear optics QIP with single photons.

Having all said, I certainly hope that the experiments presented in this Thesis, although they are only of simple nature and of proof-of-principle character, will spark further interest in the one-way model of quantum computation and therefore eventually lead to ever more exciting inventions and experimental demonstrations in QIP in the future.

Bibliography

[1] R. P. FEYNMAN, *"Simulating physics with computers,"* Int. J. Theor. Phys. **21,** 6–7, 467–488 (1982). 1, 37

[2] P. BENIOFF, *"The computer as a physical system: a microscopic quantum mechanical Hamiltonia model of computers as represented by Turing machines,"* J. Stat. Phys. **22,** 563–591 (1980). 1

[3] C. H. BENNETT, *"The thermodynamics of computation—a review,"* Int. J. Theor. Phys. **21,** 905–940 (1982). 1

[4] C. BENNETT AND R. LANDAUER, *"The Fundamental Physical Limits of Computation,"* Scientific American **253,** 48–56 (1985). 1

[5] R. P. FEYNMAN, *"Quantum mechanical computers,"* Found. Phys. **16,** 507–531 (1986). 1

[6] *"ERA-Pilot Roadmap QIST: QIPC Strategic Report v1.5 (2005),"*, http://qist.ect.it/Reports/reports.htm. 1

[7] D. DEUTSCH, *"Quantum theory, the Church-Turing principle and the universal quantum computer,"* Proc. Roy. Soc. Lond. A **400,** 97 (1985). 1, 2, 37, 41, 93, 94, 95

[8] L. K. GROVER, *"Quantum mechanics helps in searching for a needle in a heystack,"* Phys. Rev. Lett. **79,** 325 (1997). 1, 37, 89, 90, 95

[9] P. W. SHOR, *"Algorithms for quantum computation: Discrete logarithms and factoring,"* In *Proceedings of the 35th Annual Symposium on Foundations of Computer Science,* p. 124 (IEEE Computer Society Press, Los Alamitos, 1994). 1, 37, 89, 95

[10] A. BARENCO, C. H. BENNETT, R. CLEVE, D. P. DIVINCENZO, N. MARGOLU, P. SHOR, T. SLEATOR, J. A. SMOLIN, AND H. WEINFURTER, *"Elementary gates for quantum computation,"* Phys. Rev. A **52,** 3457–3467 (1995). 2, 38, 39, 43, 105

[11] M. A. NIELSEN AND I. L. CHUANG, *Quantum Computation and Quantum Information* (Cambridge University Press, Cambridge, 2000). 2, 5, 7, 11, 34, 35, 39, 87, 89, 95, 113, 114, 118, 119, 123, 124, 125, 127

[12] D. GOTTESMAN AND I. L. CHUANG, *"Demonstrating the viability of universal quantum computation using teleportatio and single-qubit operations,"* Nature **402,** 390–393 (1999). 2, 37, 43, 44

[13] E. KNILL, R. LAFLAMME, AND G. MILBURN, *"A Scheme for Efficient Quantum Computation with Linear Optics,"* Nature **409,** 46–52 (2001). 2, 37, 42, 43, 91

[14] R. RAUSSENDORF AND H. J. BRIEGEL, *"A One-Way Quantum Computer,"* Phys. Rev. Lett. **86,** 5188–5191 (2001). 2, 16, 37, 45, 104, 105, 106, 120, 121

[15] H. J. BRIEGEL AND R. RAUSSENDORF, *"Persistent Entanglement in Arrays of Interacting Particles,"* Phys. Rev. Lett. **86,** 910–913 (2001). 2, 15, 16, 17, 37, 45, 66, 104

[16] M. A. NIELSEN, *"Optical quantum computation using cluster states,"* Phys. Rev. Lett. **93,** 040503 (2004). 2, 37, 45, 104

[17] P. BÖHI, R. PREVEDEL, T. JENNEWEIN, A. STEFANOV, F. TIEFENBACHER, AND A. ZEILINGER, *"Implementation and characterization of active feed-forward for deterministic linear optics quantum computing,"* Appl. Phys. B **89,** 499–505 (2007). 2, 130

[18] R. PREVEDEL, P. WALTHER, F. TIEFENBACHER, P. BÖHI, R. KALTENBAEK, T. JENNEWEIN, AND A. ZEILINGER, *"High-speed linear optics quantum computing using active feed-forward,"* Nature **445,** 65–69 (2007). 2, 71, 76, 77, 82, 95, 97, 104, 106, 130

[19] D. DEUTSCH AND R. JOZSA, *"Rapid solutions of problems by quantum computation,"* Proc. Roy. Soc. Lond. A **439,** 553 (1992). 2, 41, 93, 94

[20] M. S. TAME, R. PREVEDEL, M. PATERNOSTRO, P. BÖHI, M. S. KIM, AND A. ZEILINGER, *"Experimental Realization of Deutsch's Algorithm in a One-way Quantum Computer,"* Phys. Rev. Lett. **98,** 140501 (2007). 3, 93, 104, 129

[21] D. FUDENBERG AND J. TIROLE, *Game Theory* (MIT Press, 1991). 3, 103, 104

[22] R. B. MYERSON, *Game Theory: An Analysis of Conflict* (MIT Press, Cambridge, MA, 1991). 3, 103, 104

[23] J. EISERT, M. WILKENS, AND M. LEWENSTEIN, *"Quantum Games and Quantum Strategies,"* Phys. Rev. Lett. **83,** 3077 (1999). 3, 103, 104, 105

[24] R. PREVEDEL, A. STEFANOV, P. WALTHER, AND A. ZEILINGER, *"Experimental realization of a quantum game on a one-way quantum compute,"* New J. Phys. **9,** 205 (2007). 3, 129

[25] P. W. SHOR, *"Scheme for reducing decoherence in quantum computer memory,"* Phys. Rev. A **52,** R2493–R2496 (1995). 3

[26] A. M. STEANE, *"Error Correcting Codes in Quantum Theory,"* Phys. Rev. Lett. **77,** 793–797 (1996). 3

[27] I. L. Chuang and Y. Yamamoto, *"Quantum Bit Regeneration,"* Phys. Rev. Lett. **76,** 4281–4284 (1996). 3

[28] L.-M. Duan and G.-C. Guo, *"Preserving Coherence in Quantum Computation by Pairing Quantum Bits,"* Phys. Rev. Lett. **79,** 1953–1956 (1997). 3, 113, 114, 116

[29] G. M. Palma, K. A. Suominen, and A. K. Ekert, *"Quantum Computers and Dissipation,"* Proc. Roy. Soc. Lond. A **452,** 567 (1996). 3, 113, 114, 116

[30] R. Prevedel, M. S. Tame, A. Stefanov, M. Paternostro, M. Kim, and A. Zeilinger, *"Experimental demonstration of decoherence-free one-way information transfer,"* Phys. Rev. Lett. **99,** 250503 (2007). 3, 130

[31] B. Schumacher, *"Quantum coding,"* Phys. Rev. A **51,** 2738–2747 (1995). 5

[32] J. V. Neumann, *Mathematische Grundlagen der Quantenmechanik* (Springer, 1955). 7, 9

[33] A. Uhlmann, *"The "transition probability" in the state space of a *-algebra,"* Rep. Math. Phys. **9,** 273 – 279 (1976). 9

[34] E. Schrödinger, *"Die gegenwärtige Situation in der Quantenmechanik,"* Naturwissenschaften **V23,** 807 (1935). 11

[35] J. S. Bell, *"On the Einstein Podolsky Rosen Paradox,"* Physics **1,** 195–200 (1964). 12, 69

[36] C. H. Bennett and S. J. Wiesner, *"Communication via One- and Two-Particle Operators on Einstein-Podolsky-Rose States,"* Phys. Rev. Lett. **69,** 2881 (1992). 12

[37] K. Mattle, H. Weinfurter, P. G. Kwiat, and A. Zeilinger, *"Dense Coding in Experimental Quantum Communication,"* Phys. Rev. Lett. **76,** 4656 (1996). 12

[38] C. H. Bennett and G. Brassard, *"Quantum cryptography: Public Key Distribution and coin-tossing,"* Proceedings of IEEE International Conference on Computers, Systems and Signal Processing, Bangalore, India pp. 175–179 (1984). 12

[39] A. K. Ekert, *"Quantum Cryptography Based on Bell's Theorem,"* Phys. Rev. Lett. **67,** 661–663 (1991). 12

[40] C. H. Bennett, G. Brassard, and N. D. Mermin, *"Quantum Cryptography Without Bell's Theorem,"* Phys. Rev. Lett. **68,** 557–559 (1992). 12

[41] T. Jennewein, C. Simon, G. Weihs, H. Weinfurter, and A. Zeilinger, *"Quantum Cryptography with Entangled Photons,"* Phys. Rev. Lett. **84,** 4729–4732 (2000). 12

[42] C. H. Bennett, G. Brassard, C. Crépeau, R. Jozsa, and A. P. an W. K. Wootters, *"Teleporting an unknown quantum state via dual classical and Einstein-Podolsky-Rose channels,"* Phys. Rev. Lett. **70,** 1895–1899 (1993). 12

[43] D. Bouwmeester, J.-W. Pan, K. Mattle, M. Eibl, H. Weinfurte, and A. Zeilinger, *"Experimental Quantum Teleportation,"* Nature **390,** 575 (1997). 12, 56

[44] S. J. van Enk, N. Lutkenhaus, and H. J. Kimble, *"Experimental procedures for entanglement verification,"* Phys. Rev. A **75,** 052318 (2007). 12

[45] W. K. Wootters, *"Entanglement of Formation of an Arbitrary State of Two Qubits,"* Phys. Rev. Lett. **80,** 2245–2248 (1998). 12, 13, 89

[46] D. Bruss, *"Characterizing entanglement,"* J. Math. Phys. **43,** 4237–4251 (2002). 13

[47] C. H. Bennett, H. J. Bernstein, S. Popescu, and B. Schumacher, *"Concentrating partial entanglement by local operations,"* Phys. Rev. A **53,** 2046–2052 (1996). 13

[48] C. H. Bennett, S. Popescu, D. Rohrlich, J. A. Smolin, and A. V. Thapliyal, *"Exact and asymptotic measures of multipartite pure-state entanglement,"* Phys. Rev. A **63,** 012307 (2000). 14

[49] L. Lamata, J. León, D. Salgado, and E. Solano, *"Inductive classification of multipartite entanglement under stochastic local operations and classical communication,"* Phys. Rev. A **74,** 052336 (2006). 14

[50] F. Verstraete, J. Dehaene, B. De Moor, and H. Verschelde, *"Four qubits can be entangled in nine different ways,"* Phys. Rev. A **65,** 052112 (2002). 14, 18

[51] W. Dür, G. Vidal, and J. I. Cirac, *"Three qubits can be entangled in two inequivalent ways,"* Phys. Rev. A **62,** 062314 (2000). 14

[52] D. M. Greenberger, M. A. Horne, and A. Zeilinger, *"Going beyond Bell's Theorem,"* in *Bell's Theorem, Quantum Theory, and Conceptions of the Universe*, M. Kafatos, ed., (Kluwer, Dordrecht, 1989), p. 69. 14

[53] D. M. Greenberger, M. A. Horne, A. Shimony, and A. Zeilinger, *"Bell's Theorem Without Inequalities,"* Am. J. Phys. **58,** 1131–1143 (1990). 14

[54] A. Zeilinger, M. A. Horne, and D. M. Greenberger, NASA Conf. Publ. (NASA, Washington, DC, 1997) . 14

[55] W. Dür and J. I. Cirac, *"Multiparticle entanglement and its experimental detection,"* J. Phys. A: Math. Gen. **34,** 6837 (2001). 14

[56] G. Vidal, *"Entanglement monotones,"* J. Mod. Opt. **47,** 355 (2000). 15

[57] D. Schlingemann and R. F. Werner, *"Quantum error-correcting codes associated with graphs,"* Phys. Rev. A **65,** 012308 (2001). 16

[58] W. Dür, H. Aschauer, and H.-J. Briegel, *"Multiparticle Entanglement Purification for Graph States,"* Phys. Rev. Lett. **91,** 107903 (2003). 16

[59] M. Hein, J. Eisert, and H. J. Briegel, *"Multiparty entanglement in graph states,"* Phys. Rev. A **69,** 062311 (2004). 16, 91

[60] V. Scarani, A. Acín, E. Schenck, and M. Aspelmeyer, *"Nonlocality of cluster states of qubits,"* Phys. Rev. A **71,** 042325 (2005). 16

[61] P. Walther, M. Aspelmeyer, K. J. Resch, and A. Zeilinger, *"Experimental Violation of a Cluster State Bell Inequality,"* Phys. Rev. Lett. **95,** 020403 (2005). 16

[62] O. Gühne, G. Tóth, P. Hyllus, and H. J. Briegel, *"Bell Inequalities for Graph States,"* Phys. Rev. Lett. **95,** 120405 (2005). 16

[63] W. Dür and H.-J. Briegel, *"Stability of Macroscopic Entanglement under Decoherence,"* Phys. Rev. Lett. **92,** 180403 (2004). 16

[64] S. Wu and Y. Zhang, *"Multipartite pure-state entanglement and the generalized Greenberger-Horne-Zeilinger states,"* Phys. Rev. A **63,** 012308 (2000). 17

[65] D. Bouwmeester, J.-W. Pan, M. Daniell, H. Weinfurter, and A. Zeilinger, *"Observation of Three-Photon Greenberger-Horne-Zeilinger Entanglement,"* Phys. Rev. Lett. **82,** 1345 – 1349 (1999). 19

[66] J.-W. Pan, M. Daniell, S. Gasparoni, G. Weihs, and A. Zeilinger, *"Experimental Demonstration of Four-Photon Entanglement and High-Fidelity Teleportation,"* Phys. Rev. Lett. **86,** 4435 – 4438 (2001). 19

[67] Z. Zhao, Y.-A. Chen, A.-N. Zhang, T. Yang, H. J. Briegel, and J.-W. Pan, *"Experimental demonstration of five-photon entanglement and open-destination teleportation,"* Nature **430,** 54–58 (2004). 19

[68] A.-N. Zhang, C.-Y. Lu, X.-Q. Zhou, Y.-A. Chen, Z. Zhao, T. Yang, and J.-W. Pan, *"Experimental construction of optical multiqubit cluster states from Bell states,"* Phys. Rev. A **73,** 022330 (2006). 19, 53, 91, 95, 104

[69] C.-Y. Lu, X.-Q. Zhou, O. Gühne, W.-B. Gao, J. Zhang, Z.-S. Yuan, A. Goebel, T. Yang, and J.-W. Pan, *"Experimental entanglement of six photons in graph states,"* Nature Phys. **3,** 91–95 (2007). 19, 91, 95, 104, 112, 131

[70] C. A. Sackett *et al.*, *"Experimental entanglement of four particles,"* Nature **404,** 256–259 (2000). 19

[71] D. Leibfried *et al.*, *"Creation of a six-atom 'Schrödinger cat' state,"* Nature **438,** 639–642 (2005). 19

[72] R. J. Nelson, D. G. Cory, and S. Lloyd, *"Experimental demonstration of Greenberger-Horne-Zeilinger correlations using nuclear magnetic resonance,"* Phys. Rev. A **61,** 022106 (2000). 19

[73] P. Walther, K. J. Resch, T. Rudolph, E. Schenck, H. Weinfurter, V. Vedral, M. Aspelmeyer, and A. Zeilinger, *"Experimental one-way quantum computing,"* Nature **434,** 169–176 (2005). 19, 49, 52, 53, 54, 59, 71, 74, 77, 90, 95, 98, 101, 104, 105, 106, 107, 108, 120, 121

[74] N. Kiesel, C. Schmid, U. Weber, G. Tóth, O. Gühne, R. Ursin, and H. Wein-furter, *"Experimental Analysis of a Four-Qubit Photon Cluster State,"* Phys. Rev.Lett. **95,** 210502 (2005). 19, 53

[75] Y. Tokunaga, S. Kuwashiro, T. Yamamoto, M. Koashi, and N. Imoto, *"Generation of High-Fidelity Four-Photon Cluster State and Quantum-Domain Demonstration of One-Way Quantum Computing,"* Phys. Rev. Lett. **100,** 210501 (2008). 19

[76] K. Chen, C.-M. Li, Q. Zhang, Y.-A. Chen, A. Goebel, S. Chen, A. Mair, and J.-W. Pan, *"Experimental Realization of One-Way Quantum Computing with Two-Photon Four-Qubit Cluster States,"* Phys. Rev. Lett. **99,** 120503 (2007). 19, 126

[77] G. Vallone, E. Pomarico, P. Mataloni, F. D. Martini, and V. Berardi, *"Realization and Characterization of a Two-Photon Four-Qubit Linear Cluster State,"* Phys. Rev. Lett. **98,** 180502 (2007). 19, 126

[78] D. DiVincenzo, *"The Physical Implementation of Quantum Computation,"* Fortschr. Phys. **48,** 771–783 (2000). 21, 39

[79] J. I. Cirac and P. Zoller, *"Quantum Computations with Cold Trapped Ions,"* Phys. Rev. Lett. **74,** 4091 (1995). 21, 27

[80] C. E. Wieman, D. E. Pritchard, and D. J. Wineland, *"Atom cooling, trapping, and quantum manipulation,"* Rev. Mod. Phys. **71,** S253–S262 (1999). 21, 27

[81] D. Kielpinski, C. Monroe, and D. Weinland, *"Architecture for a large-scale ion-trap quantum computer,"* Nature **417,** 709–711 (2002). 21, 27

[82] D. Leibfried, R. Blatt, C. Monroe, and D. Wineland, *"Quantum dynamics of single trapped ions,"* Rev. Mod. Phys. **75,** 281–324 (2003). 21, 27

[83] L. M. K. Vandersypen and I. L. Chuang, *"NMR techniques for quantum control and computation,"* Rev. Mod. Phys. **76,** 1037 (2004). 21

[84] S. L. Braunstein, C. M. Caves, R. Jozsa, N. Linden, S. Popescu, and R. Schack, *"Separability of Very Noisy Mixed States and Implications for NMR Quantum Computing,"* Phys. Rev. Lett. **83,** 1054–1057 (1999). 21, 104

[85] I. L. Chuang, L. M. Vandersypen, X. Zhou, D. W. Leung, and S. Lloyd, *"Experimental realization of a quantum algorithm,"* Nature **393,** 143–146 (1998). 21, 95

[86] N. A. Gershenfeld and I. L. Chuang, *"Bulk Spin-Resonance Quantum Computation,"* Science **275,** 350–356 (1997). 21, 95

[87] J. A. Jones, *"Quantum computing: Fast searches with nuclear magnetic resonance computers,"* Science **280,** 229 (1998). 21, 95

[88] I. Chiorescu, Y. Nakamura, C. J. P. M. Harmans, and J. E. Mooij, *"Coherent Quantum Dynamics of a Superconducting Flux Qubit,"* Science **299,** 1869–1871 (2003). 22

[89] Y. Nakamura, Y. A. Pashkin, and J. Tsai, *"Coherent control of macroscopic quantum states in a single-Cooper-pair box,"* Nature **398,** 786–788 (1999). 22

[90] J. Q. You, J. S. Tsai, and F. Nori, *"Scalable Quantum Computing with Josephson Charge Qubits,"* Phys. Rev. Lett. **89,** 197902 (2002). 22

[91] T. Yamamoto, Y. A. Pashkin, O. Astafiev, Y. Nakamura, and J. S. Tsai, *"Demonstration of conditional gate operation using superconducting charge qubits,"* Nature **425,** 941 (2003). 22, 42

[92] A. Blais, R.-S. Huang, A. Wallraff, S. M. Girvin, and R. J. Schoelkopf, *"Cavity quantum electrodynamics for superconducting electrical circuits: An architecture for quantum computation,"* Phys. Rev. A **69,** 062320 (2004). 22, 27

[93] M. H. Devoret and J. M. Martinis, *"Implementing Qubits with Superconducting Integrated Circuits,"* Quantum Information Processing **3,** 163–203 (2005). 22, 27

[94] S. Braunstein and H. Lo, *"Experimental Proposals for Quantum Computation,"* Fortschr. Phys. (Special Issue) **48,** 769 (2000). 22

[95] P. Kok, W. J. Munro, K. Nemoto, T. C. Ralph, J. P. Dowling, and G. J. Milburn, *"Linear optical quantum computing with photonic qubits,"* Rev. Mod. Phys. **79,** 135–174 (2007). 22, 29, 43, 44, 53, 95, 130

[96] C. Santori, D. Fattal, J. Vuckovic, G. S. Solomon, and Y. Yamamoto, *"Single-photon generation with InAs quantum dots,"* New J. Phys. **6,** 89 (2004). 22, 91, 131

[97] Z. Yuan, B. E. Kardynal, R. M. Stevenson, A. J. Shields, C. J. Lobo, K. Cooper, N. S. Beattie, D. A. Ritchie, and M. Pepper, *"Electrically Driven Single-Photon Source,"* Science **295,** 102–105 (2002). 22, 91, 131

[98] D. Klyshko, *Photons and Nonlinear Optics* (Gordon & Breach Science Publishers Ltd., 1988). 22, 23

[99] B. Saleh and M. Teich, *Fundamentals of Photonics* (John Wiley & Sons, Inc., 1991). 22, 28

[100] E. Hecht, *Optics* (Addison-Wesley Publishing Co., 1998). 22, 28, 75

[101] V. Dmitriev, G. Gurzadyan, and D. Nikogosyan, *Handbook of nonlinear optical crystals* (Springer, 1991). 23

[102] L. Mandel and E. Wolf, *Optical Coherence and Quantum Optics* (Cambridge University Press, 1995). 23

[103] P. G. Kwiat, K. Mattle, H. Weinfurter, A. Zeilinger, A. V. Sergienk, and Y. Shih, *"New High-Intensity Source of Polarization-Entangled Photon Pairs,"* Phys. Rev. Lett. **75,** 4337–4342 (1995). 24, 25, 56, 80, 107

[104] G. Weihs, Ph.D. thesis, University of Vienna, 1999. 25

[105] H. Weinfurter and M. Zukowski, *"Four-photon entanglement from down-conversion,"* Phys. Rev. A **64,** 010102 (2001). 26, 27

[106] M. Zukowski, A. Zeilinger, and H. Weinfurter, *"Entangling Photons Radiated by Independent Pulsed Sources,"* In *Fundamental Problems in Quantum Theory: A Conference Held in Honor of Professo John A. Wheeler*, D. M. Greenberger and A. Zeilinger, eds., Annals of the New York Academy of Sciences pp. 91–102 (New York Academy of Sciences, New York, 1995). 27, 60

[107] G. Di Giuseppe, L. Haiberger, F. De Martini, and A. V. Sergienko, *"Quantum interference and indistinguishability with femtosecond pulses,"* Phys. Rev. A **56,** R21–R24 (1997). 27

[108] R. Ursin *et al.*, *"Entanglement based quantum communication over 144 km,"* Nat. Phys. **3,** 481 (2007). 27

[109] M. Zukowski, A. Zeilinger, M. A. Horne, and A. K. Ekert, *""Event-Ready-Detectors" Bell experiment via entanglement swapping,"* Phys. Rev. Lett **71,** 4287–4290 (1993). 27

[110] W. P. Grice and I. A. Walmsley, *"Spectral information and distinguishability in type-II down-conversion with a broadband pump,"* Phys. Rev. A **56,** 1627–1634 (1997). 27

[111] M. Atatüre, A. V. Sergienko, B. M. Jost, B. E. A. Saleh, and M. C. Teich, *"Partial Distinguishability in Femtosecond Optical Spontaneous Parametric Down-Conversion,"* Phys. Rev. Lett. **83,** 1323–1326 (1999). 27

[112] T. E. Keller and M. H. Rubin, *"Theory of Two-Photon Entanglement for Spontaneous Parametric Down-Conversio Driven by a Narrow Pump Pulse,"* Phys. Rev. A **56,** 1534 (1997). 27

[113] W. P. Grice, R. Erdmann, I. A. Walmsley, and D. Branning, *"Spectral distinguishability in ultrafast parametric down-conversion,"* Phys. Rev. A **57,** R2289–R2292 (1998). 27

[114] M. Reck, A. Zeilinger, H. Bernstein, and P. Bertani, *"Experimental realization of any discrete unitary operator,"* Phys. Rev. Lett. **73,** 58 – 61 (1994). 28, 43

[115] C. Schmid, Ph.D. thesis, Ludwig-Maximilians-University Munich, 2004. 29

[116] A. Zeilinger, *"General properties of lossless beam splitters in interferometry,"* Am. J. Phys. **49,** 882–883 (1981). 29

[117] J.-W. Pan, S. Gasparoni, R. Ursin, G. Weihs, and A. Zeilinger, *"Experimental Entanglement Purification,"* Nature **423,** 417–422 (2003). 30, 56, 58, 60, 61, 62

[118] P. Walther, J.-W. Pan, M. Aspelmeyer, R. Ursin, S. Gasparon, and A. Zeilinger, *"De Broglie wavelength of a non-local four-photon state,"* Nature **429,** 158–161 (2004). 30

[119] P. WALTHER, Ph.D. thesis, University of Vienna, 2005. 30, 49, 50, 61

[120] D. JAMES, P. KWIAT, W. MUNRO, AND A. WHITE, *"Measurement of qubits,"* Phys. Rev. A **64,** 52312 (2001). 32, 33, 34, 66, 85, 97, 99, 108, 121, 123, 127

[121] G. STOKE, Trans. Cambridge Philos. Soc. **9,** 399 (1852). 32

[122] I. CHUANG AND M. NIELSEN, *"Prescription for experimental determination of the dynamics of a quantum black box,"* J. Mod. Opt. **44,** 2455 (1997). 34, 119, 123, 127

[123] J. F. POYATOS, J. I. CIRAC, AND P. ZOLLER, *"Complete Characterization of a Quantum Process: The Two-Bit Quantum Gate,"* Phys. Rev. Lett. **78,** 390–393 (1997). 34, 127

[124] M. W. MITCHELL, C. W. ELLENOR, S. SCHNEIDER, AND A. M. STEINBERG, *"Diagnosis, Prescription, and Prognosis of a Bell-State Filter by Quantum Process Tomography,"* Phys. Rev. Lett. **91,** 120402 (2003). 34

[125] A. G. WHITE, A. GILCHRIST, G. J. PRYDE, J. L. O'BRIEN, M. J. BREMNER, AND N. K. LANGFORD, *"Measuring Controlled-NOT and two-qubit gate operation,"* J. Opt. Soc. Am. B **24,** 72–183 (2007). 35, 36

[126] J. L. O'BRIEN, G. J. PRYDE, A. GILCHRIST, D. F. V. JAMES, N. K. LANGFORD, T. C. RALPH, AND A. G. WHITE, *"Quantum Process Tomography of a Controlled-NOT Gate,"* Phys. Rev. Lett. **93,** 080502 (2004). 35, 36, 123

[127] D. DEUTSCH AND A. EKERT, *"Quantum Computation,"* Physics World **11,** 47 (March 1998). 37

[128] A. EKERT AND R. JOZSA, *"Quantum algorithms: entanglement enhanced information processing,"* Phil. Trans. Roy. Soc. Lond. A **356,** 1779–1782 (1998). 37

[129] S. LLOYD, *"Almost Any Quantum Logic Gate is Universal,"* Phys. Rev. Lett. **75,** 346–349 (1995). 38

[130] T. SLEATOR AND H. WEINFURTER, *"Realizable universal quantum logic gates,"* Phys. Rev. Lett. **74,** 4087 (1995). 38

[131] D. DEUTSCH, *"Quantum Computational Networks,"* Proc. R. Soc. London A **425,** 73 (1989). 39, 42

[132] D. BRUSS, A. EKERT, S. F. HUELGA, J.-W. PAN, AND A. ZEILINGER, *"Quantum Computing with Controlled-Not and Few Qubits,"* Phil. Trans. R. Soc. Lond. A **355,** 2259–2266 (1997). 41

[133] J. L. O'BRIEN, G. J. PRYDE, A. G. WHITE, T. C. RALPH, AND D. BRANNING, *"Demonstration of an all-optical quantum controlled-NOT gate,"* Nature **426,** 264 (2003). 42, 53, 105

[134] S. GASPARONI, J.-W. PAN, P. WALTHER, T. RUDOLPH, AND A. ZEILINGER, *"Realization of a Photonic Controlled-NOT Gate Sufficient for Quantum Computation,"* Phys. Rev. Lett. **93,** 20504 (2004). 42, 53, 105, 110

[135] D. Leibfried, B. DeMarco, V. Meyer, D. Lucas, M. B. an J. Britton, W. M. Itano, B. Jelenkovic, C. Langer, T. Rosenban, and D. J. Wineland, *"Experimental demonstration of a robust, high-fidelity geometric two ion-qubit phase gate,"* Nature **422,** 412–415 (2003). 42, 75, 85

[136] F. Schmidt-Kaler, H. Häffner, M. Riebe, S. Gulde, G. P. T. Lancaste, T. Deuschle, C. Becher, C. F. Roos, J. Eschner, and R. Blatt, *"Realization of the Cirac–Zoller controlled-NOT quantum gate,"* Nature **422,** 408–411 (2003). 42

[137] http://en.wikipedia.org/wiki/Kerr-effect. 43

[138] N. Lütkenhaus, J. Calsamiglia, and K.-A. Suominen, *"Bell measurements for teleportation,"* Phys. Rev. A **59,** 3295–3300 (1999). 43

[139] L. Vaidmann and N. Yoran, *"Methods for reliable teleportation,"* Phys. Rev. A **59,** 116 (1999). 43

[140] N. Lütkenhaus, J. Calsamiglia, and K.-A. Suominen, *"Bell measurements for teleportation,"* Phys. Rev. A **59,** 3295 – 3300 (1999). 44

[141] E. Knill, *"Quantum computing with realistically noisy devices,"* Nature **434,** 39–44 (2005). 44

[142] T. C. Ralph, A. G. White, W. J. Munro, and G. J. Milburn, *"Simple scheme for efficient linear optics quantum gates,"* Phys. Rev. A **65,** 12314 (2001). 45

[143] J. D. Franson, M. M. Donegan, M. J. Fitch, B. C. Jacobs, and T. B. Pittman, *"High-Fidelity Quantum Logic Operations Using Linear Optical Elements,"* Phys. Rev. Lett. **89,** 137901 (2002). 45

[144] N. Yoran and B. Reznik, *"Deterministic Linear Optics Quantum Computation with Single Photon Qubits,"* Phys. Rev. Lett. **91,** 037903 (2003). 45

[145] A. J. F. Hayes, A. Gilchrist, C. R. Myers, and T. C. Ralph, *"Utilizing encoding in scalable linear optics quantum computing,"* J. Opt. B **6,** 533–541 (2004). 45

[146] F. M. Spedalieri, H. Lee, and J. P. Dowling, *"High-fidelity linear optical quantum computing with polarization encoding,"* Phys. Rev. A **73,** 012334 (2006). 45

[147] R. Raussendorf and H. J. Briegel, *"Quantum computing via measurements only,"* quant-ph/0010033 (2001). 45

[148] R. Raussendorf, D. E. Browne, and H. J. Briegel, *"The one-way quantum computer - a non-network model of quantum computation,"* J. Mod. Opt. **49,** 1299 (2002). 45

[149] M. A. Nielsen and C. M. Dawson, *"Fault-tolerant quantum computation with cluster states,"* Phys. Rev. A **71,** 042323 (2005). 45

[150] P. KOK, *"Lecture notes on Optical Quantum Computing,"* arXiv:quant-ph/0705.4193 (2007). 46, 47, 53

[151] M. NIELSEN, *"Cluster-state quantum computing,"* Rep. Math. Phys. **57,** 147 (2006). 48, 89

[152] T. B. PITTMAN, B. C. JACOBS, AND J. D. FRANSON, *"Probabilistic quantum logic operations using polarizing beam splitters,"* Phys. Rev. A **64,** 062311 (2001). 52

[153] T. C. RALPH, N. K. LANGFORD, T. B. BELL, AND A. G. WHITE, *"Linear optical controlled-NOT gate in the coincidence basis,"* Phys. Rev. A **65,** 062324 (2002). 52

[154] T. B. PITTMAN, B. C. JACOBS, AND J. D. FRANSON, *"Demonstration of Nondeterministic Quantum Logic Operations Using Linear Optical Elements,"* Phys. Rev. Lett. **88,** 257902 (2002). 52

[155] T. B. PITTMAN, M. J. FITCH, B. C. JACOBS, AND J. D. FRANSON, *"Experimental controlled-NOT logic gate for single photons in the coincidence basis,"* Phys. Rev. A **68,** 32316 (2003). 52, 105

[156] Z. ZHAO, A.-N. ZHANG, Y.-A. CHEN, H. ZHANG, J.-F. DU, T. YANG, AND J.-W. PAN, *"Experimental Demonstration of a Nondestructive Controlled-NOT Quantum Gate for Two Independent Photon Qubits,"* Phys. Rev. Lett. **94,** 030501 (2005). 53

[157] N. K. LANGFORD, T. J. WEINHOLD, R. PREVEDEL, K. J. RESCH, A. GILCHRIST, J. L. O'BRIEN, G. J. PRYDE, AND A. G. WHITE, *"Demonstration of a Simple Entangling Optical Gate and Its Use in Bell-State Analysis,"* Phys. Rev. Lett. **95,** 210504 (2005). 53, 66, 105, 108

[158] R. OKAMOTO, H. F. HOFMANN, S. TAKEUCHI, AND K. SASAKI, *"Demonstration of an Optical Quantum Controlled-NOT Gate without Path Interference,"* Phys. Rev. Lett. **95,** 210506 (2005). 53, 105

[159] N. KIESEL, C. SCHMID, U. WEBER, R. URSIN, AND H. WEINFURTER, *"Linear Optics Controlled-Phase Gate Made Simple,"* Phys. Rev. Lett. **95,** 210505 (2005). 53, 95, 104, 105

[160] C. K. HONG, Z. Y. OU, AND L. MANDEL, *"Measurement of subpicosecond time intervals between two photons by interference,"* Phys. Rev. Lett **59,** 2044–2046 (1987). 53, 60

[161] D. E. BROWNE AND T. RUDOLPH, *"Resource-efficient linear optical quantum computation,"* Phys. Rev. Lett. **95,** 010501 (2005). 53

[162] C. KURTSIEFER, M. OBERPARLEITER, AND H. WEINFURTER, *"High-Efficiency Entangled Photon Pair Collection in Type-II Parametri Fluorescence,"* Phys. Rev. A **64,** 23802 (2001). 56

[163] R. KALTENBAEK, Ph.D. thesis, University of Vienna, 2007. 56, 61, 65

[164] T. J. Herzog, J. G. Rarity, H. Weinfurter, and A. Zeilinger, *"Frustrated Two-Photon Creation via Interference,"* Phys. Rev. Lett. **72,** 629 (1994). 56

[165] C. Simon and J.-W. Pan, *"Polarization Entanglement Purification using Spatial Entanglement,"* Phys. Rev. Lett. **89,** 257901 (2002). 58

[166] S. Gasparoni, Ph.D. thesis, University of Vienna, 2004. 58, 60, 61

[167] A. White, D. James, P. H. Eberhard, and P. G. Kwiat, *"Nonmaximally entangled states: production, characterization, and utilization,"* Phys. Rev. Lett. **83,** 3103–3107 (1999). 66, 85, 97, 99, 127

[168] G. Tóth and O. Gühne, *"Detecting Genuine Multipartite Entanglement with Two Local Measurements,"* Phys. Rev. Lett. **94,** 060501 (2005). 66, 85, 97, 108

[169] R. Horodecki, P. Horodecki, and M. Horodecki, *"Violating Bell ineqaulity by mixed spin-$\frac{1}{2}$ states: necessar and sufficient condition,"* Phys. Lett. A **200,** 340–344 (1995). 69

[170] M. Horodecki, P. Horodecki, and R. Horodecki, *"Separability of mixed states: necessary and sufficient conditions,"* Phys. Lett. A **223,** 1–8 (1996). 69, 89, 100

[171] R. Ursin, T. Jennewein, M. Aspelmeyer, R. Kaltenbaek, M. Lindenthal, P. Walther, and A. Zeilinger, *"Quantum teleportation across the Danube,"* Nature **430,** 849 (2004). 74, 75, 130

[172] S. Giacomini, F. Sciarrino, E. Lombardi, and F. D. Martini, *"Active teleportation of a quantum bit,"* Phys. Rev. A **66,** 030302(R) (2002). 74, 75, 130

[173] T. B. Pittman, B. C. Jacobs, and J. D. Franson, *"Demonstration of feed-forward control for linear optics quantum computation,"* Phys. Rev. A **66,** 052305 (2002). 74, 75, 130

[174] T. B. Pittman, B. C. Jacobs, and J. D. Franson, *"Demonstration of quantum error correction using linear optics,"* Phys. Rev. A **71,** 052332 (2005). 74, 75

[175] L. M. K. Vandersypen, M. Steffen, G. Breyta, C. S. Yannoni, M. H. Sherwood, and I. L. Chuang, *"Experimental realization of Shor's quantum factoring algorithm using nuclear magnetic resonance,"* Nature **414,** 883 – 887 (2001). 75, 85

[176] A. Poppe *et al.*, *"Practical quantum key distribution with polarization entangled photons,"* Opt. Exp. **12,** 3865–3871 (2004). 80, 116

[177] M. Riebe *et al.*, *"Quantum teleportation with atoms,"* Nature **429,** 734 – 737 (2004). 85

[178] M. D. Barrett *et al.*, *"Quantum teleportation with atomic qubits,"* Nature **429,** 737 – 739 (2004). 85

[179] V. Coffman, J. Kundu, and W. K. Wootters, *"Distributed entanglement,"* Phys. Rev. A **61,** 052306 (2000). 89

[180] J. Ahn, T. C. Weinacht, and P. H. Bucksbaum, *"Information Storage and Retrieval Through Quantum Phase,"* Science **287,** 463–465 (2000). 89

[181] S. Takeuchi, J. Kim, Y. Yamamoto, and H. H. Hogue, *"Development of a high-quantum-efficiency single-photon counting system,"* Appl. Phys. Lett. **74,** 1063–1065 (1999). 91, 132

[182] J. Kim, S. Takeuchi, Y. Yamamoto, and H. H. Hogue, *"Multiphoton detection using visible light photon counter,"* Appl. Phys. Lett. **74,** 902–904 (1999). 91, 132

[183] G. N. Gol'tsman, O. Okunev, G. Chulkova, A. Lipatov, A. Semenov, K. Smirnov, B. Voronov, A. Dzardanov, C. Williams, and R. Sobolewski, *"Picosecond superconducting single-photon optical detector,"* Appl. Phys. Lett. **79,** 705–707 (2001). 91, 132

[184] A. Verevkin, J. Zhang, R. Sobolewski, A. Lipatov, O. Okunev, G. Chulkova, A. Korneev, K. Smirnov, G. N. Gol'tsman, and A. Semenov, *"Detection efficiency of large-active-area NbN single-photon superconducting detectors in the ultraviolet to near-infrared range,"* Appl. Phys. Lett. **80,** 4687–4689 (2002). 91, 132

[185] A. E. Lita, A. J. Miller, and S. W. Nam, *"Counting near-infrared single-photons with 95% efficiency,"* Opt. Exp. **16,** 3032–3040 (2008). 91, 132

[186] C. Kurtsiefer, S. Mayer, P. Zarda, and H. Weinfurter, *"Stable Solid-State Source of Single Photons,"* Phys. Rev. Lett. **85,** 290–293 (2000). 91, 131

[187] A. Beveratos, R. Brouri, T. Gacoin, A. Villing, J.-P. Poizat, and P. Grangier, *"Single Photon Quantum Cryptography,"* Phys. Rev. Lett. **89,** 187901 (2002). 91, 131

[188] F. Jelezko, I. Popa, A. Gruber, C. Tietz, J. Wrachtrup, A. Nizovtsev, and S. Kilin, *"Single spin states in a defect center resolved by optical spectroscopy,"* Appl. Phys. Lett. **81,** 2160–2162 (2002). 91, 131

[189] J. McKeever, A. Boca, A. D. Boozer, R. Miller, J. R. B. an A. Kuzmich, and H. J. Kimble, *"Deterministic Generation of Single Photons from One Atom Trapped in a Cavity,"* Science **303,** 1992–1994 (2002). 91, 131

[190] A. Kuhn, M. Hennrich, and G. Rempe, *"Deterministic Single-Photon Source for Distributed Quantum Networking,"* Phys. Rev. Lett. **89,** 679011–679014 (2002). 91, 131

[191] R. M. Stevenson, R. J. Young, P. Atkinson, K. Cooper, D. A. Ritchie, and A. J. Shields, *"A semiconductor source of triggered entangled photon pairs,"* Nature **439,** 179–182 (2006). 91, 131

[192] Y. Soudagar, F. Bussières, G. Berlín, S. Lacroix, J. M. Fernandez, and N. Godbout, *"Cluster-state quantum computing in optical fibers,"* J. Opt. Soc. Am. B **24,** 226–230 (2007). 91

[193] J. A. JONES, M. MOSCA, AND R. H. HANSEN, *"Implementation of a quantum search algorithm on a quantum computer,"* Nature **393,** 344–346 (1998). 95

[194] D. G. CORY, A. F. FAHMY, AND T. F. HAVEL, *"Ensemble quantum computing by NMR spectroscopy,"* Proc. Nat. Ac. Sc. **94,** 1634–1639 (1997). 95

[195] B. P. LANYON, T. J. WEINHOLD, N. K. LANGFORD, M. BARBIERI, D. F. V. JAMES, A. GILCHRIST, AND A. G. WHITE, *"Experimental Demonstration of a Compiled Version of Shor's Algorithm with Quantum Entanglement,"* Phys. Rev. Lett. **99,** 250505 (2007). 95

[196] M. MOHSENI, J. S. LUNDEEN, K. J. RESCH, AND A. M. STEINBERG, *"Experimental Application of Decoherence-Free Subspaces in an Optical Quantum-Computing Algorithm,"* Phys. Rev. Lett. **91,** 187903 (2003). 95, 120

[197] A. PERES, *"Separability Criterion for Density Matrices,"* Phys. Rev. Lett. **77,** 1413–1415 (1996). 100

[198] M. S. TAME, M. PATERNOSTRO, M. S. KIM, AND V. VEDRAL, *"Quantum-information processing with noisy cluster states,"* Phys. Rev. A **72,** 012319 (2005). 100

[199] M. PATERNOSTRO, M. S. TAME, AND M. S. KIM, *"Hybrid cluster state proposal for a quantum game,"* New J. Phys. **7,** 226 (2005). 101, 104, 105, 107

[200] P. E. TURNER AND L. CHO, *"Prisoner's dilemma in an RNA virus,"* Nature **398,** 441–443 (1999). 103

[201] D. A. MEYER, *"Quantum strategies,"* Phys. Rev. Lett. **82,** 1052–1055 (1999). 103

[202] S. C. BENJAMIN AND P. M. HAYDEN, *"Multiplayer quantum games,"* Phys. Rev. A **64,** 030301 (2001). 103, 105

[203] C. LEE AND N. JOHNSON, *"Let the quantum games begin,"* Physics World **15,** 25 (2002). 103

[204] J. DU, H. LI, X. XU, M. SHI, J. WU, X. ZHOU, AND R. HAN, *"Experimental Realization of Quantum Games on a Quantum Computer,"* Phys. Rev. Lett. **88,** 137902 (2002). 104

[205] R. RAUSSENDORF, D. E. BROWNE, AND H. J. BRIEGEL, *"Measurement-based quantum computation on cluster states,"* Phys. Rev. A **68,** 022312 (2003). 104, 120

[206] M. S. TAME, M. PATERNOSTRO, M. S. KIM, AND V. VEDRAL, *"Natural three-qubit interactions in one-way quantum computing,"* Phys. Rev. A **73,** 022309 (2006). 109

[207] W. J. MUNRO, K. NEMOTO, AND T. P. SPILLER, *"Weak nonlinearities: a new route to optical quantum computation,"* New J. Phys. **7,** 137 (2005). 110

[208] P. G. KWIAT, A. J. BERGLUND, J. B. ALTEPETER, AND A. G. WHITE, *"Experimental Verification of Decoherence-Free Subspaces,"* Science **290,** 498–501 (2000). 113, 114, 115, 120, 124, 126

[209] D. A. Lidar, I. L. Chuang, and K. B. Whaley, *"Decoherence-Free Subspaces for Quantum Computation,"* Phys. Rev. Lett. **81,** 2594–2597 (1998). 113, 114, 116

[210] P. Zanardi and M. Rasetti, *"Noiseless Quantum Codes,"* Phys. Rev. Lett. **79,** 3306–3309 (1997). 113, 114, 116

[211] J. Preskill, *"Reliable quantum computers,"* Proc. Roy. Soc. Lond. A **454,** 469 (1998). 114

[212] D. A. Lidar, D. Bacon, and K. B. Whaley, *"Concatenating Decoherence-Free Subspaces with Quantum Error Correcting Codes,"* Phys. Rev. Lett. **82,** 4556–4559 (1999). 114, 126

[213] A. Beige, D. Braun, B. Tregenna, and P. L. Knight, *"Quantum Computing Using Dissipation to Remain in a Decoherence-Free Subspace,"* Phys. Rev. Lett. **85,** 1762–1765 (2000). 114

[214] L.-A. Wu and D. A. Lidar, *"Creating Decoherence-Free Subspaces Using Strong and Fast Pulses,"* Phys. Rev. Lett. **88,** 207902 (2002). 114, 126

[215] M. S. Tame, M. Paternostro, and M. S. Kim, *"One-way quantum computing in a decoherence-free subspace,"* New J. Phys. **9,** 201 (2007). 115, 116, 117, 119, 120, 126, 130

[216] D. A. Lidar, D. Bacon, J. Kempe, and K. B. Whaley, *"Decoherence-free subspaces for multiple-qubit errors. I. Characterization,"* Phys. Rev. A **63,** 022306 (2001). 116

[217] D. Bacon, D. A. Lidar, and K. B. Whaley, *"Robustness of decoherence-free subspaces for quantum computation,"* Phys. Rev. A **60,** 1944–1955 (1999). 116

[218] D. Kielpinski, V. Meyer, M. A. Rowe, C. A. Sackett, W. M. Itano, C. Monroe, and D. J. Wineland, *"A Decoherence-Free Quantum Memory Using Trapped Ions,"* Science **291,** 1013–1015 (2001). 116, 120

[219] L. Viola, E. M. Fortunato, M. A. Pravia, E. Knill, R. Laflamme, and D. G. Cory, *"Experimental Realization of Noiseless Subsystems for Quantum Information Processing,"* Science **293,** 2059–2063 (2001). 116, 120, 126

[220] D. Jaksch, H.-J. Briegel, J. I. Cirac, C. W. Gardiner, and P. Zoller, *"Entanglement of Atoms via Cold Controlled Collisions,"* Phys. Rev. Lett. **82,** 1975–1978 (1999). 116

[221] J.-C. Boileau, R. Laflamme, M. Laforest, and C. R. Myers, *"Robust Quantum Communication Using a Polarization-Entangled Photon Pair,"* Phys. Rev. Lett. **93,** 220501 (2004). 116

[222] K. Banaszek, A. Dragan, W. Wasilewski, and C. Radzewicz, *"Experimental Demonstration of Entanglement-Enhanced Classical Communication over a Quantum Channel with Correlated Noise,"* Phys. Rev. Lett. **92,** 257901 (2004). 116

[223] K. KRAUS, *States, Effects and Operations: Fundamental Notions of Quantum Theory* (Springer, 1983). 118

[224] D. GROSS, K. KIELING, AND J. EISERT, *"Potential and limits to cluster-state quantum computing using probabilistic gates,"* Phys. Rev. A **74,** 042343 (2006). 120

[225] C. M. DAWSON, H. L. HASELGROVE, AND M. A. NIELSEN, *"Noise Thresholds for Optical Quantum Computers,"* Phys. Rev. Lett. **96,** 020501 (2006). 120

[226] M. BOURENNANE, M. EIBL, S. GAERTNER, C. KURTSIEFER, A. CABELLO, AND H. WEINFURTER, *"Decoherence-Free Quantum Information Processing with Four-Photon Entangled States,"* Phys. Rev. Lett. **92,** 107901 (2004). 120

[227] J. E. OLLERENSHAW, D. A. LIDAR, AND L. E. KAY, *"Magnetic Resonance Realization of Decoherence-Free Quantum Computation,"* Phys. Rev. Lett. **91,** 217904 (2003). 120

[228] P. WALTHER, M. ASPELMEYER, K. J. RESCH, AND A. ZEILINGER, *"Experimental Violation of a Cluster State Bell Inequality,"* Phys. Rev. Lett. **95,** 020403 (2005). 120

[229] J. B. ALTEPETER, D. BRANNING, E. JEFFREY, T. C. WEI, P. G. KWIAT, R. T. THEW, J. L. O'BRIEN, M. A. NIELSEN, AND A. G. WHITE, *"Ancilla-Assisted Quantum Process Tomography,"* Phys. Rev. Lett. **90,** 193601 (2003). 127

[230] P. P. ROHDE, G. J. PRYDE, J. L. O'BRIEN, AND T. C. RALPH, *"Quantum-gate characterization in an extended Hilbert space,"* Phys. Rev. A **72,** 032306 (2005). 127

[231] M. HOWARD, J. TWAMLEY, C. WITTMANN, T. GAEBEL, F. JELEZKO, AND J. WRACHTRUP, *"Quantum process tomography and Linblad estimation of a solid-state qubit,"* New J. Phys. **8,** 33 (2006). 127

[232] R. PREVEDEL, M. ASPELMEYER, C. BRUKNER, T. JENNEWEIN, AND A. ZEILINGER, *"Photonic entanglement as a resource in quantum computation and quantum communication,"* J. Opt. Soc. Am. B **24,** 241 (2007). 130

[233] W.-B. GAO, C.-Y. LU, X.-C. YAO, P. XU, O. GÜHNE, A. GOEBEL, Y.-A. CHEN, C.-Z. PENG, Z.-B. CHEN, AND J.-W. PAN, *"Experimental demonstration of a hyperentangled ten-qubit Schrödinger cat state,"* arXiv:0809.4277 . 131

[234] M. D. LUKIN AND A. IMAMOĞLU, *"Nonlinear Optics and Quantum Entanglement of Ultraslow Single Photons,"* Phys. Rev. Lett. **84,** 1419–1422 (2000). 131

[235] M. LUKIN AND A. IMAMOGLU, *"Controlling photons using electromagnetically induced transparency,"* Nature **413,** 273–276 (2001). 131

[236] I. FRIEDLER, G. KURIZKI, AND D. PETROSYAN, *"Giant nonlinearity and entanglement of single photons in photonic bandgap structures,"* Europhys. Lett. **68,** 625–631 (2004). 131

[237] C. ŚLIWA AND K. BANASZEK, *"Conditional preparation of maximal polarization entanglement,"* Phys. Rev. A **67,** 030101 (2003). 131

[238] P. Walther, M. Aspelmeyer, and A. Zeilinger, *"Heralded generation of multiphoton entanglement,"* Phys. Rev. A **75,** 012313 (2007). 131

[239] J. D. Franson, B. C. Jacobs, and T. B. Pittman, *"Quantum computing using single photons and the Zeno effect,"* Phys. Rev. A **70,** 062302 (2004). 131

[240] B. Julsgaard, J. Sherson, J. I. Cirac, J. Fiurasek, and E. S. Polzik, *"Experimental demonstration of quantum memory for light,"* Nature **432,** 482 – 486 (2004). 132

[241] T. Chaneliere, D. N. Matsukevich, S. D. Jenkins, S.-Y. Lan, T. Kennedy, and A. Kuzmich, *"Storage and retrieval of single photons transmitted between remote quantum memories,"* Nature **438,** 833 (2005). 132

[242] D. N. Matsukevich and A. Kuzmich, *"Quantum State Transfer Between Matter and Light,"* Science **306,** 663 – 666 (2004). 132

[243] B. Zhao, Y.-A. Chen, X.-H. Bao, T. Strassel, C.-S. Chuu, X.-M. Jin, J. Schmiedmayer, Zhen-Sheng, Y. S. Chen, and J.-W. Pan, *"A millisecond quantum memory for scalable quantum networks,"* Nature Physics **5,** 95 – 99 (2009). 132

[244] R. Zhao, Y. O. Dudin, S. D. Jenkins, C. J. Campbell, D. N. Matsukevich, T. A. B. Kennedy, and A. Kuzmich, *"Long-lived quantum memory,"* Nature Physics **5,** 100 – 104 (2009). 132

[245] M. Fleischhauer and M. D. Lukin, *"Quantum memory for photons: Dark-state polaritons,"* Phys. Rev. A **65,** 022314 (2002). 132

[246] M. D. Eisaman, A. André, F. Massou, M. Fleischhauer, A. S. Zibrov, and M. D. Lukin, *"Electromagnetically induced transparency with tunable single-photon pulses,"* Nature **438,** 837–841 (2005). 132

[247] K. S. Choi, H. Deng, J. Laurat, and H. J. Kimble, *"Mapping photonic entanglement into and out of a quantum memory,"* Nature **452,** 67–71 (2008). 132

[248] X. Maître, E. Hagley, G. Nogues, C. Wunderlich, P. Goy, M. Brune, J. M. Raimond, and S. Haroche, *"Quantum Memory with a Single Photon in a Cavity,"* Phys. Rev. Lett. **79,** 769–772 (1997). 132

[249] P. Kok, *"Limitations on building single-photon-resolution detection devices,"* IEEE: Sel. Top. Quantum Electronics **9,** 1498–1501 (2003). 132

[250] M. J. Fitch, B. C. Jacobs, T. B. Pittman, and J. D. Franson, *"Photon-number resolution using time-multiplexed single-photon detectors,"* Phys. Rev. A **68,** 043814 (2003). 132

[251] K. Banaszek and I. A. Walmsley, *"Photon counting with a loop detector,"* Opt. Lett. **28,** 52–54 (2003). 132

[252] E. Waks, K. Inoue, W. Oliver, E. Diamanti, and Y. Yamamoto, *"High-efficiency photon-number detection for quantum information processing,"* Selected Topics in Quantum Electronics, IEEE Journal of Quantum Electronics **9,** 1502–1511 (2003). 132

[253] D. Rosenberg, A. E. Lita, A. J. Miller, and S. W. Nam, *"Noise-free high-efficiency photon-number-resolving detectors,"* Phys. Rev. A **71,** 061803 (2005). 132

[254] D. F. V. James and P. G. Kwiat, *"Atomic-Vapor-Based High Efficiency Optical Detectors with Photon Number Resolution,"* Phys. Rev. Lett. **89,** 183601 (2002). 132

[255] A. Imamoḡlu, *"High Efficiency Photon Counting Using Stored Light,"* Phys. Rev. Lett. **89,** 163602 (2002). 132

[256] P. Kok, H. Lee, and J. P. Dowling, *"Single-photon quantum-nondemolition detectors constructed with linear optics and projective measurements,"* Phys. Rev. A **66,** 063814 (2002). 132

[257] M. Brune, S. Haroche, V. Lefevre, J. M. Raimond, and N. Zagury, *"Quantum nondemolition measurement of small photon numbers by Rydberg-atom phase-sensitive detection,"* Phys. Rev. Lett. **65,** 976–979 (1990). 132

[258] W. J. Munro, K. Nemoto, R. G. Beausoleil, and T. P. Spiller, *"High-efficiency quantum-nondemolition single-photon-number-resolving detector,"* Phys. Rev. A **71,** 033819 (2005). 132

[259] G. J. Pryde, J. L. O'Brien, A. G. White, S. D. Bartlett, and T. C. Ralph, *"Measuring a Photonic Qubit without Destroying It,"* Phys. Rev. Lett. **92,** 190402 (2004). 132

[260] G. Nogues, A. Rauschenbeutel, S. Osnaghi, M. Brune, J. M. Raimond, and S. Haroche, *"Seeing a single photon without destroying it,"* Nature **400,** 239–242 (1999). 132

[261] A. Politi, M. J. Cryan, J. G. Rarity, S. Yu, and J. L. O'Brien, *"Silica-on-Silicon Waveguide Quantum Circuits,"* Science **320,** 646–649 (2008). 132

Acknowledgements

Experimental physics is teamwork. During my time as a PhD candidate I was lucky to work with a number of people without who this Thesis would not have been possible. Let me take this opportunity to thank them for their continuing support and assistance.

First of all, I have to express my gratitude to Prof. Anton Zeilinger not only for giving me the chance to write my PhD Thesis in his wonderful group but also for allowing me the freedom to work on whatever project I found interesting. His open way of thinking and leading the group provided us all with an unrivaled research environment that enabled and facilitated many of the experiments in this Thesis.

At this point I would also like to thank Prof. Markus Arndt who was actually responsible that I chose a career in quantum optics and who was always willing to help and kindly offered his advice when asked.

I also want to thank the senior postdocs of our group that often served as close supervisors for my work. Thanks to André Stefanov, Philip Walther, Rupert Ursin, Markus Aspelmeyer, Thomas Jennewein, Felix Tiefenbacher and Nathan Langford for their help, advice and many encouraging discussions.

Many of the experiments reported in this Thesis have been performed in close cooperation with theoreticians and their successful realization would not have been possible without this special support. At this point a very big thank you goes to Mark Tame and Mauro Paternostro - without their brilliance, insight and never ending request for "more data" some of the experiments presented in this Thesis could never have come into existence.

In Vienna, my theory colleagues Caslav Brukner, Johannes Kofler and Tomasz Paterek certainly deserve to be mentioned for their willingness and patience when explaining to me the basics of quantum mechanics.

Pascal Böhi and Gunther Cronenberg, my two diploma students that closely worked with me in the lab during this time shall be thanked not only for their help and support but also for patiently enduring my ever changing moods during the emotional up and downs that are inevitable in such experiments.

My fellow PhD colleagues who endured with me the difficulties of grad school shall also be thanked: Thomas Scheidl, for the mutual experiments and the fun during our gym and running sessions, Johannes Kofler for his generous (theoretical) support and the many exciting discussions, Alessandro Fedrizzi, for the great fun on our conference trips and who like noone else understood to whine with me about the odds of physics and life. Xiao-song Ma, whose equipment I have often stolen, for his willingness to help and lend stuff, Simon Gröblacher,

for his help in organizing the students conference and for throwing the best parties in town, Rupert Ursin for teaching me the basics of experimental quantum optics and for the wonderful mountain trips and Rainer Kaltenbaek, who wrote most of the data acquisition software for my experiments. But also thanks to the whole Molecule group and the rest of the Quantum team for the amazing atmosphere, all the funny and/or stimulating discussions on physical and not-so-physical topics during coffee and lunch breaks.

Furthermore I want to thank my close friends who gladly distracted me from my work at the university and who got me outdoors on weekends: Herwig, Lukas, Sohmi - thanks for dragging me away from the institute every now and then and for reminding me that physics is not the most important thing in life.

But most of all I am grateful to my loving family. My parents, Helmut and Waltraud, for their invaluable support, encouragement and for simply always being there for me. My sister Eva for always cheering me up and for providing me with generous advice on all aspects of my life.

Finally, a special thank you goes to my girlfriend Evi for her love, understanding and patience during so many hours at the University and for her never ending support.

<div align="right">Robert Prevedel</div>

Curriculum vitae

Personal Information

Name	Robert Prevedel
Date and place of birth	June 16, 1981, Leoben, Austria
Citizenship	Austrian

Professional History

Since 01/2006	*Research and Teaching Assistant* Faculty of Physics, University of Vienna
02/2005 – 08/2005	*Visiting Scientist* QT lab, University of Queensland, Brisbane, Australia
07/2004 – 12/2005	*Scientific Co-worker* Faculty of Physics, University of Vienna

Education

Since 01/2006	Doctoral studies of Natural Sciences (University of Vienna)
10/2000 – 12/2005	Diploma studies of Physics (University of Vienna)
09/1999 – 04/2000	Obligatory military service
09/1991 – 06/1999	Grammar school (BRG Krems an der Donau)

Grants and Honors

2007	Merit Scholarship (University of Vienna)
2006	"KWA" Scholarship (Conference Grant, University of Vienna)
2006	'International Communication" Scholarship (Travel Grant, ÖFG)
2006	Merit Scholarship (University of Vienna)
2005	Joint Study Scholarship (University of Vienna)
2005	Top-Stipendium Exchange Scholarship (State of Lower Austria)
2003	Top-Stipendium Scholarship (State of Lower Austria)